Azobenzene Photoswitching in a Supported Lipid Bilayer Using $LiYF_4$ Upconverting Nanoparticles for Biological Applications

Paola Andrea Rojas Gutiérrez

A Thesis
In
The Department
Of
Chemistry and Biochemistry

Presented in Partial Fulfillment of the Requirements
for the Degree of Doctorate of Philosophy (Chemistry) at
Concordia University
Montreal, Quebec, Canada

September 2019

CONCORDIA UNIVERSITY

School of Graduate Studies

This is to certify that the thesis prepared

By: **Paola Andrea Rojas Gutiérrez**

Entitled: **Azobenzene Photoswitching in a Supported Lipid Bilayer Using $LiYF_4$ Upconverting Nanoparticles for Biological Applications**

and submitted in partial fulfilment of the requirements for degree of

DOCTOR OF PHILOSOPHY (Chemistry)

complies with the regulations of the University and meets the accepted standards with respect to originality and quality.
Signed by the final Examining Committee:

_____ Chair
Dr. Patrick Gulick

_____ External Examiner
Dr. Luigi Bonacina

_____ External to Program
Dr. William Bukowski

_____ Examiner
Dr. Christine DeWolf

_____ Examiner
Dr. Louis Cuccia

_____ Thesis Supervisor
Dr. John A. Capobianco

Approved by _____
Dr. Yves Gelinas, Graduate Program Director

September 25, 2019 _____
Dr. Andre Roy, Dean
Dean Faculty of Arts and Science

ABSTRACT

Azobenzene Photoswitching in a Supported Lipid Bilayer Using $LiYF_4$ Upconverting Nanoparticles for Biological Applications

Paola Andrea Rojas Gutiérrez, Ph.D.

Concordia University, 2019

Medical sciences have begun to focus their attention on the use of nanomaterials to improve diagnosis and treatment with the ultimate goal of moving into personalized medicine. The need to develop more efficient drug delivery systems motivated the development of the nanomaterial proposed in this thesis based on lanthanide doped upconverting nanoparticles (UCNPs).

Upconverting nanoparticles have the attractive optical property of higher energy light production from lower energy excitation. Upon near infrared (NIR) excitation, $LiYF_4:Tm^{3+}/Yb^{3+}$ upconverting nanoparticles produce emission in the ultraviolet (UV), visible and NIR. Surface modification of the nanoparticles with a supported lipid bilayer composed of phospholipids and cholesterol provided water dispersiblility and colloidal stability to $LiYF_4:Tm^{3+}/Yb^{3+}$ upconverting nanoparticles, while protecting the emission of the nanoparticle from water-derived quenching. Additionally, the supported lipid bilayer provided a drug-loading feature. Different electron microscopy techniques were used to characterize the supported lipid bilayer on the surface of the $LiYF_4:Tm^{3+}/Yb^{3+}$ upconverting nanoparticles and steady-state spectroscopy was used for the characterization of the emission of the nanoparticles.

The development of a dynamic photo-responsive supported lipid bilayer was achieved with the incorporation of an azobenzene-derivative lipid in the supported lipid bilayer at the surface of $LiYF_4:Tm^{3+}/Yb^{3+}$ upconverting nanoparticles to photo-control the drug release. Azobenzene is a photoswitching molecule that changes from its stable *trans*-isomer to the *cis*-isomer under UV irradiation. Upon NIR excitation, UV emission is obtained *in situ* from $LiYF_4:Tm^{3+}/Yb^{3+}$ upconverting nanoparticles and transferred to the azobenzene-derivative lipid,

triggering the photoswitching and disrupting the supported lipid bilayer. The dye Nile red was loaded in the supported lipid bilayer as a model drug and its photo-control release was studied. Upon 30 minutes of NIR irradiation, $LiYF_4:Tm^{3+}/Yb^{3+}$ upconverting nanoparticle transferred 23% of its energy to the azobenzene-derivative lipid, leading to 40% release of the dye encapsulated through the disruption of the photo-responsive supported lipid bilayer. Studies on the Förster resonant energy transfer (FRET) between $LiYF_4:Tm^{3+}/Yb^{3+}$ upconverting nanoparticles and the azobenzene-derivative lipid showed that the energy transfer mechanism is mainly radiative (*via* reabsorption of light). Measurements on the absolute quantum yields of the individual emissions bands of $LiYF_4:Tm^{3+}/Yb^{3+}$ determined that the quantum yields of the each of the emission bands are significantly different.

Cellular studies of this nanomaterial were conducted using alveolar lung carcinoma cells (A549) where the cellular uptake, cytotoxicity, endocytosis mechanisms and trafficking inside the cells were studied. The cellular uptake was studied as a function of the surface properties of $LiYF_4:Tm^{3+}/Yb^{3+}$, and as a function of incubation time using ICP-MS for the quantification of the nanoparticle internalization. Through inhibitory studies of the cellular endocytosis mechanism it was found that the clathrin-mediated, caveolae-dependent and an energy-independent pathway were the main internalization mechanisms. Additionally, the trafficking and photo-controlled release of the nanomaterial was studied using confocal microscopy taking advantages of the optical properties of $LiYF_4:Tm^{3+}/Yb^{3+}$ upconverting nanoparticles and the fluorescence of the dye Nile red. It was observed that the nanomaterial was trafficked to different organelles including the endoplasmic reticulum, Golgi apparatus, lamellar and lipid bodies. Upon NIR stimulation of the nanomaterial inside the lung cancer A549 cells, a fast release of Nile red, a model hydrophobic drug was produced from the photo-responsive supported lipid bilayer.

The studies herein contribute to the development of photo-responsive nanomaterials using lanthanide upconverting nanoparticles and enrich the understanding of the nanoparticle-cell interactions for the development and design of nanomedicines.

To my lovely parents Edith and Daniel,

and brothers Dani and Pipe

ACKNOWLEDGEMENTS

First and foremost, I would like to express my gratitude to my Ph.D. supervisor Professor John Capobianco. It was a journey of 7 years in his laboratory, the Lanthanide Research Group, where I started as a M.Sc. student and fast tracked into the Ph.D. program. I will always be thankful with Professor Capobianco for the constant support and for providing me with the control and freedom to explore my scientific curiosity while learning about nanoparticles and lipids from such diverse perspectives including chemistry, physics, and biology. Moreover, I am thankful for all the edits, suggestions and discussions to disseminate my work, from which I have been learning and continue to do so; because research is not fulfilled if the findings and knowledge are not shared. I have found Professor Capobianco's approach of research is driven by passion and curiosity. He is always present for a discussion and has the right question that guides the students to research in the proper direction, empowering them to become independent scientists. I am grateful for all this guidance and it has been a pleasure to work at the Lanthanide Research Group.

I would like to thank Professor Christine DeWolf for all her guidance, support, constant critical input, and for let me work at her laboratory. The discussions during and after the committee meetings were invaluable for the development of this project. I admire and respect her career as a woman in science and I am grateful to have worked with her.

I would like to thank Professor Louis Cuccia for the constructive comments during the committee meetings and for his invaluable help every time I was having a scientific query. The door of his office was always opened for an insightful discussion with a delicious cup of coffee. I appreciate and value our friendship after 7 years of coffees and great conversations.

I would like to extend my gratitude to my collaborators Professor Jan Seuntjens and Professor Norma Ybarra from the Medical Physics Unit at McGill to give me the opportunity to work at the Cancer Research Centre at the McGill University Health Centre where I was able to develop the cellular work. I would like to thank Professor Niko Hildebrant at the Centre of NanoBioPhotonics at Université Paris-Sud, Professor Sylvestre Bonnet at Leiden Institute of

Chemistry at Leiden University, Professor Andrey Turshatov at Institute of Microstructure Technology at Karlsruhe Institute of Technology, Professor Bryce S. Richards at Light Technology Institute at Karlsruhe Institute of Technology, Dr. Ute Resch-Genger Federal Institute for Materials Research and Testing (BAM) in Germany, and Professor Luis Carlos at the Aveiro Institute of Materials at University of Aveiro for their support and critical discussion in the different projects developed.

I want to extent my gratitude to all the experts in microscopy that trained me and guided me through troubleshooting. Jean-Philippe Masse at Centre de Charactérisation Microscopique des Matériaux $(CM)^2$ at Polytechnique Montréal, Dr. Kaustuv Basu and Jeannie Mui at Facility of Electron Microscopy Research at McGill (FEMR), and Dr. Min Fu and Shi-Bo Feng at the Molecular Imaging centre at MUHC.

I want to thank my lab colleagues (past and present) for making the lab environment enjoyable (#BFZ). So many years of reactions, lasers and discussions makes us become a family. Thanks for the craziness (in the good sense), constant support, and understanding during the down moments. Special thanks to Devesh Bekah and Dr. Dan Cooper for encourage me to do myself the cellular work, to teach me some biological techniques and for their friendship.

To my dear friend Gabi Mandl, our friendship that I will call it a sisterhood, began back in 2014 during her undergrad while I was the TA (through a discussion about pens). I don't know how to express all my gratitude for your constant support not only at the lab but also with some crazy ideas (lets organize a science fair, or lets do a road trip, or lets climb a mountain!). Thank you for the encouragement through the years and especially at the end being my best grammar editor and sending good vibes all the time! I have seen your scientific growth from undergrad to M.Sc. to Ph.D. student, and I am sure a great scientific future is waiting for you and we will be collaborating! I adore you.

I want to thank Professor Rafik Naccache (WBTY) for seeing skills on me that were beyond my scientific background and postulate me to be the first organizer for the annual NSERC Science Odyssey events at Concordia University in 2017. Also, I am grateful with Professor Kim Sawchuk for the brainstorm sessions, support and empowerment she gave me to develop the project. I learned about project management, logistics, gender equality, and it enlightened me on how outstanding the research is of the different departments of FAS at Concordia University. Also, working with the students from different departments changed my perspective of thinking. Thanks to all the Ph.D. students that joined the organizing committee (Darian Stahl, Gabi Mandl, Hala Youssef, Alan de Aguilar Lopes, Franklin Chacón Huete, and Emilie St. Hilaire), Liz Faure (communication advisor of the FAS), as well all the professors, technicians and volunteers from the different departments that helped in making each of the events successful. Nevertheless I want to thanks again my supervisor Professor John Capobianco for letting me develop this project while doing my Ph.D.

I want to thank the technical staff of the department of Chemistry and Biochemistry. Maria Dochia, thank you for your friendship, care and support during the years. Khalil Rahman, thank you for the support and for the good times teaching –I always found it refreshing working with you. Alain Tessier, thanks for the constant help at CBAMS running ICP-MS and LC-MS and for always accommodating me to run smoothly all the samples that I was bringing. Vincent Lau, thank you for helping with the XRD back in the days. Dr. Rolf Schmidt, thank you for your support and constant help while developing new setups (such as the webcam project for beam profiling!) and to teach me how to use some equipment at Professor DeWolf's lab.

I would like to extend my gratitude to the staff of the Science Technical Center. Dan Duru, Richard Allix and William Chicoine, thank you for your constant help during the years fixing the lab equipment or building new setups form my project that easier the way to design my experiments, which helped me to develop and accomplish my goals.

I also want to thank the administrative staff of the Chemistry and Biochemistry department for their support through the years to help me keep my degree on track. Lisa

Montesano, Hillary Scuffell, and Maria Ciaramella thank you for your help with forms, datelines, solving questions, keys etc.

I want to extend my gratitude to Miriam Posner for all the help through the years trying to find the right lab equipment for my experiments or helping find the right person to fix our equipment always in a fast and efficient way. Also, thank you for mentoring me while organizing Science Odyssey in 2017. Elvis Tzanetakos and Donna Craven, thank you for always being helpful and friendly when I was looking for my supervisor.

I always believe its the people that make a city great, thank you my incredible Montreal friends for welcoming me and making me feel at home being away 4,533 km away! To my climbing friends lets meet at the top, to my Latin friends lets go for a dance, to my volleyball friends lets smash some balls, to my running club friends don't stop, to my Concordia, McGill, UQAM, IRNS friends thank you for sharing your graduate school experience that made understand that this journey has hard moments not matter the field and to show me to be strong! THANK YOU my dear friends for your friendship, support, understanding and good times!

To my lovely big family, gracias por su continuo apoyo durante este periodo de mi vida realizando mi doctorado. A mi Mamita y mi Papito gracias por toda la educación que me han dado y por mostrarme que trabajando con disciplina y constancia se pueden alcanzar grandes metas, sin su ejemplo y gran trabajo no hubiera podido llegar hasta acá. Gracias por su constante cariño por confiar y creer en mí. A mis hermanos Dani y Pipe, gracias por distraerme o animarme cada vez que lo necesité, y por estar siempre presente. A mi abuelita Mamá Cecilia, gracias por su ejemplo y amor, por pedirle a Dios que me cuidara todo este tiempo. Su ejemplo siempre lo he tenido presente el de una mujer independiente que sacó a su familia adelante. Los amo!

Finally, I would like to thank all the funding during the years: Programa Crédito-Beca Colfuturo (Loan-Scholarship Colfuturo, Colombia) (2012-2014), Concordia University International Tuition Fee Remission Award (2014-2016), Concordia University Partial Tuition

Scholarship for International Students (2014 and 2015), Triskelion Fellowships in Chemistry and Biochemistry at Concordia University (2016), Power Corporation of Canada Graduate Fellowship (2017), Concordia University Conference and Exposition Award (2018) and Concordia Accelerator Award (2019).

In loving memory of my grandma

Luz Ena Mora de Rojas (1929-2019)

"Don't let the behaviour of others destroy your inner peace…

…The purpose of our lives is to be happy"

Dalai Lama

Blue Flower of Hope and Strength

Picture by Daniel Rojas at 4,800 m Mount Everest, Nepal

TABLE OF CONTENTS

AUTHORS CONTRIBUTIONS

The following summarizes the contributions of each author cited in this thesis.

CHAPTER 2: "Formation of a Supported Lipid Bilayer on Faceted $LiYF_4:Tm^{3+}/Yb^{3+}$ Upconversion Nanoparticles"

P. A. Rojas-Gutierrez: experimental work and manuscript preparation

C. DeWolf: project collaborator

J. A. Capobianco: project supervisor

CHAPTER 3: "A Route to Triggered Delivery *via* Photocontrol of Lipid Bilayer Properties Using Lanthanide Upconversion Nanoparticles"

P. A. Rojas-Gutierrez: experimental work and manuscript preparation

S. Bhuckory: aided in experimental work

C. Mingoes: aided in experimental work

N. Hildebrandt: project collaborator

C. DeWolf: project collaborator

J. A. Capobianco: project supervisor

CHAPTER 4: "Absolute Upconversion Quantum Yields of Blue-Emitting $LiYF_4:Tm^{3+}/Yb^{3+}$ Upconverting Nanoparticles"

M. S. Meijer: experimental work and manuscript preparation

P. A. Rojas-Gutierrez: aided in experimental work

D. Busko: aided in experimental work

I. A. Howard: aided in experimental work

F. Frenzel: aided in experimental work

C. Würth: aided in experimental work

U. Resch-Genger: project collaborator

B. S. Richards: project collaborator

A. Turshatov: project collaborator

J. A. Capobianco: project supervisor

S. Bonnet: project supervisor

CHAPTER 5: "Cellular Uptake, Cytotoxicity and Trafficking of Supported Lipid Bilayer Coated Lanthanide Upconverting Nanoparticles in Alveolar Lung Cancer Cells"

P. A. Rojas-Gutierrez: experimental work and manuscript preparation

D. Bekah: aided in experimental work

J. Seuntjens: provide the facilities at MUCH to preformed the cellular work

C. DeWolf: project collaborator

J. A. Capobianco: project supervisor

CHAPTER 6: "Thermal Properties of Lipid Bilayers Determined Using Upconversion Nanothermometry"

A. R. N. Bastos: experimental work and manuscript preparation

C. D. S. Brites: aided in experimental work

P. A. Rojas-Gutierrez: aided in experimental work

C. DeWolf: project collaborator

R. A. S. Ferreira: project collaborator

J. A. Capobianco: project supervisor

L. D. Carlos: project supervisor

LIST OF FIGURES

LIST OF SCHEMES

LIST OF TABLES

LIST OF ABBREVIATIONS

A549	Human alveolar carcinoma epithelial cells
AZO	Azobenzene
AZO-lipid	di(6-{[4-(4-butylphenyl)azo]-phenoxy}-hexyl)phosphate
Chol	Cholesterol
DOPA	1,2-dioleoyl-sn-glycero-3-phosphate
DOPC	1,2-dioleoyl-sn-glycero-3-phosphocholine
FRET	Förster resonant energy transfer
FTIR	Fourier-transform infrared spectroscopy
ICP-MS	Inductively coupled plasma mass spectrometry
Ln	Lanthanide
LSCM	Laser scanning confocal microscopy
NIR	Near infrared
NR	Nile red
PEG	Polyethylene glycol
PDT	Photodynamic therapy
SEM	Scanning electron microscopy
SLB	Supported lipid bilayer
TEM	Transmission electron microscopy
TGA	Thermogavimetric analysis
UCNPs	Upconverting nanoparticles
UV	Ultraviolet
VIS	Visible
XRPD	X-ray powder diffraction

Chapter 1

General Introduction

The concept of nanotechnology started with the visionary ideas of Richard Feynman in 1959, explained during his lecture "There's Plenty of Room at the Bottom".[1] He proposed the development of small machines, which could potentially be developed at the atomic scale.[1] He even visualized their use in medicine as a way to cure heart diseases by introducing a small "mechanical surgeon" inside a blood vessel to go into the heart and solve a problem.[1] He proposed to scientists listening to his lecture to consider designing objects that could manoeuvre at the cellular level.[1] However, it was not until 1974 that Norio Taniguchi proposed the term "Nano-Technology" during a conference in Tokyo.[2] The term was then popularized by Eric Drexler in 1986 with his book "Engines of Creation: The Coming Era of Nanotechnology".[3]

The vision of Feynman inspired the scientific community to start developing the field of nanotechnology, which has proven to be a powerful tool in many different fields including medicine. Nano-sized materials (nanomaterials) are on the size scale of many biological molecules that can gain entry to different tissue and cellular compartments, they are usually defined to be at least smaller than a 100 nm along one axis.[4] Nanomedicine focuses attention on the use of nanomaterials to improve diagnosis and treatment of diseases with the ultimate goal of moving into personalized medicine, where person-specific treatments can be developed.[5–8] It aims to enhance bioavailability, efficacy and controlled drug release during and after therapy, while reducing side effects.[5–7]

In 1962, while studying cell membranes and using phospholipid to model them, Alec Bangham was the first person to observe a liposome: closed bilayers composed of phospholipids in aqueous media.[9] Since this discovery, liposomes have been useful to study cell membranes in biophysical research. Later, in 1971, Gregory Gregoriadis proposed liposomes as drug delivery systems.[10,11] However, it was not until 1995 that the first liposome-based drug delivery system was approved by the Food and Drug Admiration (FDA) for cancer treatment.[12] This drug delivery system, called Doxil, was the first nanomedicine.[12] Doxil carries the cancer drug doxorubicin and have shown to be superior than the free drug by decreasing cardiac toxicity and

some cases have shown to improve antitumour therapeutic effect.[12] Nowadays there are several clinically approved nanoscale drug delivery systems that have shown to reduce the toxicity of chemotherapeutics, however the therapeutic efficacy has not always been enhanced, and the treatments do not always work for every patient.[13] Moreover, even though most advances in nanomedicine have been focused towards cancer treatment,[7,14,15] the field is also developing treatments for other diseases such as arthritis,[16] atherosclerosis,[17] diabetes,[18] and cardiomyopathy.[19]

Nanoparticle-based drug delivery systems can also be designed with stimuli-responsive features to produce drug release under exogenous stimuli such as photo-irradiation, heat, ultrasound or X-rays.[7,20] The design of these nanomaterials could provide control of the drug release and reduce spontaneous and/or premature drug leakage due to internal uncontrollable biochemical changes such as pH, redox potential and enzyme degradation. Nanoparticles with optical, electrical or magnetic properties can be used to develop nanomaterials with potential use in nanomedicine with exogenous stimuli.[20,21] Additionally, nanoparticles offer a high surface area to volume ratio that can be used with subsequent surface modification to provide different physicochemical properties that could control the interactions of nanoparticles with cells and organs.[22]

Light is non-invasive and offers control both spatially and temporally when compared to other exogenous stimuli. Lanthanide-based nanoparticles have attracted attention as nanomaterials with great potential for biological and medical applications due to their optical properties.[23,24] Lanthanide doped upconverting nanoparticles (Ln-UCNPs) consist of a crystalline inorganic host matrix doped with lanthanide ions. These nanoparticles have the ability to absorb and convert near-infrared (NIR) light to visible/UV/NIR light efficiently through an upconversion process. They present high photo-stability, multi-wavelength emissions and large anti-Stokes shifts that leads to many unique advantages such as low background auto-fluorescence, deep light penetration depth in tissues and minimal photo-damage to living organisms.[25] Additionally lanthanide-based nanoparticles can be doped with paramagnetic ions such as Gd^{3+} to develop materials with both optical and magnetic properties.[26] Recently,

lanthanide-based nanoparticles synthesized with ions with high atomic number such as Lu^{3+} have shown radioluminescence properties.[27,28]

With respect to biological applications, Ln-UCNPs could be used to optimize treatments such as chemotherapy and photodynamic therapy (PDT) while decreasing the side effects of conventional cancer therapies. For example, Ln-UCNPs can be used to develop nanoparticle-based drug delivery systems with photo-irradiation stimuli to either control the drug release or activate a drug using NIR light.[29,30] Additionally, taking advantage of the different properties that lanthanide-based nanoparticles offer, there is the potential to develop materials which can both act as bioimaging probes and drug delivery systems. The potential for Ln-UCNPs to be dual-purpose nanomedicines, which could diagnose and treat diseases simultaneously could revolutionize how medical treatments are performed today.

1.1 THEORY

1.1.1 The Lanthanides

The lanthanides (Ln) are the series of elements in the periodic table with atomic numbers 57 (lanthanum, La) to 71 (lutetium, Lu). Scandium and yttrium are also often included in the group due to their similar properties, and thus are collectively referred to as the lanthanoids. Their discovery goes back to 1787 when Carl Axel Arrhenius discovered a black stone and named it Ytterbite after Ytterby (Sweden), the place where the stone was found. Shortly after, in 1794, Johann Gadolun extracted yttrium oxide from Ytterbite and named it Yttria, which was the first lanthanoid compound to be isolated. However, it was not until 1828 that Friedrich Wöhler was able to first isolate the yttrium element.[31] All of the lanthanoids were discovered during the 19th century except for promethium, which is radioactive and was only discovered in 1945.[31]

The electron configuration of the lanthanides ranges from [Xe] $5d^1 6s^2$ for lanthanum to [Xe] $4f^{14} 5d^1 6s^2$ for lutetium. The most prevalent (and usually the most stable) configuration for the lanthanides is the 3+ oxidation state, which leaves the trivalent ions with an electronic configuration of [Xe] $4f^x$ (i.e. [Xe] for La, [Xe] $4f^1$ for Ce to [Xe] $4f^{14}$ for Lu).[32] The $4f$ electrons have a poor nuclear shielding ability which causes the outer-shell electrons ($5s$, $5p$) to be more attracted to the nucleus, producing the lanthanide contraction effect (reduction in size when increasing atomic number).[32] In addition, the $4f$ orbitals are protected from external influences by the $5s^2$ and $5p^6$ filled orbitals, which extend out further from the nucleus than the $4f$ orbitals. In other words, the $4f$ electrons are shielded from the external chemical environment. It is due to the shielding property that the lanthanide ions retain their free ion-like emission even when they are in a crystal field.[32] Materials containing lanthanide ions are known to exhibit sharp and narrow emission bands similar to the ones observed in gas spectra, because the $4f \rightarrow 4f$ transitions are not affected to a significant extent by crystal field splitting when they are incorporated into a material.[32]

In principle, the $4f \rightarrow 4f$ electric dipole transitions for lanthanide ions are forbidden according to Laporte's parity selection rule (electronic transitions must be accompanied by a change in parity).[32]

However, Van Vleck in 1937 discovered that the electric dipole transitions of the $4f^n$-states could have an admixture component of the $4f^{n-1}5d$ configuration inducing an opposite parity and allowing the transition.[33] The admixture of the 5d states with the 4*f* states is induced by the odd parity components of the crystal field.[32] In asymmetrical crystal fields the optical transition probabilities increase because the perturbation between states of opposite parity is greater, allowing the parity-forbidden $4f \rightarrow 4f$ electric dipole transitions to occur.[32] On the other hand, the magnetic dipole transitions are allowed and are not that affected by the crystal field symmetry.[32]

The 4*f* electronic states of the trivalent lanthanide ions are usually denoted by the Russell-Saunders notation with the symbol $^{2S+1}L_J$.[34] In this notation, S is the total spin ($2S + 1$ is the spin multiplicity), L is the total orbital angular momentum and J is the total angular momentum ($J = L \pm S$). Although the optical properties of the trivalent lanthanide ions do not change significantly with the chemical environment, the crystal field can induce some splitting of the energy levels. The maximum splitting occurs at $(2J + 1)$ if J is an integer or $(J + 1/2)$ if J is a half integer.

The trivalent lanthanide ions have electronic states with a ladder-like energy structure, and the parity-forbidden $4f \rightarrow 4f$ transitions exhibit long lifetimes (from milliseconds to microseconds). These two properties have made it possible to develop lanthanide-based materials which exhibit an interesting optical phenomenon known as upconversion, which has been used for a wide variety of applications. For example, these materials have been used in optoelectronics,[35,36] display technology,[37] solar energy harvesting,[38] and biomedical applications.[39]

1.1.2 Lanthanides Upconverting Nanoparticles

Lanthanide upconverting nanoparticles (Ln-UCNPs) exhibit an anti-Stokes process. These nanoparticles absorb low energy excitation, typically 980 nm, and emit high energy light *via* a multiphoton sequential absorption process known as upconversion. This process is contrary to fluorescence, which follows the Stokes law –the excitation photons are at higher energy than the emitted photons.

The emission wavelengths from Ln-UCNPs can be tuned by selection of an appropriate combination of trivalent lanthanide ions, dopant concentrations, and the host material. Fluorides host materials have been the overwhelming choice for upconversion since they have low energy-lattice phonons, which decrease the non-radiative relaxation and as a result increase the efficiency of upconversion emissions.[25]

1.1.2.1 Upconverting mechanisms

Four main upconversion mechanisms have been established: excited state absorption (ESA), energy transfer upconversion (ETU), cooperative upconversion, and photon avalanche.[40] Herein, excited state absorption and energy transfer upconversion, which are the two most efficient mechanisms, will be discussed.

1.1.2.1.1 Excited state absorption (ESA)

The excited state absorption mechanism involves the sequential absorption of at least two photons by one ion *via* the excitation of the ion to real, intermediate metastable energy levels, from where it can radiatively decay.[41,42] Figure 1.1 depicts the ESA mechanism, where the ion X in the ground state (G) is excited by an incoming photon resonant with energy equivalent to the energy gap between the ground state and the excited state (E1) thus promotes ion X to the first excited energy level (E1). A second photon, resonant with the energy gap between the first and the second excited state ($E_1 \longrightarrow E_2$), is absorbed and promotes the ion X to the second excited energy level (E2). From this excited energy level (E_2) the ion X decays radiatively to the ground state (G), releasing a photon of higher energy than the incoming photons used to excite the ion X

(upconversion). Most of the lanthanides have similar energy gaps between their excited sates (ladder-like structure) that allow this kind of mechanism using just a single pump source of photons with the same energy. However, using multiple sources of excitation could be possible when the energy gaps between the excited states are different.[41]

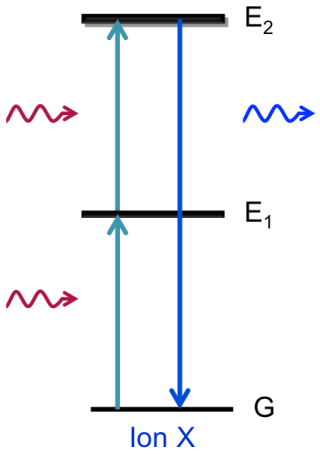

Figure 1. 1 The excited state absorption (ESA) mechanism

1.1.2.1.2 Energy Transfer Upconversion (ETU)

In 1966, François Auzel revolutionized the upconversion field when he proposed the l ' addition de photons par transferts d'energie (APTE) in the Yb^{3+}, Er^{3+} coupled system which, was later termed energy transfer upconversion.[40,43] Auzel demonstrated for the first time the possibility of upconversion from near infrared light to visible light using a the above mentioned coupled system in a glass.[44] He proposed that the energy transfer between two lanthanide ions in their excited states was possible. Before this, the energy transfer process was only considered with ions in the ground state.[40] These co-doped materials have shown to have a better upconversion efficiency than the other upconversion mechanisms.[40]

In the energy transfer upconversion mechanism, two ions are involved, referred to as a donor ion and an acceptor ion. The donor (or sensitizer) ion is excited with a pumping source and

then it transfers the energy to a second different ion called the acceptor (or activator), exciting the latter. This energy transfer process from the donor to the acceptor can then continue n-times through n-excited states of the acceptor ion, until the acceptor decays radiatively.[40] This process requires the acceptor ions to possess metastable states that act as population reservoirs to facilitate the energy transfer process. As well, the sensitizer ion requires a high absorption cross-section to facilitate its excitation.[42] Figure 1.2 shows the basics of the ETU mechanism. First, an incoming photon of an energy resonant with the energy gap of the donor (ion X) excites the ion X from the ground state to its exited state ($G \longrightarrow E_1$). The excited ion X transfers its energy (1-ET) to the acceptor ion (ion Y), promoting it from the ground state to the first exited energy level ($G \longrightarrow E_1$). A second donor ion X that is in its excited state can transfer energy (2-ET) to the already excited ion Y, promoting it from the first excited energy level to the second excited energy level ($E_1 \longrightarrow E_2$). Ion Y decays radiatively from the second excited energy level to the ground state ($E_2 \longrightarrow G$), emitting a photon with higher energy than the incoming photons used for the excitation (upconversion). It should be noted that the ESA and ETU processes could occur simultaneously, and are not mutually exclusive processes.

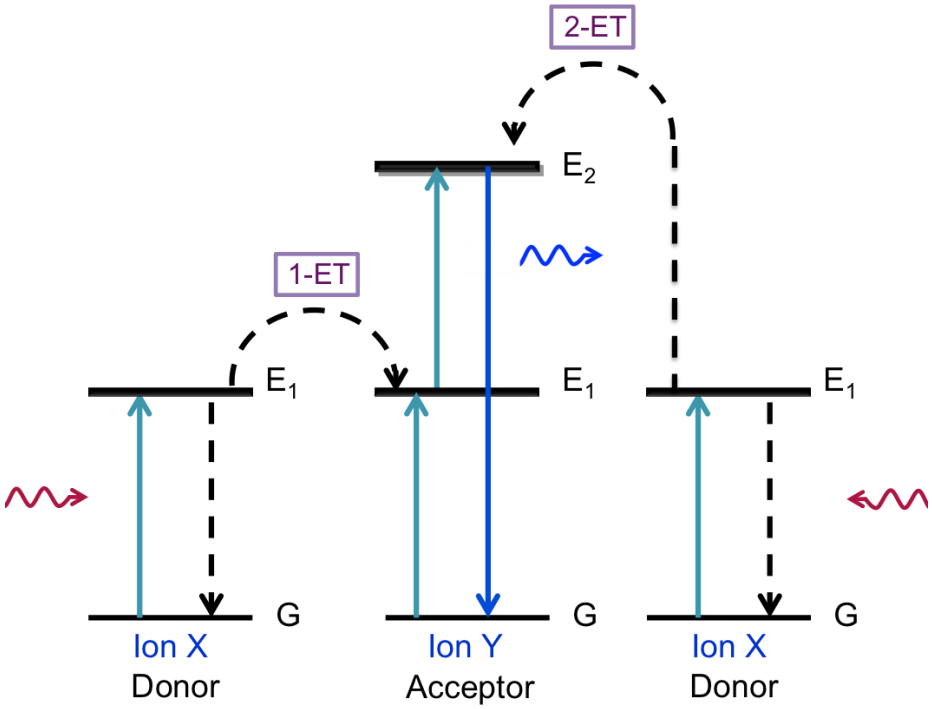

Figure 1. 2 Energy transfer upconversion (ETU) mechanism.

1.1.3 Energy transfer

As discussed previously for the ETU mechanism, an ion in the excited state can return to the ground state by transferring its energy to another ion. However, in order to produce the energy transfer between the ions, certain interactions are required. Herein, the ions will be called D (for donor) and A (for acceptor), and their excited states will be represented with (*).

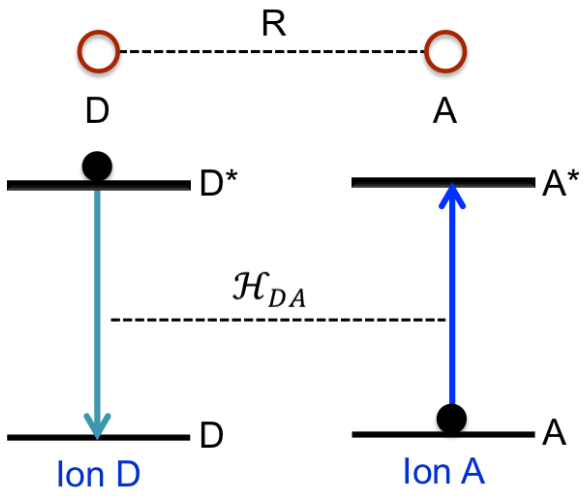

Figure 1. 3 Energy transfer between ion D (donor) and A (acceptor) at distance R. The energy level diagram, resonant between ions D and A, and the Hamiltonian interaction ($\boldsymbol{\mathcal{H}_{DA}}$) between the initial D* A and final A* D states.

Figure 1.3, represents two ions that are separated by a distance R. Ion D* is in the excited state and ion A is in the ground state. First, in order to transfer energy from D* to A, there has to be a resonance between the ions D and A. In other words, the energy difference between the ground state and the excited state of D and A has to be the same.[45] Experimentally, this could be observed when the emission spectrum of D overlaps with the absorbance spectrum of A. Second, there has to be an interaction between both ions, which could either be an exchange type, or a multipole-multipole type of interaction (i.e. electric dipole-dipole).[45] The exchange interaction depends on the wavefunction overlap (overlap of the atomic orbitals of both ions), which decreases exponentially with the distance between the ions. In the case of the multipole-multipole interactions, the intensity of the optical transition determines the strength of the interaction. However, it is difficult to determine exactly the type of interaction which is occurring.[45]

Dexter and Förster,[46,47] who worked separately on the theory of the energy transfer process during the 1950s, developed an equation to calculate the energy transfer rate (W_{ET}):

$$W_{ET} = \frac{2\pi}{\hbar} |\langle D^* A | \mathcal{H}_{DA} | D A^* \rangle|^2 \int g_D(\nu) \cdot g_A(\nu)\, d\nu \qquad (1.1)$$

The matrix component is the Hamiltonian interaction between the ions during the initial D*A state and the final DA* state, which is dependent on the distance between the ions. The integral component represents the spectral overlap between the emission spectrum of the donor $g_D(\nu)$ and the absorbance spectrum of the acceptor $g_A(\nu)$ as function of the frequency.[40,45,47,48]

When the excited ion D* decays to the ground state, it could occur *via* a radiative or non-radiative process (Figure 1.4).

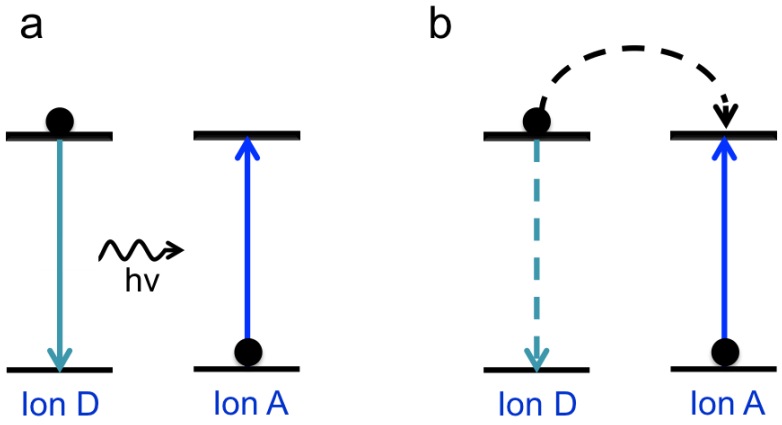

Figure 1. 4 Energy transfer processes between two ions D (donor) and A (acceptor). a) Resonant radiative transfer. b) Resonant non-radiative transfer.

The resonant radiative energy transfer process (Figure 1.4 a) occurs when D* decays emitting a photon, which is absorbed by A. The energy transfer results in the excitation of A from the

ground state to the excited state, which is followed by the emission of a photon by A* as it radiatively decays.[40,45,48] In order to facilitate the energy transfer process, the acceptor has to be within the travel-distance of the photon emitted by the donor. In other words, the ions do not need to be in close proximity as the radiative transfer process may permit long-range energy diffusion, but it would dependent on the shape of the sample.[40] Also, because the donor first emits a photon and then the photon is reabsorbed by the acceptor, the lifetime of the donor would not change because the population decay rate of the donor excited state is not affected. However, due to the spectral overlap between the donor and the acceptor, the intensity of the emission spectrum of the donor may change with the concentration of the acceptor because more light is being absorbed by the acceptor species.[40]

The probability of a resonant radiative energy transfer process can be expressed as follows:

$$W_{ET}(R) = \frac{\sigma_A}{4\pi R^2} \frac{1}{\tau_D} \int g_D(\nu) \cdot g_A(\nu)\, d\nu \tag{1.2}$$

where σ_A the absorption-integrated cross-section of the acceptor and τ_D is the lifetime of the donor. As there is no physical interaction between the donor and the acceptor, the expression depends on the photon density that the acceptor can absorb at a distance R from the photon flux that the donor emits.[40,48] Thus, in this kind of process its important to notice that the energy transfer rate will vary with the distance between the donor and the acceptor as R^{-2}.

On the resonant non-radiative energy transfer process, D* that is in the excited state, will transfer energy to the ion A, without emitting a photon, through an interaction (i.e. electric dipole-dipole) between both ions (Figure 1.4 b).[40,45,47,48] That energy transfer results in the excitation of A from the ground state to the excited state, which is followed by the emission of a photon by A*. This interaction will shorten the lifetime of the donor, as the transfer process can be regarded as an additional relaxation pathway of the donor excited state (D*). This energy transfer process is highly dependent on the distance between both ions. In the case of an electric dipole-dipole interaction, the energy transfer rate varies with the distance between the donor and the acceptor as R^{-6}. The rate of transfer can be expressed as follows:

$$W_{ET} = \frac{1}{\tau_D}\left(\frac{R_0}{R}\right)^6 \tag{1.3}$$

where R_0 is the Förster radius. R_0 is the critical distance where the radiative rate is equal to the non-radiative energy transfer. Then, if the distance between the ions D and A is greater than R_0 ($R > R_0$), the energy transfer will be most likely occur *via* a radiative process. While if the distance between the ions D and A is smaller than R_0 ($R < R_0$), the probability to have a non-radiative energy transfer process is greater.[40,45]

The quantum yield of the energy transfer process at the Förster radius is the fraction of the photons absorbed by the donor that are transferred non-radiatively to the acceptor.[49,50] This quantum yield is known as the Förster resonant energy transfer efficiency (E_{FRET}) and can be expressed as follows:[49,50]

$$E_{FRET} = 1 - \frac{\Phi_{DA}}{\Phi_D} \tag{1.4}$$

where Φ_D is the quantum yield of the donor, and Φ_{DA} is the quantum yield of the donor in the presence of the acceptor. Those quantum yields, which are the amount of photons emitted per photons absorbed, can be expressed as follows:

$$\Phi_D = \frac{W_D}{(W_D + W_{nr})} \tag{1.5}$$

$$\Phi_{DA} = \frac{W_D}{(W_D + W_{ET} + W_{nr})} \tag{1.6}$$

where W_D is the radiative decay of the donor, W_{nr} is the rate of non-radiative decays and W_{ET} is the rate of the FRET transfer. Substituting equations (1.5) and (1.6), into the equation (1.4) the FRET efficiency can be expressed as follows:

$$E_{FRET} = \frac{W_{ET}}{W_D + W_{ET} + W_{nr}} \tag{1.7}$$

as discussed above, the rate for a non-radiative energy transfer between a donor and an acceptor with a dipole-dipole interaction can be expressed in terms of the Förster radius. The FRET efficiency can be written as follows:

$$E_{FRET} = \frac{{R_0}^6}{{R_0}^6 + R^6} \tag{1.8}$$

The FRET efficiency can be measured experimentally *via* the donor emission intensities or lifetimes in the presence and absence of the activator:

$$E_{FRET} = 1 - \frac{I_{DA}}{I_D} \tag{1.9}$$

$$E_{FRET} = 1 - \frac{\tau_{DA}}{\tau_D} \tag{1.10}$$

where I_D and I_{DA} are the integrated areas under the emission curves of the donor alone, and the donor in the presence of the acceptor, respectively. In a similar way, τ_D and τ_{DA} are the lifetimes of the donor, and the donor in the presence of the acceptor, respectively.

The use of the FRET efficiency with the Förster radius has enabled the calculation of the distance between a donor and an acceptor. In molecular biology, the FRET efficiency has been used as a "spectroscopy ruler" to measure the distance between macromolecules.[49] The Förster radius between two molecules interacting *via* an electric dipole-dipole interaction has been defined as follows:[49–52]

$$R_0 = 0.02108\,(\kappa^2 \Phi_D\, n^{-4} J_{DA})^{1/6} \quad [nm] \tag{1.11}$$

$$J_{DA} = \int_0^\infty f_D(\lambda)\, \varepsilon_A(\lambda) \lambda^4 d\lambda$$

where κ^2 is the spatial orientation factor between the donor and the acceptor, n is the refractive index of the surrounding media, Φ_D is the quantum yield of the donor, and J_{DA} is the normalized spectral overlap integral of the emission spectrum of the donor $f_D(\lambda)$ and the absorption spectrum in terms of the absorption molar coefficient of the acceptor $\varepsilon_A(\lambda)$, and λ is the wavelength. The spatial orientation factor (κ^2) can vary between 0 and 4, depending on the position of the donor and the acceptor transition dipole moments. When the dipole moments between the donor and acceptor are at 90° (perpendicular) the value is zero, but when they are aligned at 0° (collinear) the value is 4.[50] However, due to the long lifetimes of lanthanides (from

microseconds to milliseconds) it is most likely that the donor and the acceptor would be rotating during the donor excited state, which bring $\kappa^2$to a value of 2/3 (dynamic averaging).[49]

The FRET transfer between two molecules has been reported up to distances of 10 nm.[53] For instance, using a lanthanide complex (donor) attached to one extreme of a DNA fragment, and a fluorescence dye (acceptor) at the other extreme, it was possible to measure the change of the DNA configuration in the presence of a protein for distances of up to 10 nm.[54] UCNPs can be used as an optical probe since the emissions produced can be used to transfer energy to different molecules. The distance between the nanoparticle and the molecule as well as their spectral overlap are important parameters for the energy transfer process. FRET efficiency measurements has been use widely to characterized the energy transfer process in this kind of systems.

1.1.4 Phospholipid bilayers

Phospholipids are biological amphiphilic molecules with two distinct regions of different polarity. The hydrophilic region composed of a phosphoric acid derivative group is called the head group, while the hydrophobic region composed of hydrocarbon chains is called the tail (Figure 1.5). Glycerophospholipids have a glycerol backbone with hydrocarbon chains at *sn*-1 and/or *sn*-2 position and the phosphate head group at the *sn*-3 position. Glycerophospholipids are commonly name by a shorthand designation that comes from the corresponding fatty acid derivative and the head group name. For example, 1,2-dioleoyl-sn-glycero-3-phosphocholine is named after oleic acid and its shorthand designation is DOPC (Appendix A contains the name of some shorthand designation of common lipids). When these molecules are dissolved in water at a concentration greater than a value known as the critical micelle concentration, they spontaneously form aggregates, which are organized structures of self-assembled molecules driven by their local interactions.

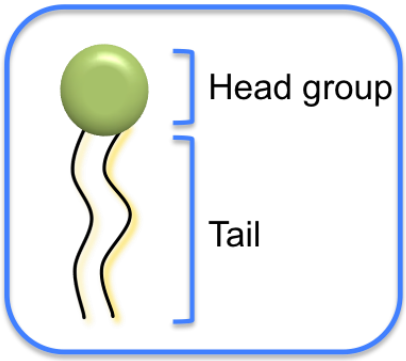

Figure 1. 5 Illustration of a phospholipid with double hydrocarbon chains.

The self-assembly of phospholipids into organized well-defined structures is driven by the free energy and the geometry of the molecules, and the thermodynamics of the system.[55] There are competing opposing forces in the phospholipid molecule when it is dissolved in water, around the head group the hydrophilic interactions with the aqueous environment tend to increase, while around the hydrophobic tail the interactions tend to decrease. As water molecules cannot form hydrogen bonds with the hydrocarbon tails to minimize the interaction, the water molecules reorganize in an ordered "cage" around the hydrocarbon tails (Figure 1.6).[56] This produces a decrease in the entropy of the system. In order to minimize the free energy, the hydrophobic tails aggregate in such a way to optimize the surface area per head group at which the total interaction free energy per phospholipid molecule is minimized (Figure 1.6).[55] This process is known as the hydrophobic effect. Depending on the molecular shape of the phospholipid molecule, different self-assembled structures can be formed.

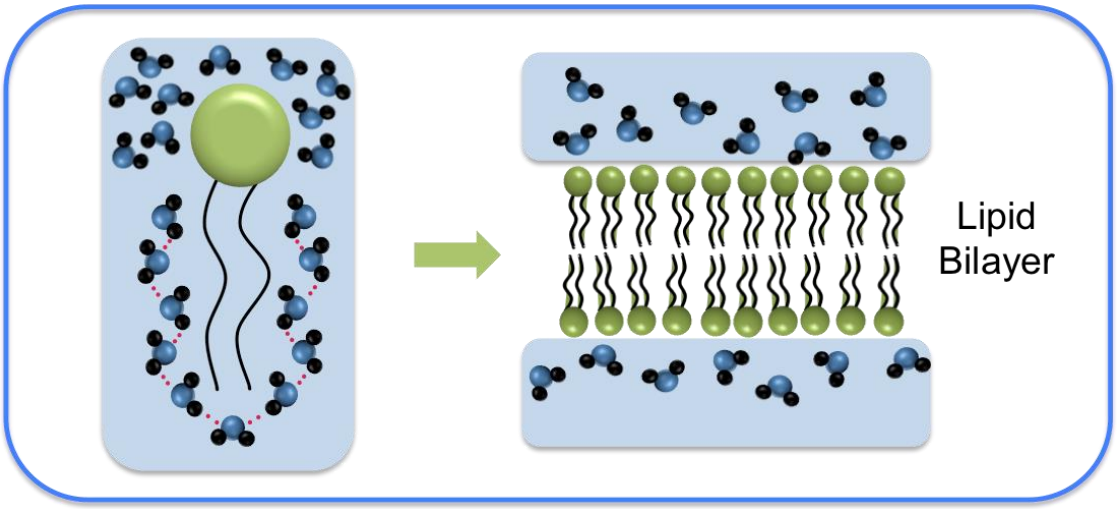

Figure 1. 6 Illustration of the hydrophobic effect. Left) Illustration of the rearrangement of water molecules when a phospholipid molecule is dissolved in water. Right) Self-assembly of phospholipids into a lipid bilayer, the head group optimized the interaction with water molecules while the hydrocarbon tails aggregate and minimize the interactions with the water molecules.

Israelachvili in 1992 proposed the packing parameter, a non-dimensional number, based on the geometrical features of the phospholipid molecular shape.[57] This number indicates the self-assembled structures that a particular phospholipids molecule could produce.[57]

The packing parameter ($\mathcal{P}$) can be defined as:

$$\mathcal{P} = \frac{v}{(a_o l_c)} \tag{1.12}$$

where v is the volume of hydrocarbon tails, a_o is surface area at the water-hydrocarbon interface, and l_c is the critical hydrocarbon chain length. For example, lipids with single chain and large head groups ($\mathcal{P} < 1$) have a cone-like packing shape that results in the self-assembly of spherical and cylindrical micelles. Lipids with small head groups and long tails ($\mathcal{P} > 1$) have an inverted cone-like packing shape and self-assemble in inverted micelles. Lipids with double-

chain ($\mathcal{P} \sim 1$) present a cylinder-like shape and usually self-assemble in lamellar structures that could be of the form of bilayer or liposome (Figure 1.7).

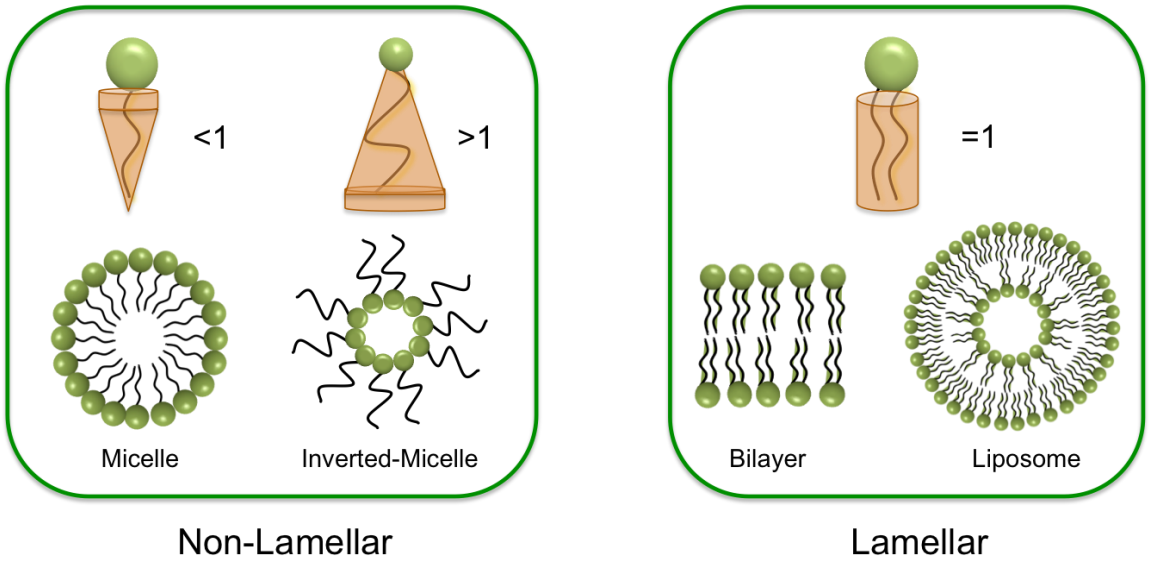

Figure 1. 7 Illustration of the packing parameter for different molecular shapes of lipids and the corresponding self-assembled structures.

There are different forces that generate a lateral pressure in the bilayer that keeps it assembled. The head group region has a repulsive component coming from entropic, steric and electrostatic interactions between the head groups.[58] The interfacial region, between the head group and the tails, has an attractive force due to the hydrophobic effect.[58] The tail region has an overall repulsive component arising from entropic and steric interactions between the hydrocarbon chains and a small attractive component from van der Waals interactions.[58] The head groups and the hydrocarbon tails produce a positive lateral pressure while the interface produces a negative pressure.[58] If the lateral pressure at the head group region is different from the one at the hydrocarbon tails region it generates a torque and the bilayer will tend to curl.[56,58] The bending

energy of a lipid bilayer will depend on the "spontaneous curvature" which results from an imbalance in the lateral pressure between the head group and the tails without compromising the interfacial region.[56,58] If the interfacial region is affected the structural stability of the bilayer will be affected.[56,58] One way to alter the lateral pressure on the bilayer is using phospholipids with a different size between the head group and the hydrocarbon tails. For example, small head groups, such as phosphatidic acid (PA) and phosphatidyl-ethanolamine (PE) or large head groups such as phosphatidylinositol (PI) could generate spontaneous curvature on the bilayer.[59]

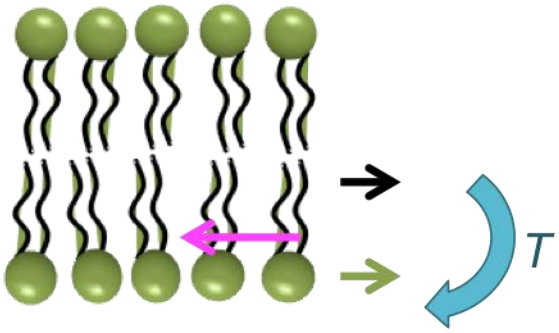

Figure 1. 8 Illustration of the lateral pressure in a lipid bilayer. Pink, black and green arrows represent the lateral pressure at the interfacial, hydrocarbon tails and head group regions respectively. (T, torque).

Lipids can present different phases depending on the temperature, pressure, hydration and their structural properties. The two main phases for lipids in lamellar structures are the gel solid phase (L_β) and the fluid liquid phase (L_α) (Figure 1.9).[56,60] In the gel phase, the hydrocarbon tails are stiff, fully extended, and packed, they can be either parallel to the bilayer, normal (L_β) or tilted ($L_{\beta'}$).[56,60] In the fluid phase, the hydrocarbon tails are packed but disordered and do not tilt. The transition temperature (T_m) is the temperature at which the lipid undergoes the phase transition from the gel phase to the fluid phase. Each type of phospholipid has its characteristic transition temperature, however it changes drastically with the unsaturation of the hydrocarbon tails; it is also affected (to a lesser extent) by the length of the hydrocarbon tail and the phosphate head

group. In general, at room temperature phospholipids with unsaturations in the hydrocarbon tails are in the fluid phase, while saturated phospholipids (depending on the length of the tail) are in the gel phase. The main reason is because the hydrocarbon chain with unsaturation kinks prevent tight packing, and the transition temperature is below 0 °C.

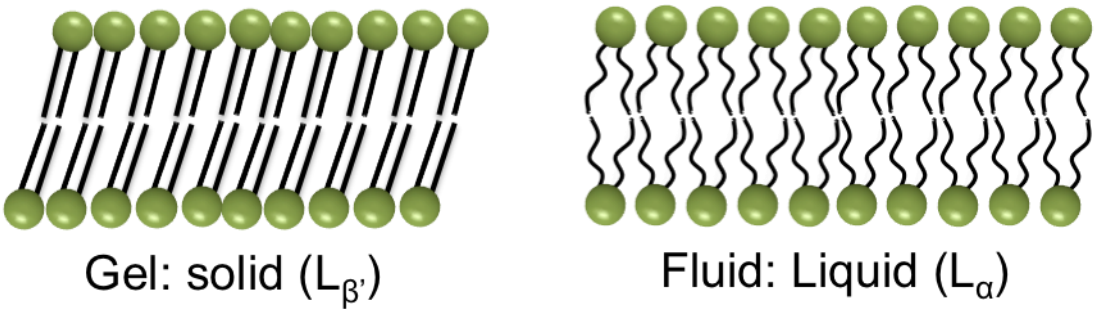

Figure 1. 9 Illustration of the phase behavior of lipid bilayers.

Incorporation of cholesterol inside lipid bilayers has shown to affect the packing and fluidity of the bilayer.[61] Cholesterol inside a bilayer tends to pack with the hydroxyl group close to the phosphate head group and with the sterol rings close to the hydrocarbon tails. When it is introduced in bilayers in the gel phase, it induces disorder and fluidized the bilayer. In contrast, in bilayers in the fluid phase, it induces order and rigidifies the bilayer (Figure 1.10).[61,62] The stiff sterol ring structure of cholesterol induces the hydrocarbon chains to orient perpendicular to the plane of the bilayer.[61,63] In the case of a fluid phase bilayer, the sterol rings produce a hydrophobic stabilization increasing the van der Waals interactions between the adjacent hydrocarbon chains, while in bilayers in the gel phase it decreases these interactions.[61,63] In addition, cholesterol has shown to increase the distance between the phosphate head groups, which in a bilayer with charged lipids helps to stabilize the electrostatic repulsions in the head group.[61,63] The maximum solubility of cholesterol in a lipid bilayer composed with lipids in the liquid phase, such as DOPC is 67 mole%, above this limit concentration cholesterol precipitates.[64]

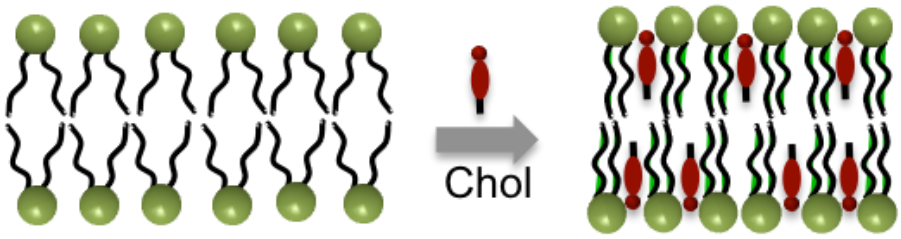

Figure 1. 10 Illustration of the condensation effect of cholesterol (chol) in a fluid phase lipid bilayer.

1.2 LITERATURE REVIEW

1.2.1 The $LiYF_4$: Tm^{3+}/Yb^{3+} UCNPs

$LiYF_4$ emerged in the 1960s as an alternative crystalline host material to $CaWO_4$ to study the emission bands of lanthanides ions and assign the transitions between the 4*f* states.[65,66] When Ln^{3+} ions substitute the Ca^{2+} ions a charged compensation is necessary, while substituting Ln^{3+} ions for Y^{3+} in $LiYF_4$ charge compensations is not required.[65,66] $LiYF_4$ proved to be an attractive material for solid-state lasers, for which this material was mainly used for several decades. It was not until 2009 that our laboratory synthesized UCNPs with $LiYF_4$ as the host material for the first time using the thermal decomposition method.[67] $LiYF_4$ has low phonon energies (424-566 cm^{-1}),[68] and a tetragonal crystal structure that allows the co-dopants Tm^{3+} and Yb^{3+} ions to produce strong upconversion in the UV, visible and NIR upon 980 nm excitation (Figure 1.11).[67] Other host materials such as $NaYF_4$ which have a cubic or a hexagonal crystal structure do not produce as strong UV emissions as the ones obtained with $LiYF_4$.[67] This could be due to the low symmetry of the tetragonal crystal structure that produces a greater crystal field splitting allowing more radiative transitions. For this reason, $LiYF_4$ is a particularly interesting host material for UCNPs when strong UV emissions are desired.

$LiYF_4$:Tm^{3+}/Yb^{3+} UCNPs exhibit two emission bands in the UV region, at 350 and 368 nm, and a weaker emission band at 290 nm. These bands are assigned to $^3P_0 \rightarrow {}^3H_6$, $^3P_0 \rightarrow {}^3F_4$, and $^1D_2 \rightarrow {}^3H_6$ transitions respectively. In the visible region, there are two blue emission bands centered at 450 and 480 nm, and a red emission band at 650 nm. These bands are assigned to $^1D_2 \rightarrow {}^3F_4$, $^1G_4 \rightarrow {}^3H_6$ and $^1G_4 \rightarrow {}^3F_4$ transitions, respectively. In the NIR region, an emission band centered at 800 nm is present corresponding to the transition $^3H_4 \rightarrow {}^3H_6$ (Figure 1.11).

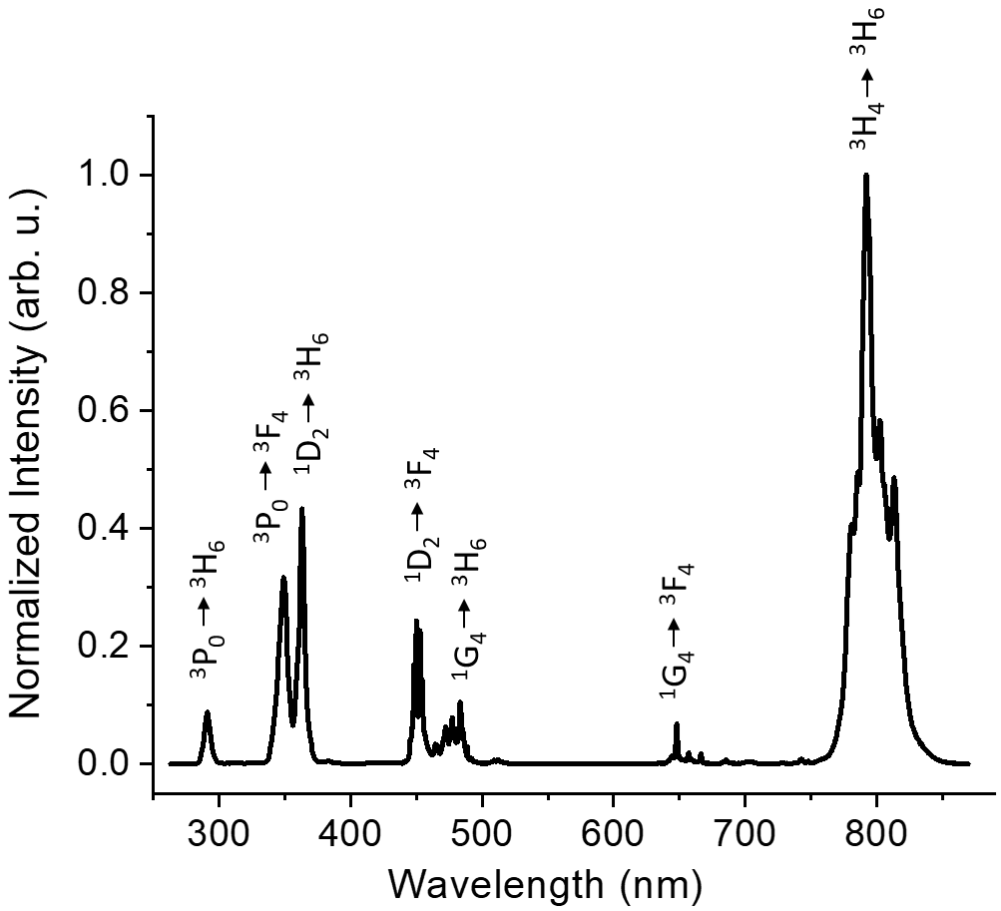

Figure 1. 11 Upconversion emission spectrum of $LiYF_4:Tm^{3+}/Yb^{3+}$ (0.5% Tm^{3+}, 25% Yb^{3+}) UCNPs in toluene excited at 980 nm.

The $LiYF_4$ is a particularly desirable host matrix for upconversion because the energy transfer process from Yb^{3+} to Tm^{3+} produce high energy emission in the UV, which requires the multiple photons. The energy transfer upconversion mechanism to produce the UV emission at 290 nm and 350 nm requires the population of the $^3P_0$ energy level of Tm^{3+} which is achieved upon absorption of 5 incident NIR (980 nm) photons. The population of the $^1D_2$, $^1G_4$, and $^3H_4$ energy levels requires 4, 3, and 2 incident photons, respectively, to produce the upconverted emissions. Mahalingam *et al*., proposed a phonon-assisted energy transfer mechanism in order to populate the $^3P_0$ energy level (Figure 1.12).[67]

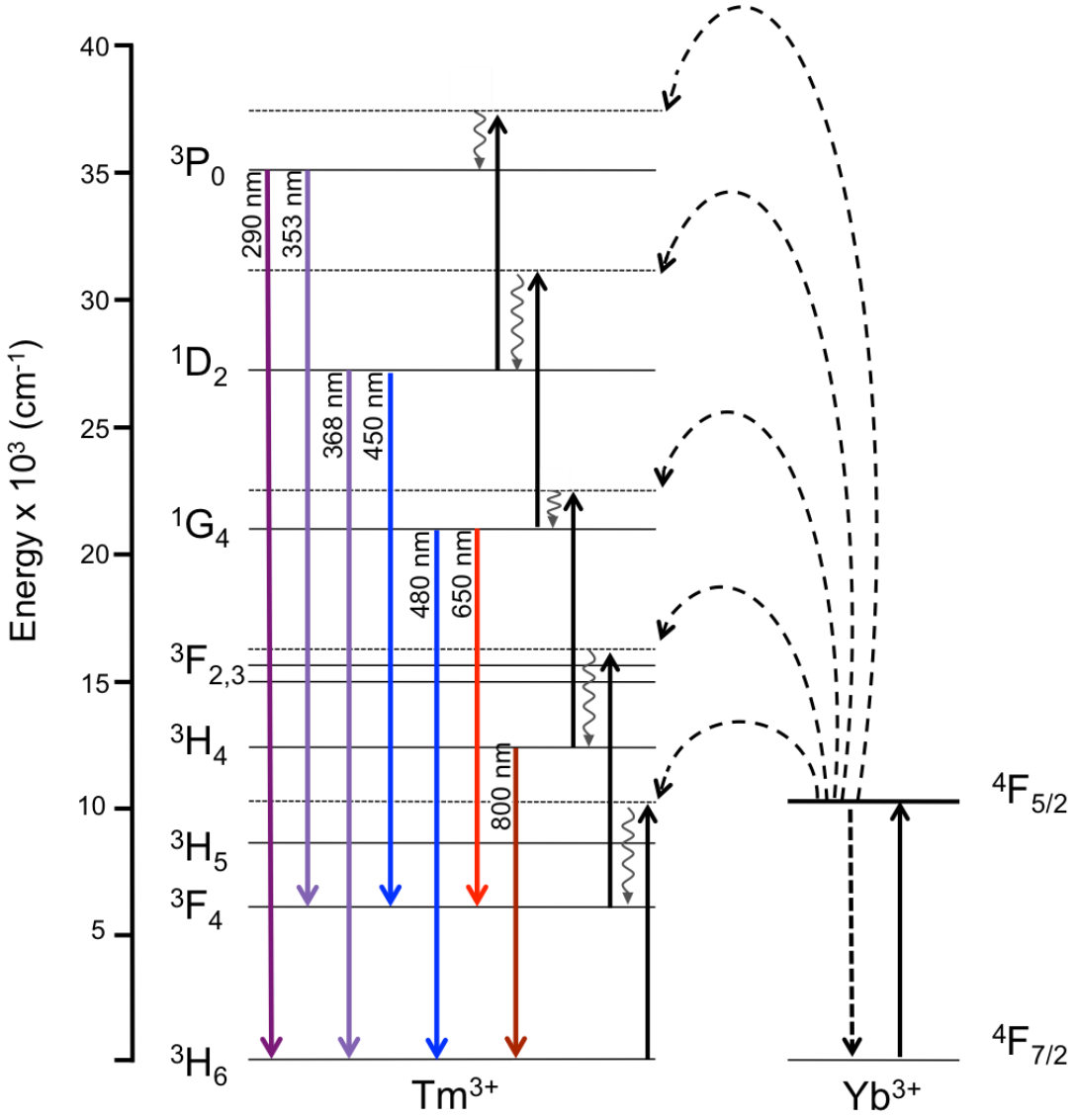

Figure 1. 12 Energy level diagram depicting the possible energy transfer upconversion mechanism for $LiYF_4:Tm^{3+}/Yb^{3+}$ UCNPs.

1.2.1.1 Biological applications of $LiYF_4:Tm^{3+}/Yb^{3+}$ UCNPs

Ln-UCNPs are attractive luminescent materials with considerable potential for biological applications. They present excellent photostability, narrowband photoluminescence, efficient anti-Stokes emission and long lifetimes.[69] In addition, lanthanides present low toxicity.[70] For example, lanthanide chlorides present a medium lethal dose (LD_{50}) values for oral administration of 5000-7650 mg/Kg/bw and for intraperitoneal injection of 440-585 mg/Kg/bw.[71] For *in vitro* and *in vivo* applications, one main advantage of these materials is that they utilize NIR excitation, which has a deeper tissue penetration in comparison to UV and visible light.[72] Also, NIR light exhibits low scattering within tissues, and does not induce auto-fluorescence of tissues, increasing the signal-to-noise ratio.[72] Due to these properties, Ln-UCNPs have been used for widespread investigations in different biological application such as bioimaging,[73] biosensing,[74] drug delivery,[29] photodynamic therapy,[30] and nanothermometry.[75]

In the particular case of $LiYF_4:Tm^{3+}/Yb^{3+}$ UCNPs, taking advantage of the emissions spanning such an extensive region, different emissions could potentially be used for different applications in the development of biological probes. For instance, the NIR emission at 800 nm could be useful for bioimaging, and the high energy emissions (i.e. the UV and blue) provides the opportunity to photo-control organic molecules *via* energy transfer.

When utilizing the high energy emissions of Tm^{3+} for photo-control of organic molecules, the efficiency of the energy transfer must be carefully considered. For the energy transfer process, in the $LiYF_4:Tm^{3+}/Yb^{3+}$ UCNPs the Tm^{3+} ions act as the donor and the organic molecule as the acceptor. As discussed previously, this phenomenon will depend on the distance between the Ln-UCNP (donor) and the organic molecule (acceptor), and the spectral overlap between the emission spectrum of the donor and the absorption spectrum of the acceptor. In our laboratory we have shown that this energy transfer process occurs from the UV and blue emissions of $LiYF_4:Tm^{3+}/Yb^{3+}$ UCNPs to organic molecules. For instance, energy transfer upon 980 nm excitation from $LiYF_4:Tm^{3+}/Yb^{3+}$ UCNPs to the photosensitizer Foscan® results in the production of singlet oxygen *via* the blue emission of the nanoparticle for application in photodynamic therapy. Also, upon 980 nm excitation, energy transfer from the UV emission of

the nanoparticle to organic molecules has been used to induce photo-cleavage and photoswitching reactions.[76,77] These investigations demonstrate the potential of these nanoparticles for use in the development of materials and systems for photo-mediated biological applications using NIR excitation.

1.2.2 Photoswitching

This is a reversible light-induced phenomenon in which molecules are transformed or "switched" between two states that have different absorption spectra.[76,78] Photoswitching has been observed in molecules that undergo either opening/closing or isomerization, such as in the case of spiropyran and azobenzene molecules, respectively.

1.2.2.1 Azobenzene

Bandara and Buredette provide an excellent review of the properties of azobenzene and its derivatives.[79] The absorption spectra of *cis*- and *trans*-azobenzene are different, however, they have some similarities. The *trans*-isomer has a strong π-π* transition near 320 nm and a weak n-π* band at 440 nm; the *cis*-isomer has a stronger n-π* transition at 450 nm and a less intense π-π* transition at 280 nm (Figure 1.13 a).[80] The *trans*→*cis* isomerization can be induced by UV light excitation and the *cis*→*trans* isomerization can be induced either by visible light, or it can occur spontaneously in the dark due to the thermodynamic stability of the *trans*-isomer. The photo-isomerization occurs at a faster rate than the thermal isomerization; this is an advantage because it is possible for the *cis*-isomer to exist for a period of time following irradiation before it switches back to the *trans*-isomer. Additionally, azobenzene shows photo-stability and it does not decompose under irradiation for prolonged periods of time.[79] Upon isomerization, there is a change in the dipole moment from 0 Debye (*trans*-isomer) to 3 Debye (*cis*-isomer) and a change in the configuration of the molecule.[81] The *trans*-azobenzene has a planar structure with a C_{2h} symmetry and the *cis*-azobenzene has a non-planar structure with a C_2 symmetry. That produces a change in the length of the molecule from 9.0 Å (*trans*-isomer) to 5.5 Å (*cis*-isomer) (Figure

1.13 b).[81] This change the geometry of the azobenzene molecule upon isomerization has been applied in the photo-control of biomolecules, such as the folding of peptides,[82] and in lipids to induce permeability in membranes.[83] However the need of UV light to induce the switching has limited its uses in *in vivo* applications.

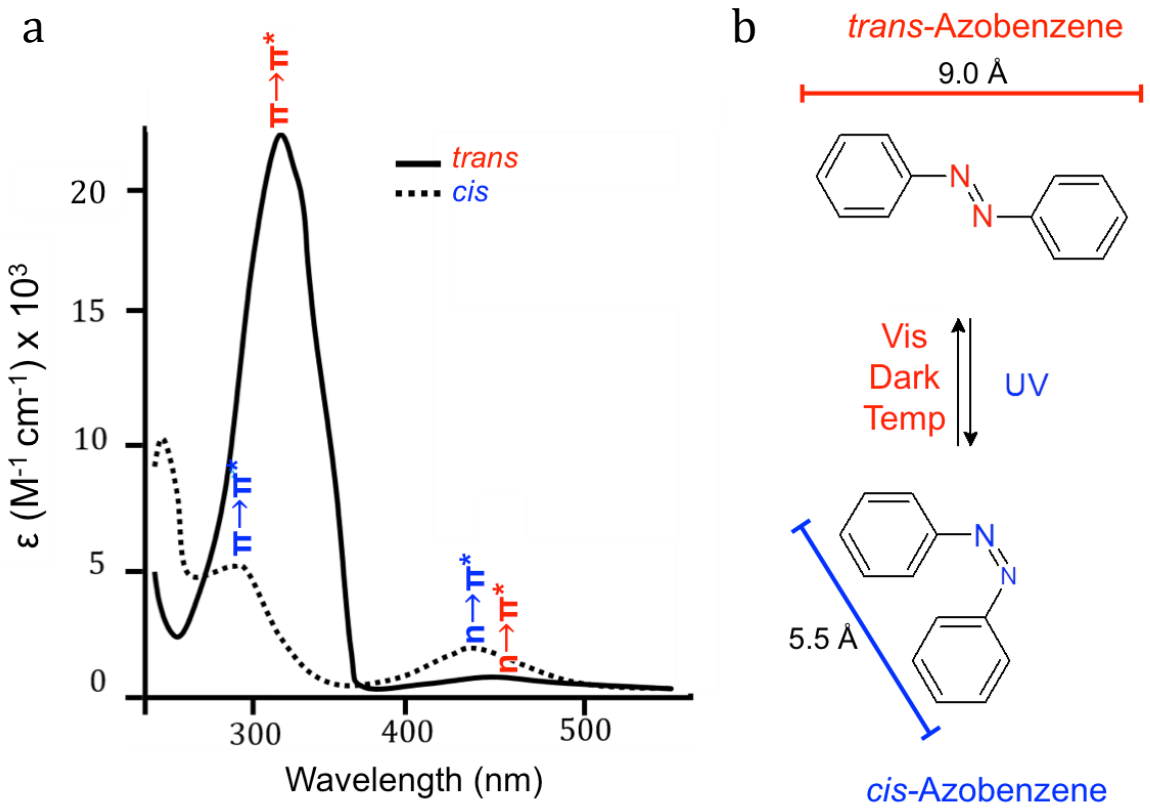

Figure 1. 13 Absorption sepectra of *trans*- and *cis*-azobencene molecule. b) chemical structure of *trans*- and *cis*-azobezene molecule. Figure (a) redrawn from Beharry and Wolley.[80]

1.2.3 Surface modification of nanoparticles

Because nanoparticles possess a high surface-to-volume ratio, their surface can be used as a scaffold for a nanoplatform, which can be chemically modified or "engineered" according to the desired application. Most synthetic protocols for the formation of high-quality Ln-UCNPs is performed using the thermal decomposition which produces nanoparticles that are capped by hydrophobic ligands. For biological applications, water dispersiblity, colloidal stability and biocompatibility are some of the most important requirements for the nanoparticles. In addition to these, solvent interactions with the surface of Ln-UCNPs has been shown to compromise the upconversion emission.[84] For instance, water molecules have high phonon energies from the O-H stretching vibrations, which can cause luminescence quenching.[84] Therefore, the surface modification of Ln-UCNPs can also be engineered to protect the optical properties of the nanoparticles in addition to acting as a nanoplatform for biological applications.

Several surface modification strategies for Ln-UCNPs have been reported in the literature, but they can be generally classified in two main groups, type-add and type-ex.[85] The type-add surface modification involves the addition of an amphiphilic molecule or silica to the already-existing capping ligand at the surface of the nanoparticle.[85] In contrast, the type-ex surface modification involves the complete exchange of the original capping ligand at the surface of the nanoparticle with a hydrophilic molecule.[85]

In the type-add modification, the hydrophobic part of the amphiphilic molecule interacts *via* van der Waals interactions with the capping ligand to produce the surface coverage. For instance, molecules or polymers such as DSPE-PEG_{2k} and poly(maleic anhydride) modified with dodecylamine (PMA), have been used in this approach to render $NaYF_4$ UCNPs water dispersible.[85] On the other hand, in the type-ex surface modification, first the capping ligand is removed from the surface of the nanoparticle and a hydrophilic molecule is grafted to the surface of the nanoparticle *via* electrostatic interactions. For example, oleate (the most commonly encountered capping ligand in Ln-UCNP synthesis) is grafted electrostatically *via* the carboxylate group to the positively charged surface of the Ln-UCNPs.[86] The surface of the nanoparticle has an overall positive charge due to the positive charge of Ln^{3+} ions and their

positions at the surface of the nanoparticle.[86] Different acid treatments have been proposed to achieve the removal of the oleate capping ligand. For instance, our laboratory proposed the removal of the oleate from the surface of the nanoparticles with an acidic solution of HCl at pH 4 to protonate the oleate and disrupt the electrostatic interaction with the surface.[86] Another well-known procedure is the removal of oleate with nitrosonium tetrafluouroborate ($NOBF_4$), which produces nitrous acid (HNO_2) and fluoroboric acid (HBF_4) *in situ.* [87] These procedures protonate the capping ligand to facilitate its removal from the surface of the nanoparticle. The second step of the type-ex surface modification requires the functionalization of small molecules or polymers containing negatively charged groups to the positively charged surface of the nanoparticle *via* electrostatic interactions. For example, citrate, and poly(acrylic acid) (PAA) have been used in this approach to render the nanoparticles water dispersible.[85] Additionally, another type-ex approach is the layer-by-layer (LbL) procedure.[85] The LbL consists of a sequential surface modification with polymers of different charges. The first step involves the surface modification using a negatively charged polymer, followed by the addition of a positively charged polymer (second layer), after which it could continue with many layers alternating negative to positively charged polymer layers. Usually between 2 to 5 layers of polymers are added using this procedure to produce water dispersability and control the surface properties of the nanoparticle, such as the surface charge.[85,88] Also, it has been reported as a method to improve biocompatibility if one of the layers is more cytotoxic it can be "hidden" by the external layers if those are less cytotoxic.[88]

1.2.4 Supported lipid bilayers coatings

Another approach to modify the surface of nanoparticles is *via* the use of supported lipid bilayers (SLB), which are continuous lipid membranes adsorbed on the surface of a solid substrate.[89] The surface modification with supported lipid bilayer using phospholipids on the surface of the nanoparticles could provide a greater biocompatibility to nanoparticles because of the natural properties of the lipids. In addition, due to the membrane-like behavior, the SLB could reduce the water penetration rate and also provide a space for the encapsulation of hydrophobic drugs. It

also allows for further surface modifications through the head groups of the phospholipids. In the next section, before describing how supported lipid bilayers are formed, the properties of phospholipids in lipids bilayers will be discussed.

1.2.4.1 Formation of supported lipid bilayers

The formation of SLB from the deposition of liposomes on top of a solid support was first proposed by McConnell's group in 1982 to study cell-cell interactions.[90] The mechanism of the SLB formation is *via* the adsorption, deformation and rupture of liposomes on the surface of the solid support.[91] When a liposome is deposited onto a solid support, it adsorbs to the surface and the contact area between the liposome and the support increases due to adhesion forces. The process continues until the liposome deformation passes its limit and breaks, then it spreads, forming the SLB (Figure 1.14). The spreading and coalescence of neighboring patches of bilayers on the support occurs thorough hydrophobic interactions at the edge of the bilayers, which have "active edges" due to the exposure of the hydrophobic core of the lipid bilayer to the aqueous environment.[91]

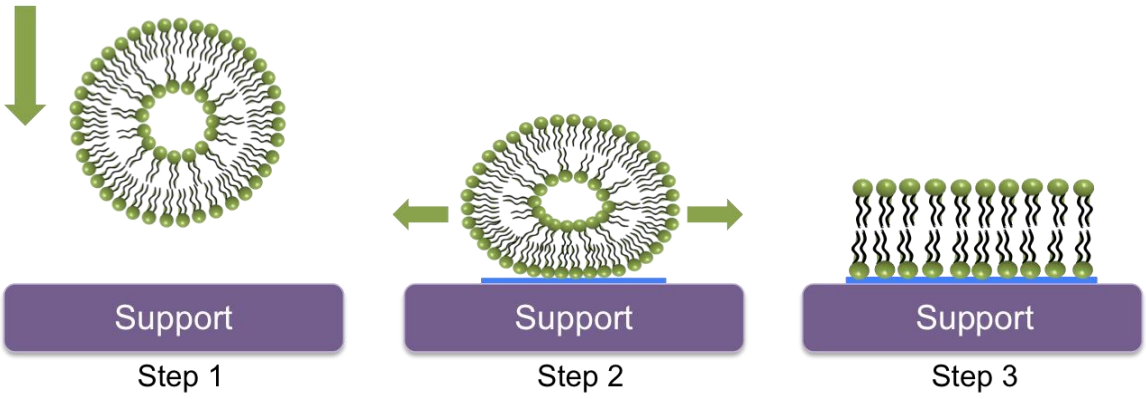

Figure 1. 14 Illustration of the formation of a supported lipid bilayer from the deposition of liposomes. Step 1: deposition of liposome on a solid support. Step 2: deformation and adhesion of the liposome on the solid support. Step 3: Liposome rupture and spreading to form the supported lipid bilayer.

The main force involved in the formation of SLB is the electrostatic interaction that leads to a strong attraction and adhesion between the bilayer and the solid support.[92] For example, one study on the formation of a SLB at the surface of a negatively charged silica support showed that liposomes with positive charged lipids (DOTAP) have a strong electrostatic interaction with the silica.[93] However, they did not form a homogeneous bilayer assembly on the silica support.[93] They found that elevated charge density of DOTAP do not provide sufficient lateral organization to produce the SLB assembly at the surface of the silica support.[93] In contrast, liposomes with mixtures of zwitterionic and negatively charge lipids (DOPC:DOPS (4:1)) allowed the assembly of the SLB with a good surface coverage. Additionally, they found that an increase in the negative charge lipid ratio inhibited the adsorption of the SLB on the negatively charged silica support.[93]

Mornet *et al.* investigated the formation of SLB on the surface of silica nanoparticles (SNPs) as a function of time in order to complete the surface coverage of the nanoparticle.[94] Using the same liposome formulation as in the previous study (DOPC:DOPS (4:1)), but mixing them with SNPs (110 nm), they found that the liposomes first adsorbed and deformed when they were in contact with the surface of the nanoparticle.[94] After some deformation of the liposome, it breaks, creating a patch of SLB at the surface of the nanoparticle. The process continues through the adsorption and deformation of different liposomes at the surface of the nanoparticles creating different patches of SLB at the surface of the nanoparticle.[94] The coalescence of neighboring patches of SLBs fuse *via* an active edge effect producing an homogeneous surface coverage of the nanoparticle.[91,94] Using cryo-TEM, they observed that the surface coverage with SLBs was homogeneous even if the nanoparticle surface has some imperfections.[94] Additionally, they also found that the electrostatic interaction between the SNPs and the liposomes was critical for the SLB formation, as well as the curvature of the nanoparticle.[94]

When decreasing the size of a spherical nanoparticle, the curvature at the surface increases. Therefore, the lipid bilayer must bend in order to adsorb to the surface of the nanoparticle. In extreme conditions with high curvature there is an increase in the void volume between the lipids of the outer leaflet, which decrease the hydrophobic interaction and therefore

affects the packing quality of the lipid bilayer. Studies have shown that lipids could reorganize to decrease the void volume to minimize water interaction with the hydrophobic core of the bilayer.[95,96] Ahmed *et al.* studied the effect of the curvature of spherical nanoparticles on the SLB formation.[95,96] They investigated SNPs with sizes between 100 and 5 nm and found that the packing of the SLB with DPPC changed when decreasing the size of the nanoparticle. They found in smaller-sized nanoparticles (15 nm) an increase in the acyl-chain organization, which was explained by lipid interdigitation in the bilayer.[96] This phenomenon decreases the void volume and improves the hydrophobic interaction between the acyl-chains of both leaflets, but decreases the bilayer thickness. However, in nanoparticles of 5 nm size the SLB did not cover completely the surface due to the high curvature of the nanoparticles. Instead, the authors observed the formation of aggregates, they hypothesized that these aggregates were nanoparticles connected with each other through SLB that acted as bridged structures.[96]

Savarala *et al*., study the SLB formation as function of lipid/SNPs surface area ratio.[97] They found that the formation of SLB with a completed coverage onto the nanoparticle surface was only obtained if the surface area of the lipid and nanoparticles was at least in a 1:1 ratio or in an excess of lipid.[97] However, for lipid deficit of up to 0.4:1, the nanoparticles were partially covered with SLB, but still stable in solution for a few days. For lower lipid ratios, the nanoparticles precipitate, producing SLB bridged structures between 2-5 nanoparticles.[97]

Different strategies have been reported for the formation of SLBs on the surface of nanoparticles.[98] The most common method involves the incubation or extrusion of nanoparticles with previously-prepared liposomes in aqueous solution as described above. However, using this method an ultrathin water layer is adsorbed between the SLB and the nanoparticle.[99] For a SLB using DMPC lipids on silica beads the water layer was measured to be 17 ± 5 Å.[99] One alternative to prevent the adsorption of water between the nanoparticle and the SLB is by using the "hydration of a dry lipid thin film" method, similar to the preparation of conventional liposomes. The nanoparticles are dispersed with the lipids in an organic solvent and form the dry lipid thin film by evaporation of the solvent. Following by hydration, extrusion or sonication the SLB is formed on the surface of the nanoparticles.[100,101]

Modification of the surface of lanthanide upconverting nanoparticles with SLB could provide greater biocompatibility and act as a barrier against water in order to prevent the luminescence quenching caused by the high phonon energies of water.

1.2.5 Azobenzene-modified lipids inside lipid bilayers

Azobenzene-modified lipids have been incorporated in the lipid bilayer of liposomes to photo-control the release of the encapsulated molecules under UV irradiation.[83,102–106] When azobenzene-modified lipids photoswitches (*trans*→ *cis*) inside the lipid bilayer under UV irradiation, it disrupts the packing of the lipid bilayer and produces the release of the encapsulated hydrophilic molecules from the aqueous core of the liposome (Figure 1.15).

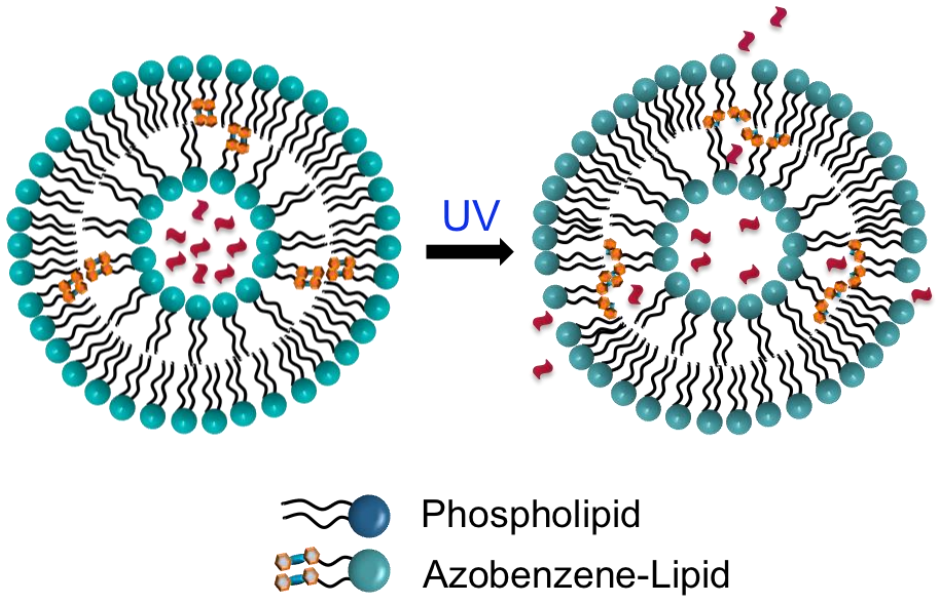

Figure 1. 15 Illustration of liposome with azobenzene-derivative lipid for the photo-control released of hydrophilic molecules. Redrawn from Morgan *et. al.*[102]

Different lipid compositions in combination with azobenzene-modified lipids have been used to prepare photo-responsive liposomes. It has been shown that formulations with gel-phase lipids requires at least 6 mole% of the azobenzene-modified lipid while in combination with fluid-phase lipids at least 20 mole% is required in order to disrupt the bilayer of the liposome and produce the release of the encapsulated molecules.[103,106] Additionally, the incorporation of cholesterol to induce a liquid-ordered phase has shown to increase the disruption effect of the bilayer under azobenzene switching.[107,108] There are reported formulations of up to 70 mole% of azobenzene-modified lipids.[103,104] However, the main challenge for these types of liposomes is to prevent leakage of the loaded drug over long periods of time when the mole% of azobenzene-modified lipids is increased.[83]

1.2.6 Nile red

Nile red **(**9-diethylamino-5H-benzo[α]phenoxazin-5-one) is a hydrophobic, solvatochromic fluorescent dye, which is highly sensitive to the polarity of its local microenvironment. The emission of Nile red varies from blue (484 nm for n-hexane) to red (638 nm for pentafluorophenol) depending on the polarity of the environment.[109] Nile red is poorly soluble in water and its fluorescence is quenched as a result. However, it is very soluble in lipids where it exhibits a strong fluorescence. Because of these properties, it has been widely used as a histochemical stain in cells and as a hydrophobic model drug for the study of potential drug delivery systems. Herein the fluorescence mechanism of Nile red and its biological applications will be discussed.

Nile red is a neutral molecule, which is planar along the benzo[α]phenoxazine conjugated system except for the diethylamino group at the 9-position. The diethylamino group has free rotation along the ethyl groups. In the excited state the molecule exhibits a large increase of its dipole moment. This has been attributed to a twisted intramolecular charge transfer (TICT).[110] The intramolecular charge transfer occurs from the amino group that acts as the donor to the oxo group in the conjugated system that acts as the acceptor.[110] In the excited state, the C-N bond between the conjugated system and the diethylamino group twist, producing an overlap of the

molecular orbitals of the donor and the acceptor.[110] This overlap hybridizes the donor/acceptor electronic states, allowing the intramolecular charge transfer to occur.[110]

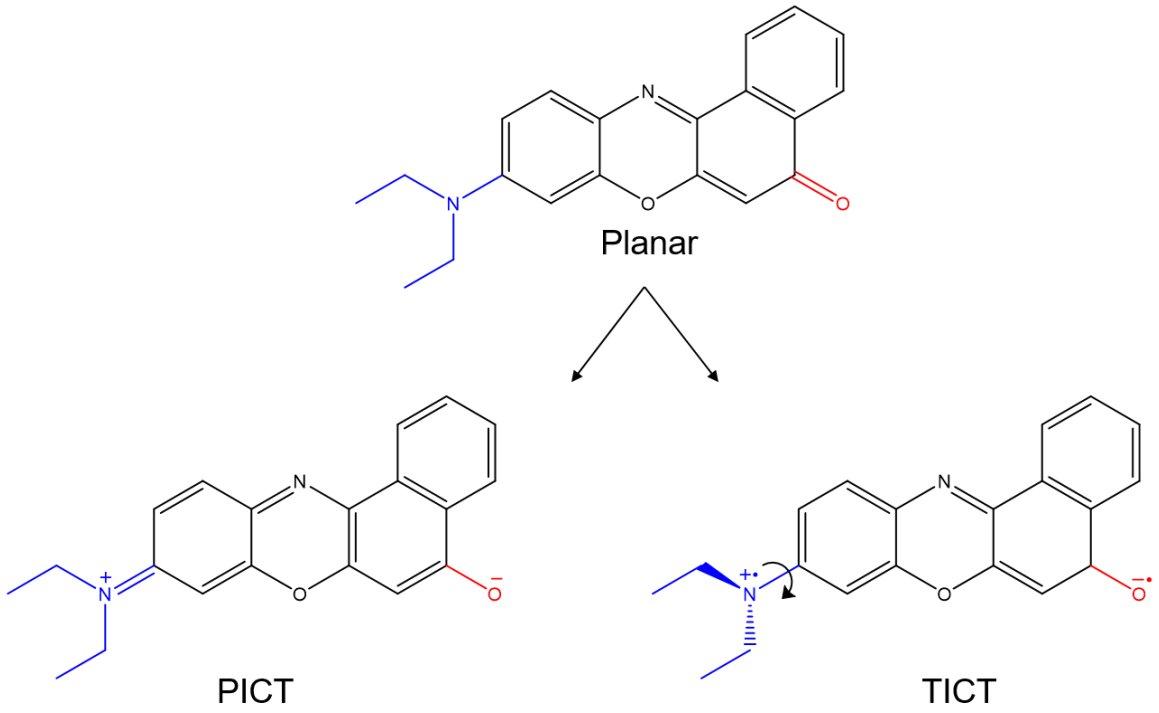

Figure 1. 16 Chemical structure of Nile red from the ground state to the two possible excited states, the planar intramolecular charge transfer (PICT) state and the twisted intramolecular charge transfer (TICT) state. Blue: donor group, red: acceptor group.

The solvatochromic property of Nile red occurs due to the stabilization of the excited state. Polar solvents with large dipole moments stabilize the TICT state to a greater degree than non-polar solvents. Therefore, in polar solvents the emission of Nile red is red-shifted, producing larger Stokes shifts while in non-polar solvents the emission is blue-shifted. It should also be noted that in polar environments the fluorescence quantum yield of Nile red is low, while in non-polar environments it is high.[111] This is because the TICT state of Nile red presents a polarity-dependent activation energy. Solvents with high polarity better stabilize the TICT state and

therefore decrease the activation energy required on the process.[111] However, that increases the rate of non-radiative processes from the TICT singlet states to the low-lying triplets and as a consequence decrease the fluorescence quantum yield of Nile red.[111] Protic solvents have also shown to decrease the quantum yields due to hydrogen-bonding effect.[111] In addition, due to its low solubility in water, Nile red forms micelle-like aggregates, which have also shown to quench the emission of the dye.[112] Those aggregates dramatically decrease the polarity of the dye's microenvironment, which inhibits the TICT process.[111] Also, self-quenching of the emission of the dye in those aggregates has been proposed as explanation for the decreased fluorescence in water.[113]

1.2.6.1 Biological Studies of Nile red

In 1985, Greenspan and Fowler carried out an extensive study on the emission and excitation of Nile red in different lipid and protein environments.[114] Table 1.1 summarizes some of their results. Using vesicles containing lipids they found that Nile red exhibits a red emission at 628 nm in the presence of the phospholipid DMPC (dimyristoyl phosphatidylcholine). However, in the presence of binary mixtures of DMPC with neutral lipids such as cholesterol and triacylglycerol the emission of Nile red was blue-shifted to a more yellow emission at 605 nm and 576 nm respectively.[114] When the emission and excitation of the dye were studied in the presence of lipoproteins, both the emission and excitation progressively blue-shifted in lipoproteins containing higher concentration of neutral lipids. In high density lipoproteins Nile red emitted at 610 nm, while in very low density lipoproteins it emitted at 576 nm.[114] When they evaluated the emission of Nile red in hydrophilic proteins such as Gelatin and Inmunoglobulin G, emission from the dye was not observed.[114] However in the presence of Albumin, which contains hydrophobic pockets, the dye emitted at 620 nm, but the emission was 10-to-100 fold lower than when it was in the presence of lipids or lipoproteins.[114] Finally, they evaluated the emission of Nile red in adipocytes and microsomal membranes, which are triacylglycerol and phospholipid rich environments, respectively. As expected, in the presence of adipocytes, the emission and excitation of the dye blue-shifted (λ_{em} 582 nm, λ_{ex} 521 nm) while in the microsomal membrane red-shifted (λ_{em} 624 nm, λ_{ex} 540 nm).[114]

These results clearly shows how Nile red emission is affected by the polarity of the near microenvironment in biological systems. Systems containing phospholipids produce a red-shift in the emission and excitation, a larger Stoke shift and decrease the intensity of Nile red in comparison to systems containing neutral lipids, which exhibits a lower polarity.

Table 1. 1 Fluorescence of Nile red in different biological components. Values obtained from Greenspan and Fowler study.[114] The Stoke shift was calculated from their values.

	Composition	Emission [nm]	Excitation [nm]	Relative Fluorescence Intensity	Stoke-shift [nm]
Lipids vesicles	DMPC	628	549	19	79
	DMPC:Chol (1:0.8)	605	549	22	56
	DMPC:Trygl (66:1)	576	529	23	47
Proteins	Albumin	620	553	3	67
	HDP	610	543	27	67
	LDL	584	531	33	53
	very LDL	576	530	33	46
Cell extract	Microsomal membrane	624	540	25	84
	Adipocyte	582	521	-	61

* Chol: cholesterol, Trygl: Triacylglycerol.

Halder *et al.,* carried out more specific studies of Nile red in the presence of different phospholipids and cholesterol by studying the emission of Nile red encapsulated in the lipid bilayer of large unilamellar vesicles (LUV).[115] It was determined that the emission of Nile red in the presence of phospholipids was independent of the type of head group, charge of head group, or length of the hydrocarbon tail.[115] However, the emission of Nile red was dependent on the saturation of the hydrocarbon chain. This study was performed exciting Nile red at an excitation wavelength of 550 nm. The emission of Nile red was blue-shifted in the presence of saturated lipids (624 nm) in comparison to unsaturated lipids (632 nm).[115] Additionally, the blue-shift was larger when the saturated lipids were in the gel phase (617 nm) than in the fluid phase (624 nm).[115] This effect occurs because bilayers composed of saturated lipids are more rigid than when they are composed of unsaturated lipids. Also, saturated lipids in the gel phase can present an all *trans* conformation of the hydrocarbon chain that provides a more restricted environment

to the Nile red. The restricted microenvironment around the Nile red decreases the stabilization of the TICT state, thereby producing the blue-shift.

The localization of Nile red inside the lipid bilayer was studied using DOPC vesicles containing different amounts of cholesterol. Mukherjee *et al.* found that Nile red preferentially localize in the interfacial region of the membrane, between the headgroup and the hydrocarbon chain, but near the phospholipid headgroup.[116] When the membrane is rigidified with cholesterol, the localization of Nile red changes to a relatively deeper interfacial region towards the hydrocarbon chains.[116] A deeper localization of Nile red towards the hydrocarbon chains in the bilayer provides a more restricted microenvironment with lower dipole moment around the dye, which decreases the stabilization of the TICT state. Those findings correlate with their observations that the emission of Nile red progressively blue-shifts with increasing the cholesterol concentration.[116]

The strong sensitivity of Nile red to different lipid-polar microenvironments coupled with its strong fluorescence in hydrophobic environments has lead to the extensive use of Nile red for the identification of different lipid compositions inside cells and tissues. For example, Nile red has been used as a histochemical stain for the identification of lipid bodies inside cells.[117–121] Greenspan *et al.,* found that lipid bodies inside the cells present a gold-yellow emission.[117] The yellow emission of Nile red in the lipid bodies was attributed to the composition of these organelles containing triacylglycerol and cholesteryl esters.[117] Additionally, Brown *et al*., were able to identify the intracellular accumulation of phospholipids in lysosomes present in Niemann-Pick disease by using Nile red.[122] They found that Nile red produces a bright orange emission in these lysosomes, which contain a high amount of a phospholipid called sphingomyelin.[122] Additionally, because the orange emission was easily discernible from the yellow emission observed in lipid bodies, they were able to differentiate both organelles through the use of Nile red.[122]

Nile red due to its strong fluorescence in hydrophobic environments and low solubility in water has been used as a hydrophobic model drug in the development of different drug delivery systems. The applications of Nile red in drug delivery systems have contribute to study the drug

encapsulation capacity, as well as, the release of the drug from the delivery systems, and the localization of the drug delivery systems inside organs and cells.

Nile red has been used to study the release efficacy from nanocarriers with stimuli-responsive properties to heat, ultrasound, pH or redox-active environments.[123–125] For example, Nile red was loaded inside a redox-responsive mesoporous organo-silica nanoparticles containing disulphide bridges (ss-NPs) to elucidate the redox-responsive property.[125] The ss-NPs were dispersed in an aqueous solution containing reduce glutathione (a peptide capable of reducing disulphide bonds) with a layer of ethyl acetate on top of the aqueous media.[125] As a function of time, the ss-NPs dispersed in the aqueous media breaks down releasing the dye, which dissolve into the organic layer due to its low water solubility.[125] Evaluating the fluorescence of Nile red in the organic solution as a function of time they observed an increase in the intensity of the dye, elucidating the redox-responsive release capacity of the ss-NPs.[125]

Nile red has also been used to study the penetration of nanocarriers in organs such as the skin, the cornea and the organ of Corti for dermal, ocular and inner ear drug delivery, respectively.[126–130] For example, excised human abdominal skin was treated with nanostructured lipid carriers (NLC) loaded with Nile red to study the intradermal accumulation of the NLCs. As Nile red presents a strong emission in lipophilic environments, using laser scanning confocal microscopy (LSCM) they were able to follow the accumulation of the NLC in the stratum corneum, viable epidermis, dermis and hair follicle.[127]

Moreover, Nile red has been also used to elucidate the uptake and intracellular distribution of nanoparticles in cells.[131–134] For example, Nile red was encapsulated in the hydrophobic core of polymer nanoparticles sensitive to reactive oxygen species (ROS).[134] The authors conjugate the polymer with the dye Alexa Fluor® 647 (Alx647), thus after internalization of the nanoparticle inside the cells they were able to image the polymer under 640 nm excitation and the Nile red under 485 nm excitation.[134] These experiments, allowed the authors to study the uptake and the co-localization of the dye with the polymer nanoparticles labelled with Alx647 inside human fibroblast and prostate cancer cells.[134]

Since 1985, Nile red has been used as dye in biological applications. Research on Nile red has lead to an understanding on its fluorescence mechanism that is extremely sensitive to the polarity of the nearby microenvironment due to its TICT state. It exhibits a strong fluorescence in hydrophobic environments but it is quenched in water. Due to these properties and its biocompatibility with biological systems this dye has been successfully use on the studies of cells, tissues, and nowadays drug delivery systems

1.2.7 Cellular Uptake of Nanoparticles

Understanding how nanoparticles are internalized inside the cells is crucial for the design of drug delivery systems. The first interaction between nanoparticles and cells occurs with the plasma membrane. The plasma membrane protects the cellular organelles from the environment and regulates the entry and exit of substances through channels receptors and transporters. To be able to traffic nanoparticles inside the cell, they must first pass through the cell membrane. This internalization process of nanoparticles into the cell can occur by five different endocytosis mechanisms: clathrin-mediated endocytosis, caveolae-dependent endocytosis, clathrin/caveolae independent endocytosis, phagocytosis, and macropinocytosis. Each endocytosis mechanism could determine the fate of nanoparticles inside the cell, and with that opens the possibility to target suborganells inside the cell.[135] By triggering the nanoparticle to be taken up by certain endocytosis mechanisms, the drug delivery could be selective, effective and safer than current medicinal treatments. A summary of these cellular mechanisms is presented here, but several detailed reviews about this topic can be found in the literature.[136–138]

1.2.7.1 Endocytosis Mechanisms

Clathrin-mediated endocytosis is the main mechanism cells utilize to uptake nutrients from the environment, such as cholesterol.[139] This mechanism can be activated *via* a receptor specific or non-receptor specific interaction.[139] The activation through a non-receptor specific interaction could occur *via* indirect binding such as hydrophobic or electrostatic interactions. However, the activation process of this pathway is still not well understood. The formation of the clathrin-

vesicle is a complex process that involves over 50 different proteins that organize and assemble in a synchronized fashion into a basket-shape vesicle (Figure 1.17).[140] Clathrin is one of the main proteins that has a triskelion shape and helps with the assembly of the vesicle. The process starts with the formation of a "coated pit" in which different cytosolic proteins including clathrin and clathrin-adaptor proteins cluster and binds to the plasma membrane.[140] The coated pit induces the bending of the membrane, which continues to grow by co-assembling with other proteins forming a complex structure to be able to stabilize the membrane curvature that would encapsulate the nanoparticle.[140] The dynamin, a membrane scission protein, binds at the neck of the curvature releasing the clathrin vesicle with the nanoparticle encapsulated into the cytosol. Finally the complex clathrin-coating disassembles allowing the vesicle to be trafficked inside the cell.[140] This vesicle could have a size between 60-150 nm,[138,140] and this vesicle leads to the formation of early endosomes that could become degradative lysosomes.[138]

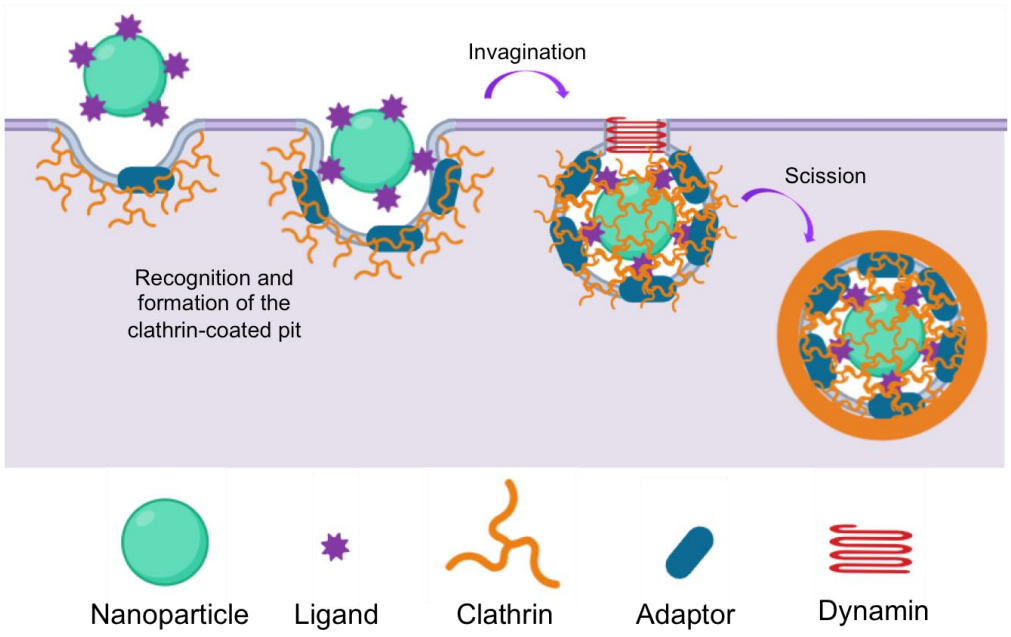

Figure 1. 17 Illustration of the clathrin-mediated endocytosis mechanisms of nanoparticles. Image adapted from Behzadi *et al.* review with ©BioRender.[136]

The caveolae-dependent endocytosis mechanism is involved in many cellular processes such as regulation of lipids, proteins, and membrane tension.[141] The caveolae are small plasma membrane bulb-shape invaginations with a diameter of 50-80 nm.[142] Thus, only smaller sized nanoparticles are likely to be uptaken by this pathway. The activation process is not well understood however, it has been postulated that lipids and cholesterol are involved in this process. It starts with the formation of nanodomains of caveolins and cavin proteins that cluster with lipid rafts at the plasma membrane.[142] Caveolin binds to cholesterol and cavin to negatively charged lipids (i.e. PS and PI(4,5)P2 lipids) to assemble together into a polyhedron structure.[142] This polyhedral structure called the caveolae vesicle could internalize nanoparticles.

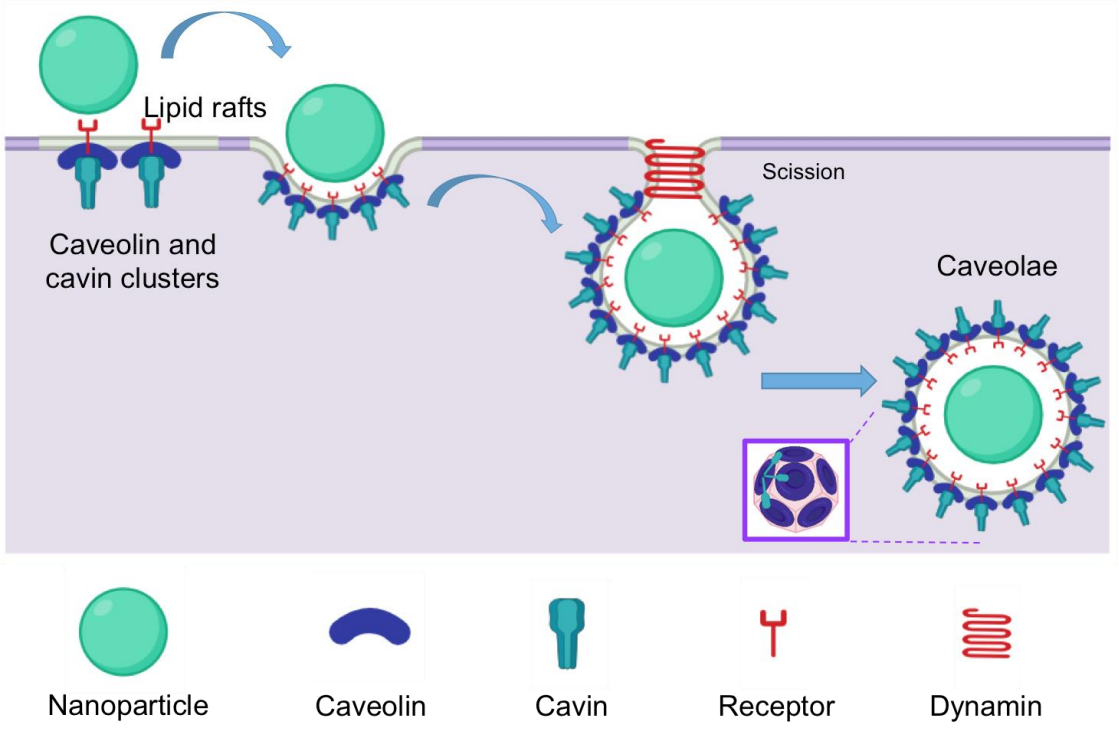

Figure 1. 18 Graphical depiction of the caveolae-mediated endocytosis mechanisms of nanoparticles. Image created with ©BioRender. Inset: illustrates the assembly between caveolins and cavins to build the polyhedral structure that forms the caveolae. Caveolin proteins assemble into flat spherical oligomers that then link with cavin trimmer proteins.

Then, the dynamin protein mediates the scission and release of the caveolae into the cytosol.[136] After internalization of the nanoparticle into the cell, the caveolae can deliver the content into caveosomes escaping the lysosomes degradative route.[143] In contrast, the caveosomes can deliver to the endoplasmic reticulum and Golgi apparatus *via* routes that are not completely understood.[143]

The clathrin/caveolae independent endocytosis mechanisms occur in cells that do not contain clathrin or caveolae proteins, such as human hepatoma 7 cells (HuH7).[144] However, many pathways of endocytosis could be used at the same time by the cell and some of them have shown to be clathrin or caveolae independent. Some of these endocytosis processes could be dynamin-dependent or dynamim-independent and are usually assisted by the actin protein polymerization machinery.[145] Dynamin-dependent endocytosis forms small vesicles (< 0.2 μm), while the dynamin-independent pathway could be involved in the formation of larger micrometer-sized endocytosis vesicles.[145] These mechanisms utilize different pathways to internalize the cargo that depends on hormones and protein receptors and specific lipid compositions.[145,146]

Phagocytosis is a process in which the cell membrane engulfs substances through a receptor-initiated response. It mainly occurs in specialized cells such as macrophages, neutrophils and dendritic cells, however, it could occur in fibroblast, epithelial, and endothelial cells to a lesser extent.[138] The phagocytosis process starts first by the opsonization (adsorption) of antibodies or proteins, called opsonins, at the surface of the nanoparticle, usually while travelling through the blood stream.[138] These opsonins at the surface of the nanoparticle act as ligands, activating phagocytosis *via* a ligand-receptor interaction to trigger the engulfment of the nanoparticle. The ligand-receptor interaction activates the actin protein polymerization machinery to be able to extend the plasma membrane around the opsonized nanoparticle and produce the engulfment.[147] Usually the phagosome (vesicle) takes the shape of the nanoparticle that has been ingested. This process can take between 30 minutes to hours.[148] Also, studies have shown that this process is

more common with larger nanoparticles (i.e. 0.5-2 µm).[136,138] Particles larger than 5 µm are thought to be uptaken by a different molecular mechanism.[147]

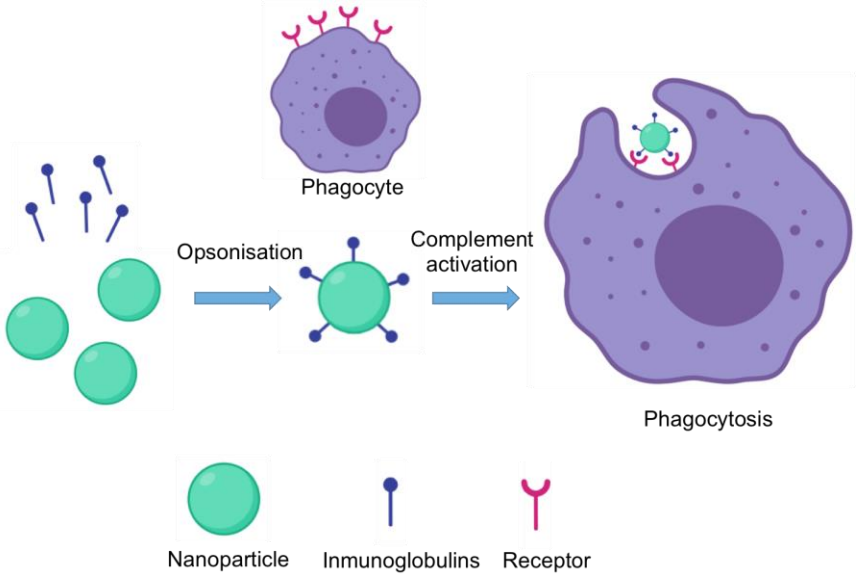

Figure 1. 19 Illustration of the phagocytosis endocytosis mechanisms of nanoparticles. Image redraw it from Behzadi *et all.* review with ©BioRender.[136]

Macropinocytosis is an endocytosis mechanism that does not involve interaction with ligands and can be initiated spontaneously or in response to the stimulation of the growth factor receptor.[147] The process involves the formation of ruffles (sheet-like extensions of cell membrane), which are assisted by the actin protein polymerization machinery.[147] The ruffles build a cup structure that engulfs the cargo with extracellular fluid and combines back with another portion of the cell membrane.[147] Then, after both sides of the ruffles fuse, the vesicle separates from the membrane into the cytoplasm. These vesicles are called macropinosomes and have a size between 0.2-10 µm.[147] After internalization, depending on the cell type, the macropinosome could traffic and fuse with degradative lysosomes or it could recycle back the content to the cell surface.[138]

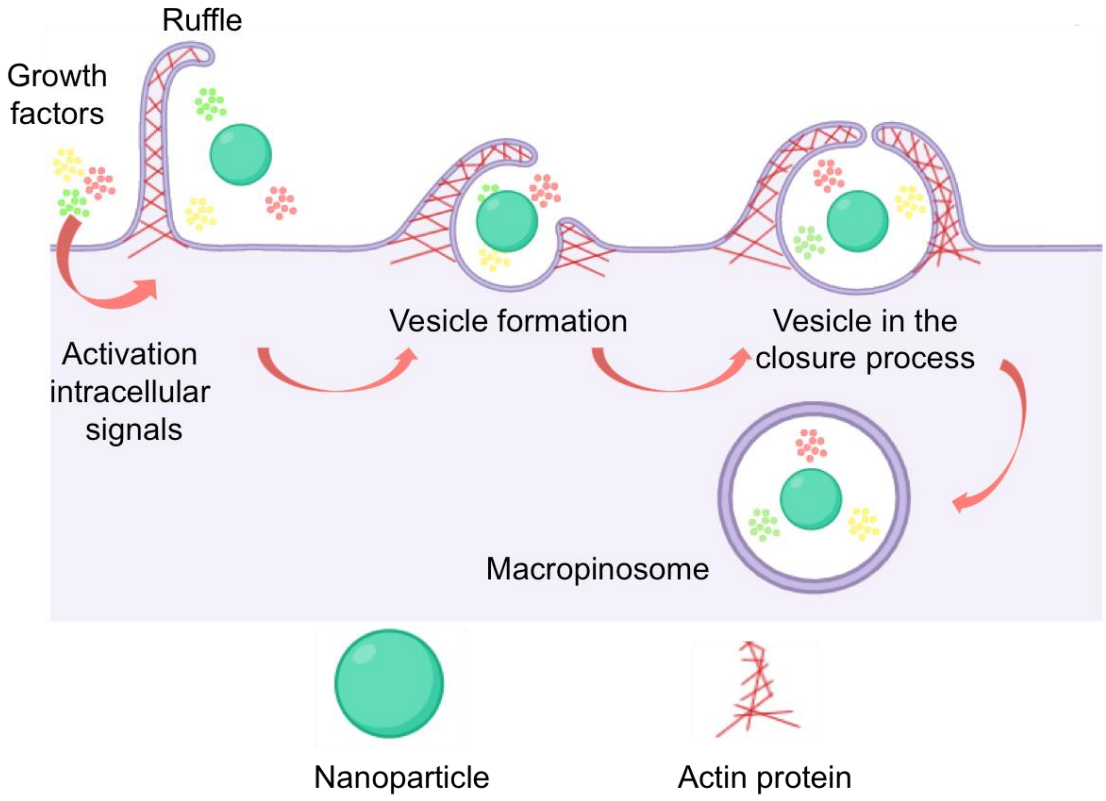

Figure 1. 20 Illustration of the macropinocytosis endocytosis mechanism of nanoparticles. Image created with ©BioRender.

1.2.7.2 Inhibition trafficking through the plasma membrane

In the field of cell biology and medicinal chemistry, there has been important progress made in the development of small molecules that inhibit intracellular membrane trafficking.[149,150] Small molecules could target specific molecules, protein domains or inactivate enzymes in order to block pathways in a dose-dependent fashion.[149] Different molecules have been found to inhibit certain cellular endocytosis mechanisms, which have been used to study the internalization of viruses, the effects of drugs, and recently the uptake mechanisms of nanoparticles. The following section summarizes the most common inhibitors used in nanoparticles studies.

The clathrin-mediated endocytosis pathway can be inhibited with sucrose or chlorpromazine. Sucrose in a high concentration (i.e. 0.45 M) produces a hypertonic solution that prevents the association of the clathrin proteins.[151] Chlorpromazine is a cationic amphiphilic drug that has been shown to alter the plasma membrane dynamics. It disrupts the binding of the AP-2 clathrin-adaptor into the plasma membrane, inhibiting the formation of the clathrin-coated pits.[152,153] Both sucrose and chlorpromazine, disable the clathrin lattice preventing the formation of the clathrin vesicles and as a result blocks the clathrin-mediated endocytosis pathway.

The caveolae-depended endocytosis mechanism can be blocked using cholesterol binding agents such as nystatin,[154] filipin,[155] and methyl-β-cyclodextrin.[156,157] Depletion of cholesterol has been shown to inhibit the caveolae pathway because cholesterol binds to Caveolin-1 in a 1:1 molar ratio for the formation of the bulb-shaped caveolae vesicle.[142] Macropinocytosis can be blocked by three different ways which prevent the membrane ruffling for the engulfment of the extracellular material.[158] (1) Inhibitors of the actin protein polymerization, which block the remodeling of the cytoskeleton (i.e. Cytochalasin D),[159] (2) inhibitors of the sodium hydrogen (Na^+/H^+) exchangers, which increases the acidification of the submembrane and produces dysfunctions in the membrane (i.e. amiloride compounds),[160] and (3) phosphatidylinositol-3kinase (PI3K) blockers, which inhibit the membrane fusion between the ruffles that forms the macropinosome (i.e. Wortmannin).[161]

1.2.8 Effects of the physicochemical properties of the nanoparticles on the cellular uptake

The interaction of the nanoparticles with the cellular membrane depends on different physicochemical features of the nanomaterial such as the size, shape, charge, surface chemistry and even the flexibility or porosity of the material. However, the interaction of the nanoparticles with the cells may occur through different pathways which are unique to the cell line being studied because the metabolism, and cell membrane composition (lipids and receptors) differs between cell types which are specialized in different physiological functions. Thus, a discussion

of the interactions of nanomaterials with cells necessitates that the type of cell line used in the experiments must be specified, as described in the following sections.

1.2.8.1 Size effects

Chaudhuri et al. studied the effect of nanoparticle size on cellular uptake through a computational study of spherical particles coated with a ligand.[162] They found that the minimum radius of a particle required to be wrapped completely by the cell membrane depends on the adhesion strength between the ligand-receptor interaction and the cell membrane rigidity.[162] In other words, it depends on the energy released from the ligand-receptor binding and the energy required for bending the membrane.[162] Additionally, the bending process of the cell membrane depends on domains with some phase separation such as lipid rafts that decrease the rigidity of the membrane.[163]

Chithrani *et al.,* compared the cellular uptake of spherical gold nanoparticles with different diameters (14 nm up to 100 nm), finding that the optimal size to achieve the highest cellular uptake in cervical cancer (HeLa) cells is approximately 50 nm.[164] Similar results were obtained studying the internalization of calcium oxalate nanoparticles of different size (50, 100, and 1000 nm) into renal epithelial (Vero) cells.[165] The 50 nm size nanoparticles had the lager cellular uptake in comparison to the other two sizes studied.[165] In agreement with these results, Jiang *et al.* studied the cellular uptake of gold nanoparticles of different size (2-200 nm) modified with the cancer drug Herceptin on breast cancer cells (SK-BR-3).[166] They found that gold nanoparticles with sizes between 40 and 50 nm had a greater internalization compared to the smaller or larger nanoparticles.[166] They conclude that large particles will require higher energy for the cell membrane to wrap them completely, and small particles do not have the ability to bind multiple receptors to induce the engulfment.[166]

Additionally, Zhu *et al.,* found that the nanoparticle size can stimulate different endocytosis mechanisms in the cell and, as a result, affect the cellular uptake.[167] They evaluate the cellular uptake of three different size of silica nanoparticles using HeLa cells, finding that the

cellular uptake was size-dependent (55.6 >167.8 > 307.6 nm).[167] However, they also found that different endocytosis mechanisms were activated for different nanoparticle sizes. The 55.6 nm size nanoparticles were uptaken by the clathrin-mediated endocytosis, caveolae-dependent endocytosis, and a non energy-dependent mechanism, as the nanoparticles were also uptaken at 4 °C.[167] The middle size nanoparticles (167.8 nm), were uptaken by the clathrin-mediated and caveolae-mediated pathway, while the large nanoparticles (307.6 nm) were mostly uptaken by the clathrin-mediated pathway.[167]

In addition to the size of the nanoparticles, if the nanoparticles have a tendency to aggregate, they can interact with the cell in a different fashion, thereby affecting the cellular uptake. For instance, Albanese and Chan studied the effect of nanoparticle aggregation on the cellular uptake of gold nanoparticles using HeLa and lung cancer cells (A549).[168] They found that aggregated nanoparticles exhibited a 25% decrease in uptake compared to dispersed nanoparticles and that the aggregated-nanoparticles were internalized by different mechanisms compared to single particles of the same size of the aggregate.[168]

Most of the studies agree that the size of approximately 50 nm is the optimal size to have the greatest cellular uptake using spherical nanoparticles in different cell lines. However, when it comes to more complex morphologies, the uptake becomes more complicated.

1.2.8.2 Shape effects

Scientists have been able to develop many different nanoparticle shapes of different materials; some authors even refer to the vast variety of shapes as a "zoo" of nanoparticles.[169] Figure 1.21 shows some of the most basic shapes of nanoparticles, such as rods, worms, triangles, stars and hexagons. Different studies have found that the geometry can influence the uptake mechanism and also the fate of the nanoparticles inside the cells. However, there are still discrepancies about what kind of shape is the best for the cellular uptake, because it is not an easy variable to study. When it comes to discussing the effect of the shape of a nanomaterial on the cellular uptake, several variables are involved. The following section will discuss the shape with respect to the

aspect ratio, the size, the curvature of the edges, and even the orientation of the nanoparticle with respect to the cell membrane.

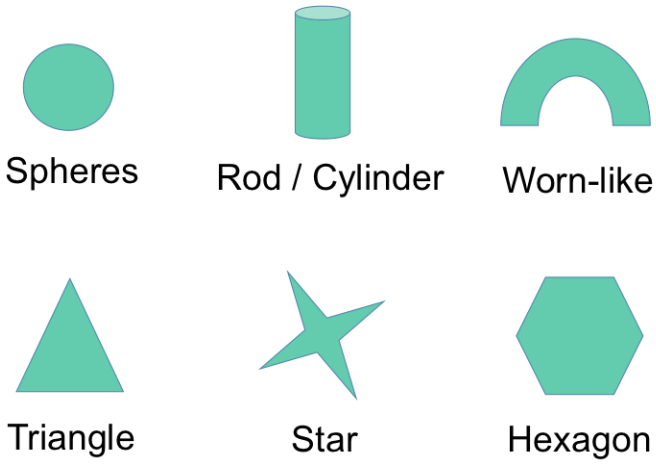

Figure 1. 21 Illustration of some nanoparticles shapes

Spherical and rod-shaped nanoparticles

Chithrani et al. studied the cellular uptake of spheres and rods of gold nanoparticles in two different sizes using HeLa cells. They compared two samples of spherical nanoparticles (14 and 74 nm, aspect ratio 1 for both) with two samples of nanorods (14×40 and 14×74 nm, aspect ratio 3 and 5). They found that spherical nanoparticles had a greater uptake than the nanorods. Also, nanoparticles with lower aspect ratio present a higher cellular uptake.[164] Qui *et al.,* also evaluated the effect of the aspect ratio of four different nanorods with respect to the cellular uptake using gold nanorods in breast cancer cells (MCF-7).[170] They found that nanoparticles with lower aspect ratio had a greater cellular uptake (33×30 > 40×21 > 50×17 > 55×14 nm, aspect ratios: ~ 1, 2, 3, and 4 respectively).[170]

Contradictory results have been found with silica nanoparticles from those found with gold nanoparticles when studying sphere and rod shape nanoparticles. Meng *et al.*, studied the cellular uptake of rods and sphere-shaped mesoporous silica nanoparticles using HeLa and A549

cells.[171] They compare the cellular uptake of three different nanorods (120×70, 175×75 and 280×60 nm, aspect ratio: 1.7, 2.3, and 4.6 respectively) with a spherical nanoparticles of 110 nm size.[171] They found that all nanorods had a greater uptake than the spherical nanoparticles. Furthermore, the nanorods with the intermediate length and aspect ratio of 2.3 were the ones with the highest and most rapid uptake.[171] Shao et al. also studied the shape effect of spheres *vs.* rods on the cellular uptake of magnetic mesoporus silica nanoparticles using human hepatocellular carcinoma (HepG2) cells.[172] They compared the cellular uptake of two different nanorods (150×300 and 100×400 nm, aspect ratio 2, and 4 respectively) with spherical nanoparticles of 250 nm size.[172] They found as well that the nanorods had a larger cellular uptake than spherical nanoparticles. However, contrary to the previous study, they found that greater cellular uptake occurred at higher aspect ratios of the rods.[172] They suggested that nanoparticles with larger aspect ratio have a greater cellular uptake due to a larger contact area with the membrane surface.[172] It is worth mentioning that in both of the studies discussed on silica nanoparticles, all nanorods had one dimension smaller than the diameter of the sphere nanoparticle, which may have facilitated the cellular internalization of the nanorods over the spherical nanoparticles.

Herd *et al.,* determined that the orientation of nanoparticles with different geometries could align in different fashions with respect to the plasma membrane, thereby altering the degree of cellular uptake. They studied the cellular uptake of spheres (214 nm), rods (214×428 nm, aspect ratio 2) and worm-like (232×1348 nm, aspect ratio 5.8) silica nanoparticles using murine leukemia macrophages (RAW 264.7) and A549 cells.[173] They found that the cellular uptake of these nanoparticles had a time-dependent pattern. Spherical nanoparticles were internalized more quickly than rods and worm-like nanoparticles, but after 24 hours, all nanoparticles reached an equilibrium on their cellular uptake.[173] In addition, they evaluated the endocytosis mechanisms and found that the spherical nanoparticles were primarily internalized *via* the clathrin-mediated pathway, while rods and worm-like nanoparticles were uptaken mostly by macropinocytosis.[173] However, they found that some rods and worm-like nanoparticles were also uptaken by the

clathrin-mediated pathway, which is unusual due to the size of those nanoparticles.[173] They argue that the orientation of the rods and the worm-like nanoparticles, when interacting with the cell membrane, was along their smallest side as to enable cellular uptake *via* the clathrin-mediated pathway.[173]

Other nanoparticles shapes

Xie *et al*., studied the cellular uptake of triangle, star, and rod shaped gold nanoparticles by RAW 264.7 cells.[174] These three kind of nanoparticles had similar sizes (~ 50 nm), however, the authors found that the endocytosis mechanism was dependent on the shape of the nanoparticles, and therefore affected the degree of cellular uptake.[174] The nanotriangles exhibited the greatest cellular uptake, followed by the nanorods and then the nanostars.[174] All three shapes were uptaken by the clathrin-mediated endocytosis mechanism.[174] However, the nanorods were also dependent on the caveolae-mediated mechanism, while the nanotriangles were highly dependent on the macropinocytosis and other dynamin-dependent pathways. The activation of multiple endocytosis pathways by the nanotriangle was attributed to the greater degree of uptake than the other two morphologies.[174] The authors speculate that the nanostars require a higher binding energy in order to activate the membrane bending for their cellular uptake due to their multiple spikes.[174]

Tree-Undom *et al.*, studied the effect of the nanoparticles shape-curvature with respect to the nanoparticle-membrane interaction using $NaYF_4$ UCNPs and DOPC liposomes. They used spheres (27 nm), elongated spheres (25×38 nm) and hexagonal prisms (96×64 nm) with a fluorophore at the surface of the nanoparticles to study their association with large unilamellar liposomes using a confocal microscope. They observed that the nanoparticles with the highest association to the liposome membrane were the elongated spheres, followed by the spheres, and with minimal association, the hexagonal nanoparticles. They explain that the elongated spheres, when associated with the membrane along their long side, produce a smaller membrane curvature than the spheres or hexagonal nanoparticles, which requires the least energy to induce the cellular uptake, and therefore can be uptaken most efficiently. Furthermore, they studied the cellular uptake of these nanoparticles with human melanoma (A-375) cells, finding the cellular

uptake was greatest for the elongated spheres, followed by spheres and then hexagonal nanoparticles, confirming the importance of the nanoparticle shape-curvature in the cellular uptake.

Computational studies

A computational study on the translocation of nanoparticles with different shapes across a lipid bilayer found that the penetration depends on the shape and initial orientation of the nanoparticle with respect to the lipid bilayer, as previously discussed with respect to the findings of Herd *et al*.[175] The computational study determined that penetration is more difficult when the contact area between the nanoparticle and lipid bilayer increases.[175] For instance, they found that in spherical particles, the penetration becomes more difficult when increasing the volume of the nanoparticle because the degree of contact with the bilayer is larger.[175] However, with anisotropic nanoparticles, the penetration was found to be almost independent of the volume of the nanoparticle, and could even become easier with increasing volume if the nanoparticles are perpendicular with respect to the lipid bilayer.[175] For example, when an ellipsoidal particle penetrates the lipid bilayer perpendicularly, the translocation becomes easier than when it penetrates parallel to the lipid bilayer due to the lower degree of contact, resulting in a less time-consuming process (Figure 1.21).[175]

Another molecular dynamics calculation analyzed the energy required for a membrane to wrap around a nanoparticle.[169] They study the curvature energy of a membrane and the adhesion energy of the membrane-nanoparticle interaction with respect to the nanoparticle shape (sphere, rods, cubes with different aspect ratio and edge curvature).[169] They found that the aspect ratio and size of a nanoparticle are not sufficient to determine the cellular uptake; however geometrical parameters related to the curvature of the nanoparticle could change the wrapping behavior quality for the endocytosis of the nanoparticle. For instance, they found that nanoparticles with morphologies containing sharp angles (cubic-like) requires a greater deformation of the membrane to be able to wrap the lateral sides of the nanoparticle. In addition, they found that the aspect ratio and the curvature of the edges of nanorods influence on how they orient with respect to the membrane for endocytocis.[169] Nanorods with high aspect ratios and

round tips prefer to enter with the long side first parallel to the membrane in a "submarine mode".[169] While nanorods with small aspect ratios and flat tips enters first by the tips and then along the long side in a perpendicular way with respect to the membrane in a "rocket mode".[169]

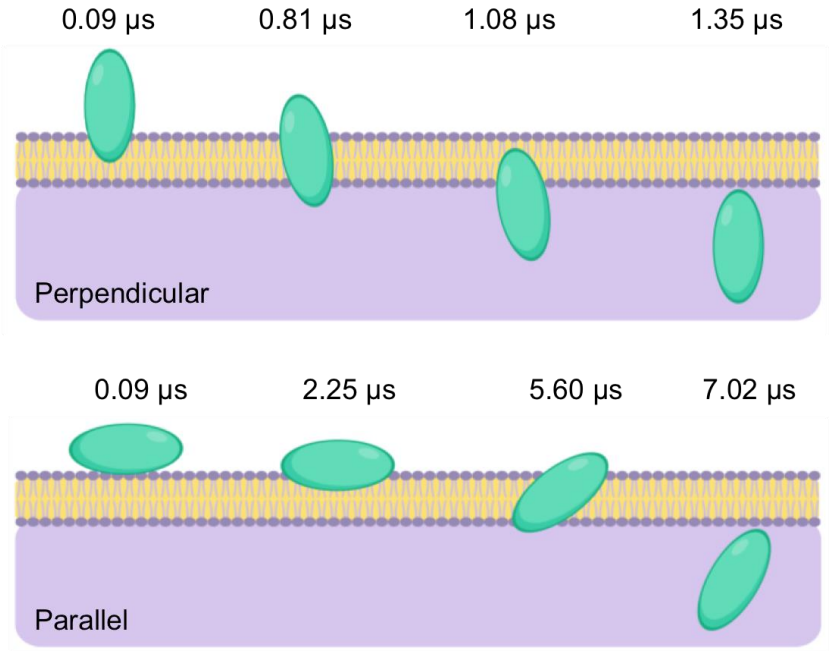

Figure 1. 22 Illustration of the translocation of an ellipsoidal nanoparticle through a lipid bilayer starting with two different orientations. The illustration is based on the molecular dynamics calculations found by Yang and Ma.[175] In their results its possible to observe that the lipid membrane bends while the nanoparticle translocates.[175] Image created with ©BioRender.

Computational and experimental studies have helped researchers to understand that the initial orientation of the nanoparticle, the angles between the faces of the material, and the curvature of the edges are as important as the size and the aspect ratio of the nanoparticle. Most of the studies on gold nanoparticles have been done on nanoparticles below 100 nm, while in silica nanoparticles the studies mostly evaluate nanoparticles greater than 100 nm. It is possible that in larger nanoparticles, those variables may have a greater effect on the cellular uptake. The studies on sphere *vs.* rod shaped gold nanoparticles indicate that spheres have greater cellular uptake

than rods. However, the studies with silica nanoparticles and $NaYF_4$ UCNPs indicate that is not always the case, as the curvature and the orientation affects the uptake. Also, it is not always true that at smaller aspect ratio, the greater the uptake. The aspect ratio together with the curvature of the edges could lead to different orientations of the nanoparticle with respect to the membrane, thereby affecting the uptake. Additionally, if the aspect ratio is small and the nanoparticles have a cubic-like shape, the wrapping of the nanoparticle by the cell membrane is more difficult and therefore the uptake is less efficient. Finally, studies suggest that different geometries activate different endocytosis mechanisms, but the reasons are still unknown.

1.2.8.3 Charge effect

The surface charge of the nanoparticles has also been shown to play an important role in the cellular uptake. The plasma membrane is constituted by hundreds of different lipids, and has an asymmetric distribution of lipids in the inner and outer leaflets of the membrane.[176] The inner leaflet of the cell membrane has a higher concentration of negatively charged lipids, while the outer leaflet has a higher concentration of neutral and positively charged lipids.[176] The plasma membrane contains 30% of PS lipids and 0.3% of PIP_2 negative charge lipids that produce a negative surface potential of -25 mV.[177,178] Additionally, the cell interior has an overall negative charged compared to the extracellular environment that is enriched with Ca^{2+} and Na^{+} ions.[177] The electrostatic interaction between the plasma membrane and extracellular species, such as proteins, has been shown to drive different cell signaling processes for the regulation of physiological activities.[178] Thus, it can be said that cellular uptake is strongly affected by the degree of electrostatic interaction between the membrane and the species interacting with it. Studies on nanoparticles with different surface charges have shown that the surface charge does affect the cellular uptake rates and produces different cytotoxicity effects.[179] Different surface charges can be achieved by controlling the properties of the ligands at the surface of the nanoparticle.

Neutral nanoparticles (using zwitterionic molecules or non-charged functional groups) have shown to have a lower cellular uptake compared to charged nanoparticles.[180] This could be

due to lower affinity with the cell membrane.[180] Additionally, non-charged groups such as OH- increase the hydrophilicity creating a hindrance effect and therefore decreasing its interaction with proteins and the cell membrane.[180] Neutral nanoparticles have shown to present a lower uptake by phagocyte cells, but they can be uptaken by non-phagocyte cells without distinction between normal and carcinoma cells.[181]

Positively charged nanoparticles have been shown to have a higher cellular uptake than negatively charged nanoparticles due to a stronger electrostatic interaction with the cell membrane.[182,183] Generally, this can be explained by the greater attraction of the positively charged nanoparticles with the overall negatively charged plasma membrane. However, the stronger the interaction of the positively charged nanoparticles with the cell membrane, the greater the disruption of the membrane due to the increased uptake, and therefore greater toxic effects are observed.[179,184] Additionally, because of the strong electrostatic interaction with the cell membrane, positively charged nanoparticles have not shown predilection by cell type on their uptake. Positively charged nanoparticles can be uptaken by phagocytes and non-phagocytes at the same rate.[185]

Negatively charged nanoparticles have been shown to have a lower cellular uptake than positive charged nanoparticles. A computational study showed that negatively charged nanoparticles present a higher energy barrier due to electrostatic repulsion with the negatively charged membrane.[186] That energy barrier is translated into a low adhesion and translocation of the nanoparticle through the membrane due to weaker interaction with the cell membrane.[186] It is possible that the internalization of negatively charged nanoparticles occurs by the depolarization (shifts towards more positive membrane potential) of nanodomains on the cell membrane to favors their cellular uptake.[177] Negatively charged nanoparticles have shown to be uptaken by both phagocytic and non-phagocytic cells. Interestingly, however, it has been observed that there may be greater uptake in some carcinoma cells than in normal cells.[185,187] For example, cerium oxide nanoparticles were modified with three different surface coatings to evaluate the charge effect on the uptake of the nanoparticles by healthy (cardiac myocytes H9c2 and human embryonic kidney HEK293) and carcinoma cells (lung cancer cells A549).[185] The cerium oxide

nanoparticles were coated with polyacrylic acid, aminated-polyacrylic acid and dextran for a negative, positive and neutral surface charge, respectively.[185] They found that positively charged and neutral nanoparticles were internalized in both types of cells, while negatively charged nanoparticles were only uptaken by the carcinoma cells.[185] Li et al., also observed this phenomenon using UCNPs with different surface charges.[187] These findings suggest that the surface charge may impart some selectivity of nanoparticle uptake between cancer cells and healthy cells.

Guller *et. al.*, modified the surface on $NaYF_4$ UCNPs with the positively charged polymer PEI (polyethylenimine) and then using a layer by layer approach modified the surface of the PEI-coated nanoparticles with a second polymer, but this time with different negative charges. They found that the positively charged nanoparticles with PEI were more cytotoxic than the other nanoparticles with the negatively charged polymers.[88] In general, studies have shown that nanoparticles with a positively charged surface could be more toxic than negatively charged and neutral nanoparticles.[179] Liu *et. al.,* have found that after internalization, positively charged nanoparticles associated better with mitochondrias, producing a greater cytoxicity.[187]

1.2.9 Alveolar Lung Carcinoma Cells A549

The cell line A549 is composed by alveolar type I and type II carcinoma epithelial cells for the lung distal. Studies of the endocytosis mechanism and trafficking of nanoparticles in this cell line could give a better understanding of the nanoparticle-cell interactions for the development of novel nanomedicines for lung distal diseases, including lung cancer.

The type I cells are squamous flat cells (0.2 μm thick) with an approximately surface area of 5000 μm^2 per cell covering the 95% of the alveolus. They do not present many organelles, but present several vesicles to carry molecules intracellular. The thin morphology of these cells is thought to allow free gas exchange at the alveolar surface and act as a microbial barrier.

However, they do not have the capacity to undergo mitosis then they have to be replaced by their progenitor the type II cells.[188]

Type II cells are cuboidal with a surface area of 250 μm^2 per cell covering only 5% of the alveolus.[189] They are highly metabolic a difference from type I cells. They contain microvilli, a large nucleus, abundant mitochondria and lamellar bodies, extensive endoplasmic reticulum and Golgi apparatus. The lamellar bodies are the most characteristic organelle of the type II cells. This organelle is important for the assembly, storage and secretion of pulmonary surfactant. This kind of cells are the key on the functionality of the alveolus by controlling the production and homeostasis of surfactant and generation of cell type I.[188]

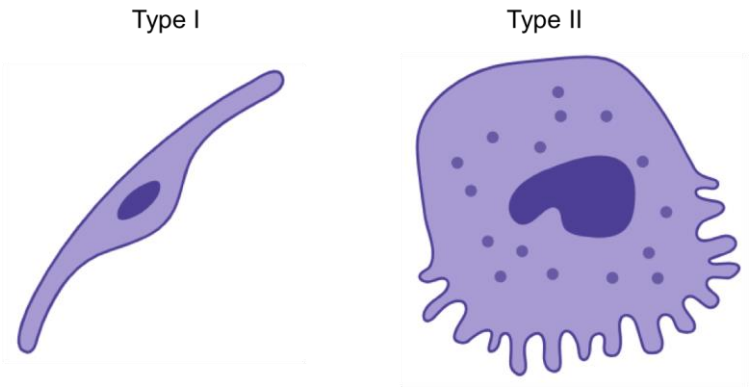

Figure 1. 23 Illustration of type I (squamous) and type II (cuboidal) cells. Images created with ©BioRender.

Human alveolar cells can contain between 200-500 lamellar bodies with sizes between 100-2400 nm and a pH ~5.5.[190] This organelle stores lipids and surfactant proteins without degradation to be secreted after into the lumen in order to keep the surfactant homeostasis inside the alveoli. The lipids and surfactant proteins stored inside the lamellar bodies comes from recycled material of the alveoli lumen and from new biosynthesized material. The recycle material comes *via*

endocytic pathways and the new materials are synthesized in the reticulum endoplasmic, transport to the Golgi and then transported to the lamellar bodies. Both surfactant materials are combined and transported in multilamellar vesicular bodies to the lamellar bodies. [191]

The internal membranes of the multilamellar vesicle bodies are involved in the biosynthesis of the lamellar bodies. This membrane contains a high amount of cholesterol, which is important for the packing and organization of the surfactants inside the lamellar bodies.[192] However, there is no evidence that cholesterol is biosynthesized internally in this kind of cell. Therefore, it is postulated that all the cholesterol comes from the circulation *via* the recycling pathway and its levels are regulated independently from phospholipids.[192] Orgeig and Daniels studied the distribution of cholesterol and phopholipids inside the lamellar bodies by radiolabelling [^{3}H]cholesterol and phospholipids ([^{14}C]choline).[193] They found that 76% of the cholesterol forms part of the lamellar bodies membrane while the remaining is distributed in the core, in contrast the phospholipids are equally distributed inside the lamellar bodies.[193]

The major pulmonary lipids are DPPC (41%), unsaturated PC (25%), PG (9%), other phospholipid (4%), cholesterol (8%) and other neutral lipids (5%).[188] PC lipids are more commonly found in the outer leaflet on the cell membrane involved in the membrane cell signaling. Acidic phospholipids (PG and PI) are thought to suppress viral infection and inflammatory in the lungs.[188] Neutral lipids such as cholesterol are important to maintain the fluidity and packing of the surfactant film.[188] The 10% of the total lipid composition correspond to serum proteins and four surfactant proteins. SP-A and SP-D are hydrophilic proteins while SP-B and SP-C are the hydrophobic proteins.[188]

1.3 STATEMENT OF THE PROBLEM

There is a lot of excitement in the nanomedicine field to revolutionize how medicine is practiced today, however there is currently a low clinical translation of nanomaterials into actual nanomedicines in order to improve the patient outcomes.[13,194] The complex interactions between nanomaterials and biological systems remain in their initial stages of understanding.[13] Studies on nanoscience could lead into a better understanding of the nanomaterial properties and the bio-nano interactions. For example, physicochemical characterization of the properties of the nanomaterials combined with the study of the effects of these properties in a cellular environment would provide a better understanding of the nanoparticle-cell interaction.

In order to utilize nanoparticles in biological applications, it is important to engineer nanomaterials, which are biocompatible and colloidally stable in aqueous and biological media. One of the major advantages of liposome-based drug delivery systems is the high biocompatibility due to the nature of phospholipids, which are the main building block of these types of systems.[195] Phospholipids are the major component of cell membranes and can be used to mimic biological structures. Combinations of nanoparticles with lipids could provide novel nanoparticle-based drug delivery systems while taking advantages of the properties of both nanoparticles and lipids.

In the work reported herein, a surface coating using a supported lipid bilayer on lanthanide upconverting nanoparticles ($LiYF_4$:Tm^{3+}/Yb^{3+}) was developed. Optimization of the surface coating through different charged lipids was studied in order to produce a continuous surface coating that rendered the nanoparticles water dispersible and protected the emission of the nanoparticle from water-derived quenching. Incorporation of an azobenzene-derivative lipid in the supported lipid bilayer produced a dynamic and multifunctional surface coating where a hydrophobic model drug was encapsulated and the properties of the bilayer were photo-controllable *via* energy transfer from the upconverting nanoparticle. The energy transfer mechanism to photo-control the lipid bilayer and produce the release of the model drug was

thoroughly studied *via* steady-state and time-resolved photoluminescence spectroscopy. The encapsulation and release profile of the model drug were characterized. Cellular studies of this novel nanomaterial were conducted using alveolar lung carcinoma cells (A549) where the cellular uptake, cytotoxicity, endocytosis mechanisms and trafficking inside the cells were studied. Photo-controlled release of the model drug from the nanoparticle-based delivery system uptaken by the A549 cells was achieved using NIR photo-irradiation. These studies enrich the understanding of photo-stimulated nanomaterials using Ln-UCNPs and demonstrate the possibility for a novel biocompatible nanoparticle-based drug delivery system for hydrophobic and/or lipophilic drugs using Ln-UCNPs with a supported lipid bilayer with potential use as a nanomedicine.

1.4 OUTLINE

This section outlines the format of this manuscript-based thesis

Chapter 1: General Introduction

This chapter provides a general introduction about lanthanides and lanthanide upconverting nanoparticles and the theory about upconversion, energy transfer and phospholipid bilayers. It provides the literature review with the necessary background information to read this thesis starting with the development of $LiYF_4$ upconverting nanoparticles and its biological applications. This discussion is followed by the different surface modification approaches on Ln-UCNPs and the formation of supported lipid bilayers, with specific emphasis on nanoparticles. This chapter also provides a discussion on the azobenzene photoswitching mechanism and its applications in lipid bilayers. It covers the Nile red fluorescence mechanism and its biological applications as a model drug in the studies of drug delivery systems and as a stain in cells. Additionally, this chapter includes a description on the different endocytosis mechanisms of nanoparticles and a review on the effect of the physicochemical properties (size, shape and surface charge) of nanoparticles on cellular uptake. Finally, a brief overview of the alveolar lung cancer cell line A549 is presented.

Chapter 2: "Formation of a Supported Lipid Bilayer on Faceted $LiYF_4:Tm^{3+}/Yb^{3+}$ Upconversion Nanoparticles"

This chapter discusses the formation of a supported lipid bilayer on diamond-shaped $LiYF_4:Tm^{3+}/Yb^{3+}$ upconverting nanoparticles. The surface modification was characterized by different transmission electron microscopy techniques where the formation of a non-interdigitated supported lipid bilayer with a continuous coverage of the nanoparticle was observed, despite the acute angles in the morphology of the nanocrystals. The effectiveness of

the surface coverage was dependent on the negatively charged lipid composition. Additionally, the supported lipid bilayer yields water dispersible Ln-UCNPs and protects the emission of the nanoparticle from quenching with phonon energies from the water. This novel system is envisioned as a nanoparticle-based drug delivery system for encapsulation of hydrophobic drugs inside the supported lipid bilayer.

Chapter 3: "A Route to Triggered Delivery *via* Photocontrol of Lipid Bilayer Properties Using Lanthanide Upconversion Nanoparticles"

Motivated by the previous studies, this chapter discussed the formation of a dynamic multifunctional supported lipid bilayer on $LiYF_4:Tm^{3+}/Yb^{3+}$ upconverting nanoparticles. The supported lipid bilayer provides encapsulation and controlled release of small hydrophobic drugs using a photo-irradiation stimulus. The physicochemical properties of the lipid bilayer are photo-controlled with the introduction of an azobenzene-derivative lipid molecule in the supported lipid bilayer *via* energy transfer from the Ln-UCNPs. The energy transfer from the Ln-UCNP to the azobenzene derivative lipid was found to be dominated by a radiative reabsorption mechanism. Additionally, the NIR photo-controlled released and encapsulation of a hydrophobic drug was proof by using the dye Nile red as a model drug.

Chapter 4: "Absolute Upconversion Quantum Yields of Blue-Emitting $LiYF_4:Tm^{3+}/Yb^{3+}$ Upconverting Nanoparticles"

This chapter discusses the characterization of the absolute upconversion quantum yields of the individual emission bands of $LiYF_4:Tm^{3+}/Yb^{3+}$. The effect on the excitation power densities and wavelength, and sample temperature on the quantum yields were also evaluated. This project was developed in collaboration with multiple laboratories where the reproducibility of the quantum yield measurements was demonstrated.

Chapter 5: "Cellular Uptake, Cytotoxicity and Trafficking of Supported Lipid Bilayer Coated Lanthanide Upconverting Nanoparticles in Alveolar Lung Cancer Cells"

This chapter discusses the investigation on the cellular uptake and trafficking of diamond-shaped $LiYF_4:Tm^{3+}/Yb^{3+}$ upconverting nanoparticles in human alveolar lung cancer cells (A549). The cellular uptake and cytotoxicity of $LiYF_4:Tm^{3+}/Yb^{3+}$ UCNPs with different surface properties was also evaluated. The surface coating with the supported lipid bilayer produced negligible cytotoxicity on A549 lung cancer cells. Oleate-caped and oleate-free $LiYF_4:Tm^{3+}/Yb^{3+}$ produce a lower but still significant cytotoxicity to A549 lung cancer cells. Additionally, the quantification on the cellular uptake of the nanoparticles using ICP-MS showed different amount of nanoparticles internalized due to the different surface properties. Using inhibition studies of the endocytosis mechanisms and cellular imaging with confocal microscopy the internalization of the nanoparticles with a supported lipid bilayer was studied, finding that the nanoparticles internalized *via* clathrin-mediated and caveolae-dependent endocytosis mechanisms, and also through a non-energy dependent mechanism. The nanoparticles were observed to be trafficked to the endoplasmic reticulum, Golgi apparatus, lamellar and lipid bodies. Additionally the photo-triggered released of the model drug, Nile red, from the nanoparticles inside the A549 lung cancer cells was demonstrated using NIR photo-irradiation stimulus. The results were discussed in terms of the physicochemical properties (size, shape, and surface charge) of the nanoparticle in order to be able to understand the nanoparticle-cell interactions.

Chapter 6: "Thermal Properties of Lipid Bilayers Determined Using Upconversion Nanothermometry"

This Chapter discusses the characterization of $LiYF_4:Er^{3+}/Yb^{3+}$ with a supported lipid bilayer as a luminescent nanothermometry probe for thermal sensing bio-applications. The thermal conductivity of the lipid bilayer at the surface of the nanoparticles was measured and the temperature gradients across the lipid bilayer were detected using the luminescence properties of

the nanoparticles. In addition, a lumped model was developed to measure the directional heat transfer between the nanoparticle, lipid bilayer and the surrounding environment. This project was developed in collaboration with professor Luís D. Carlos at University of Aveiro in Portugal.

Chapter 7

This chapter provides the conclusions of the worked presented in this thesis.

Chapter 8

This chapter presents some suggestions for future work.

Chapter 2

Formation of a Supported Lipid Bilayer on Faceted $LiYF_4:Tm^{3+}/Yb^{3+}$ Upconversion Nanoparticles

Publish as:

Paola A. Rojas-Gutierrez, Christine DeWolf, and John A. Capobianco*

Particle and Particle System Characterization. **2016**, *33* (12), 865–870.

Department of Chemistry and Biochemistry, and Centre for NanoScience Research, Concordia University, Montreal, Quebec, H4B 1R6, Canada.

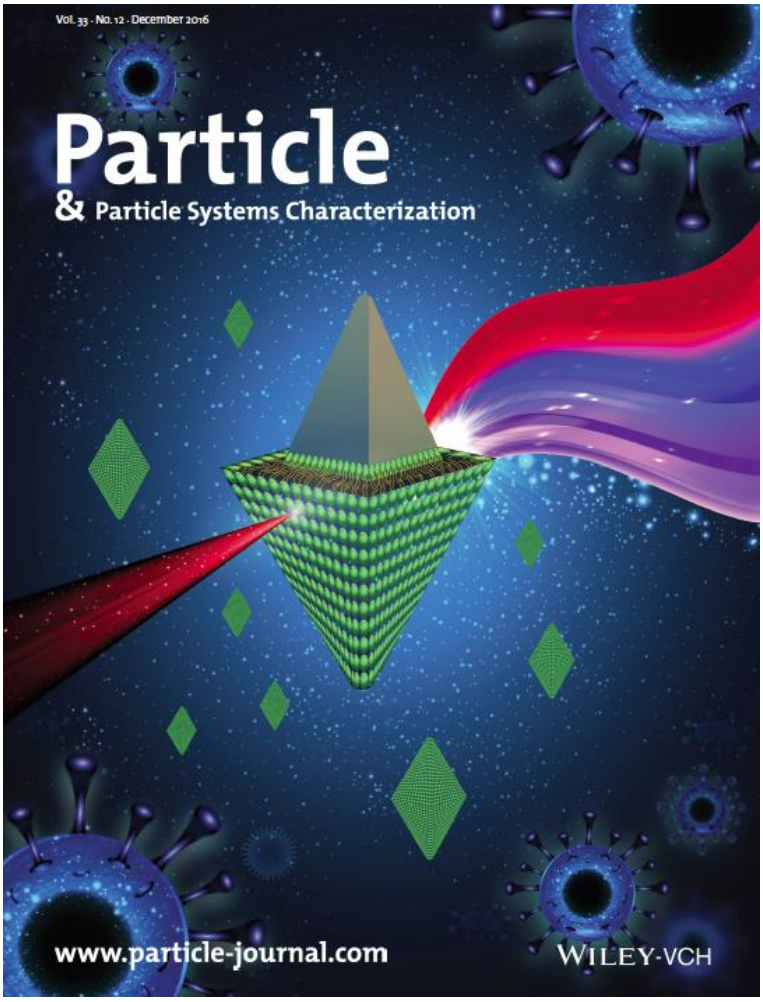

Scheme 2. 1 Upconversion Nanoparticles: Formation of a supported lipid bilayer on faceted $LiYF_4:Tm^{3+}/Yb^{3+}$ Upconversion Nanoparticles (Cover Picture on Part. Part. Syst. Charact. 12/2016, Page 859)[196]

"Supported lipid bilayers mimic cell membranes and may be an alternative method to produce water dispersible nanoparticles with high biocompatibility and provide the possibility of drug encapsulation inside the lipid bilayer. On page 865, J. A. Capobianco and co-workers apply this approach to lanthanide-doped upconverting nanoparticles that convert low energy light (NIR) to UV and visible".

2.1 Abstract

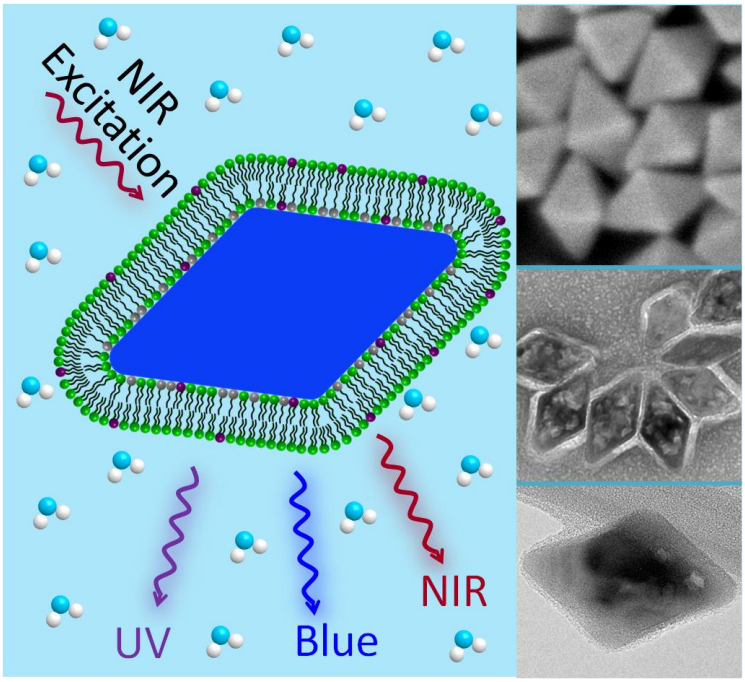

Scheme 2. 2 Graphical table of content of Formation of a "Supported Lipid Bilayer on Faceted $LiYF_4:Tm^{3+}/Yb^{3+}$ Upconversion Nanoparticles."

Lanthanide-doped upconverting nanoparticles (Ln-UCNPs) convert low energy near-infrared (NIR) absorbed light to ultraviolet, visible and NIR emissions. For biological applications, water dispersibility, bio-compatibility and high colloidal stability must be achieved. Enveloping nanoparticles with supported lipid bilayer (SLB) is an alternative method to solve this problem. In the present work we show the formation and characterization of a SLB on $LiYF_4:Tm^{3+}/Yb^{3+}$ UCNPs.

2.2 Introduction

Lanthanide doped nanomaterials have garnered significant attention, particularly in the past two decades, predominantly due to their versatile optical properties. Of great interest is the fact that the lanthanides can emit light under a multiphoton excitation process, where they are able to convert low energy light such as near-infrared (NIR) to ultraviolet and visible emissions in a process known as upconversion. At the nanoscale, lanthanide-doped upconverting nanoparticles (Ln-UCNPs) have ushered the way for developments of novel applications ranging from display devices and optical sensors, bio-imaging and diagnostic optical probes to drug delivery and therapeutics.[23,197,198] The driver behind the biological applications has been the developments of synthetic routes to produce colloidal lanthanide-doped upconverting nanoparticles. However, several other requirements must be met before Ln-UCNPs achieve their full promise and potential that they hold for their ultimate use in biological applications.[70] These include water dispersibility, bio-compatibility, high colloidal stability under biological conditions, and the possibility of functionalization with appropriate targeting agents. To date, fluoride based nanoscale upconverting materials such as hexagonal and cubic $NaY(Gd)F_4$ and tetragonal $LiYF_4$ have been synthesised doped with the two more popular lanthanide ions Er^{3+} or Tm^{3+}.[67,199,200] The current synthetic route for the preparation of the high quality Ln-UCNPs is based on oil-phase methods. This yields hydrophobic Ln-UCNPs, which have no intrinsic aqueous dispersibility and lack functional moieties for subsequent biological functionalization. Thus, they require post synthetic treatments to render them hydrophilic and give them biological activity. Encapsulation to produce water dispersible Ln-UCNPs has been demonstrated but usually yields two major drawbacks. First, the brightness of the emission is considerably reduced and secondly the intensity ratio between certain transitions changes, for example between the $^2H_{11/2}/^4S_{3/2} \rightarrow {}^4I_{15/2}$ transitions of Er^{3+} green upconverted luminescence and the red emission from the $^4F_{9/2} \rightarrow {}^4I_{15/2}$ transition. The gap between these two states can be bridged efficiently by high-energy vibrational groups present on the surface. For example, hydroxyl (OH) groups generate high-energy vibrational modes at 3200-3660 cm^{-1}, which contribute to the increase of the $^4F_{9/2}$ excited state population by increasing the probability of multiphonon relaxation from the $^2H_{11/2}/^4S_{3/2}$ to

$^4F_{9/2}$ resulting in a change of the ratio of the $I_{green/red}$.[85,86] Therefore, both the decrease in brightness and the intensity ratio between transitions of Ln-UCNPs in water compared to the hydrophobic Ln-UCNPs are affected and can be attributed to the nonradiative decay of the electronically excited states of the dopant lanthanide ions caused by surface ligands and water molecules.

Approaches for encapsulation (and hence protection of the surface from water) vary and in a recent manuscript Wilhelm et al. introduced an appropriate terminology, Type-ex and Type-add, to describe the procedures used to convert the surface from hydrophobic to hydrophilic.[85] Type-ex involves the exchange of the oleate ligand by a hydrophilic ligand including both small molecules and polymers. Whereas, Type-add is the addition of an amphiphilic layer, a mesoporous or silica coating or an appropriate polymer while maintaining the original hydrophobic capping ligand (e.g. oleate). Capobianco *et al.* proposed the removal of the oleate capping ligand using a straightforward and simple acid treatment to obtain water-dispersible ligand-free Ln-UCNPs, which facilitates the direct conjugation of electronegative groups such –SH, -COOH, $-NH_2$ and -OH in aqueous solution.[86] Lipid-polymer monolayers have also been used to cover the surface of the nanoparticles by hydrophobic interactions between the capping ligand and the lipid chain while the hydrophilic polymer bonds to the lipid head rendering the nanoparticles water dispersible.[201–203]

Approaches to creating supported lipid bilayer (SLB) coatings to nanoparticles usually follow a type-add approach, using the organic film as the inner leaflet. SLB coatings have been successfully added to silica,[94,204] calcium phosphate,[101] metallic (Au and Ag),[205,206] quantum/carbon dots[207,208] and magnetic (Fe_2O_3) particles.[209] Often these coatings comprise interdigitated leaflets (also referred to in the literature as micellar complexes and pseudo "monolayers") with film thicknesses of 2-3 nm. However such films may yield less encapsulation capacity for hydrophobic active ingredients than a non-interdigitated bilayer. PEG lipids are often used as stabilizers and these films have recently been applied to lanthanide-doped UCNPs ($NaGdF_4$).[203] The large PEG headgroup provides increased coverage for the less tightly-packed, lower curvature outer leaflet, however the PEG may also alter the release and diffusion

characteristics for encapsulated active ingredients as well as the nanoparticle interaction with cells and biomolecules, as PEGs are frequently used to limit cell adhesion and protein interactions with surfaces.[210]

Most reports of lipid bilayer coatings are for spherical nanoparticles. One of the challenges with Ln-UCNPs is their crystal morphology, which in general is not spherical. Such a coating has been reported for highly irregular TiO_2 particles, however the inner leaflet was chemically attached to the TiO_2 surface and for hexagonal plates of $NaYF_4$ in which an interdigitated, PEG stabilized film was created.[201,211] Herein we report of the formation of a non-interdigitated lipid bilayer coating on highly-faceted, diamond-shaped, $LiYF_4$:$Tm^{3+/}Yb^{3+}$ nanoparticles with acute angles (Figure 2S.1-2S.4, Supporting Information) without the use of PEG-stabilizers. We reasoned that this approach could provide a potential solution to the problem of decrease in brightness of the Ln-UCNPs. In addition, the supported phospholipid bilayer renders the Ln-UCNPs water dispersible and provides excellent biocompatibility since phospholipids mimic the composition and functionality of the cell's external membrane.

2.3 Results and Discussion

Figure 2.1 shows the proposed nanostructure composed of: the $LiYF_4$:Tm^{3+}/Yb^{3+} nanoparticle with a bilayer coating comprising residual oleate, 1,2-di-(9Z-octadecenoyl)-*sn*-glycero-3-phosphate (DOPA), 1,2-di-(9Z-octadecenoyl)-*sn*-glycero-3-phosphocholine (DOPC) and cholesterol. Cholesterol was added to decrease the water-permeability of the coatings as it is known to create a tighter packing in lipid films comprising unsaturated fatty acid chains.[212] The hydrophobic tail of the lipid DOPA interacts with the oleate already on the surface of the Ln-UCNPs *via* hydrophobic van der Waals interactions. The negative charge on the headgroup of the lipid DOPA interacts electrostatically with the positive charge on the surface of the Ln-UCNPs. In contrast to the usual picture painted of an oleic acid capped film providing complete surface coverage of the Ln-UCNPs, thermal gravimetric analysis showed a weight loss of only 1.78% (Figure 2.S5, Supporting Information). This represents 3.8×10^{17} molecules of oleate on

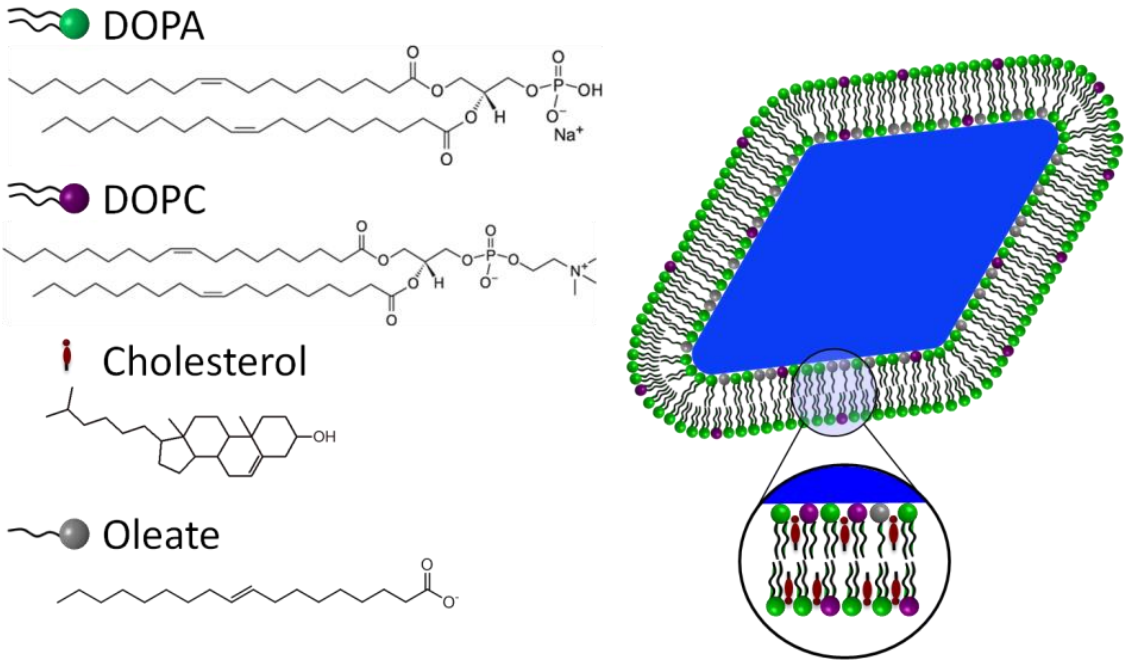

Figure 2. 1 Schematic illustration showing the nanoconstruct synthesized from oleate-capped $LiYF_4:Tm^{3+}/Yb^{3+}$ upconverting nanoparticles and a supported lipid bilayer DOPA, DOPC and cholesterol.

the surface and a surface coverage of approximately 40%, corroborating the likelihood for presence of DOPA in the inner leaflet, driven by electrostatic interactions. The excess lipid interacts *via* hydrophobic interactions with the monolayer of lipid on the Ln-UCNPs to produce the SLB. The role of the lipid DOPC is to prevent repulsion between the negatively charged head groups of DOPA. We will provide evidence that DOPA, DOPC and cholesterol forms a supported lipid bilayer encapsulating the $LiYF_4:Tm^{3+}/Yb^{3+}$nanoparticles, despite the faceted form of the nanoscale particles.

Transmission electron microscopy (TEM) provides high spatial resolution and has been and is applied extensively to determine the structure, size and morphology of materials of nanoscale dimensions. Not withstanding the fact that high spatial resolution is achieved using

TEM, low mass elements such as carbon, oxygen, nitrogen and phosphorus, which make up the supported lipid bilayer, lead to low contrast and hence difficulties in imaging. The imaging contrast in TEM is due to the electrons as they pass through the sample and regions with high atomic number scatter more electrons than low atomic number areas of the same thickness. Typically a thin amorphous carbon film is utilized to support the sample under the electron beam. Because the carbon film is similar in thickness and composition to the supported lipid bilayer, imaging it against the carbon film background is challenging. In addition, the interaction of high-energy electrons with organic molecules on the surface of the nanoparticles can lead to the formation of amorphous carbonaceous material.[213]

The deposition of additional carbonaceous material was directly observed in a series of experiment that examined the TEM images as a function of time and beam current density for samples deposited on lacey carbon grids. Using the lacey carbon grids increases the likelihood that the nanoparticles are found in the "holes", which limits the exposure of the carbon surface to the electron beam. **Figure 2.2**a shows the nanoconstruct found in a hole with one of its edges protruding over the hole and irradiated at minimum current density. The particle is clearly surrounded by a continuous organic layer, the thickness of which is approximately 3.8 ± 0.4 nm. Figure 2b is taken 60 seconds later at 2 times the current density and shows no significant increase in the organic coating surrounding the particle. Figure 2.2c shows the same particle imaged at 4 times the current density, measured directly following the previous image (Figure 2.2b). After 120 seconds of exposure at this current density, one can already observe a significant increase in the film thickness. This procedure is repeated at 9 times the original current density and the coating continues to exhibit growth (Figure 2.2d).

We attribute this increase in thickness of the layer surrounding the nanoparticle to organic molecules on the surface of the sample being imaged that diffuse toward the edge. In addition, if the electron beam has a diameter that is larger than the nanoparticles being imaged the beam will also illuminate the grid, which will contribute to the diffusion of carbon material towards the edge at higher current densities. However, this effect was not observed on the oleate-capped $LiYF_4$:Tm^{3+}/Yb^{3+}nanoparticles, which we attribute to the lower (40%) organic coverage

of the nanoparticle surface (Figure 2S.5). Thus precautions must be taken to ensure that the layers observed are not artifacts of the measurement itself.

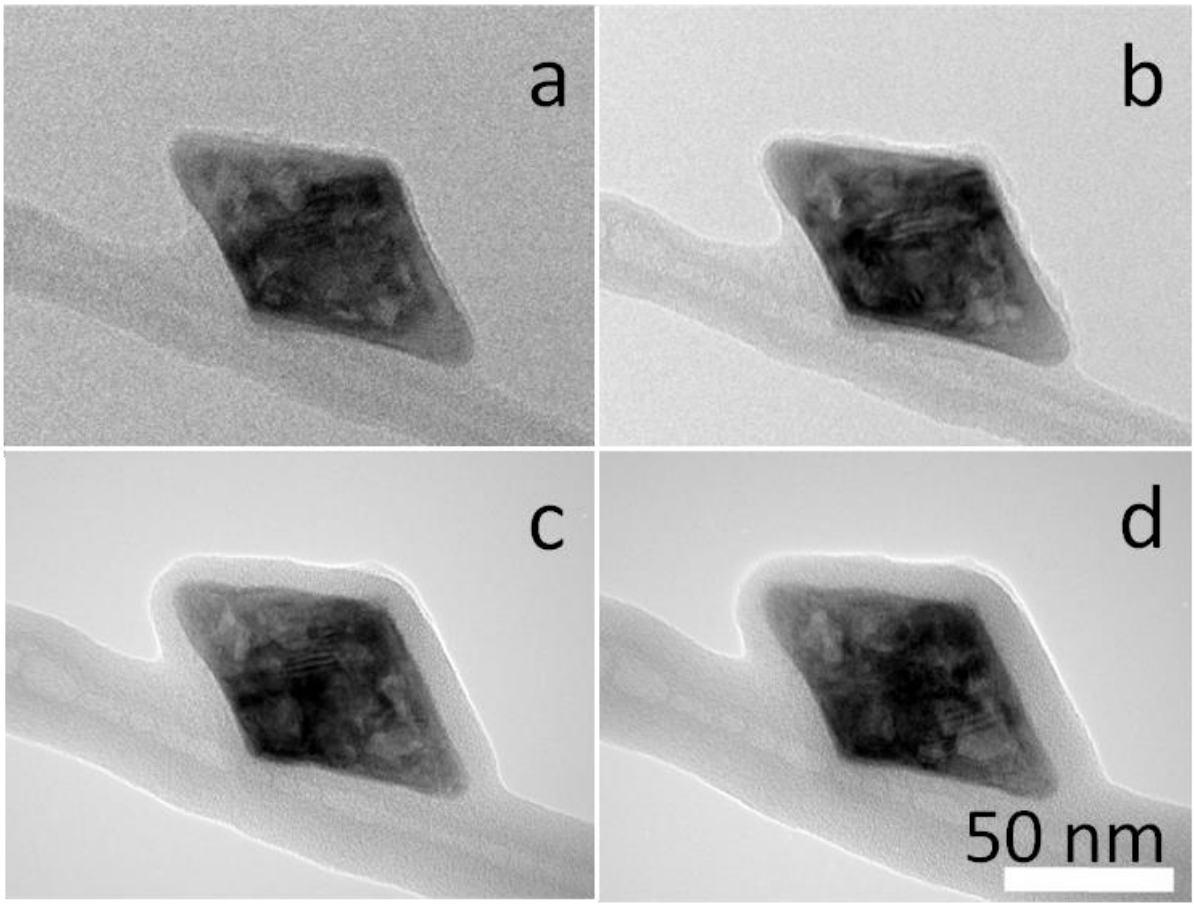

Figure 2. 2 TEM images of the same SLB-$LiYF_4$:Tm^{3+}/Yb^{3+} UCNP on a lacey carbon grid varying the electron beam current density and the exposure time. Images a-d are taken sequentially: a) image taken with low current density, SLB thickness 3.8 ± 0.4 nm, a) image taken after an additional 60 s exposure at 2 times the current density, SLB thickness 4.1 ± 0.4 nm, c) image taken after an additional 120 s exposure at 4 times the current density, SLB thickness 9.1 ± 0.6 nm, d) image taken after an additional 120 s exposure at 9 times the current density, SLB thickness 12.6 ± 0.7 nm.

Two techniques have been developed to overcome the lack of contrast and to mitigate electron induced damage and film growth. One is the method of negative staining and the other is cryo-electron microscopy (cryo-TEM). Negative staining mitigates electron induced sample damage by coating the surface with reagents containing heavy atoms. Uranyl formate is one of the most commonly used to enhance the contrast.[214] Cryo-TEM involves imaging a sample that has been frozen either at liquid nitrogen or liquid helium temperature. At low temperature the extent of radiation damage is reduced, thus imaging can be carried out at much higher electron doses, which enhances the resolution.[215]

Figure 2.3a-c shows TEM images of the $LiYF_4:Tm^{3+}/Yb^{3+}$ nanoparticles coated with a with a lipid mixture comprising DOPA, DOPC and cholesterol (64:7:29 mole %) after vortexed and extruded 41 times after extrusion through a polycarbonate membrane (200 nm). They are deposited on a carbon coated grid and then stained with uranyl formate. We observe a mixture of liposomes, nanoparticles encapsulated in liposomes and nanoparticles surrounded by what appears to be a supported lipid bilayer (Figure 2.3a-c, respectively).

In order to remove the free liposomes and the nanoparticles encapsulated in the interior of liposomes the solution was additionally centrifuged for 30 minutes at 12000 rpm and for 20 minutes at 5000 rpm. The supernatant was removed and the pellet was rehydrated with HEPES buffer (1 mL, pH 7.4). In Figure 3d the negative stain TEM images are shown. The contrast in the image is due to increased electron scattering from nanoparticles covered by the stain. The bright layer surrounding the nanoparticles demonstrates that the lipid layer covered by the uranyl formate scatters the electrons less. Thus, the image reveals that the oleate-capped $LiYF_4:Tm^{3+}/Yb^{3+}$ UCNPs are surrounded by a continuous layer of material (bright area) that adheres to the rough surface of the nanoparticles, separated from the nanoparticle edge by approximately 4.7 ± 1.0 nm. This distance is in excellent agreement with the known thickness of a lipid bilayer.[94,212]

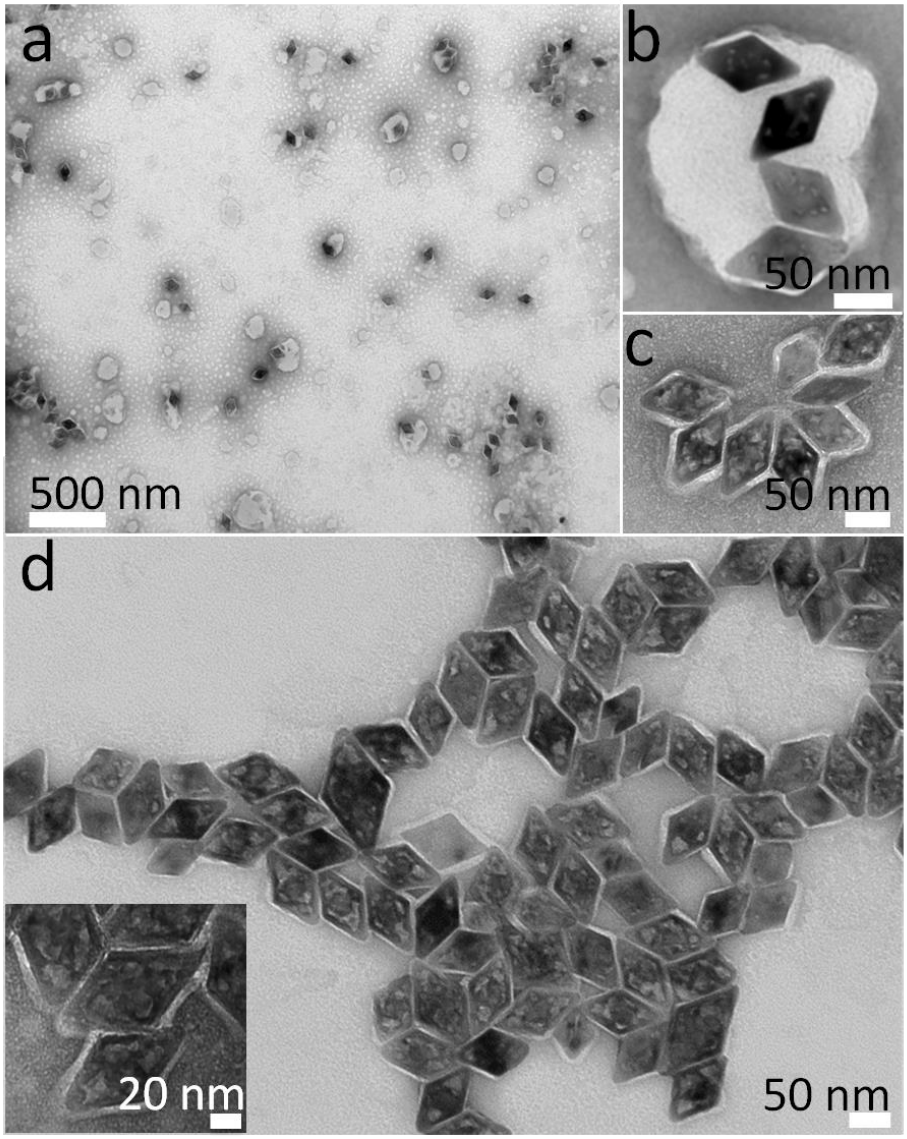

Figure 2. 3 Negative stain-TEM images of the nanoconstruct preparaed with the lipid mixture (DOPA, DOPC, cholesterol 64:7:29 mole %). a-c) oleate-capped $LiYF_4$ Tm^{3+}/Yb^{3+} UCNPs after vortex and extrusion with the lipid mixture. a) Mixture of liposomes, encapsulated nanoparticles and nanoparticles with a supported bilayer, b) Oleate-capped $LiYF_4$ Tm^{3+}/Yb^{3+} UCNPs encapsulated in a liposome, c) Oleate-capped $LiYF_4$ Tm^{3+}/Yb^{3+} UCNPs coated with a supported lipid bilayer, d) Oleate-capped $LiYF_4$:Tm^{3+}/Yb^{3+} UCNPs coated with a supported after micro-centrifugation.

Additional evidence supporting the formation of the lipid bilayer can be seen in **Figure 2.4**a,b,c that demonstrates the effect of defocus on the contrast in cryo-TEM. The images were obtained after extrusion only, which allows us to also observe the liposomes formed. As the defocus is increased from Figure 4a-c the most obvious change is an increase in the contrast. The liposomes are more apparent in the under focus images Figure 4b,c. However, in the near focus image Figure 4a, the lack of contrast makes it difficult to discern the thickness of the lipid bilayers. The thickness of the lipid bilayers in the defocus images was measured to be approximately 4.0 ± 0.4 nm for the liposomes. The same effect resulting from defocus is observed for the nanoconstruct, which clearly shows the supported lipid bilayer in the defocus images (Figure 2.4b and 2.4d). The supported lipid bilayer is approximately 4.4 ± 0.4 nm, which is in excellent agreement with the thickness of the lipid bilayer found for the liposome.

The upconversion luminescence spectrum, **Figure 2.5**a (iii), of the oleate capped nanoparticles, upon irradiation with 980 nm light exhibited the characteristic emission peaks of Tm^{3+}ions in the UV, visible and NIR regions. The upconverted UV emissions at 295, 353 and 368 nm are assigned to the $^3P_0 \rightarrow {}^3H_6$, $^3P_0 \rightarrow {}^3F_4$ and $^1D_2 \rightarrow {}^3H_6$ transitions, respectively. The blue emissions at 450 and 480 nm, the red emission at 650 nm and the NIR at 800 nm, are assigned to the $^1D_2 \rightarrow {}^3F_4$, $^1G_4 \rightarrow {}^3H_6$, $^1G_4 \rightarrow {}^3F_4$ and $^3H_4 \rightarrow {}^3H_6$ transitions respectively. To investigate the effect of the supported lipid bilayer on the upconversion spectra of the $LiYF_4:Tm^{3+}/Yb^{3+}$ nanoparticles, measurements were carried out on the nanoconstruct dispersed in H_2O as well as in D_2O upon 980 nm excitation and are presented in Figure 2.5a (ii, i). We observed that the upconversion intensity (spectra normalized with respect to the NIR of the oleate spectrum) is enhanced for the nanoconstruct dispersed in D_2O compared to that in H_2O. This result is not unexpected and provides evidence of the isotope effect that reduces the nonradiative pathways. The overall intensity of the nanoconstruct dispersed in H_2O is higher than the oleate capped nanoparticles in non-polar solvents as previously reported.[85,201,203] This may be due to limited solubility of water in toluene (0.033%).[27] The comparison of the spectra in D_2O and H_2O is indicative that the films are still somewhat permeable to water, despite the addition of cholesterol to increase the chain ordering.[216]

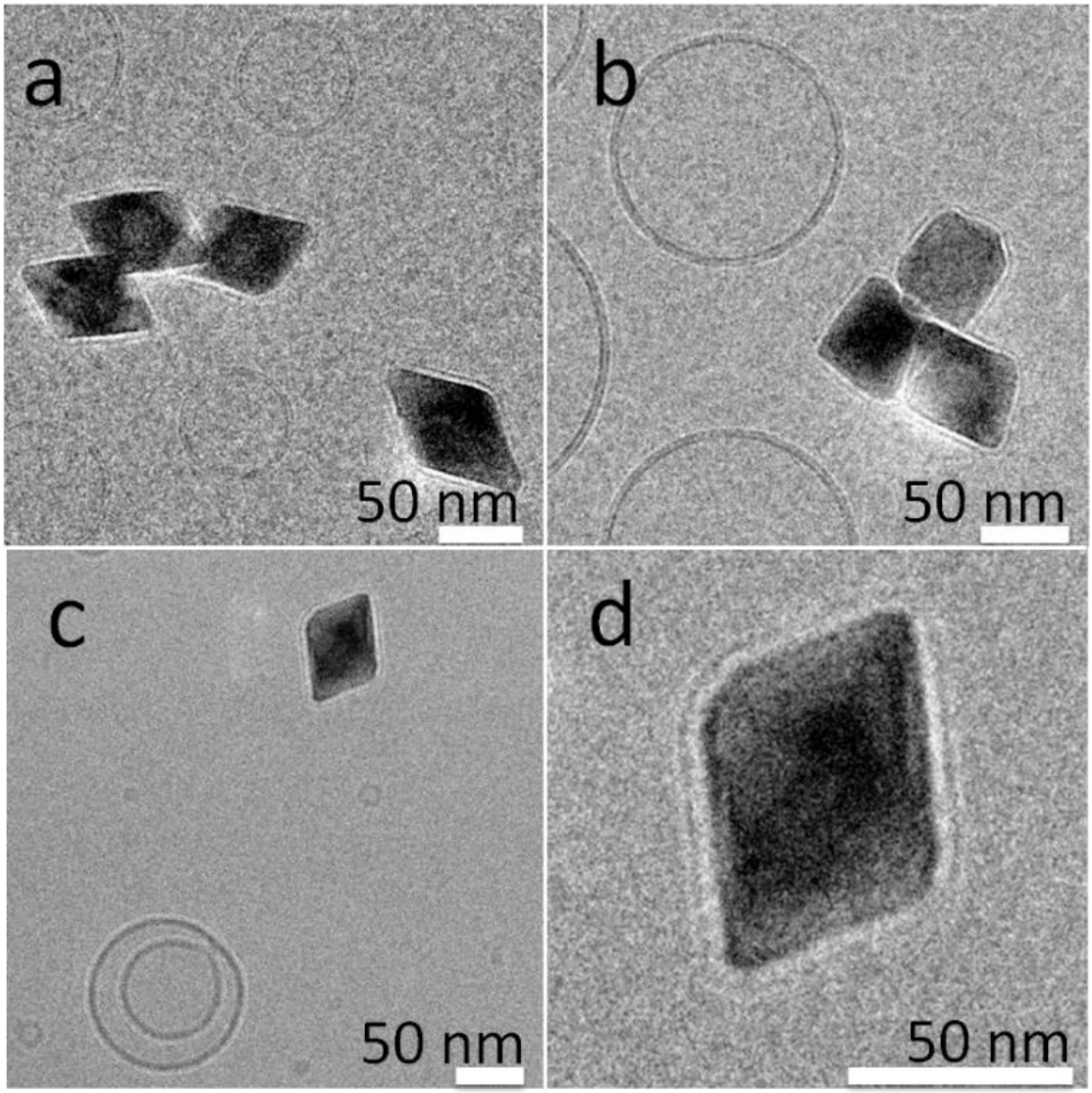

Figure 2. 4 Cryo-TEM images of oleate-capped $LiYF_4$ Tm^{3+}/Yb^{3+} UCNPs coated by a supported lipid bilayer after extrusion and free liposomes. Images obtained using different defocus levels a) -1 μm, b) -3 μm, c) -7 μm, d) Expanded view of nanoconstruct in image c (defocus -7 μm). Thickness of supported lipid bilayer, 4.4 ± 0.4 nm

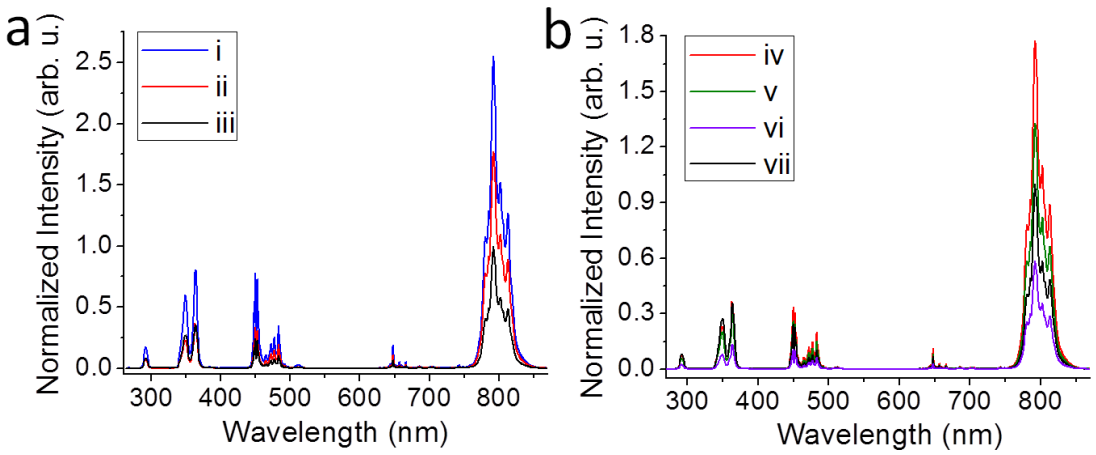

Figure 2. 5 a) Emission spectra of (i) Nanoconstruct DOPA:DOPC:Chol (64:7:29 mole %) in D_2O, (ii) Nanoconstruct DOPA:DOPC:Chol (64:7:29 mole %) in H_2O, (iii) Oleate-capped $LiYF_4:Tm^{3+}/Yb^{3+}$ UCNPs in toluene. b) Emission spectra of (iv) Nanoconstruct DOPA:DOPC:Chol (64:7:29 mole %) in H_2O, (v) Nanoconstruct DOPA:DOPC:Chol (35.5:35.5:29 mole %) in H_2O, (vi) Nanoconstruct DOPC:Chol (71:29 mole %) in H_2O, (vii) Oleate-capped $LiYF_4:Tm^{3+}/Yb^{3+}$ UCNPs in toluene. Excitation wavelength, 980 nm.

To assess the effectiveness of the SLB in providing a more efficient coverage of the surface of the nanoparticles, the ratio of DOPA:DOPC was varied, while keeping the amount of cholesterol constant. The effect of changing the ratio of DOPA:DOPC on the overall charge of the nanoconstruct was investigated *via* zeta potential measurements. The zeta potential is a measure of the magnitude of electrical repulsive forces between particles and it is predictive of colloidal stability. Particles with zeta potential values greater than +25 mV or less than -25 mV typically have high degree of stability. This is described by the classical DLVO (Derjaguin, Landau, Verwey, Oberbeek) theory of colloidal interactions that predicts that in the absence of van der Waals attraction, the interaction between like-charged colloidal particles is repulsive.[217,218]

Table 2.1 shows the measured zeta potentials of the nanoconstruct as a function of the DOPA:DOPC ratio (the cholesterol content is maintained at 29 mole %). The value of the zeta potential for the oleate-free nanoparticles is +22 mV in excellent agreement with the literature value, which indicates a stable colloidal system that is the absence of coagulation.[86] In the presence of only zwitterionic DOPC and neutral cholesterol, the particles adopt a relatively neutral zeta potential (0.7 mV). The presence of DOPA in the nanoconstruct induces a negative zeta potential that becomes more negative as the proportion of negatively charged DOPA increases (relative to the DOPC and cholesterol lipid components). At neutral pH the phosphatidic acid headgroup of the lipid DOPA is negatively charged thus it interacts with the positive charge present on the surface of the nanoparticles that is present because only 40% of the surface is capped by the oleate ligand. The second layer of the lipid interacts *via* hydrophobic interactions with the first lipid monolayer (inner leaflet) on the Ln-UCNPs to produce a supported lipid bilayer. High negative values of the measured zeta potential, -52 mV and -54 mV, are obtained with 64% DOPA and 71% DOPA, respectively.

Table 2. 1 Zeta potential values for $LiYF_4:Tm^{3+}/Yb^{3+}$ UCNPs nanoconstructs with different DOPA:DOPC lipid ratios the proportion of cholesterol in the mixture remains constant at 29 mole %.

$LiYF_4:Tm^{3+}/Yb^{3+}$ UCNPs	DOPA mole %	DOPC mole %	Cholesterol mole %	ζ-potential [mV]	STDEV
Oleate-free	-	-	-	22	1.0
DOPC:Chol	0	71	29	1	0.2
DOPA:DOPC:Chol	35.5	35.5	29	-8	0.6
DOPA:DOPC:Chol	64	7	29	-52	0.8
DOPA:Chol	71	0	29	-54	1.8

To investigate the effect of the changing the proportion of negatively charged DOPA ratio on the upconversion spectra, measurements were carried out on the oleate capped nanoparticles dispersed in toluene as well as aqueous dispersions of nanoparticles coated with

lipid bilayers formed with variation in the DOPA:DOPC ratio (Figure 2.5b and Figure 2S.8 Supporting Information). Comparing the spectra reveals that the upconversion intensity decreases as the DOPA:DOPC ratio decreases. The decrease in the upconversion intensity may be explained by two factors. First, as the DOPC concentration increases the degree of stability of the colloidal solution decreases as described by the classical DLVO theory, resulting in aggregation, which induces precipitation of the nanoconstruct that may decrease the number of nanoparticles in the path of the laser beam. Secondly, it appears that formation of a continuous supported lipid bilayer is hindered at high DOPC compositions, as is shown in the negative stain TEM images in Figure 2S.7 Supporting Information. As the proportion of DOPC increases, the SLB does not form as well on the nanoparticle surface and there is more free lipid on the TEM grid. This is likely a direct consequence of the 40% oleate coverage on the Ln-UCNP surface such that as the amount of DOPC increases (to the exclusion of DOPA), so does the amount of DOPC in the inner leaflet. Wang and Liu noted that when DOPC had to reorient to enable a fusion of the phosphate to a TiO_2 surface, the resulting steric repulsion hindered SLB formation.[211] Yao *et al.* had also reported difficulty forming a pure DOPC bilayer on $NaGdF_4$ UCNPs, especially with small size nanoparticles (down to 4 nm) due to curvature.[209] Here, we postulate that the destabilization of the DOPC SLB is due to the repulsion of the exposed positively charged choline with the positive charge present on the nanoparticle surface, either directly or by forcing a reorientation of the headgroup to expose the negatively charged phosphate thus inducing steric repulsion. The less well-formed bilayer presumably allows more water to interact with the surface resulting in the quenching of the Ln-UCNPs emission.

2.4 Conclusions

In this work, we have demonstrated that a type-add approach can be used to coat Ln-UCNPs with supported lipid bilayers, despite a low initial coverage of oleate on the surface. The method yielded water dispersible Ln-UCNPs that were easily separated from excess liposomes. The SLB was sufficiently continuous to protect the Ln-UCNPs from water-derived quenching of the emission, although the effectiveness of the film was a function of composition with a greater

proportion of negatively charged lipids in the film yielding better formed layers. The film thickness suggests that it is a non-interdigitated lipid bilayer rather than a monolayer or micellar complex which is anticipated to provide better encapsulation capacity for hydrophobic active ingredients. Finally, the film appears continuous despite the acute angles present due to the crystal morphology.

2.5 Supporting Information (Experimental)

2.5.1 Synthesis of oleate-capped $LiYF_4:Tm^{3+}/Yb^{3+}$ (UCNPs)

Thulium oxide (Tm_2O_3, 99.99+ %), ytterbium oxide (Yb_2O_3, 99.99%), yttrium oxide (Y_2O_3, 99.99+ %), triflouroacetic acid (CF_3COOH, 99%), lithium trifluoroacetate (CF_3COOLi, 98%), oleic acid (technical grade, 90%), and 1-octadecene (technical grade, 90%) were all purchased from Sigma-Aldrich and were used without further purification. $LiYF_4:Tm^{3+}$/ Yb^{3+} UCNPs were synthesized *via* the thermal decomposition, which was comprised of a two-step process.[67] In the first step, a mixture of water/trifluoroacetic acid (10 mL, 1:1) was added to a 3-neck round-bottom flask containing Tm_2O_3 (0.0024 g, 6.25×10^{-6} mol, 0.5 mole % Tm^{3+}), Yb_2O_3 (0.1232 g, 3.13×10^{-4} mole, 25 mole % Yb^{3+}), and Y_2O_3 (0.2103 g, 9.31×10^{-4} mol), the cloudy solution was heated (80 °C) under reflux until it was clear. The resulting solution was then dried at 60 °C to form the trifluoroacetate lanthanide precursors. In the second step, CF_3COOLi (0.2999 g, 2.50×10^{-3} mol) was added to the dried precursor solids along with oleic acid (20 mL) and 1-octadecene (20 mL) and the mixture was degassed for 30 min at 120 °C. Then the temperature was increased at a rate of 10 °C/min to 315 °C under an argon atmosphere. The reaction mixture was maintained at 315 °C under stirring for 60 min under an argon atmosphere. After cooling to room temperature, absolute ethanol was added to the reaction solution to precipitate the $LiYF_4:Tm^{3+}$, Yb^{3+} UCNPs, which were subsequently isolated *via* centrifugation (3000 rpm, 15 min). The pellet was washed with a 1:3 hexane/ethanol mixture twice to remove any impurities.

2.5.2 Synthesis of oleate-capped $LiYF_4:Tm^{3+}/Yb^{3+}$ (UCNPs) with supported lipid bilayer

1,2-di-(9Z-octadecenoyl)-*sn*-glycero-3-phosphate (DOPA) and 1,2-di-(9Z-octadecenoyl)-*sn*-glycero-3-phosphocholine (DOPC) were purchased from Avanti Polar Lipids Inc., cholesterol (99+ %), was purchased from Sigma-Aldrich and chloroform (ACS grade) was purchased from Fisher Scientific. Deuterium oxide (D_2O 99.9%) was purchased from Cambridge Isotope Laboratories, Inc. HEPES was purchased from Bioshop ®. Sodium acetate (99+%) was purchased from Sigma-Aldrich. All water used for the experiments was ultrapure (18.2 MΩ·cm) obtained from a Barnstead system.

Oleate-capped $LiYF_4:Tm^{3+}$, Yb^{3+} (UCNPs) with a supported lipid bilayer were synthesized following the below procedure which is a variation of the hydration dry lipid film method used to prepared liposomes.[56,98] Typically stock solutions of DOPA, DOPC and cholesterol in chloroform (10 mM) were prepared from which mixed lipid solutions comprising different ratios of DOPA, DOPC and cholesterol were prepared (5 mM). The concentration of cholesterol was maintained at 29 mole% in all samples. The amount of cholesterol was selected to induce sufficient condensation of the alkyl chains to limit water permeability and yet be far enough from the miscibility limit of cholesterol in the lipids. The latter is important to prevent crystallization and phase separation of cholesterol (usually 60 mol% cholesterol) should the proportion of lipid adsorbed on the surface vary slightly from the initial lipid mixture.[212,216]

In summary, oleate-capped $LiYF_4:Tm^{3+}/Yb^{3+}$ UCNPs (2 mg) were dispersed in chloroform (1% m/v) and sonicated (10 minutes at 70W), after the lipid mixture solution were added (700 uL). The mixture of nanoparticles and lipids was sonicated (10 minutes) and then the solvent was evaporated under reduce pressure to form the dry lipid film. This cycle was repeated 3 times by solvating the mixture using chloroform (1 mL) in order to increase the interaction between the lipids and the surface of the nanoparticle. After the last cycle, the dry lipid film with the nanoparticles was left it under vacuum to remove all solvent traces (45 minutes). The dry lipid film was hydrated for an hour with HEPES buffer (1 mL, 5mM HEPES, 5mM sodium acetate, 30mM NaCl, pH adjusted to 7.4 with NaOH). Subsequently it was vortex, sonicated and

extruded (41 times) through a 200 nm polycarbonate membrane filter. The sample was centrifuged (30 minutes at 12000 rpm, and for 20 minutes at 5000 rpm), the supernatant was removed and the pellet was rehydrated with HEPES buffer (1 mL) to obtain oleate-capped $LiYF_4:Tm^{3+}$, Yb^{3+} (UCNPs) with a supported lipid bilayer. The same protocol was followed for samples in D_2O.

2.6 Supporting Information (Characterization)

2.6.1 Characterization of oleate-capped $LiYF_4:Tm^{3+}/Yb^{3+}$ UCNPs

Figure 2S.1 shows the X-Ray power diffraction (XRPD) of the oleate-capped $LiYF_4:Tm^{3+}/Yb^{3+}$ UCNPs and the calculated standard of JCPDS pattern. The peak positions correspond closely to the reported pattern of tetragonal $LiYF_4$ (JCPDS no. 81-2254).

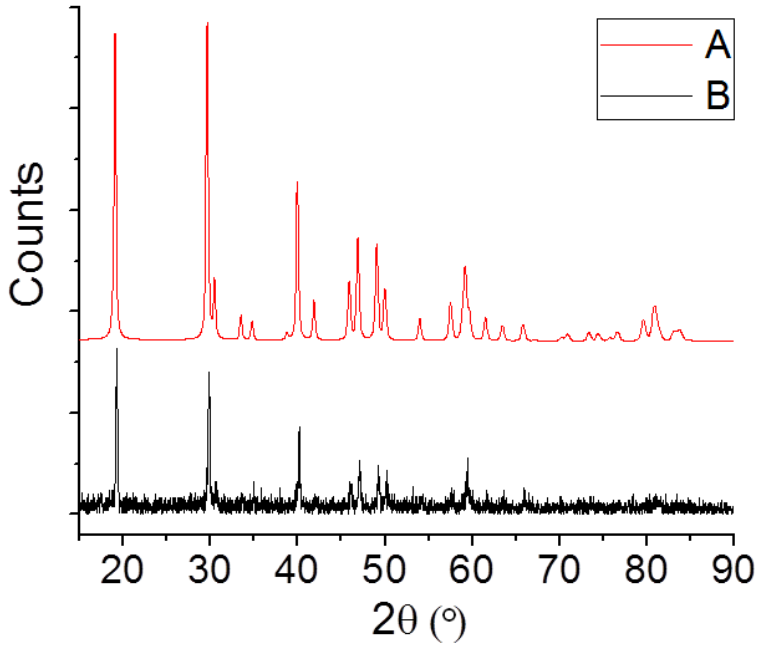

Figure 2S. 1 Calculated standard (A) and experimental (B) XRPD Patterns of $LiYF_4$ A) Reference Pattern JCPDS File No. 81-2254, and B) Oleate-capped $LiYF_4:Tm^{3+}/Yb^{3+}$UCNPs.

High transmission electron microscopy (HRTEM) was used to evaluate the morphology and particle size distribution (PSD) of the prepared nanoparticles. Approximately 300 particles were evaluated to obtain the distribution. The oleate-capped $LiYF_4:Tm^{3+}/Yb^{3+}$ UCNPs showed a diamond-like morphology with an average size of 97 nm (±14 nm) long diagonal length and a small diagonal length of 59 nm (±8 nm).

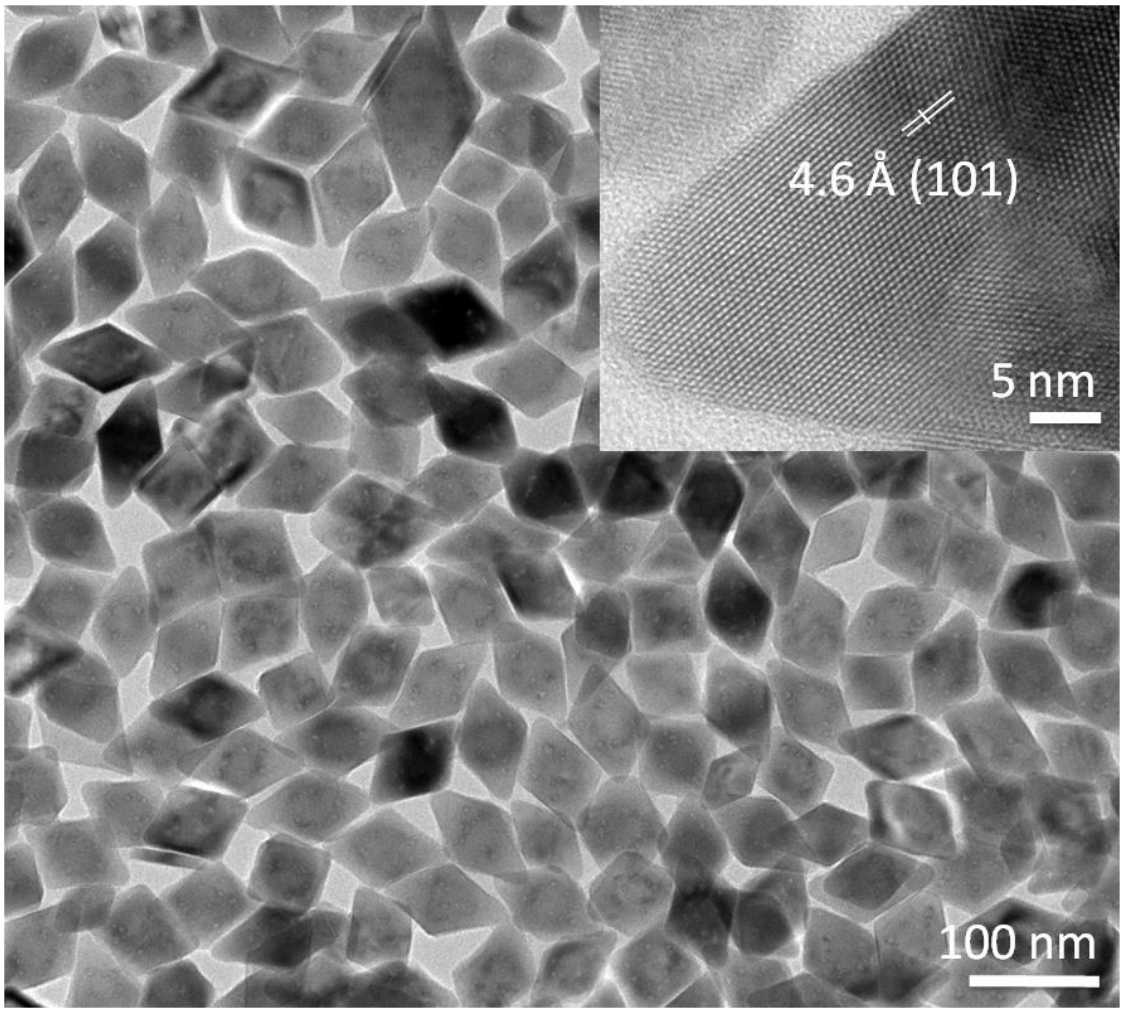

Figure 2S. 2 Transmission electron microscopy image of oleate-capped $LiYF_4:Tm^{3+}/Yb^{3+}$ UCNPs (1 mg/ml on toluene). Inset: high resolution TEM image showing the lattice fringes of the atoms in the crystals. The distance between the adjacent planes (d-spacing) was measured to be 4.6 Å, which is accordance with the (101) plane for tetragonal phase $LiYF_4$.

The particle size distribution was obtained by counting 300 nanoparticles. Assuming a square base bipyramidal shape we calculate the surface area and volume of the nanoparticle to be 8847 nm^2 and 56737 nm^3 respectively. From the reported density for $LiYF_4$ bulk material (3.995 g/cm^3) it was possible to calculate the mass of the nanoparticle to be $2.27x10^{-17}$ g.[65]

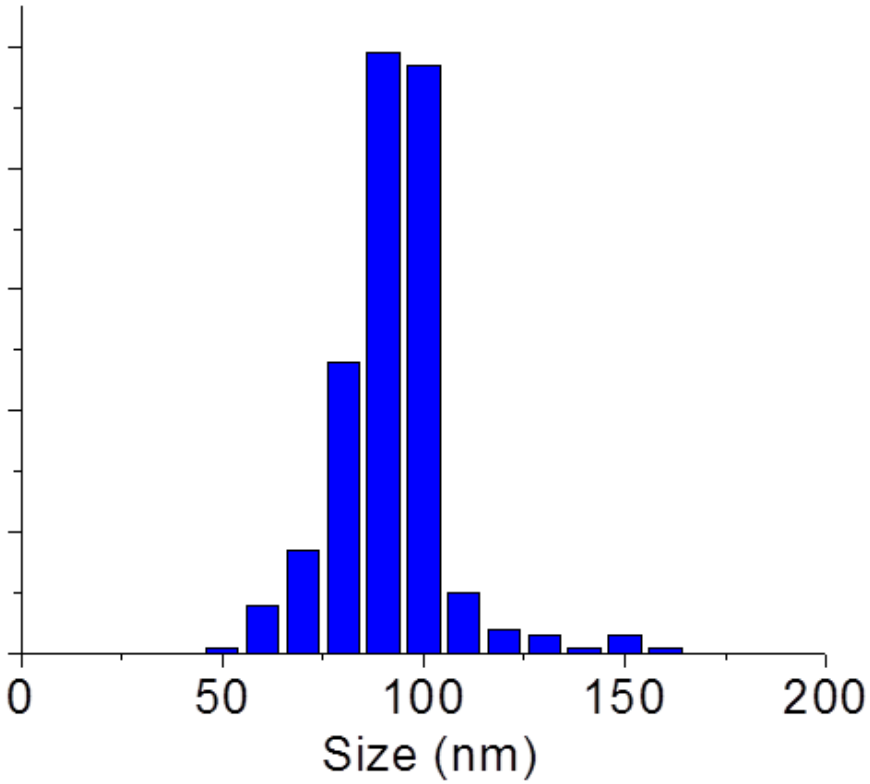

Figure 2S. 3 Particle size distribution of oleate-capped $LiYF_4:Tm^{3+}/Yb^{3+}$ UCNPs obtained from the long diagonal. Average particle size was determined to be 97±14 nm.

Field Emission Scanning Electron Microscopy (FE-SEM) was used to elucidate the faceted morphology of the oleate-capped $LiYF_4$: Tm^{3+}/Yb^3 UCNPs.

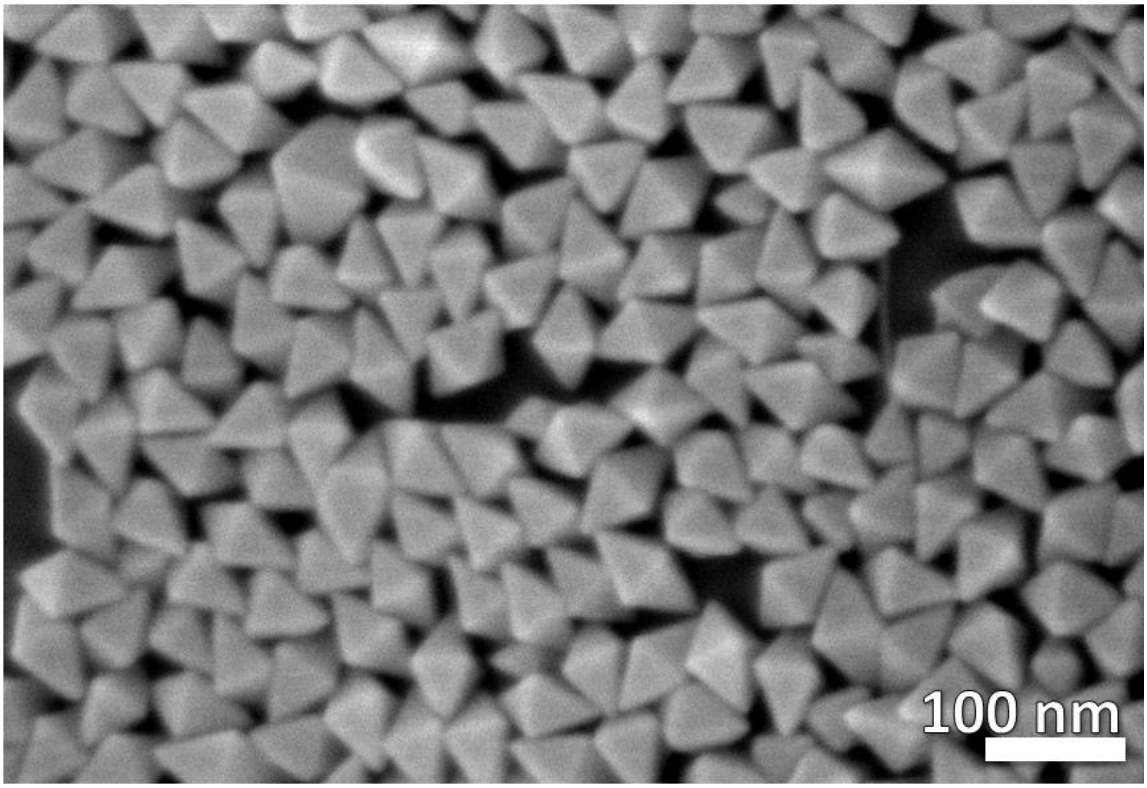

Figure 2S. 4 Field Emission Scanning electron microscopy of oleate-capped $LiYF_4$:Tm^{3+}/Yb^{3+} UCNPs. The nanoparticles show a square bipyramidal structure.

2.6.2 Determination of the amount of oleate on the oleate-capped $LiYF_4:Tm^{3+}/Yb^{3+}$ UCNPs

Thermogravimetric analysis (TGA) of oleate-capped UCNPs showed a mass loss of 1.78% between (280°C and 480°C) where the oleic acid (OA), which is bonded by weak electrostatically interactions was desorbed.[199,219] For the total mass of 10.01mg of oleate-capped nanoparticles evaluated, the weight loss represents 3.8 $x10^{17}$ molecules of OA. The oleate molecule has been reported to have a surface area of 0.4 nm^2,[220] thus the nanoparticle surface coverage is approximately 40%.

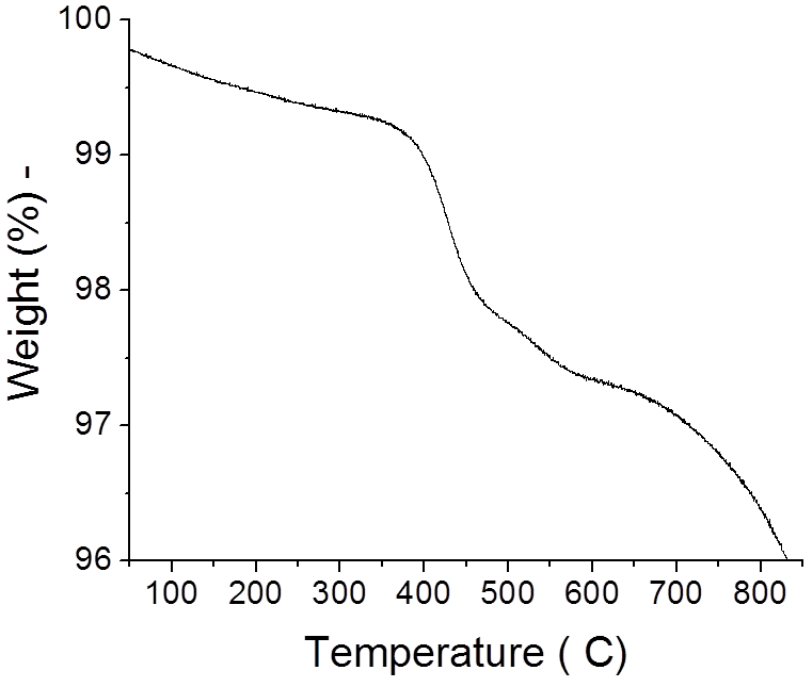

Figure 2S. 5 Thermogravimetric analysis curve of oleate-capped $LiYF_4:Tm^{3+}/Yb^{3+}$ UCNPs.

2.6.3 Evaluation of carbonaceous material deposition using TEM (lacey grids) on oleate-capped $LiYF_4:Tm^{3+}/Yb^{3+}$ UCNPs

The possible deposition of carbonaceous material on oleate-capped $LiYF_4:Tm^{3+}/Yb^{3+}$ UCNPs was directly studied in a series of experiments that examined the TEM images as a function of time and beam current density. Figure 2S.6a shows an oleate-capped $LiYF_4:Tm^{3+}/Yb^{3+}$ UCNPs found partially in a hole and overlapping with the carbon portion of the lacey carbon grid irradiated at minimum current density. From this image it is difficult to ascertain the organic material (oleate molecules) around the nanoparticle. Figures 2S.6b shows the image of the same nanoparticle after 50 seconds of irradiation at 2 times the current density. Figure 2S.6c is taken 170 seconds at 4 times the current density, measured directly following the previous image and Figure 2S.6d is taken after 260 seconds at 9 times the current density. The images at different times and power density do not show any discernable changes thus demonstrating no additional formation of a carbonaceous material around the nanoparticle.

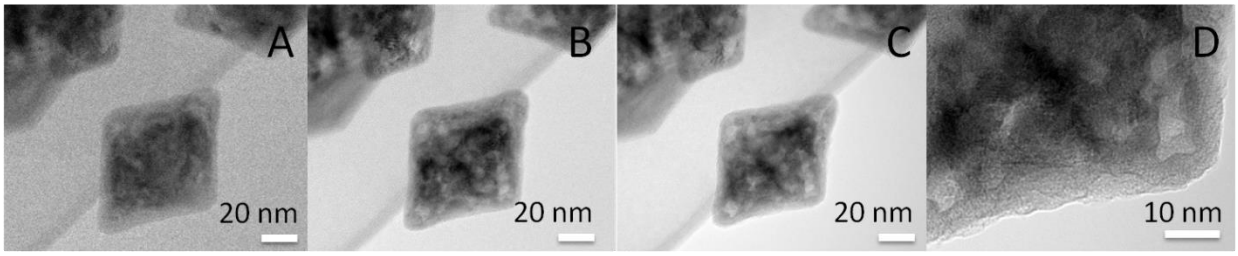

Figure 2S. 6 TEM images of an oleate-capped $LiYF_4:Tm^{3+}/Yb^{3+}$ UCNPs on a lacey grid varying the current density and the exposure time of the electron beam. The images were taken sequentially in the following order a) Initial scan with the lowest current density b) After 50 s of exposure at 2 times the current density c) After 170 s of exposure at 4 times the current density d) After 260 s of exposure at 9 times the current density. No significant carbonaceous growth is observed.

2.6.4 Estimation of the SLB- $LiYF_4:Tm^{3+}/Yb^{3+}$ UCNPs concentration and surface coverage

Inductively Coupled Plasma Mass Spectrometry (ICP-MS) measurements were performed to determine the concentration of nanoparticles and lipid after the surface modification with the supported lipid bilayer. Phosphorous and Yttrium were evaluated in order to calculate the lipid and nanoparticles concentration, respectively. CertiPUR™ Phosphorous 1000 mg/L ICP standard from EMD chemicals Inc and Multi-element solution 10 mg/L (Ce, Dy, Er, Eu, Gd, Ho, La, Lu, Nd, Sc, Sm, Tb, Th, Tm, Y, Yb) from Spex CertiPrep were used to prepare the calibration curve for P and Y respectively in 5% of HNO_3 solution (HNO_3, Trace metal grade from Fisher). Both calibration curves were prepared between 0.01 ppm and 5 ppm.

The volume of 250 µL of each sample were first digested using 900 µL of concentrated HCl (Trace metal grade from Fisher) with 100 µL of H_2O_2 (Ultratrex® Ultrapure reagent from Avantor Performance Materials, Inc.) and heated at 100 °C for 24 h under reflux, then samples were dried and re-dispersed in 2 mL of 5% HNO_3. After digestion, the samples were injected and analyzed. For the determination of the Yttrium concentration samples were diluted additionally 10 times in 1 mL of solution.

Table 2S. 1 ICP-MS results of the concentration of yttrium present in the samples and the concentration of nanoparticles after the surface modification with the SLB.

$LiYF_4:Tm^{3+}/Yb^{3+}$ UCNPs	Y [pmm]	$LiYF_4:Tm^{3+}/Yb^{3+}$ [mg]	$LiYF_4:Tm^{3+}/Yb^{3+}$ [mg/mL]
Oleate	2.87	0.007	0.55
DOPA:DOPC:Chol (64:7:29)	5.69	0.014	1.10
DOPA:DOPC:Chol (35.5:35.5:29)	4.87	0.012	0.94
DOPA:Chol (71:29)	5.85	0.014	1.13
DOPC:Chol (71:29)	3.98	0.010	0.77

From the ICP-MS results the concentrations (ppm) of Y and P were calculated. The results are shown in **Table 2S.1** and 2S.2 respectively. The concentration of the nanoparticles were subsequently calculated assuming one mole of $LiYF_4$ doped 25 mole% with Yb^{3+} and 0.5 mol% Tm^{3+} for each mole of Y present. To estimate the amount of SLB coverage, it was similarly assumed that for each mole of P there is one mole of phospholipid (DOPA or DOPC), which comprises 71% of the total lipid (cholesterol makes up the remaining 29%). Assuming that an unsaturated lipid such DOPC has a surface area of 0.49 nm^2 and cholesterol 0.40 nm^2 for a bilayer with a 30% of cholesterol content ,[4] the total surface area of lipid and cholesterol ($S_{A\ Lip/Chol}$) was calculated (**Table 2S.2**).

Table 2S. 2 ICP-MS results for the amount of phosphorous present in the samples and calculation of the surface area for lipid and cholesterol.

$LiYF_4:Tm^{3+}/Yb^{3+}$ UCNPs	P [ppm]	Lipid molecules $x10^{16}$	Cholesterol molecules $x10^{16}$	$S_{A\ Lip/Chol}$ $x10^{16}$ [nm^2]
DOPA:DOPC:Chol (64:7:29)	0.79	3.4	1.4	2.2
DOPA:DOPC:Chol (35.5:35.5:29)	0.48	2.1	8.4	1.3
DOPA:Chol (71:29)	0.68	2.9	1.2	1.9
DOPC:Chol (71:29)	1.91	8.2	3.3	5.3

To approximate the amount of lipid needed to coat the particles with a SLB, one needs to account for both the inner and outer leaflets of the SLB. The surface area of a nanoparticle is approximately 8847 nm^2 (see section 2.6.1), however only 60% of the surface area can be covered by lipids to form the inner leaflet of the bilayer as 40% is covered by oleate (see section 2.6.2). To calculate the surface area required for the outer leaflet of the bilayer, the dimensions must be adjusted to account for the thickness of the inner leaflet which was assumed to be 2.3 nm and therefore the dimensions for the outer leaflet.[4] Using this approach, the surface area for the outer leaflet was estimated to be approximately 10230 nm^2. Then the total lipid needed to

cover the nanoparticle with a SLB ($S_{A\ leaflets}$) is the sum of the 60% of the inner leaflet with the surface area of the outer leaflet, found it to be approximately 15538 nm^2.

Table 2S. 3 Calculations for the surface coverage of the lipid bilayer per nanoparticle.

$LiYF_4:Tm^{3+}/Yb^{3+}$ UCNPs	Number of UCNPs $x10^{12}$	$S_{A\ Lip/Chol}$ $x10^{16}$ [nm^2]	$S_{A\ leaflets}$ $x10^{16}$ [nm^2]	Coverage [%]
DOPA:DOPC:Chol (64:7:29)	1.2	2.2	1.9	117
DOPA:DOPC:Chol (35.5:35.5:29)	1.0	1.3	1.6	84
DOPA:Chol (71:29)	1.2	1.9	1.9	98
DOPC:Chol (71:29)	0.85	5.3	1.3	406

It must be noted that these are very rough approximations of surface coverage and the values obtained for all lipid layers, with the exception of DOPC:Chol (71:29), are reasonable and suggest good particle surface coverage in agreement with the negative stain TEM images that show UCNPs are surrounded by a continuous layer of material (bright area, Figure 2S.7). For DOPC:Chol (71:29) a surface coverage estimate of 406% is obtained which implies a significant excess of lipid. This excess lipid can clearly be observed in the negative stain TEM image (Figure 2S.7d). Additionally, the ζ-potential results for the DOPC:Chol (71:29) SLB were found to be neutral (+1mV). According to the theory of colloidal interactions this lack of surface charge may produce agglomeration making it more difficult to remove the excess lipid.

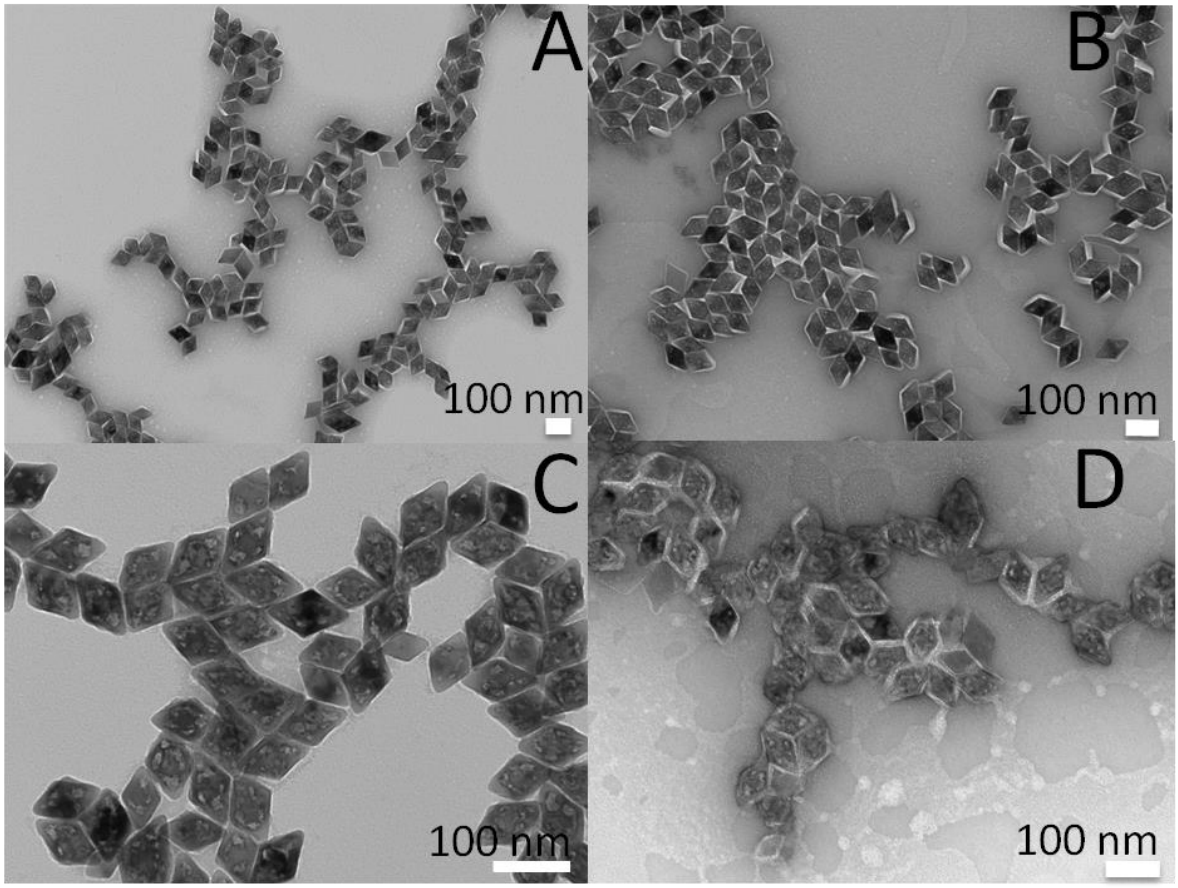

Figure 2S. 7 Negative stain TEM images of the nanoconstructs with different lipid ratios after extrusion, vortex and micro-centrifugation. a) DOPA:DOPC:Chol(64:7:29 mole %) b) DOPA:DOPC:Chol (35.5:35.5:29 mole %) c) DOPA:Chol (71:29 mole%) $LiYF_4:Tm^{3+},Yb^{3+}$ UCNPs d) DOPC:Chol (71:29 mole %).

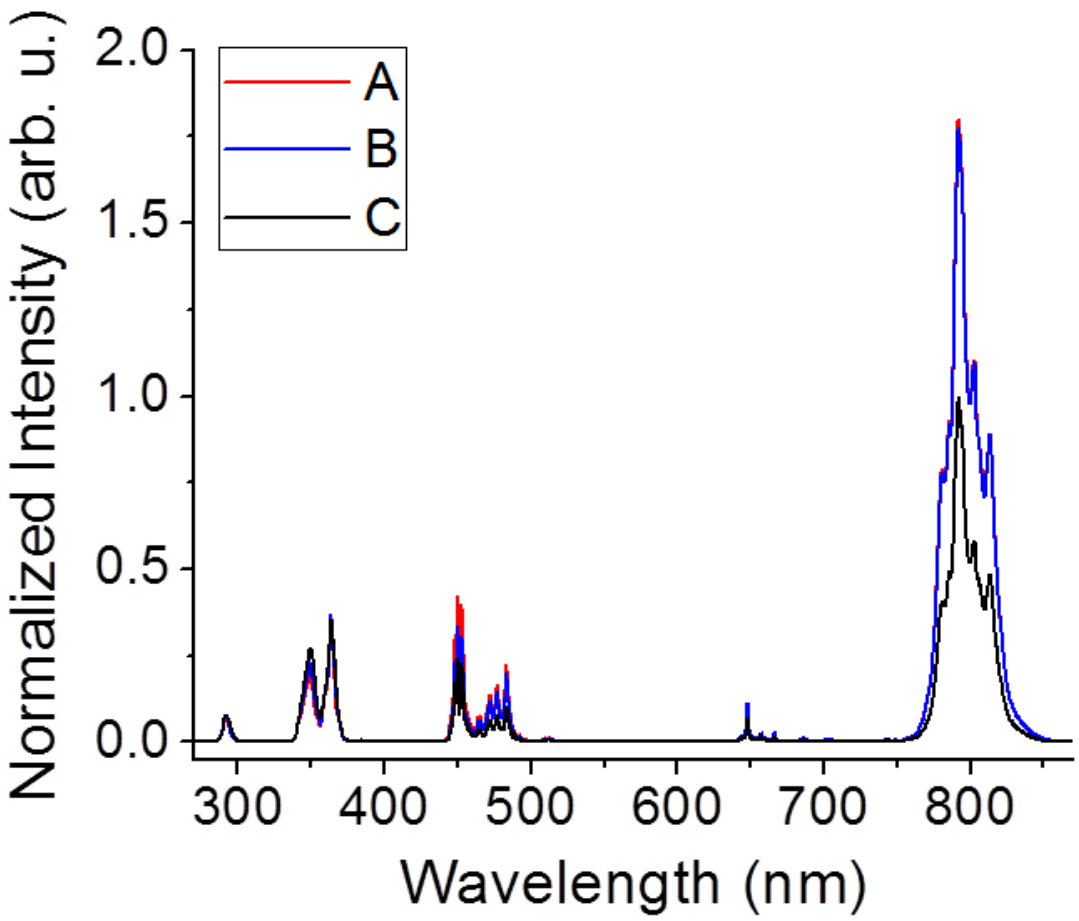

Figure 2S. 8 Emission spectra of the nanoconstruct with different DOPA:DOPC ratio in aqueous solution. a) DOPA:Chol (71:29 mole%) b) DOPA:DOPC:Chol (64:7.5:29 mole%) c) Oleate-capped $LiYF_4:Tm^{3+}/Yb^{3+}$ UCNP in toluene.

2.6.5 Upconversion mechanism for $LiYF_4:Tm^{3+}/Yb^{3+}$ UCNPs

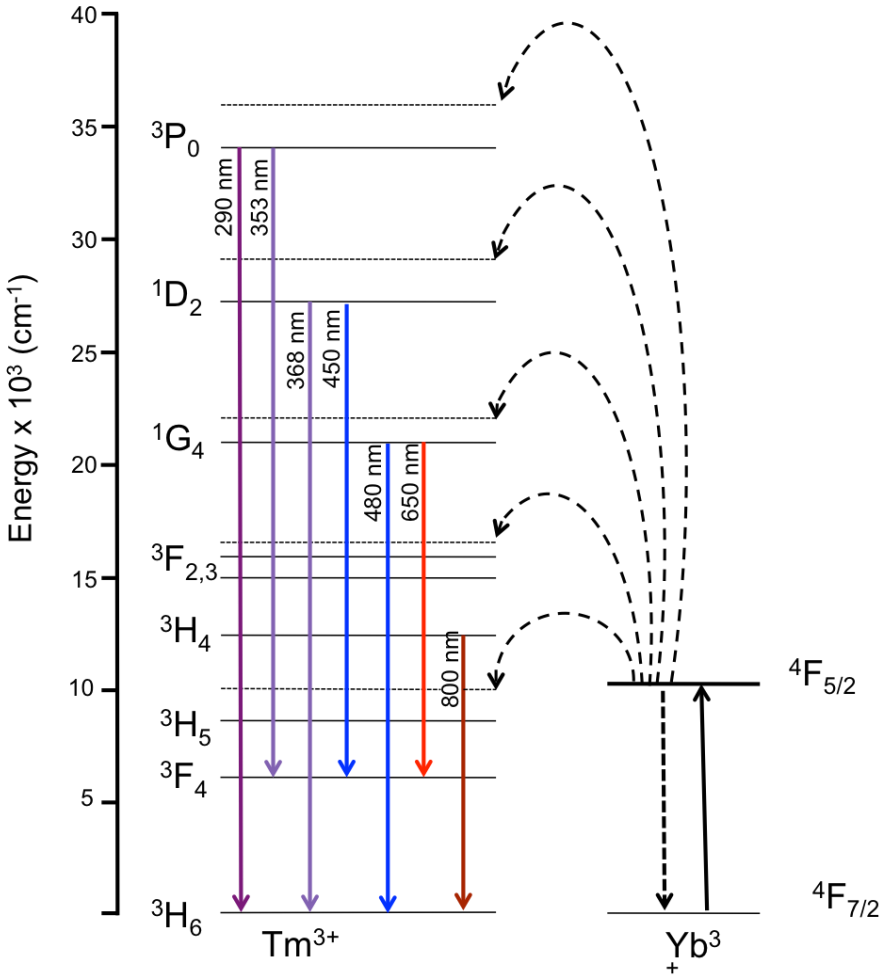

Figure 2S. 9 Upconversion mechanism for $LiYF_4:Tm^{3+},Yb^{3+}$ UCNPs

2.6.6 X-Ray power diffraction (XRPD)

The patterns for $LiYF_4$: Tm^{3+}/Yb^{3+} UCNPs were collected at room temperature using a Scintag XDS-2000 diffractometer equipped with a Si(Li) Peltier-cooled solid state detector, CuKα source at a generator power of 45 kV and 40 mA, divergent beam (2 mm and 4 mm) and receiving beam slits (0.5 mm and 0.2 mm). Scan range was set from 15-90° 2θ with a step size of 0.02° and a count time of 2 sec. A quartz zero background insert disk was used as sample holder.

2.6.7 High Resolution Transmission Electron Microscopy (HRTEM)

The micrographs of $LiYF_4$: Tm^{3+}/Yb^{3+} were collected using a Jeol JEM-2100F microscope operating at 200 kV capable of imaging resolution of 0.1 nm. Samples were prepared by dropping sample solutions (1 mg/mL in toluene) onto a 300-mesh Formvar/carbon coated copper grid (3 mm in diameter) followed by the evaporation of the solvent. Also 300-mesh Lacey carbon copper grids were used, in this case the sample were prepared by dipping the grid in the solution followed by evaporation of the solvent.

2.6.8 Field Emission Scanning Electron Microscopy (FE-SEM)

The FE-SEM image was obtained using a Hitachi SU8230 microscope operating at 0.7 kV. Samples were prepared by dropping sample solutions (1 mg/mL in toluene) onto a 300-mesh Formvar/Carbon coated copper grid (3 mm in diameter) followed by the evaporation of the solvent.

2.6.9 Thermogravimetric Analysis (TGA)

The thermograms for the oleate-capped $LiYF_4$:Tm^{3+}/Yb^{3+} UCNPs were recorded using an Exstar6000 Thermal Instrument from Seiko. The samples were kept under an argon atmosphere. The heating rate was set at 10°C min^{-1} between 25 °C and 700 °C.

2.6.10 Negative-stain Transmission Electron Microscopy (TEM)

Negative stain images were obtained using a Tecnai 12 Biotwin TEM microscope (FEI Electron Optics) equipped with a Tungsten filament at 120 kV and AMT XR80C CCD Camera System.

Samples were prepared by dropping 5 μL of sample solution (1 mg/mL) onto 200-mesh carbon coated SPI grid and leaving it to be adsorbed during 1 min before drying it softly with a filter paper. Immediately after, they were stained with 5 μL of 1.5% uranyl formate in 5M NaOH solution, after 1 min the excess solution was removed using a filter paper.

2.6.11 Cryogenic Transmission Electron Microscopy (cryo-TEM)

Cryo-TEM images were obtained using a FEI Titan Krios 300 kV Cryo-STEM equipped with FEI Phase Plate, Falcon 2 Direct Detection Device (DDD; FEI Inc.), and Gatan Imaging Filter (GIF2002). C-flat holey carbon sample support grids R2/2 for cryo-TEM (Protochips, USA) were used to prepare the sample. The grid were first glow discharged to converts the hydrophobic carbon layer into hydrophilic. 3 μl of sample was added to grids the excess fluid was blotted, and then the sample was flash frozen hydrated by plunging into a bath of liquid ethane using FEI Vitrobot Mark IV Grid Plunging System (FEI Electron Optics). The grids were then stored in liquid nitrogen until observation. Images were taken at magnification of 22.5kx (pixel size 3.69 Å) and defocus level ranging from −1.0 to −7.0μm, under low dose conditions.

2.6.12 Upconversion Luminescence Spectroscopy

The upconversion visible emission spectra of the oleate-capped $LiYF_4$:Tm^{3+}/Yb^{3+} and SLB-$LiYF_4$: Tm^{3+}/Yb^{3+} UCNPs were obtained upon 980 nm excitation, using a Coherent 6-pin fiber-coupled F6 series 980 nm laser diode (power of 615 mW), coupled to a 100 μm (core) fiber. For the upconversion studies, the samples (0.55 mg/mL in water, toluene and D_2O) were placed in 1 cm path-length quartz cuvettes (Hellma, QS). The upconverted visible emissions were collected at right angle with respect to the incident beam and subsequently dispersed by a 1m Jarrell-Ash Czerny-Turner double monochromator with an optical resolution of ~0.15 nm. The visible emissions were detected by a thermoelectrically cooled Hamamatsu R943-02 photomultiplier tube. A preamplifier, model SR440 Standard Research Systems, processed the photomultiplier signals and a gated photon counter model SR400 Standard Research Systems data acquisition system was used as an interface between the computer and the spectroscopic hardware. The signal was recorded under computer control using the Standard Research Systems SR465

software data acquisition/analyzer system. The UV emissions were collected using a Spex Minimate 1⁄4 m monochromator and detected with an Oriel 70680 photomultiplier tube.

2.6.13 Inductively Coupled Plasma Mass Spectrometry (ICP-MS)

ICP-MS measurements were performed to determine the nanoparticles concentration after the surface modification with the supported lipid bilayer. The samples were analyzed using an Agilent 7500ce ICP-MS equipped quartz scott-type spray chamber, an off-axis Omega lens ion focusing, an octopole reaction system with a quadrupole mass spectrometer analyzer. It was operated at 3MHz.

2.6.14 ζ-Potential

The surface charge of the oleate-free $LiYF_4:Tm^{3+}/Yb^{3+}$ and SLB- $LiYF_4:Tm^{3+}/Yb^{3+}$ UCNPs samples were measured using a Zetasizer Nano-S (Malvern Instruments Ltd, Worcestershire, UK). All experiments were carried out using a disposable folded capillary cell (Malvern). For each experiment, 10 measurements comprising of 20 runs were recorded. For each sample, experiments were repeated three times. The concentration of the samples was 0.15 mg/mL in ultrapure water using 0.7 mL.

2.7 Author's Notes And Significance Of This Paper

This publication on the surface modification of $LiYF_4:Tm^{3+}/Yb^{3+}$ upconverting nanoparticles with a supported lipid bilayer is groundbreaking in the field of lanthanide upconverting nanoparticles. Biological applications of lanthanide upconverting nanoparticles require coatings that yield water dispersible and biocompatible nanoparticles, but at the same time protect the emission of the nanoparticles. Here the supported lipid bilayer acts a soft-matter shell protecting the emission of the nanoparticle from quenching with the high-energy vibrational modes of the OH groups of water. The vibrational modes of the OH groups are well known to produce the depopulation of the electronic states *via* non-radiative mechanisms.

Motivated by the previous results and taking advantages of the optical properties $LiYF_4:Tm^{3+}/Yb^{3+}$ upconverting nanoparticles, the subsequent chapter provides the development of a photo-responsive supported lipid bilayer at the surface of the nanoparticle. Incorporation of an azobenzene-derivative lipid in the supported lipid bilayer provide a route to trigger the delivery of a hydrophobic model drug *via* energy transfer with $LiYF_4:Tm^{3+}/Yb^{3+}$ upconverting nanoparticles upon NIR photo-irradiation.

Chapter 3

A Route to Triggered Delivery *via* Photocontrol of Lipid Bilayer Properties Using Lanthanide Upconversion Nanoparticles

Publish as:

[1]Paola A. Rojas-Gutierrez, [2]Shashi Bhuckory, [2]Carlos Mingoes, [2]Niko Hildebrandt, [1]Christine DeWolf,* and [1]John A. Capobianco*

ACS Applied Nano Materials. **2018**, *1* (9), 5345–5354.

[1]Department of Chemistry and Biochemistry, and Centre for NanoScience Research, Concordia University, Montreal, Quebec, H4B 1R6, Canada. [2]NanoBioPhotonics (nanofret.com), Institute for Integrative Biology of the Cell, Université Paris-Saclay, Université Paris-Sud, CNRS, CEA, 91400 Orsay, France.

3.1 Abstract

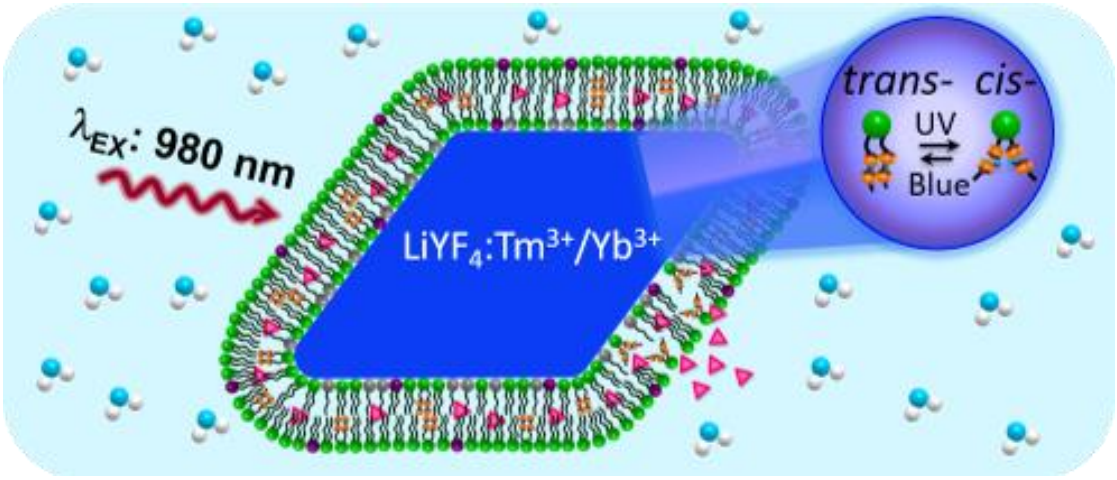

Scheme 3. 1 Graphical table of content of "A Route to Triggered Delivery *via* Photocontrol of Lipid Bilayer Properties Using Lanthanide Upconversion Nanoparticles."

Soft matter shells for nanoparticles provide an alternative approach to the more traditional inorganic core-shell nanoconstructs. In the latter, functionality and biocompatibility often requires the addition of a hydrophilic organic coating. Herein, a supported lipid bilayer serves as a soft matter shell that has the physicochemical properties that enable a dynamic system capable of providing biocompatibility, encapsulation and release of small molecule active agents. Direct coupling of the conformal, supported lipid bilayer containing an azobenzene-derivatized lipid with an upconversion nanoparticle provides the means to photocontrol the bilayer properties, generating a multifunctional coating. The close contact of the bilayer with the nanoparticle surface eliminates problems associated with Brownian motion for the energy transfer; the mechanism of energy transfer was determined to be dominated by radiative reabsorption using time-resolved photoluminescence. Release of an encapsulated dye was achieved with significantly lower proportions of azobenzene-derivatized lipid than has been reported for UV-triggered release from liposomes. This work highlights the potential of the described nanoconstruct for light controlled delivery applications, especially in a biological context and in

vivo applications, for which NIR excitation is of paramount importance for low toxicity and deeper tissue penetration.

3.2 Introduction

The interaction of nanoparticles with lipid membranes has been widely studied in recent years, with an emphasis on understanding the impact of such interactions on cell membrane stability, integrity and function. However, lipid bilayers also provide a simple means to coat nanoparticles to produce an inherently biocompatible, soft matter shell. Such supported lipid bilayers retain many of the characteristics of natural membranes including their lateral fluidity and impermeability to ionic species.[221–224] Frequently these bilayers are used as a protective coating for spherical particles, in particular silica micro- and nanoparticles, providing biocompatibility and making the particles as cell mimetics.[225] Coating such a bilayer around a drug-loaded mesoporous silica particle has been suggested for long-circulation, slow release drug carriers;[226] the close contact of the bilayer to the solid support enables electrostatic interactions that can yield increased stability, and therefore shelf-life, over liposomal formulations. Triggered release has been also achieved in a similar nanoconstruct combining mesoporous silica and a chemically reducible bilayer.[227] Recently, metal-organic framework (MOF) nanoparticles were coated with a supported lipid bilayer to prevent premature drug release. The authors emphasized the importance of developing mechanisms for triggered release that can be incorporated into the lipid bilayer.[228]

Photoresponsive molecules provide one mechanism for controlled release of molecules. For example, phototriggered release has been reported using azobenzene as "a gatekeeper" within the pores of mesoporous silica.[229] However, azobenzene has limited uses for *in vivo* applications due to the cytotoxicity of UV light required for photoswitching and the limited tissue penetration of UV or blue light.[72] One approach to overcome this limitation has involved chemical modification of the azobenzene moiety to shift the absorption to longer wavelengths.[230,231] However, as highlighted by Woolley *et al.*,[230] these chemical modifications can generate potential issues that include altering thermal relaxation rates (leading to a smaller

fraction of the *cis*-isomer at steady state) and changing the relative energies of the *cis*- and *trans*-ground states. An alternative approach was proposed by Liu *et al*. who demonstrated that conjugation of azobenzene to mesoporous silica coated lanthanide upconversion nanoparticles (Ln-UCNPs) enabled light-controlled release of a drug from the pores as a result of azobenzene switching.[232] On the other hand, the necessity to use a silica coating and chemical conjugation can be avoided by directly incorporating the azobenzene derivative into a biocompatible lipid membrane. Yao *et al*. encapsulated phospholipid coated Ln-UCNPs in the interior of a liposome where the outer liposome contains a single-chained azobenzene surfactant.[233] However, freestanding bilayers can undergo physical changes that affect the stability of such liposomal formulations.[234] Photoswitching enabled release of water-soluble drugs that were co-encapsulated with the nanoparticles in the inner compartment of the liposome. In this approach, both the Ln-UCNPs and the drug are freely diffusing in the inner compartment.[233] This requires close proximity of the Ln-UCNP, liposome wall (where the azobenzene disruption occurs) and drug, for the emitted light to enable drug translocation and release. We have previously demonstrated energy transfer from an Ln-UCNP to a photoswitchable molecule (bis-spiropyran) and a photosensitizer (Foscan® that enables production of singlet oxygen).[235] In the case of the former, the energy transfer efficiency is reduced by half when the bis-spiropyran is freely tumbling in solution compared to direct conjugation onto the Ln-UCNP surface.[76] Therefore, in order to avoid the effect of Brownian motion on the energy transfer, we have devised a simple nanoconstruct comprising an Ln-UCNP with a supported lipid bilayer coating that contains an azobenzene-derivatized lipid that is in close contact with the Ln-UCNP surface. We have previously shown that the bilayer coating is sufficient to avoid significant water quenching without the need for a core-shell structure.[236]

Photoresponsive molecules provide one mechanism for controlled release of molecules. For example, phototriggered release has been reported using azobenzene as "a gatekeeper" within the pores of mesoporous silica.[229] However, azobenzene has limited uses for *in vivo* applications due to the cytotoxicity of UV light required for photoswitching and the limited tissue penetration of UV or blue light.[72] One approach to overcome this limitation has involved

chemical modification of the azobenzene moiety to shift the absorption to longer wavelengths.[230,231] However, as highlighted by Woolley *et al.*,[230] these chemical modifications can generate potential issues that include altering thermal relaxation rates (leading to a smaller fraction of the *cis*-isomer at steady state) and changing the relative energies of the *cis*- and *trans*-ground states. An alternative approach was proposed by Liu *et al*. who demonstrated that conjugation of azobenzene to mesoporous silica coated lanthanide upconversion nanoparticles (Ln-UCNPs) enabled light-controlled release of a drug from the pores as a result of azobenzene switching.[232] On the other hand, the necessity to use a silica coating and chemical conjugation can be avoided by directly incorporating the azobenzene derivative into a biocompatible lipid membrane. Yao *et al*. encapsulated phospholipid coated Ln-UCNPs in the interior of a liposome where the outer liposome contains a single-chained azobenzene surfactant.[233] However, freestanding bilayers can undergo physical changes that affect the stability of such liposomal formulations.[234] Photoswitching enabled release of water-soluble drugs that were co-encapsulated with the nanoparticles in the inner compartment of the liposome. In this approach, both the Ln-UCNPs and the drug are freely diffusing in the inner compartment.[233] This requires close proximity of the Ln-UCNP, liposome wall (where the azobenzene disruption occurs) and drug, for the emitted light to enable drug translocation and release. We have previously demonstrated energy transfer from an Ln-UCNP to a photoswitchable molecule (bis-spiropyran) and a photosensitizer (Foscan® that enables production of singlet oxygen).[235] In the case of the former, the energy transfer efficiency is reduced by half when the bis-spiropyran is freely tumbling in solution compared to direct conjugation onto the Ln-UCNP surface.[76] Therefore, in order to avoid the effect of Brownian motion on the energy transfer, we have devised a simple nanoconstruct comprising an Ln-UCNP with a supported lipid bilayer coating that contains an azobenzene-derivatized lipid that is in close contact with the Ln-UCNP surface. We have previously shown that the bilayer coating is sufficient to avoid significant water quenching without the need for a core-shell structure.[236]

Herein, we report the photoswitching of the azobenzene modified lipid analogue, di(6-{[4-(4-butylphenyl)azo]-phenoxy}-hexyl)phosphate (hereafter referred to as AZO-lipid) *via*

energy transfer from $LiYF_4:Tm^{3+}/Yb^{3+}$ (0.5% Tm^{3+}, 25% Yb^{3+}) UCNPs (see **Scheme 3.2**). Moreover, we show the incorporation of the AZO-lipid into a supported lipid bilayer (SLB) encapsulating the $LiYF_4:Tm^{3+}/Yb^{3+}$ UCNPs. The supported lipid bilayer mimics the cell membrane, renders the nanoparticles water-dispersible and biocompatible, and prevents water-derived quenching of the emission.[236] In addition, the bilayer offers protection from *in vivo* reduction and/or hydrolysis of the azobenzene, that have been reported as potential drawbacks.[237] The photoswitching of the AZO-lipid inside the supported lipid bilayer using 980 nm excitation and energy transfer from the Ln-UCNP highlights its potential for biological applications such as drugs delivery that can be controlled with light. One of the major challenges of the pharmaceutical industry is the development of new formulations that can deliver hydrophobic drugs, which comprise the majority of drugs developed. As such, this delivery system is designed to encapsulate hydrophobic drugs in the hydrophobic core of the supported lipid bilayer and as a proof-of-principle, Nile red, a hydrophobic drug model, is encapsulated within the nanoconstruct, AZO-SLB-UCNPs, and subsequently released *via* remote triggering using 980 nm excitation.

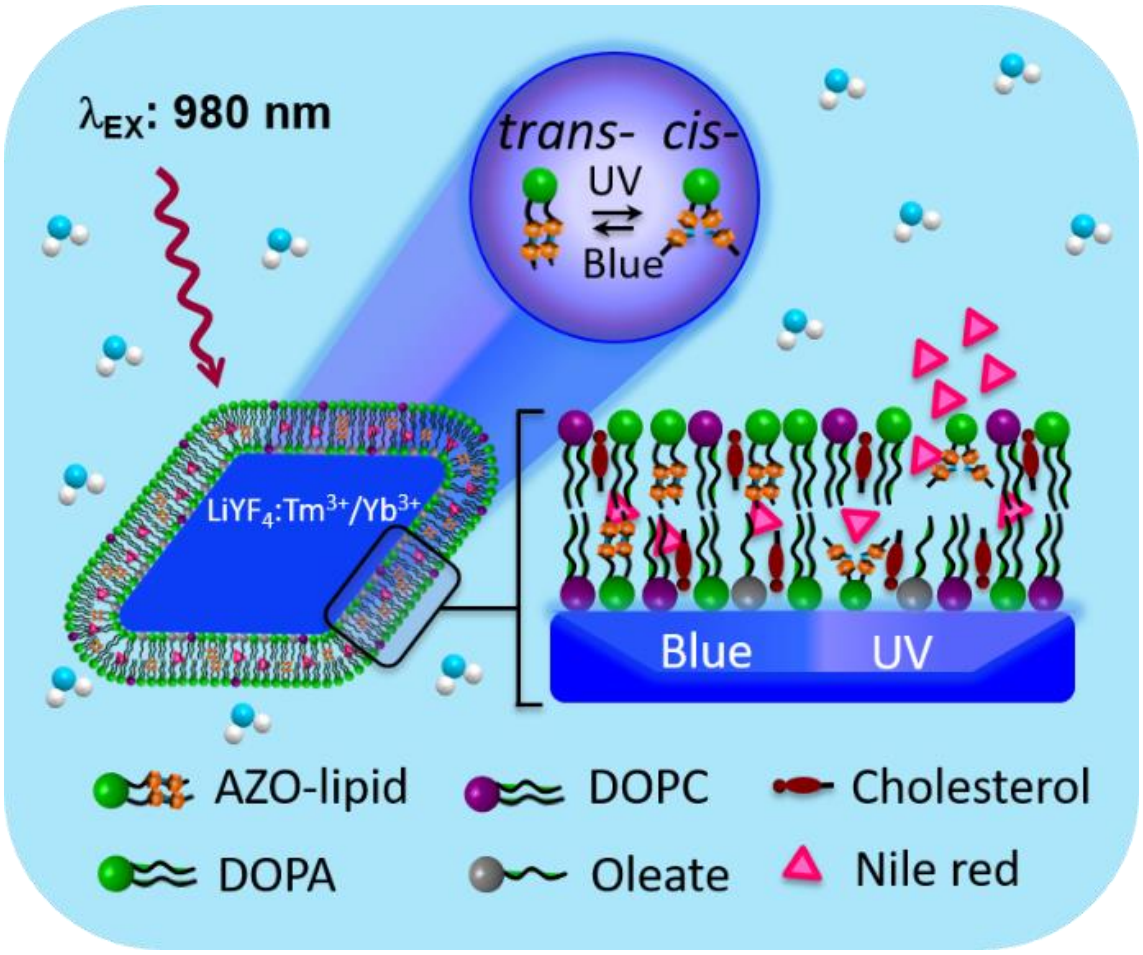

Scheme 3. 2 Illustration of the nanoconstruct AZO-SLB-UCNPs with Nile red encapsulated. Upon 980 nm irradiation AZO-lipid photoswitches *via* reabsorption of the upconverting light from the UCNP producing the release of Nile red due to the disruption of the supported lipid bilayer.

3.3 Results and Discussion

Tetragonal $LiYF_4:Tm^{3+}/Yb^{3+}$ upconversion nanoparticles (Ln-UCNPs) were selected because of their strong UV and blue emissions ($^3P_0 \rightarrow {}^3H_6$ (290 nm), $^3P_0 \rightarrow {}^3F_4$ (353 nm) and $^1D_2 \rightarrow {}^3H_6$ (368 nm)) of Tm^{3+} ions,[67] which overlap with the broad absorption band corresponding to the π-π* transition at 350 nm of azobenzene, providing the potential for energy transfer. Additionally, the tetragonal structure of $LiYF_4$ yields 8 identical {101} faces that all have equal surface energies (0.82 J m^{-2}) and thus identical interactions with the physisorbed lipids.[238,239] This surface topography promotes formation of a uniform coating. Excitation using 980 nm light has the advantages of deep tissue penetration, no known phototoxicity, and reducing autofluorescence.[72] Ln-UCNPs using Nd^{3+} as dopant ions are also good candidates since their excitation is in the first biological window,[240,241] however, more complicated multiple shell strategies are needed to achieve strong UV emission. Moreover, modulation of the 980 nm laser beam (chopping or using a pulsed laser) significantly decreases any potential heating effects.[242,243] In a recent review, Wu and Butt stated that the intervals between pulses, even for femtosecond lasers, is sufficient to efficiently reduce any thermal effects, i.e. to produce an athermal process.[244] The use of pulsed frequencies at similar power densities of 980 nm light to those used here (13 W cm^{-2}), have already been employed for treatment in humans of traumatic brain injury.[245] Chemical conjugation of the azobenzene moieties into the alkyl chain of a lipid enables its facile incorporation into a supported lipid bilayer. Such azobenzene-derivatized lipids have been used for photocontrolled release of dyes from liposomes.[83,102–106] These studies demonstrated that the release is less sensitive to the composition when both acyl chains are derivatized with azobenzene.[108] Therefore, the azobenzene derivative, AZO-lipid, in which both chains contain the azobenzene moiety, was prepared following the synthetic route proposed by Kuiper and confirmed by NMR and ESI-mass spectrometry (Figure 3S.1, in the Supporting Information).[246]

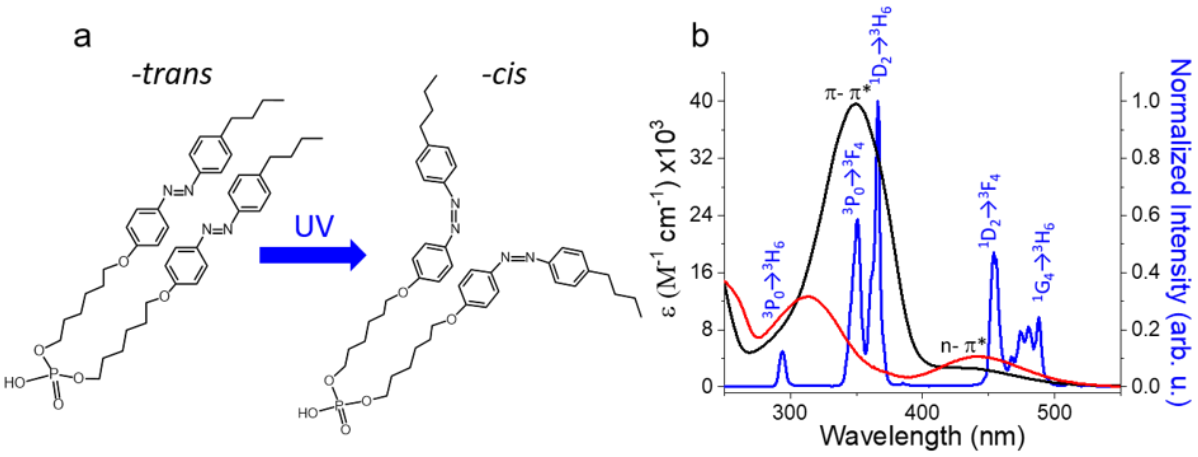

Figure 3. 1 a) *trans*- and *cis*-isomers of AZO-lipid. b) Overlap of the absorption spectrum of *trans*- AZO-lipid (black) and *cis*-AZO-lipid (red) (2.6×10^{-5}M in propylene glycol and ethanol mixture 1:1) with the photoluminescence spectra of $LiYF_4:Tm^{3+}/Yb^{3+}$ UCNPs (blue) excited at 980 nm (0.1 wt% in propylene glycol and ethanol mixture 1:1).

The *trans*-AZO-lipid isomer shows a strong π-π* transition at approximately 350 nm and a weak n-π* band at 450 nm; the *cis*-AZO-lipid isomer has a stronger n-π* transition at 450 nm and a less intense π-π* transition at 320 nm **(Figure 3.1**b). The photoswitching of the *trans*-AZO-lipid to the *cis*-isomer, required for configuration change (Figure 3.1a), can be directly triggered using UV irradiation, with a photo-stationary state being achieved after 30 seconds (Figure 3S.2a), in the Supporting Information). In order to avoid the problems associated with UV irradiation in biological systems and to assess the potential for photoswitching *via* energy transfer from a Ln-UCNP, the overlap of absorption of the synthesized AZO-lipid with the emission of the Ln-UCNPs was confirmed (Figure 3.1b).

The energy transfer from the Ln-UCNPs to the AZO-lipid was evaluated using only the AZO-lipid analogue conjugated to the surface. This surface modification was achieved using the as-synthesized nanoparticles with a size of 91 ± 12 nm with respect the long diagonal and a tetragonal crystal structure (Figure 3S.3, in the Supporting Information). Previously we demonstrated that the surface of the $LiYF_4:Tm^{3+}/Yb^{3+}$ UCNPs is 40% covered by oleate

molecules, to be referred to as oleate-UCNPs, which leaves 60% of the surface available for modification.[236] The AZO-lipid is co-adsorbed at the surface of the oleate-capped nanoparticles (to be referred to as AZO-UCNPs) by incubating the nanoparticles with AZO-lipid molecules in chloroform. The adsorption of the AZO-lipid occurs *via* electrostatic interaction of its negatively charged phosphate head group with the positively charged surface of the nanoparticles. Conjugation of the AZO-lipid at the surface of the oleate-capped nanoparticles was confirmed using FTIR spectroscopy (Figure 3S.4, in the Supporting Information). ICP-MS (Table S1 and S2, in the Supporting Information) and absorption spectroscopy (Figure 3S.5, in the Supporting Information) were used to determine that there are approximately 1.15 x 10^4 (± 0.05 x 10^4) molecules of AZO-lipid on the surface of each nanoparticle.

The energy transfer from the $LiYF_4$:Tm^{3+}/Yb^{3+} UCNPs to the conjugated AZO-lipid was then confirmed by photoluminescence spectroscopy. **Figure 3.2**a shows the upconversion photoluminescence spectra of the oleate-UCNPs (0.64 mg/mL in propylene glycol and ethanol mixture 1:1) and the AZO-UCNPs (0.64 mg/mL in propylene glycol and ethanol mixture 1:1). A decrease in the photoluminescence intensities of the peaks centered at 290 nm, 353 nm, 368 nm and 450 nm is observed for the AZO-UCNPs in comparison to the oleate-UCNPs. From the emission spectra it is evident that the peaks centered at 368 nm and 353 nm are the principle contributors of the energy transfer from the $LiYF_4$:Tm^{3+}/Yb^{3+} UCNPs to the azobenzene moiety since these emission peaks show the best overlap with the π- π* transition (absorption band) of the *trans*-AZO-lipid. The energy transfer efficiency from the $LiYF_4$:Tm^{3+}/Yb^{3+} UCNPs to the AZO-lipid conjugated at the surface was calculated to be 40%, using eq 3.1:

$$E = 1 - (I_{DA}/I_D) \tag{3.1}$$

where E is the energy transfer efficiency, I_{DA} is the area under the curve ($^3P_0 \rightarrow {}^3H_6$, $^3P_0 \rightarrow {}^3F_4$, and $^1D_2 \rightarrow {}^3F_4$) for the normalized photoluminescence intensity of the AZO-UCNPs and I_D is the area under the curve ($^3P_0 \rightarrow {}^3H_6$, $^3P_0 \rightarrow {}^3F_4$, and $^1D_2 \rightarrow {}^3F_4$) for the normalized photoluminescence intensity of the oleate-UCNPs.

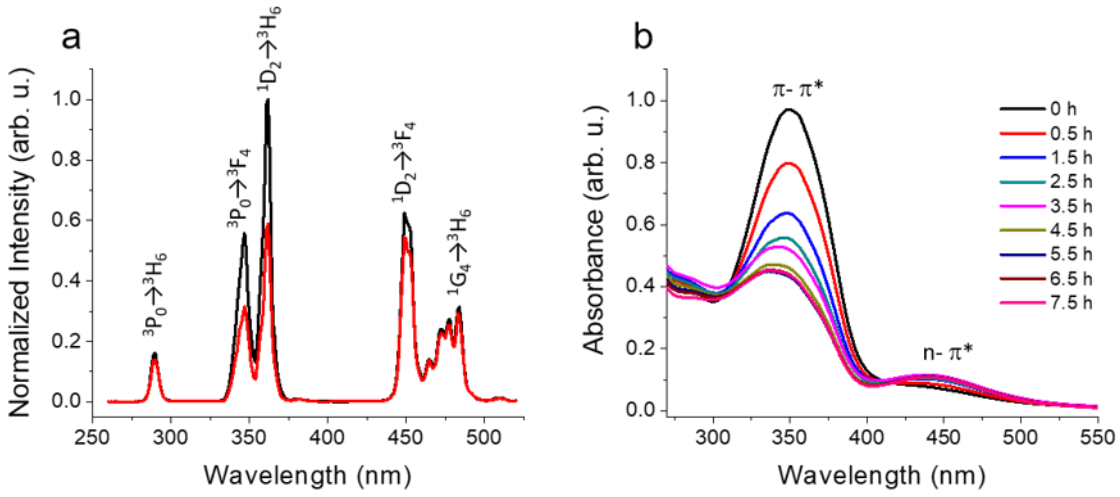

Figure 3. 2 a) Photoluminescence spectra of oleate-UCNPs (black) and AZO-UCNPs (red) using 980 nm excitation. b) Absorbance spectra of AZO-UCNPs (0.64 mg/mL) dispersed in ethanol and propylene glycol (1:1) as a function of the 980 nm irradiation time.

To ensure that only the thermodynamically stable isomer, *trans*-AZO-lipid, was present on the surface of the $LiYF_4:Tm^{3+}/Yb^{3+}$ UCNPs, the dispersion was stored in the dark for three days. Figure 3.2b shows the absorption spectra of AZO-UCNPs as a function of 980 nm irradiation time and clearly demonstrates a decrease in the intensity of the π-π* band (*trans*-AZO-lipid) and an increase in the intensity of the n-π* band (*cis*-AZO-lipid), confirming the light-induced isomerization. Additionally, the peak maximum for the π-π* transition exhibits a hypsochromic shift as the proportion of *cis*-AZO-lipid increases (i.e. the peak represents a weighted average of the *trans*- and *cis*-isomers). The shift of the π-π* transition is ascribed to the large dipole moment change from 0 D in the *trans*-isomer to 3.0 D in the *cis*-isomer.[247] The percentage of AZO-lipid (see **Table 1**) that undergoes *trans*→*cis* isomerization due to 980 nm excitation of the $LiYF_4:Tm^{3+}/Yb^{3+}$ UCNPs and subsequent energy transfer can be estimated using eq 3.2:

$$\%cis_t = 1 - \frac{A_t - A_{cis}}{A_{trans} - A_{cis}} \times 100 \qquad (3.2)$$

where $\%cis_t$ is the percentage of AZO-lipid in the *cis*-configuration, A_t is absorbance at 350 nm for a given irradiation time, A_{trans} is the absorbance at 350 nm when all molecules are in *trans*-configuration and A_{cis} is the absorbance at 350 nm when all molecules are in *cis*-configuration (A_{trans} and A_{cis} are taken from the spectra in Figure 3S.6, in the Supporting Information). After 5.5 h irradiation, a photo-stationary state was obtained because the absorbance band of the *cis*-AZO-lipid at 450 nm overlaps the emission transitions ($^1D_2 \rightarrow {}^3F_4$ and $^1G_4 \rightarrow {}^3H_6$) of the Tm^{3+} ions in $LiYF_4:Tm^{3+}/Yb^{3+}$ UCNPs inducing a *cis*→*trans* isomerization that switches AZO-lipid back to the *trans*-isomer due to a stronger n-π* band for the *cis*-isomer than the *trans*-isomer.

We have previously reported the formation of a supported lipid bilayer (SLB) on the surface of $LiYF_4:Tm^{3+}/Yb^{3+}$ UCNPs comprising residual oleate, 1,2-di-(9Z-octadecenoyl)-sn-glycero-3-phosphate (DOPA), 1,2-di-(9Z-octadecenoyl)-sn-glycero-3-phosphocholine (DOPC) and cholesterol.[236] Using a similar strategy, AZO-lipid molecules were incorporated in the supported lipid bilayer on the surface of $LiYF_4:Tm^{3+}/Yb^{3+}$UCNPs.

Table 3. 1 Percentage of the *cis*-isomer formation as function of time upon 980 nm excitation of the nanoparticle

Time (h)	Absorbance at 350 nm	*cis*-%
0.5	0.80	27
1.5	0.63	52
2.5	0.55	64
3.5	0.52	70
4.5	0.46	79
5.5	0.43	83
6.5	0.43	83
7.5	0.43	83

Bilayer disruption by azobenzene has been found to be highly dependent on cholesterol content.[107,108] The presence of a cholesterol-induced liquid ordered phase enhances the release compared to liposomes comprising only liquid disordered phases that have a greater capacity to reorganize and accommodate the change in chain volume upon photoswitching.[107] The extent of release has been correlated to the fraction of liquid-ordered phase present.[107] On the other hand, while a critical amount of azobenzene is required for efficient release, a high concentration can limit liposome stability.[108] Our previous work demonstrated that a 64:7:29 ratio of DOPA:DOPC:Chol formed a stable bilayer coating.[236] A proportion of DOPA was replaced by AZO-lipid, since they both carry a negatively charged phosphate head group that interacts with the positively charged surface of the $LiYF_4$:Tm^{3+}/Yb^{3+}UCNPs, with the other lipid proportions remaining constant. The AZO-lipid comprised 14 mol% of the total added lipid (equivalent to 19 mol% of the phospholipid), namely a composition of DOPA:DOPC:Chol:AZO-lipid (50:7:29:14) was used. The supported lipid bilayer was prepared using the same procedure as described previously [236] except that the hydration of the dry lipid film was carried out in darkness at 50 °C to ensure the AZO-lipid molecules were in the *trans*-configuration. It was determined that there are approximately 6000 molecules of AZO-lipid per nanoparticle, corresponding to approximately 16 mol% of the phospholipid content of the supported lipid bilayer per nanoparticle (Section 3.6.5, in the Supporting Information). This value is, within experimental error, in agreement with the ratio initially used.

Incorporating AZO-lipid into the supported lipid bilayer led to a decrease in the photoluminescence intensities of the Tm^{3+} transitions centered at 290 nm, 353 nm, 368 nm and 450 nm, relative to the supported lipid bilayer without the presence of AZO-lipid (**Figure 3.3**a). The energy transfer efficiency (eq 3.1) was determined to be 23%, which is lower than the efficiency (40%) obtained for the AZO-lipid conjugated on the $LiYF_4$:Tm^{3+}/Yb^{3+}UCNPs.

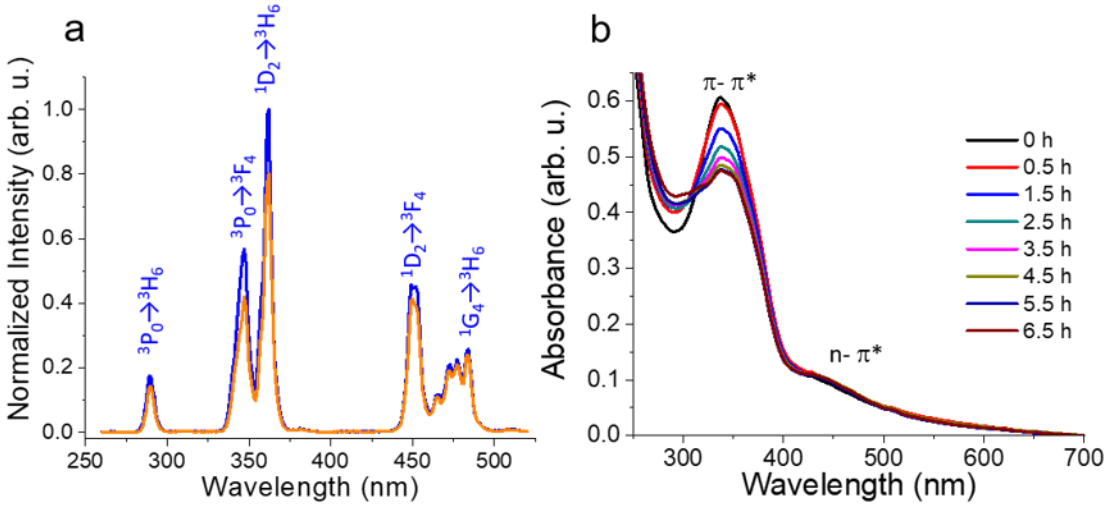

Figure 3. 3 a) Photoluminescence spectra of SLB-UCNPs (blue) and AZO-SLB-UCNPs (orange) excited at 980 nm. b) Absorbance spectra of AZO-SLB-UCNPs as function of the irradiation time with 980 nm. All measurements are made with a nanoparticle concentration of 0.61 mg/mL.

This is clearly correlated with the number of AZO-lipid molecules at the surface, i.e. 6000 incorporated in the supported lipid bilayer coating in comparison to 11500 conjugated directly to the nanoparticle surface. Although the supported lipid bilayer contains approximately half the number of AZO-lipid molecules, leading to a lower energy transfer efficiency, this must be balanced with the potential loss of liposomal stability if the proportion of AZO-lipid in the supported lipid bilayer were to be increased.[103]

Although Tm^{3+} ion photoluminescence quenching was evident for both SLB-UCNPs and AZO-UCNPs, the mechanistic origins of this energy transfer are not accessible from steady-state photoluminescence spectra, which reflect contributions from all radiative and non-radiative quenching mechanisms. Using time-resolved spectroscopy, we have previously found that energy transfer from Ln-UCNP donors can be attributed to both radiative energy transfer (reabsorption, r^{-2} distance dependence) and non-radiative Förster resonance energy transfer

(FRET, r^{-6} distance dependence).[248] The strong distance dependence of FRET and the very low photoluminescence quantum yields for upconversion photoluminescence limit the availability of FRET donors to Tm^{3+} ions close to the $LiYF_4$:Tm^{3+}/Yb^{3+} UCNP surface. Only these ions are in a sufficient proximity to the AZO-lipid for FRET. Taking into account the particle size of our $LiYF_4$:Tm^{3+}/Yb^{3+} UCNPs (ellipsoids of *ca.* 52 x 91 nm – *vide supra*), the majority of Tm^{3+} ions will not be able to transfer their energy *via* FRET to AZO-lipid and it can be expected that reabsorption plays an important role in $LiYF_4$:Tm^{3+}/Yb^{3+} UCNP-to-AZO-lipid energy transfer. To evaluate the contribution of FRET, photoluminescence decays of $LiYF_4$:Tm^{3+}/Yb^{3+} UCNPs and SLB- $LiYF_4$:Tm^{3+}/Yb^{3+} UCNPs with and without AZO-lipid (Figure 3S.7, 3S.8 and 3S.9, in the Supporting Information) were recorded and analyzed by multiexponential decay fitting (Table 3S.4 and 3S.5, in the Supporting Information). Average rise and decay times of the $^1D_2 \rightarrow {}^3H_6$ (368 nm) (and partly $^3P_0 \rightarrow {}^3F_4$ (353 nm)) photoluminescence transition (365 ± 13 nm bandpass filter) and the resulting FRET efficiencies are shown in Table 2. Similar to the steady-state photoluminescence measurements, the energy transfer efficiencies are higher for the $LiYF_4$:Tm^{3+}/Yb^{3+} UCNPs without the SLB. However, the difference is approximately 4-fold, whereas it was only 2-fold for the steady-state energy transfer. This larger difference can be explained by the stronger distance dependence of FRET ($\sim r^{-6}$) compared to reabsorption ($\sim r^{-2}$) in combination with the longer Tm^{3+}-donor-to-AZO-lipid-acceptor distances when the $LiYF_4$:Tm^{3+}/Yb^{3+} UCNPs are coated with the SLB (not all AZO-lipids are located in the inner leaflet of the bilayer). In addition to the relative differences, the absolute energy transfer efficiency values are significantly smaller for FRET (9% vs. 40% without and 2% vs. 23% with the SLB). As mentioned above, the particle size of the $LiYF_4$:Tm^{3+}/Yb^{3+} UCNPs restricts FRET to only a small part of Tm^{3+} ions and the majority can be quenched only by reabsorption. Moreover, the FRET efficiency is independent of the number of donor-acceptor pairs and therefore the larger amount of AZO-lipid for the $LiYF_4$:Tm^{3+}/Yb^{3+} UCNPs without SLB (11500 vs. 6000) only influences the reabsorption.

The strong distance dependence of FRET can be used to estimate the photoluminescence quantum yield of the FRET donors, namely the emitting lanthanide ions (in our case Tm^{3+}) close

to the $LiYF_4:Tm^{3+}/Yb^{3+}$ UCNP surface (*i.e.* those that can participate in FRET). Due to the multistep excitation and de-excitation processes generally involved in lanthanide upconverting nanoparticles, the surface-ion quantum yields can be quite different from that of the entire upconverting nanoparticle. When taking into consideration the spectral overlap of $LiYF_4:Tm^{3+}/Yb^{3+}$ UCNP emission and AZO-lipid absorption (Figure 3S.10, in the Supporting Information), and surface-to- AZO-lipid distances of *ca.* 1.7 nm for the monolayer (Figure 3S.11, in the Supporting Information) and *ca.* 2.3 nm on average for the bilayer (Figure 3S.12, in the Supporting Information), a Tm^{3+} ion photoluminescence quantum yield of 0.03% would correspond to FRET efficiencies of 0.087 and 0.021 (Table 3S.6, in the Supporting Information), respectively. These values are in excellent agreement with those found within the time-resolved photoluminescence analysis (**Table 3.2**). The surface Tm^{3+} ion quantum yield is approximately 300 times larger than the estimated overall $LiYF_4:Tm^{3+}/Yb^{3+}$ UCNP quantum yield of 0.0001%, which would have led to negligible FRET efficiencies (below 0.1% even for the close Tm^{3+}-to-AZO-lipid distance). Although the surface Tm^{3+} ion quantum yield value may not be exact when taking into consideration our low FRET efficiencies, the correlation of distance estimations and time-resolved FRET analysis clearly shows the importance of distinguishing between the photoluminescence properties of the surface and core emitting ions in Ln-UCNPs.

Table 3. 2 Average rise and decay times from time-resolved photoluminescence of $LiYF_4:Tm^{3+}/Yb^{3+}$ UCNPs and SLB-UCNPs with and without AZO-lipid.

Coating-$LiYF_4:Tm^{3+}/Yb^{3+}$ UCNPs	Rise time (μs)	Decay time 1 (μs)	Decay time 2 (μs)	Average Decay time (μs)	E_{FRET}
Oleate	240 ± 30	490 ± 50	1200 ± 120	530 ± 60	
AZO	250 ± 30	440 ± 50	1000 ± 100	480 ± 50	0.092 ± 0.012
SLB	260 ± 30	470 ± 50	1200 ± 120	500 ± 50	
AZO-SLB	270 ± 30	450 ± 50	1100 ± 120	490 ± 50	0.022 ± 0.004

Decay curves and fitting procedures can be found in (SI). Decay time 1 corresponds to the surface-emitting Tm^{3+} ions; decay time 2 corresponds to the core-emitting Tm^{3+} ions

The absorption spectra of AZO-SLB-UCNPs dispersed in an aqueous solution and irradiated at 980 nm as a function of time is shown in **Figure 3.4**b. The decrease in the intensity of the π-π* transition confirms the *trans→cis* isomerization of AZO-lipid in the supported lipid bilayer *via* the upconverted UV emission of the $LiYF_4:Tm^{3+}/Yb^{3+}$ UCNPs and the formation of a photostationary state after 5.5 hours of irradiation. The intensity changes in the n-π* transition are difficult to observe as the AZO-SLB-UCNPs system has a lower concentration of AZO-lipid compared to AZO-UCNPs. This is a result of the background absorption from the nanoparticles and the SLB both of which absorb in this region (Figure 3S.13, in the Supporting Information). The n-π* transition of the AZO-lipid has a low molar extinction coefficient of 2422 $m^{-1}cm^{-1}$, which can be obscured by this background, an effect also observed for azobenzene derivatives in mesoporous silica-coated Ln-UCNPs and Ln-UCNPs encapsulated in liposomes.[232,233] Although there is no change to the time to reach a photostationary state, the π-π* transition is blue shifted to 337 nm when the AZO-lipid is incorporated into the supported lipid bilayer. This hypsochromic shift can be caused by a change in environment polarity or aggregation of the AZO-lipid.[103,249] Such aggregation has been observed in self-assembled monolayers of azobenzene-derivatized long chain thiols and liposomes comprising azobenzene modified lipids.[103,250] An azobenzene absorption wavelength between 330 and 340 nm has been reported to correspond to dimeric chromophores,[251] which correlates well with the di-substitution in AZO-lipid or weak H-aggregation (clustered azobenzenes but not phase separated azobenzene nanodomains).[103]

In the bilayer, the local order induced by the inclusion of cholesterol could conformationally restrict the AZO-lipid promoting possible intra and/or intermolecular aggregation of the AZO-lipid. It has been reported that the *trans→cis* isomerization of azobenzene induces a volume change of 0.12 nm^3.[252] It has previously been shown that self-assembled monolayers of single component alkanethiol derivatized azobenzenes do not have enough free volume to permit photoswitching but the required free volume can be created using

mixed monolayers (on both planar substrates and colloidal particles).[253] Additionally, physisorbed films on solid substrate and Langmuir monolayers at the air water interface,[254,255] wherein the molecules are not covalently bonded to a specific surface site, have additional degrees of freedom that enable switching. More importantly, photoswitching of azobenzene derivatized lipids has been demonstrated in fluid bilayers where, but only when monomeric and dimeric forms, rather than extensive H-aggregation (λ_{max} approximately 300 nm), are present.[103] The use of DOPC and DOPA ensures a fluid bilayer matrix in which 14 mol% AZO-lipid is embedded, providing the free volume necessary to permit photoswitching.

To examine the nanoconstruct as a potential delivery vehicle, the capacity to encapsulate and release Nile red, (9-diethylamino-5H-benzo[α]phenoxazin-5-one) was evaluated. Nile red is a fluorescent dye, which is highly sensitive to the polarity of its local environment. In polar solvents such as water its fluorescence is quenched. Additionally, its emission maximum shifts from red to yellow depending on the hydrophobicity of its environment. Nile red was encapsulated within the hydrophobic core of the supported lipid bilayer with and without the presence of AZO-lipid.

The amount of Nile red encapsulated within the supported bilayer can be estimated as 40 molecules per nanoconstruct with the AZO-lipid and 172 molecules without AZO-lipid (Figure S3.14, Table S3.7, in the Supporting Information). Additionally, when both Nile red and AZO-lipid are present in the bilayer, the amount of AZO-lipid incorporated is also reduced from approximately 6000 molecules per nanoparticle to approximately 3000 molecules per nanoparticle (equivalent to 12 mol% of the phospholipid) (Table 3S.2, in the Supporting Information). Both Nile red and AZO-lipid compete for the same free space in the bilayer and the bulkier side chains of the AZO-lipid may therefore restrict the available space for Nile red encapsulation and *vice-versa*. The nanoconstruct containing Nile red in the absence of AZO-lipid was irradiated with 980 nm laser for up to 4.5 hours and no release of the dye was observed confirming that AZO-lipid is required to induce the triggered release (Figure 3S.15, in the Supporting Information).

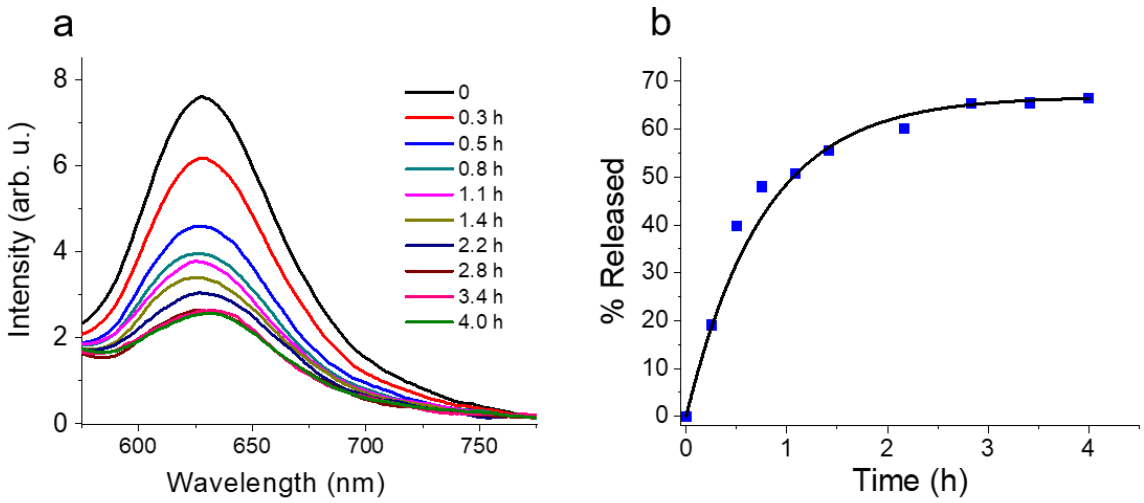

Figure 3. 4 a) Fluorescence spectra of Nile red embedded in the AZO-SLB-UCNPs as a function of the 980 nm irradiation time (excitation of the dye at 553 nm). b) Release profile of Nile red as a function of time fitted to a single exponential function.

The triggered release of Nile red from the supported lipid bilayer was monitored using the fluorescence spectra of Nile red as a function of time upon 980 nm excitation of the nanconstruct. The fluorescence quenching (Figure 3.4a) of Nile red clearly demonstrates that the dye was released from the supported lipid bilayer to the surrounding aqueous environment. The release profile shown in Figure 4b demonstrates that 50% of the encapsulated Nile red was released after 1 hour of irradiation. The amount released reaches a plateau after approximately 3 hours with a release of 65%. Fitting a single exponential to the release profile generates a time constant of 38 minutes (Eq 3S.1, in the Supporting Information), which represents the time to reach 50% of the plateau value. As discussed in relation to the photostationary state, the *cis*→*trans* isomerization switches back to the *trans*-isomer due to the overlap of the n-π* band of the *cis*-isomer with the blue emission of the nanoparticles. The lipophilicity and relatively low

water solubility of Nile red may also contribute to the incomplete release of the dye. The absorption spectra of the AZO-lipid show the same profile (Figure 3S.16, in the Supporting Information) as in Figure 3.4b confirming the phototriggered *trans*→*cis* isomerization.

Previous work has demonstrated that dyes encapsulated in the aqueous interior of a liposome can be released *via* azobenzene switching. Kuiper and Engberts determined that more than 20 mol% azobenzene derivatized lipid was required to release calcein dye from DOPC liposomes and that the photoswitching was only possible in these liposomes when the azobenzene was either in a dimeric form or loosely, but not extensively, aggregated.[103] Moreover, achieving comparable levels of dye release to that observed here required more than 50 mol% of the azobenzene lipid. Earlier work has shown that the release mechanism, in this case for encapsulated carboxyfluorescein,[256] is highly dependent on the lipid phase. In fluid phase liposomes, release occurs due the formation of small defects leading to a slow leakage through the membrane. In gel phase liposomes, the photoswitching led to a complete liposome rupture. In the current work we have demonstrated that we have the low-aggregation states and fluid phase needed to enable photoswitching and slow release of the hydrophobic dye, Nile red. However, for the AZO-supported lipid bilayer, addition of 14 mol% AZO-lipid (yielding 12 mol% of the phospholipid content) was able to induce significantly more dye release than was previously reported for liposomes. This may be attributed to several factors. First, the incorporation of cholesterol into the bilayer increases the lipid packing density and may enhance the impact of the photoswitching on the release. Additionally, the Nile red dye is embedded within the bilayer itself, not encapsulated within the inner aqueous phase. Thus, defects induced in the outer membrane alone can enable release whereas for dyes that must cross the bilayer, the total bilayer permeability must be altered and leakage requires defects in both leaflets of the membrane.

3.4 Conclusions

We have demonstrated that $LiYF_4:Tm^{3+}/Yb^{3+}$ UCNPs that are excited with 980 nm can be used to photoswitch an azobenzene-derivatized lipid incorporated into the soft matter shell of the nanoparticles. In the case of a supported lipid bilayer, the isomerization, which induces a volume change in the bilayer, enables release of molecules embedded within the hydrophobic core of the bilayer. We show that a large proportion of an encapsulated dye, Nile red, can be released with a relatively low proportion of AZO-lipid incorporated into the supported lipid bilayer. The incomplete dye release was attributed to a combination of the partition coefficient for Nile red and the influence of the reverse *cis→trans* isomerization. Time-resolved spectroscopy revealed that the energy transfer mechanism is predominantly radiative (reabsorption) with a minor contribution of non-radiative FRET. This has implications for that go beyond our nanoconstruct for future design of "donors" and "acceptors", whereby the FRET distance and molecular orientation do not play a significant role. The photoswitching of an AZO-lipid within a supported lipid bilayer excited at 980 nm inducing an energy transfer from $LiYF_4:Tm^{3+}/Yb^{3+}$ UCNPs highlights the potential of this AZO-SLB-UCNP nanoconstruct for light controlled delivery applications, especially in a biological context and *in vivo* applications, for which NIR excitation is of paramount importance for low toxicity and deeper tissue penetration.

3.5 Experimental Section

3.5.1 Synthesis of AZO-lipid

Butylaniline (97%), phenol (99.0+ %), carbon tetrachloride (99.9%), and pyridine (anhydrous, 99.8%) were purchased from Sigma-Aldrich; 6-bromohexanol (97%), trimethylamine (99%), and phosphorous trichloride (98%) were purchased from Alfa Aesar. All reagents were used without any further purification. The AZO-lipid was synthesized following the synthetic route proposed by Kuiper.[246] 4-butyl-4'-hydroxy-azobenzene was synthesized by a diazotization and an azo coupling reaction of butylaniline and phenol. The product was purified by column

chromatography using a (4:1) mixture of toluene and acetone with a 91% of yield. Using the Williamson reaction, 6-bromohexanol was added to the 4th position of the azobenzene (ABZ) by a nucleophilic substitution of bromine, forming an ether bond and producing 6-{[4-(4-butylphenyl)azo]-phenoxy}-hexan-1-ol. The product was purified by column chromatography using a mixture of (1:1) hexane and diethyl ether obtaining a 52% yield. Subsequently, ABZ dialkyl phosphonate was synthesized *via* the Arbuzov reaction using phosphorous trichloride and pyridine. The product was purified by recrystallization from ethanol obtaining a 20% yield. To produce the ABZ dialkyl phosphate (HO-PO(OR)$_2$) molecules from the ABZ dialkyl phosphonate (H-PO(OR)$_2$), the following synthetic route was used; ^{31}P NMR was used to monitor the reaction *via* observation of the substitution of the hydrogen in the phosphonate group for the hydroxyl group. Specifically, the phosphonate (^{31}P NMR 7.80 ppm) was treated with carbon tetrachloride and triethylamine to produce trichloromethyl esters (^{31}P NMR -12.84 ppm). Following evaporation of the solvent, the mixture was treated with acetic acid to produce the anhydride compound (^{31}P NMR -0.37 ppm). Subsequently through a mild acidic hydrolysis Di(6-{[4-(4-butylphenyl)azo]-phenoxy}-hexyl)phosphate was obtained (^{31}P NMR 1.46 ppm), referred to as AZO-lipid. The product was purified by recrystallization from ethanol with an 82% yield obtaining a yellow powder.

3.5.2 Synthesis of oleate-LiYF4:Tm3+/Yb3+ (UCNPs)

Thulium oxide (99.99+ %), ytterbium oxide (99.99%), yttrium oxide (99.99+ %), triflouroacetic acid (99%), lithium trifluoroacetate (98%), oleic acid (technical grade, 90%), and 1-octadecene (technical grade, 90%) were all purchased from Sigma-Aldrich and were used without further purification. Oleate-LiYF$_4$:Tm^{3+}, Yb^{3+} (0.5% Tm^{3+}, 25% Yb^{3+}) UCNPs were synthesized *via* the thermal decomposition, as described in detail previously.[236]

3.5.3 Synthesis of AZO-UCNPs

As synthesized oleate-LiYF$_4$:Tm^{3+}/Yb^{3+} UCNPs (2 mg) dispersed in chloroform (1% m/v) were incubated with a solution of AZO-lipid in chloroform (300 μL, 6 mM), followed by sonication (10 minutes at 70W) and evaporation of the solvent. This cycle, sonication/evaporation, was

repeated 5 times by solvating the mixture (nanoparticles and AZO-lipid) using chloroform (1 mL) in order to increase the interaction between the unattached AZO-lipid and the surface of the nanoparticle. The AZO-lipid $LiYF_4:Tm^{3+}/Yb^{3+}$ UCNPs were washed 5 times with ethanol to remove the free AZO-lipid and recovered *via* centrifugation (5000 rpm, 10 min). We obtained yellow nanoparticles confirming the modification of the surface with AZO-lipid. Finally, the modified nanoparticles were dispersed in a mixture of ethanol and propylene glycol.

3.5.4 Synthesis of the nanoconstruct AZO-SLB-UCNPs

1,2-di-(9Z-octadecenoyl)-*sn*-glycero-3-phosphate (DOPA) and 1,2-di-(9Z-octadecenoyl)-*sn*-glycero-3-phosphocholine (DOPC) were purchased from Avanti Polar Lipids Inc., cholesterol (99+ %), was purchased from Sigma-Aldrich and chloroform (ACS grade) was purchased from Fisher Scientific. AZO-lipid was synthesized as previously described above. HEPES was purchased from Bioshop®. Sodium acetate (99+ %) was purchased from Sigma-Aldrich. All water used for the experiments was ultrapure (18.2 MΩ·cm) obtained from a Barnstead system.

Oleate-$LiYF_4:Tm^{3+}/Yb^{3+}$ UCNPs with a supported lipid bilayer were synthesized following the procedure reported previously with minor modifications for the incorporation of AZO-lipid.[236] Stock solutions of DOPA, DOPC, AZO-lipid and cholesterol in chloroform (10 mM) were prepared from which mixed lipid solutions comprising with defined mole ratio of DOPA, AZO-lipid, DOPC and cholesterol (50:14:7:29) were prepared (4.4 mM). The oleate-$LiYF_4:Tm^{3+}/Yb^{3+}$ UCNPs (2 mg) were dispersed in chloroform (1% m/v) and sonicated (10 minutes at 70W) to ensure the nanoparticles were completely dispersed. Then the dispersed nanoparticles were incubated with the lipid mixture solution (1 mL). The mixture of nanoparticles and lipids was sonicated (5 minutes at 70W) and then the solvent was evaporated under reduced pressure to form a dry lipid film. This cycle (sonication/evaporation) was repeated 3 times by solvating the mixture using chloroform (1 mL) in order to increase the interaction between the lipids and the surface of the nanoparticle. After the last cycle, the dry lipid film with the nanoparticles was left under vacuum to remove all traces of solvent (1 hour). The dry lipid film was hydrated overnight at 50 °C with HEPES buffer (1 mL, 5 mM HEPES, 5 mM sodium acetate, 30 mM NaCl, pH adjusted to 7.4 with NaOH) for the samples containing the lipid AZO-

lipid and at room temperature for the other samples. Subsequently it was vortexed (10 min), sonicated (2 minutes at 70 W) and extruded (41 times using Avanti® Mini-extruder) through a polycarbonate membrane filter (200 nm). The sample was centrifuged (30 minutes at 12000 rpm then 20 minutes at 5000 rpm) to remove free lipids and liposomes, the supernatant was removed and the pellet rehydrated with HEPES buffer (1 mL) between the centrifugation steps. After the last rehydration of the pellet, oleate-$LiYF_4$:Tm^{3+}/Yb^{3+} UCNPs with a supported lipid bilayer were obtained.

3.5.5 Nile red embedded in SLB-UCNPs

9-diethylamino-5H-benzo[α]phenoxazin-5-one (Nile red) was purchased from Sigma-Aldrich (98+ %) and a solution in chloroform was prepared (3.2 mM). The embedding of the Nile red inside the supported lipid bilayer was done with the following modification to the procedure described above. In the third cycle of sonication/evaporation, the nanoparticles and lipid mixture were solvated in chloroform (1 mL) and then a Nile red solution (56 μL, 4 mol% of the total lipid used for the SLB) was added to the mixture. Two additional cycles of sonication/evaporation and hydration with 1mL of chloroform were performed. After the last cycle, the dry lipid film with the nanoparticles was left under vacuum to remove all traces of solvent (1 hour). The rest of procedure was followed as described above. The nanoconstruct was obtained after centrifugation step where free lipids and liposomes where eliminated, the samples were filter using a PTFE membrane filter (0.2 μm) to remove any free dye.

3.6 Supporting information

3.6.1 Characterization of AZO-lipid

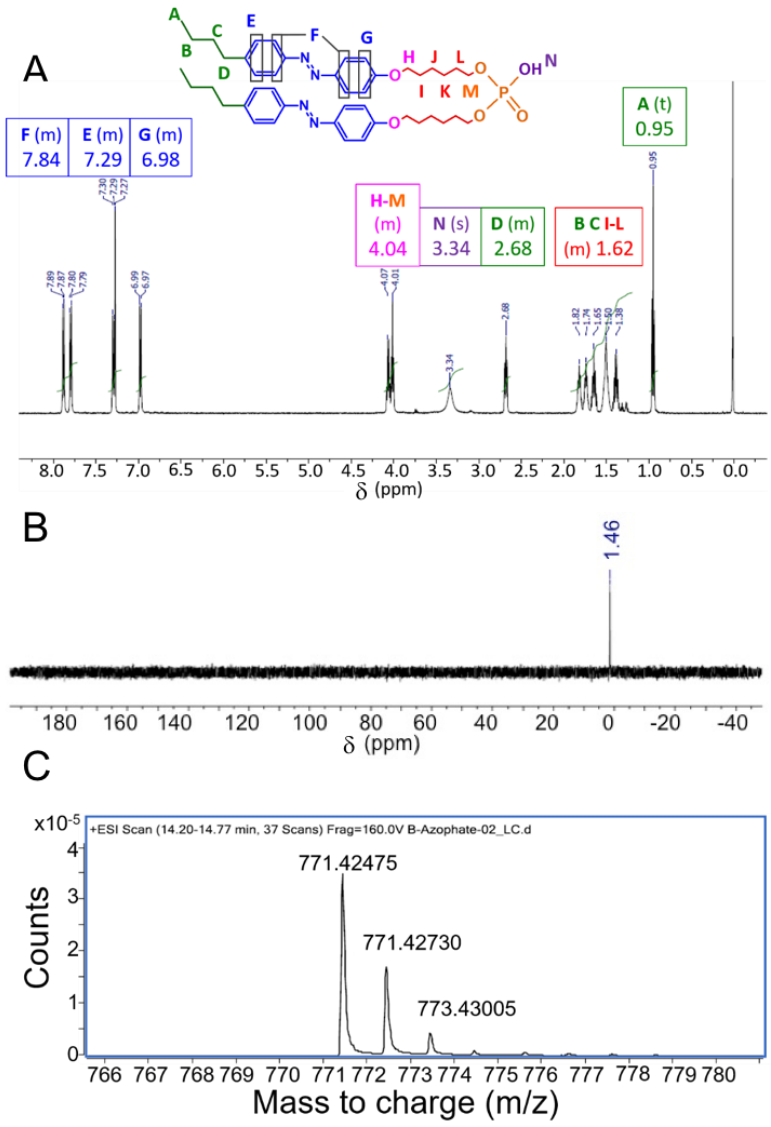

Figure 3S. 1 Characterization of the synthesized AZO-lipid. A) ^{1}H NMR with proton environments labelled with letters correspondingly marked in the molecular structure. ^{1}H NMR (500 MHz, $CDCl_3$, δ): 0.95 (t, J = 7.2 Hz, 6 H), 1.38-1.82 (m, 24 H), 2.68 (m, 4 H), 3.34 (s, 1 H), 4.01-4.07 (m, 8 H), 6.97-6.99

(m, 4 H), 7.27-7.30 (m, 4 H), 7.79-7.89 (m, 8 H). B) ^{31}P NMR (202 MHz, $CDCl_3$, δ): 1.46 (s). C) HRMS (ESI) m/z: $[M + H]^+$ calculated for $C_{44}H_{60}O_6N_4P$, 771.42475; found, 771.42450.

3.6.2 Characterization of *trans*- and *cis*-isomerization of AZO-lipid in solution

The photoswitching of the AZO-lipid was investigated using UV/Vis absorption spectroscopy. A solution of 2.4 x 10^{-5} M of AZO-lipid in a mixture of ethanol/propylene glycol (EtOH/PG) (1:1) was kept in the dark for three days to obtain the *trans*-stable isomer; the *cis*-isomer was produced when the solution was exposed to 365 nm light. The *trans*-AZO-lipid has a strong π-π* band near 350 nm and a weak n- π* band at 450 nm; the *cis*-isomer has a stronger n- π* 450 nm band and a less intense π-π* band at 320 nm.

The *trans*→*cis* isomerization of AZO-lipid was produced when exposed to 365 nm light. A photo-stationary state was obtained after 30 seconds of irradiation with a standard UV lamp. In order to assess the *cis*→*trans* thermal relaxation, the solution was irradiated for 30 min with 365 nm light to produce the *cis*-isomer after which the solution was then kept in the dark at room temperature (RT) and allowed to relax back to the *trans*-isomer. The absorbance of the solution, was measured as a function of time kept in the dark to ascertain the time required for thermal relaxation to the *trans*-isomer (Figure S3.2 B and C). The *cis*→*trans* isomerization of AZO-lipid follows first order kinetics with a half-life of 23 hours at room temperature. At 50 °C the half-life of *cis*→*trans* isomerization was found to be 18 min. To ensure that the AZO-lipid is in the *trans*-configuration, it was kept in the dark for at least three times longer than its half-life. For instance, at room temperature the samples were kept in the dark for 3 days. At 50°C one hour in the dark is required to ensure the *trans*-isomerization. The latter is important for the hydration of the lipid film during the formation of the SLB with the *trans*-AZO-lipid.

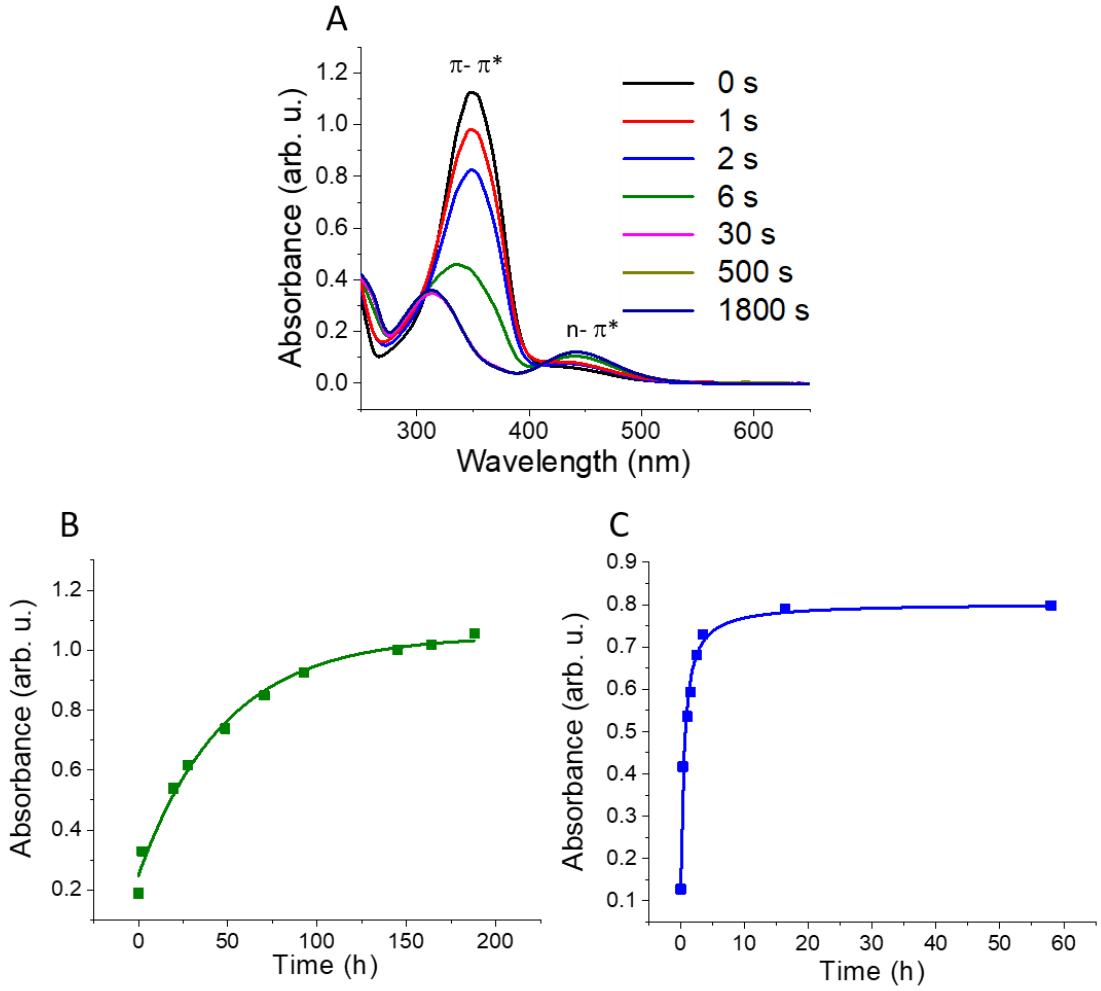

Figure S3. 2 A) Absorption spectra of the trans→cis photoisomerization as function of the irradiation time using 365 nm lamp. B) and C) Thermal relaxation of cis→trans isomerization of AZO-lipid at room temperature and at 50 °C, respectively.

3.6.3 Characterization of oleate-$LiYF_4$:Tm^{3+}/Yb^{3+} UCNPs using TEM and XRPD

The oleate-$LiYF_4$:Tm^{3+}/Yb^{3+} UCNPs (Figure 3S.3A) showed a diamond-like morphology with an average size of 91 nm (± 12 nm) long diagonal length and a small diagonal length of 52 nm (± 5 nm). The particle size distribution was obtained by counting 300 nanoparticles (Figure 3S.3B).

The X-ray powder diffraction confirms the tetragonal crystal structure of the nanoparticles (Figure 3S.3C). Assuming a square base bipyramidal shape we calculate the surface area and volume of the nanoparticle to be 7249 nm^2 and 41219 nm^3 respectively. From the reported density for $LiYF_4$ bulk material (3.995 g/cm^3) it was possible to calculate the mass of the nanoparticle to be $1.65x10^{-13}$ mg.[65]

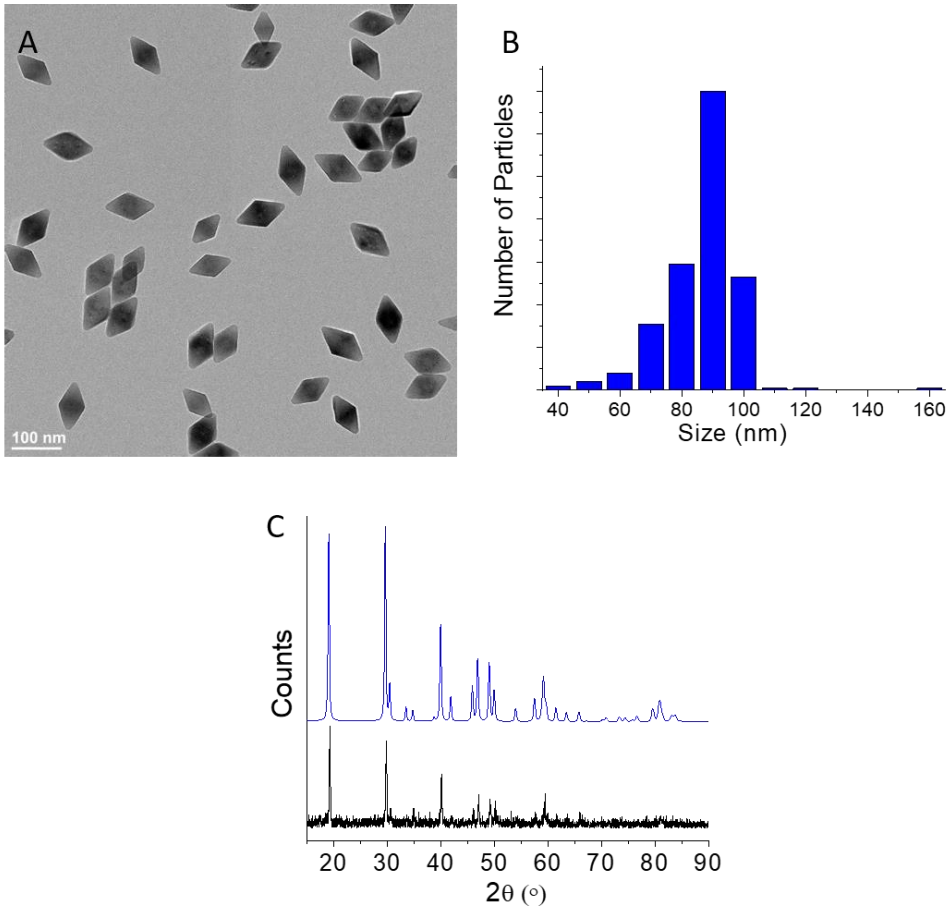

Figure 3S. 3 A) TEM image of oleate-$LiYF_4$:Tm^{3+}/Yb^{3+} UCNPs. B) Particle size distribution with respect the long diagonal, 91 ± 12 nm. The particle aspect ratio is 1.75 (the short diagonal is 52 ± 5 nm). C) XRPD pattern of oleate-$LiYF_4$:Tm^{3+}/Yb^{3+}UCNPs in black and the standard reference pattern of $LiYF_4$ (JCPDS File No. 81-2254) in blue.

3.6.4 Characterization of AZO-UCNPs

The characterization of the surface modification of $LiYF_4:Tm^{3+}/Yb^{3+}$ UCNPs with AZO-lipid (AZO-UCNPs) was characterized by FTIR spectroscopy (Figure 3S.4). The oleate-UCNPs exhibit C-H stretching bands at 2923 and 2852 cm^{-1} and the asymmetric and symmetric stretching bands of the carboxylate at 1560 and 1464 cm^{-1} respectively (Figure 3S.4a). The spectra for both the free AZO-lipid (Figure 3S.4b) and AZO-UCNPs (Figure 3S.4c) show C-O, P-O-R bands that overlap at 1250 cm^{-1} and phenyl-N= stretching band at 1141 cm^{-1}. The free AZO-lipid has the P-OH stretch at 1012 cm^{-1} however it exhibits the PO_4^- symmetric stretching bands at 1109 and 1013 cm^{-1} (the asymmetric stretch of PO_4^- overlaps at 1250 cm^{-1}) when physisorbed to the surface of the nanoparticle, confirming the successful conjugation of AZO-lipid.

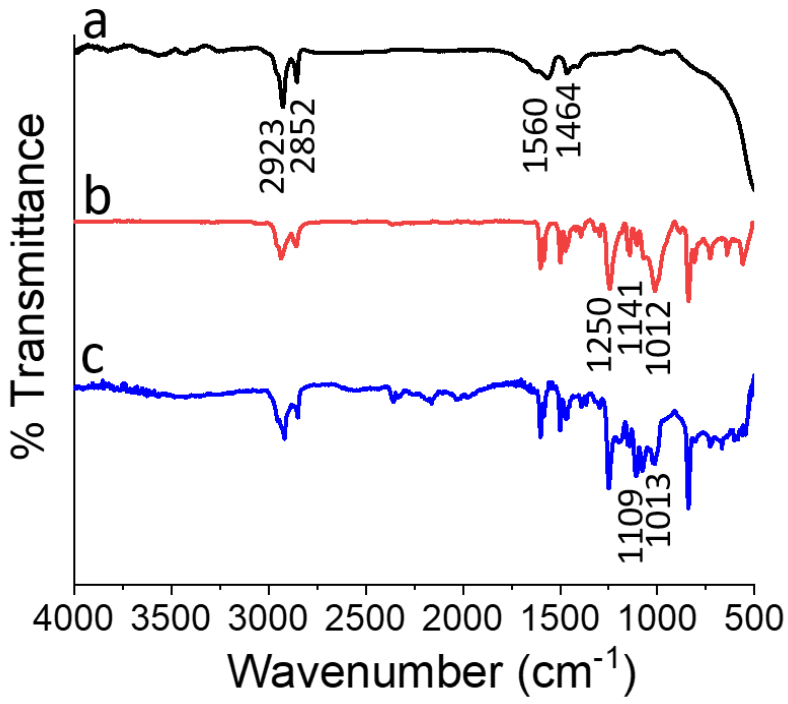

Figure 3S. 4 FTIR spectra of a) oleate-UCNPs b) AZO-lipid c) AZO-UCNPs.

3.6.5 Determination of the concentration and surface coverage of the modified nanoparticles using ICP-MS and absorption spectroscopy

Inductively Coupled Plasma Mass Spectrometry (ICP-MS) measurements were performed to determine the concentration of nanoparticles and lipid after the surface modification. Phosphorous and yttrium were evaluated in order to calculate the lipid and nanoparticles concentration, respectively. CertiPUR™ Phosphorous 1000 mg/L ICP standard from EMD chemicals Inc and Multi-element solution 10 mg/L (Ce, Dy, Er, Eu, Gd, Ho, La, Lu, Nd, Sc, Sm, Tb, Th, Tm, Y, Yb) from Spex CertiPrep were used to prepare the calibration curve for P and Y respectively in 5% of HNO_3 solution (HNO_3, Trace metal grade from Fisher). Both calibration curves were prepared in the concentration range between 0.01 ppm and 5 ppm.

100 µL of each sample were first digested using 1000 mL of concentrated HCl (Trace metal grade from Fisher) with 100 µL of H_2O_2 (Ultratrex® Ultrapure reagent from Avantor Performance Materials, Inc.) and heated at 115 °C for 12 h under reflux. The samples were then dried and re-dispersed in 2 mL of 5% HNO_3. After digestion, the samples were injected and analyzed. For the determination of the yttrium concentration, samples were diluted 20 fold.

Table 3S. 1 ICP-MS results of the concentration of yttrium present in the samples and the concentration of nanoparticles after the surface modification.

-Coating $LiYF_4:Tm^{3+}/Yb^{3+}$ UCNPs	Y [pmm] ± 5%	$LiYF_4:Tm^{3+}/Yb^{3+}$ [mg] x 10^{-3} ± 5%	$LiYF_4:Tm^{3+}/Yb^{3+}$ [mg/mL] ± 5%	No. NPs x 10^{11} ± 5%
Oleate (PG/EtOH)	3.30	6.38	1.59	8.62
AZO (PG/EtOH)	1.33	2.56	0.64	3.88
SLB (DOPA:DOPC:Chol)	2.07	4.00	0.89	5.42
AZO-SLB	1.96	3.78	0.61	3.69
SLB-NR	0.64	1.23	0.27	1.67
AZO-SLB-NR	0.56	1.09	0.24	1.48

Table 3S. 2 ICP-MS results of the concentration of phosphorous present in the samples and the number of molecules containing phosphorous per nanoparticle after the surface modification.

-Coating $LiYF_4:Tm^{3+}/Yb^{3+}$ UCNPs	P [pmm] ± 8%	molecules x 10^{-15} ± 8%	molecules/NPs x 10^4 ± 8%	AZO-lipid [%]
AZO (PG/EtOH)	0.11	4.1	1.1	-
SLB (DOPA:DOPC:Chol)	0.68	28.3	5.2	-
AZO-SLB	0.34	13.7	3.7	16 ± 5
SLB-NR	0.15	5.7	3.4	-
AZO-SLB-NR	0.11	3.9	2.6	12 ± 6

From the ICP-MS results, the concentrations (ppm) of Y and P were calculated. The results are shown in Table 3S.1 and 3S.2, respectively. The concentrations of the nanoparticles were subsequently calculated assuming one mole of $LiYF_4$ doped 25 mol% with Yb^{3+} and 0.5 mol% Tm^{3+} for each mole of Y present. To calculate the number of nanoparticles in 100 µL, it was assumed that the mass of one nanoparticle is $1.65x10^{-13}$mg (see section 3.6.3). These concentrations were used to determine the dilutions required to measure the emission spectrum at equal nanoparticle concentrations.

To estimate the amount of lipid at the surface of the nanoparticles, it was assumed that for each mole of phosphorous, there is one mole of phospholipid (DOPA, DOPC or AZO-Lipid), which comprises 71% of the total lipid (cholesterol makes up the remaining 29%). The percentage of AZO-lipid incorporated within the SLB was calculated from the amount of AZO-lipid obtained from the absorption spectrum (Table 3S.3) and compared to the total amount of phosphorous per nanoparticle. These values are within the experimental error of the theoretical value of AZO-lipid incorporated in the SLB (14 mol%).

3.6.5.1 Absorption spectroscopy

UV-Vis spectroscopy was carried out in order to determine the concentration and number of AZO-lipid molecules on the surface of $LiYF_4:Tm^{3+}/Yb^{3+}$ UCNPs. A calibration curve of AZO-lipid in a mixture of EtOH/PG (1:1) was established (range 4.2 x 10^{-6} M to 2.6 x 10^{-5} M) and the absorbance at 350 nm was determined after keeping the samples in the dark for three days.

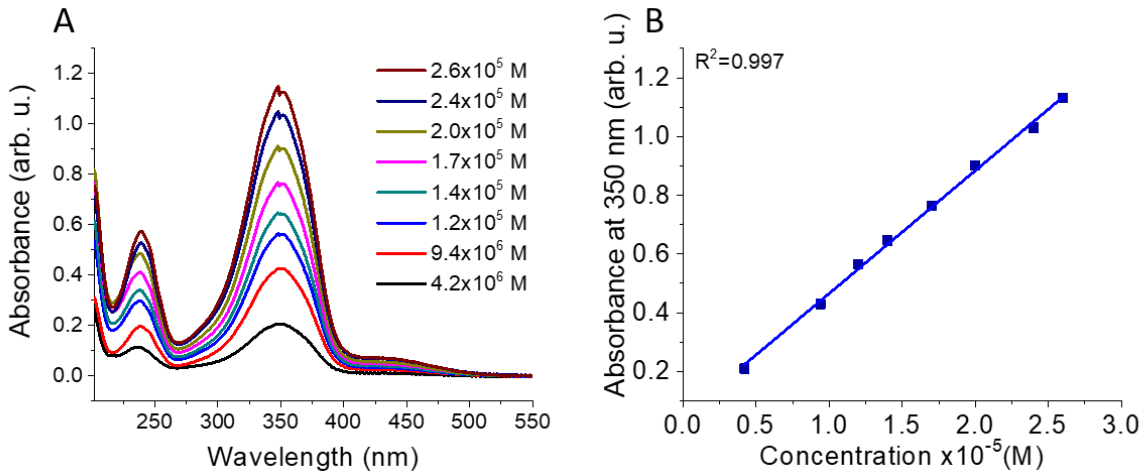

Figure 3S. 5 A) Absorption spectra of the *trans*-AZO-lipid at different concentrations (range 4.2 x 10^{-6} M to 2.6 x 10^{-5} M) in propylene glycol and ethanol (1:1). B) Calibration curve of *trans* AZO-lipid. The *trans*-AZO-lipid was obtained after keeping all samples in the dark for three days.

Table S3 shows the amount of AZO-lipid conjugated to the nanoparticle or incorporated within the SLB of the nanoconstruct. These results were calculated using the absorption spectrum of a 150 µL sample with a nanoparticle concentration calculated by ICP-MS (Table 3S.1). The concentration of AZO-lipid was calculated from the absorbance maximum of the π-π* transitions at 350 nm and using the calibration curve showed in Figure S5. Subsequently, calculating the number of nanoparticles in 150 µL of sample it was possible to approximate the number of

AZO-lipids per nanoparticle, as well the number of azobenzene moieties (2 moieties per each AZO-lipid molecule).

Table 3S. 3 Amount of AZO-lipid conjugated to the nanoparticle or incorporated within the SLB of the nanoconstruct calculated from absorption spectroscopy.

-Coating $LiYF_4:Tm^{3+}/Yb^{3+}$ UCNPs	Conc. [M] x 10^{-5}	Molecules x 10^{15}	AZO-lipid /NPs x10^4	ABZ /NPs x10^4
*AZO (PG/EtOH)**	2.21	2.0	1.2 ± 0.1	2.4 ± 0.2
AZO-SLB	1.53	3.2	0.6 ± 0.1	1.2 ± 0.2
AZO-SLB-NR	0.75	0.7	0.3 ± 0.1	0.6 ± 0.2

*Concentration of nanoparticles was diluted to 0.18 mg/mL

3.6.6 Reference absorption spectra for the AZO-UCNPs

The absorption spectra of the *trans*- and *cis*-AZO-UCNPs was characterized (Figure 3S.6). To obtain the *trans*-AZO-UCNPs, the solution of the modified nanoparticles was stored in the dark for three days while the *cis*-AZO-UCNPs was obtained by irradiating the solution at 365 nm for 30 min.

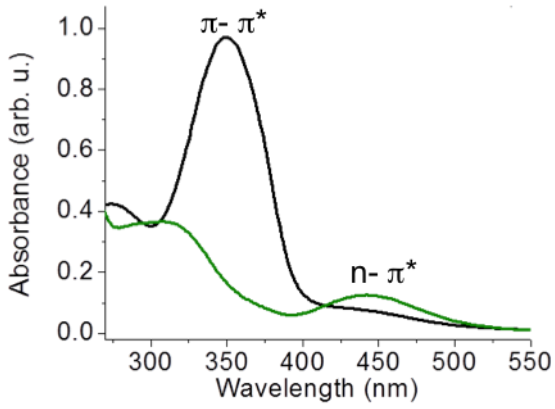

Figure 3S. 6 Absorption spectra of the *trans*- (black) and *cis*- (green) forms of the AZO-UCNPs in propylene glycol and ethanol (1:1).

3.6.7 Photoluminescence decay

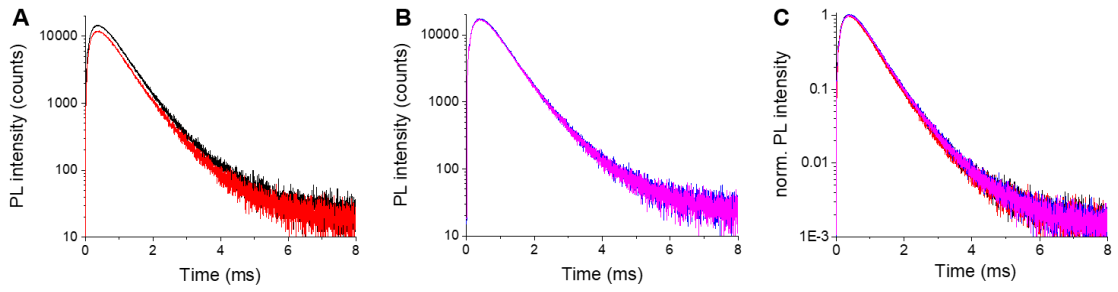

Figure 3S. 7 Photoluminescence decays of comparable systems with and without AZO-lipid. A) oleate-UCNPs (black) and AZO-UCNPs (red), B) SLB-UCNPs (blue) and AZO-SLB-UCNPs (magenta). C) All four systems with normalized intensities**.**

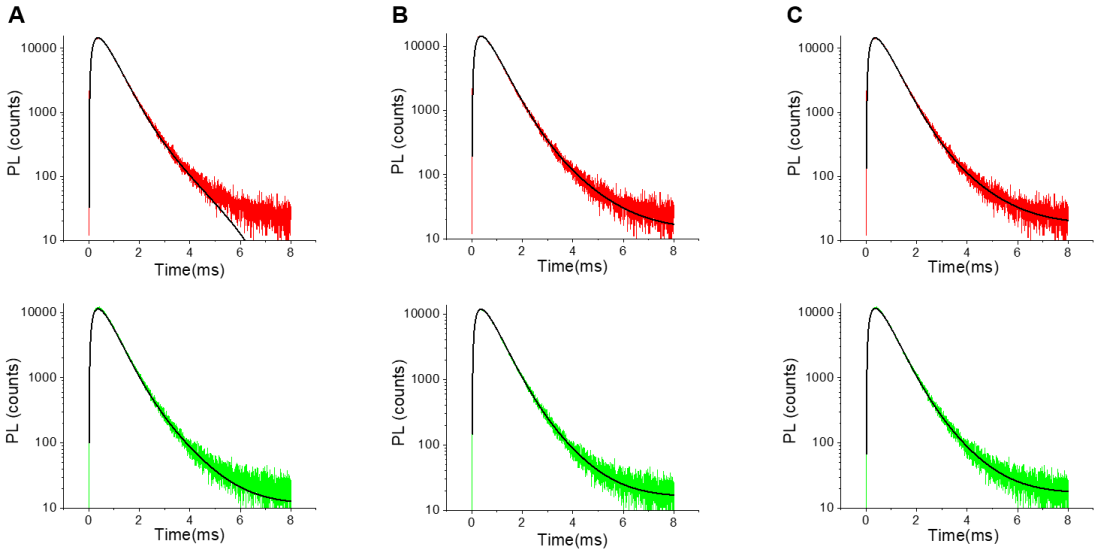

Figure 3S. 8 Photoluminescence decays of oleate-UCNPs (red) and AZO-UCNPs (green) and the fitted decay curves (black). Fitting ranges were 0.08 to 5.0 ms (A), 0.08 to 6.0 ms (B), and 0.08 to 7.0 ms (C).

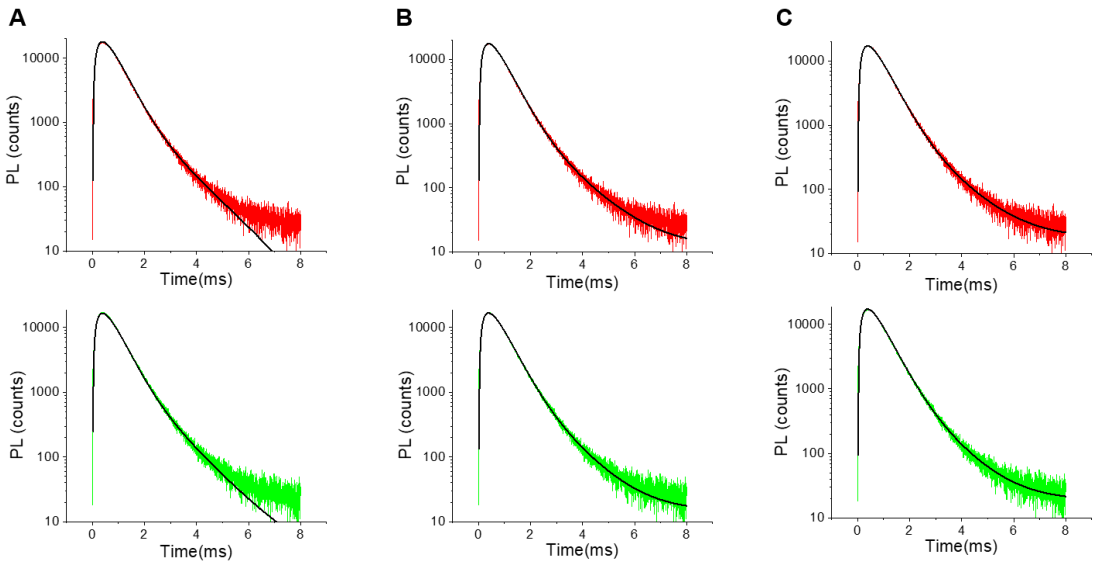

Figure 3S. 9 Photoluminescence decays of SLB-UCNPs (red) and AZO-SLB-UCNPs (green) and fitted decay curves (black). Fitting ranges were 0.08 to 5.0 ms (A), 0.08 to 6.0 ms (B), and 0.08 to 7.0 ms (C).

The FRET efficiencies were calculated using $E_{FRET} = 1 - \tau_{DA}/\tau_D \mathrm{E_{FRET}} = 1 - \tau_{\mathrm{DA}}/\tau_{\mathrm{D}}$, with τ_{DA} being the average decay time in the presence of azobenzene and τ_D being the average decay time in the absence of azobenzene. The average decay time was calculated by the following equation: $\tau = (A_1 \times \tau_1 + A_2 \times \tau_2)/(A_1 + A_2) \tau = (\mathrm{A_1} \times \tau_1 + \mathrm{A_2} \times \tau_2)/(\mathrm{A_1} + \mathrm{A_2})$ where A_i is the amplitude of the decay components in the multi-exponential fit. (Table 3S.4 and 3S.5).

Table 3S. 4 Rise and decay times taken from the fits of the photoluminescence decay curves in Figure 3S.8.

Fitting range [ms]	*-Coating* $LiYF_4:Tm^{3+}/Yb^{3+}$ UCNPs	Rise time [µs]	Decay Time 1 [µs]	Decay Time 2 [µs]	Average Decay lifetime [µs]	E_{FRET}
0.08 - 5	*Oleate*	240	480	1200	517	
	AZO	260	430	1000	471	8.9
0.08 - 6	*Oleate*	240	500	1200	534	
	AZO	250	450	1000	490	8.2
0.08 - 7	*Oleate*	230	500	1200	532	
	AZO	250	450	1000	490	8.0

Table 3S. 5 Rise and decay times taken from the fits of the photoluminescence decay curves in Figure 3S.9.

Fitting range [ms]	*-Coating* $LiYF_4:Tm^{3+}/Yb^{3+}$ UCNPs	Rise time [µs]	Decay time [µs]	Decay time [µs]	Average Decay lifetime [µs]	E_{FRET}
0.08 - 5	*SLB*	270	450	1200	482	
	AZO-SLB	280	430	1100	464	3.8
0.08 - 6	*SLB*	260	470	1200	502	
	AZO-SLB	270	460	1100	494	1.5
0.08 - 7	*SLB*	260	480	1200	511	
	AZO-SLB	260	470	1100	504	1.4

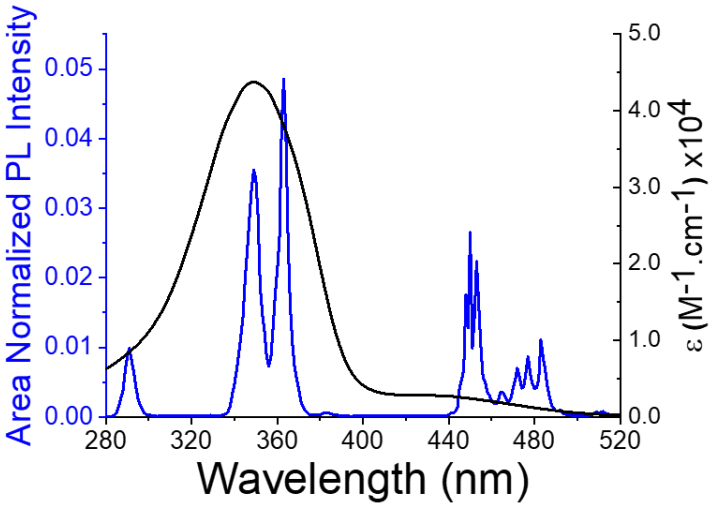

$$J = \int \bar{I}_D(\lambda)\ \varepsilon_A(\lambda)\ \lambda^4\, d\lambda = \int \bar{I}_D(\tilde{\nu})\ \varepsilon_A(\tilde{\nu})\ \frac{d\tilde{\nu}}{\tilde{\nu}^4}$$

$$\int \bar{I}_D(\lambda)\ d\lambda = \int \bar{I}_D(\tilde{\nu})\ d\tilde{\nu} = 1$$

With J calculated in $M^{-1}cm^{-1}nm^4$:

$$R_0 = 0.02108\ \left(\kappa^2 \Phi_D n^{-4} J\right)^{1/6}\ \text{nm}$$

$$E_{FRET} = \frac{{R_0}^6}{{R_0}^6 + R^6}$$

index of ref.	n=1.35	n=1.45	n=1.35	n=1.45
overlap range	280 - 520 nm	280 - 520 nm	280 - 400 nm	280 - 400 nm
Φ_D (%)	R_0 (nm)	R_0 (nm)	R_0 (nm)	R_0 (nm)
1	2.0	2.1	2.2	2.1
0.5	1.8	1.8	1.9	1.8
0.1	1.3	1.4	1.5	1.4
0.05	1.2	1.3	1.3	1.3
0.01	0.92	0.96	1.0	0.96
0.005	0.82	0.86	0.9	0.86
0.001	0.62	0.65	0.69	0.65

Figure 3S. 10 Spectral overlap of oleate-UCNPs photoluminescence (blue) and AZO-lipid absorption (black). The overlap integral was calculated between 280 nm and 400 nm (J = 5.88 x 10^{14} M^{-1} cm^{-1} nm^4) and between 280 nm and 520 nm (J = 4.45 x 10^{14} M^{-1} cm^{-1} nm^4) using the equations given on the right. Förster distances (R_0) were calculated using the equations given on the right and using κ^2=2/3 (dynamic averaging), n=1.35 (aqueous buffer) or n=1.45 (organic solvent), and different values for the donor photoluminescence quantum yield (Φ_D), which is the quantum yield of the emitting Tm^{3+} ions.

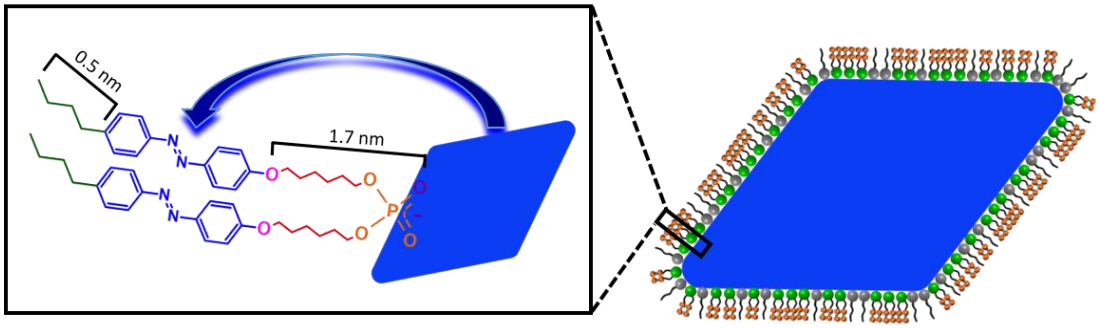

Figure 3S. 11 The distance from the $LiYF_4:Tm^{3+}/Yb^{3+}$ UCNPs surface to the azobenzene moieties is approximately 1.7 nm. This was approximated assuming C-C and C-O bond angles of 109.5 °, a C-C bond length of 154 pm, a C-O bond length of 143 pm and a diameter of the phosphate group of 786 pm.[257]

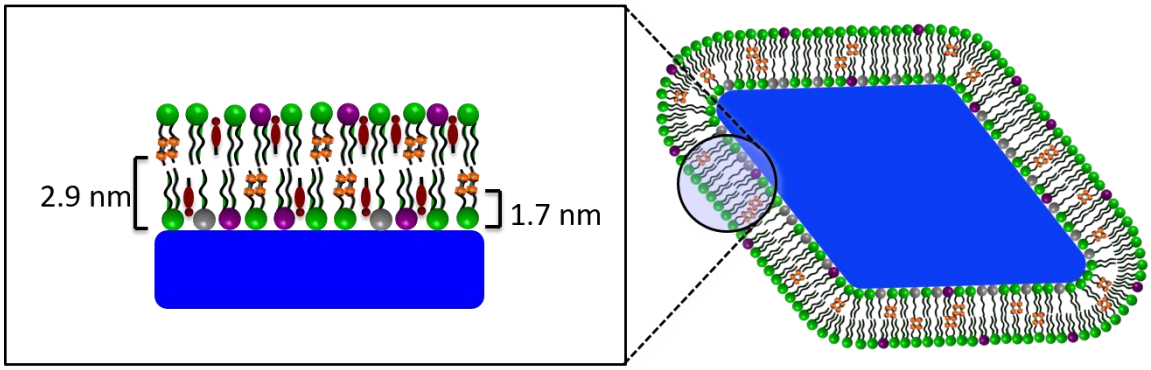

Figure 3S. 12 Within the SLB, azobenzene moieties can be found in both leaflets of the bilayer. The supported lipid bilayer has been reported to have a thickness of 4.7 nm [236]. For the azobenzene moieties that are at the surface of the nanoparticle (inner leaflet) the distance to the $LiYF_4:Tm^{3+}/Yb^{3+}$ UCNPs surface is 1.7 nm (Figure 3S.11). For the azobenzene moieties that are in the outer leaflet of the bilayer, the distance was estimated as 2.9 nm. This distance was calculated as the thickness of the inner leaflet plus the distance of the 4 carbons of the butyl tail of the AZO-lipid (2.35 nm + 0.5 nm). The average distance is 2.3 nm.

Table 3S. 6 Taking into consideration the estimated $LiYF_4:Tm^{3+}/Yb^{3+}$ UCNPs-to-azobenzene distances (Figures 3S.11 and 3S.12) and the Förster distances in the 280 to 400 nm spectral overlap range for the appropriate index of refraction (Figure 3S.10), the FRET efficiencies of 0.092 and 0.022 (Table 3.2) correspond to a photoluminescence quantum yield of the emitting Tm^{3+} ions of ca. 0.03%.

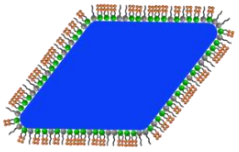

UCNP-to-azobenzene distance: **ca. 1.7 nm**

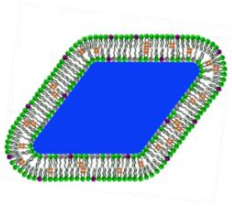

UCNP-to-azobenzene distance: **ca. 2.3 nm**

index of ref.	n=1.45	donor-acceptor distance	FRET efficiency
overlap range	280 - 400 nm		
Φ_D (%)	R_0 (nm)	*R (nm)*	E_{FRET}
1	2.1	1.7	0.78
0.1	1.4	1.7	0.24
0.05	1.3	1.7	0.17
0.03	1.2	1.7	0.087
0.01	0.96	1.7	0.031
index of ref.	n=1.35	donor-acceptor distance	FRET efficiency
overlap range	280 - 400 nm		
Φ_D (%)	R_0 (nm)	*R (nm)*	E_{FRET}
1	2.2	2.3	0.43
0.1	1.5	2.3	0.071
0.05	1.3	2.3	0.032
0.03	1.2	2.3	0.021
0.01	1.0	2.3	0.0067

3.6.8 Background absorption of the oleate-$LiYF_4:Tm^{3+}/Yb^{3+}$ UCNPs

The inherent absorption of the oleate-$LiYF_4:Tm^{3+}/Yb^{3+}$ UCNPs can introduce a background absorption in a concentration-dependent manner. In order to minimize this effect, the concentration was kept below 1 wt% for all measurements.

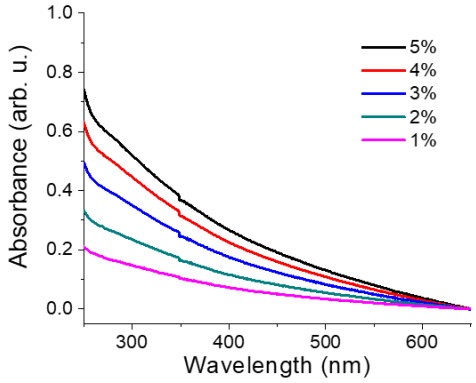

Figure 3S. 13 Absorption spectra of oleate-$LiYF_4$:Tm^{3+}/Yb^{3+} UCNPs in propylene glycol and ethanol (1:1) at different nanoparticle concentrations (wt %).

3.6.9 Nile red embedded in SLB-$LiYF_4$:Tm^{3+}/Yb^{3+} (UCNPs)

The amount of dye embedded in the nanoconstruct was quantified by fluorescence spectroscopy. A calibration curve of Nile red in methanol was established (range 2.9 x 10^{-7} M to 1.5 x 10^{-5} M) by exciting the solutions at 553 nm and recording the intensity at the maximum 338 nm (Figure 3S.13).

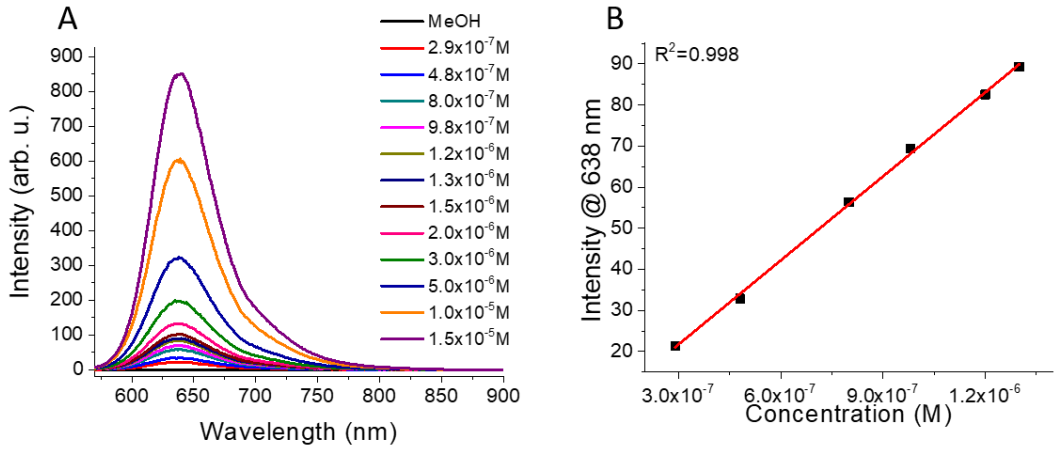

Figure 3S. 14 A) Fluorescence spectra of Nile red as a function of concentration in methanol. Excitation at 553 nm. B) Calibration curve for Nile red.

Table 3S.7 summarizes the amounts of Nile red embedded within the supported lipid bilayer of the nanoconstruct determined using the calibration curve for excitation at 553 nm (Figure 3S.14B). The nanoparticle concentration in the sample was calculated using ICP-MS (Table 3S.1), enabling the number of Nile red molecules per nanoparticle to be estimated.

Table 3S. 7 Amount of Nile red embedded in the supported lipid bilayer of the nanoconstruct calculated from fluorescence spectroscopy.

-Coating $LiYF_4:Tm^{3+}/Yb^{3+}$ UCNPs	Conc. [M] x 10^{-7}	Molecules x 10^{12}	NR /NPs
SLB-NR	4.76	43	172
AZO-SLB-NR	0.92	8.3	40

3.6.10 Control experiment: Nile red embedded within SLB-UCNPs

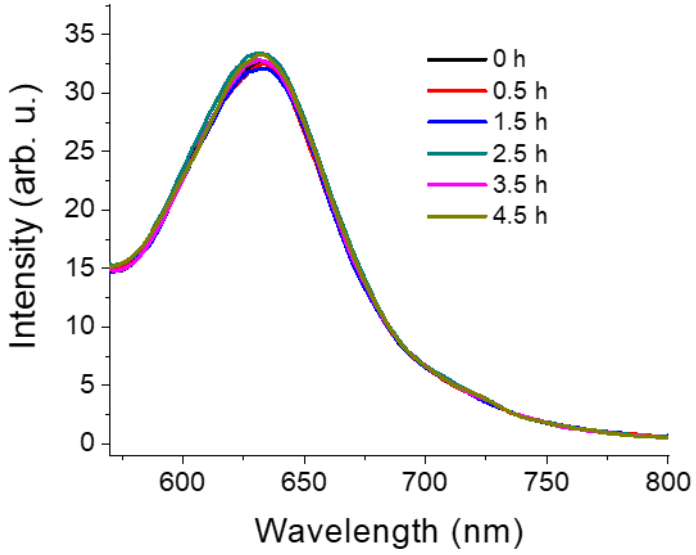

Figure 3S. 15 Fluorescence spectra of Nile Red embedded within SLB-UCNPs as function of the irradiation time at 980 nm excitation (in the absence of AZO-lipid). The Nile red emission was recorded at 553 nm.

3.6.11 Photoswitching of the AZO-lipid within the SLB-UCNPs with embedded Nile red

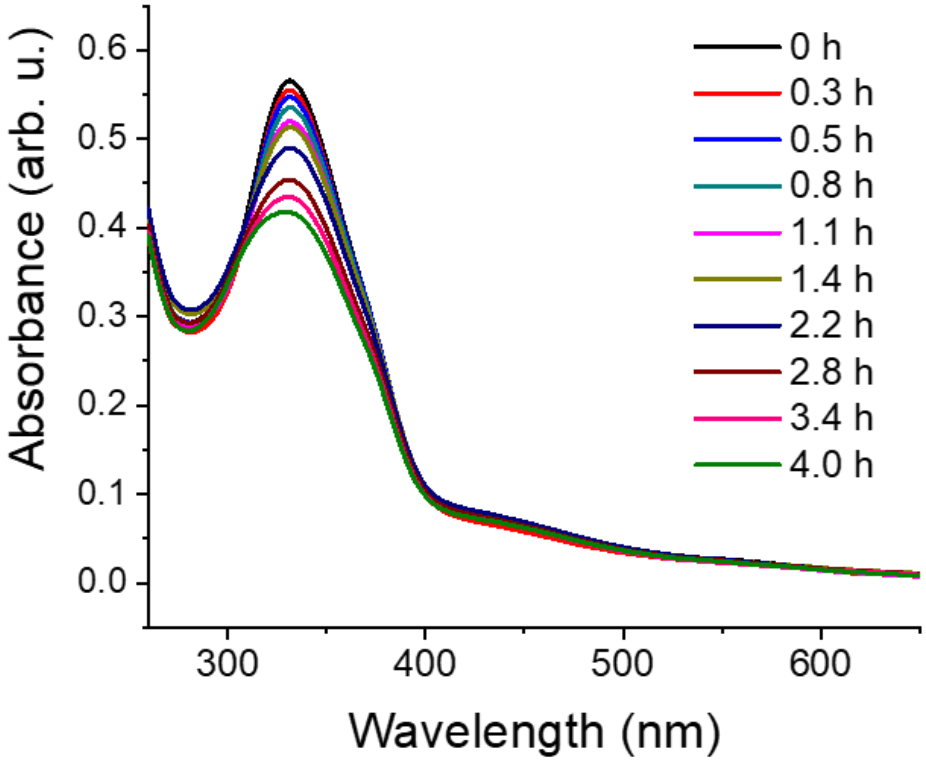

Figure 3S. 16 Absorption spectra of AZO-SLB-UCNPs with embedded Nile red as a function of irradiation time at 980 nm excitation.

The Nile red release in Figure 3.5b was fitted to a single exponential release function where y is the % of dye released upon 980 nm irradiation time, A is the amplitude and t is the time constant. The time constant was found to be 0.64 ± 0.06 h (38 min).

$$y = y_0 + A^{(-x/t)} \tag{3S.1}$$

3.6.12 Beam Profiling

A beam profiler was used to measure the beam irradiation area in order to calculate the power density. The set-up consisted of a Logitech HD PRO C920 Webcam, where the front optical lenses were removed exposing the photovoltaic sensor of the webcam. Beam profilers using webcams have been previously reported.[258,259] Two neutral density filters ND 25 (2.6 mm of thickness, Hoya Corporation) were placed in front of the laser beam (before reaching the photovoltaic sensor). The digital images taken with the webcam with the exposed photovoltaic sensor were calibrated using a microscope micrometer calibration ruler such that an image of size 3.8 x 2.85 mm correlated to 640 x 480 pixels. The beam profile image was taken using the same set-up for the sample, while placing the webcam at the same distance from the sample (Figure 3S.18). ImageJ was used for data analysis using the contour plotter plugin to define isolines at the desired beam power intensity from which the area was calculated.[260]

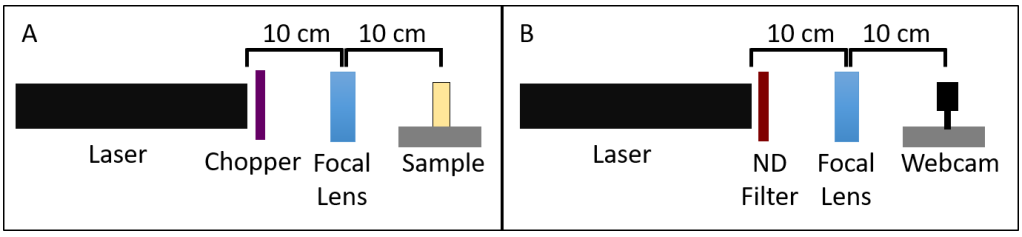

Figure 3S. 17 A) Set-up used to irradiate the sample with the 980 nm laser. B) Set-up to obtain the beam profile using the webcam.

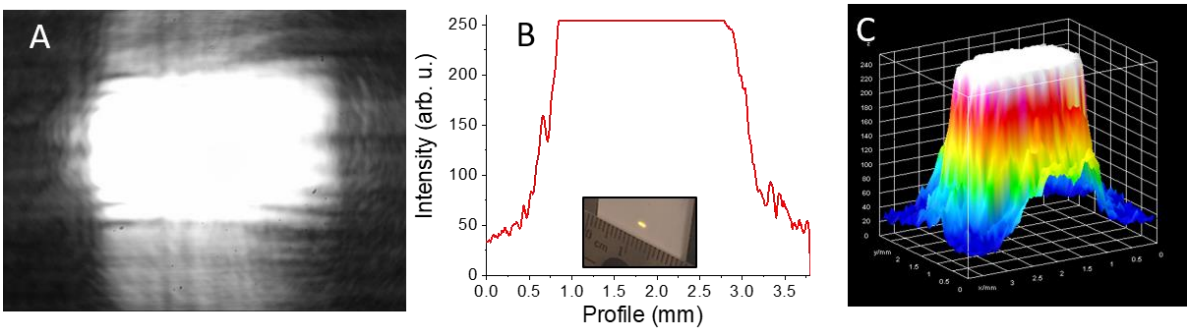

Figure 3S. 18 Handheld Sky-laser beam profile. A) Beam image in grey scale taken with the webcam. B) Beam profile calculated with ImageJ across image A. Inset: laser beam shape on an infrared sensor with the rectangular shape of the beam shown in yellow. C) Surface plot of the beam profile (from A) generated using ImageJ.

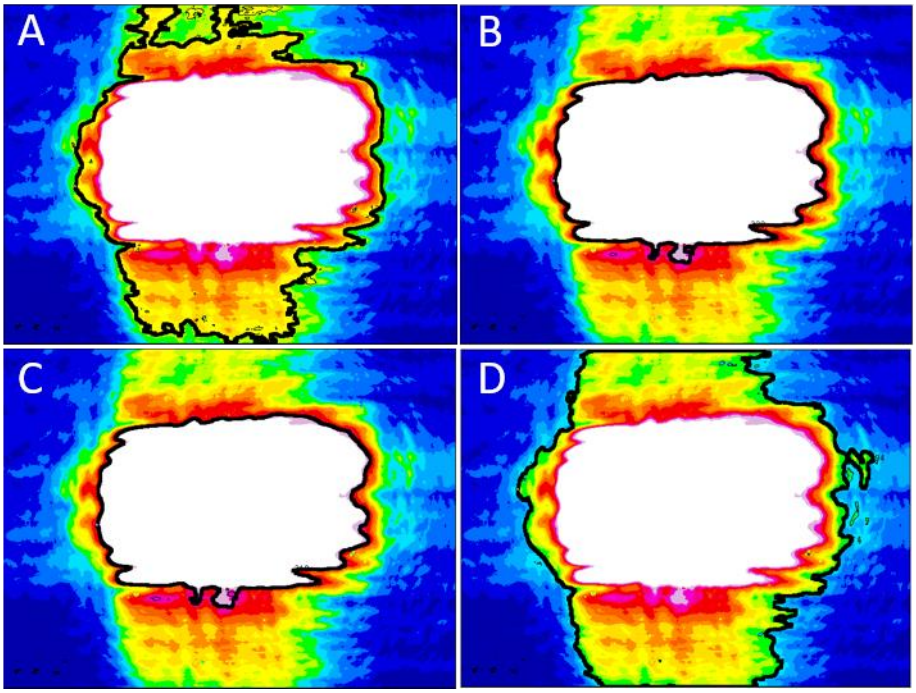

Figure 3S. 19 Different power intensity isolines of the 980 nm Sky-laser beam. Images were generated using ImageJ from picture A and analyzed with the contour plotter plugin. Isolines at A) 50 % (HPBW), B) 86.6 % ($1/e^2$), C) 86 % (D86), and D) 37% (1/e), intensity of the maximum beam power.

The area inside the isolines on Figure 3S.19 was calculated using ImageJ. Four different criteria were used to define the cross-sectional area to calculate the power densities. The half-power beam width (HPBW) is the cross-section area where the power is at 50% of the beam maximum intensity. $1/e^2$ is the cross-section area where the maximum intensity of the beam drops 13.5% ($1/e^2$). D86 in the cross-sectional area where the intensity of the beam is 86%. 1/e is the cross-sectional area where the intensity of the beam is 1/e (0.368) times the maximum intensity. The power of the laser was 0.8 W, measured using a laser power and energy meter (Solo P/E, Gentec-E). The power densities at different percentages of the maximum intensity of the beam are reported on Table S8.

Table 3S. 8 Power density of the Sky-laser 980 nm laser using different beam width definitions at different percent intensity of the maximum beam intensity.

Model	Intensity [%]	Area [cm^2]	Power Density [W/ cm^2]
1/e	37	0.060	13
HPBW	50	0.050	16
D86	86	0.029	28
$1/e^2$	86.5	0.029	28

3.6.13 Liquid Chromatography- Mass Spectrometry (LC-MS)

AZO-lipid mass analysis was performed using a Agilent Technologies time-of-flight liquid chromatography-mass spectrometer (TOF LC/MS) operating in positive mode electrospray ionization (ESI). The column used was Atlantis dC18, 2.1 x 50 mm, 3 □m particle size from Waters. The eluents used were water and acetonitrile both containing 0.1% of formic acid. The gradient used ranged from 70% to 95% acetonitrile over 8 min for a total run of 20 min. The flow rate was of 0.5 mL min^{-1}.

3.6.14 Nuclear Magnetic Resonance (NMR)

Characterization of the AZO-lipid synthesized was done using proton and phosphorous NMR (^{1}H-NMR) (^{31}P-NMR) using a 500 MHz Varian VNMRS-500 in deuterated chloroform. The chemical shifts are reported in parts per million (ppm) and referenced to tetramethylsilane (TMS) signal for ^{1}H-NMR. The multiplicity is given as s = singlet, d = doublet, t = triplet, q = quartet and m = multiplet.

3.6.15 Transmission Electron Microscopy (TEM)

The micrographs of $LiYF_4$:Tm^{3+}/Yb^{3+} UCNPs were collected using a Jeol JEM-2100F microscope operating at 200 kV capable of imaging resolution of 0.1 nm. Samples were prepared by dropping sample solutions (1 mg/mL in toluene) onto a 300-mesh Formvar/carbon coated copper grid (3 mm in diameter) followed by the evaporation of the solvent.

3.6.16 X-Ray Powder Diffraction (XRPD)

The patterns for $LiYF_4$: Tm^{3+}/Yb^{3+} UCNPs were collected at room temperature using a Scintag XDS-2000 diffractometer equipped with a Si(Li) Peltier-cooled solid state detector, CuKα source at a generator power of 45 kV and 40 mA, divergent beam (2 mm and 4 mm) and receiving beam slits (0.5 mm and 0.2 mm). Scan range was set from 15-90° 2θ with a step size of 0.02° and a count time of 2 sec. A quartz zero background insert disk was used as sample holder.

3.6.17 Attenuated total reflection (ATR-FTIR)

The surface modification of the nanoparticle with AZO-lipid was characterized using ATR-FTIR. The samples were dried under vacuum prior to the analysis. The ATR-FTIR measurements were carried out using a Nicolet iS5 FT-IR spectrometer with a Thermo Scientific iD5 diamond ATR and equipped with Omnic software v.9. Analysis is carried out using a 4 cm^{-1} resolution and a scan count of 100.

3.6.18 UV-visible Absorption Spectroscopy

UV-visible absorption spectra of AZO-lipid, AZO-UCNPs in a mixture of propylene glycol and ethanol (1:1) and AZO-SLB-UCNPs and AZO-SLB-UCNPs with embedded Nile red in 5mM HEPES buffer were placed in 1 cm path-length, 100 µL quartz cuvette (Hellma® Analytics, QS). The absorption spectra were recorded using a Cary 100 Bio UV-Vis spectrophotometer. For the measurements as function of irradiation time with 980 nm excitation, a portable 980 nm laser (0.8 W) from Sky-laser was used. The laser was chopped at 4 kHz using a 30 slot optical chopper blade controlled by a SR540 chopper controller from Stanford Research Systems Inc. The samples were placed in the spectrophotometer only after excitation with the 980 nm laser. A handheld UV lamp at 365 nm (UVGL-58, from UVP LLC) 6 W Hg lamp with power density 1.2 mW/cm^2 was used for experiments involving UV irradiation.

3.6.19 Inductively Coupled Plasma Mass Spectrometry (ICP-MS)

ICP-MS measurements were performed to determine the nanoparticles concentration after the surface modification with the supported lipid bilayer, AZO-lipid and embedded Nile red. The samples were analyzed using an Agilent 7500ce ICP-MS equipped quartz Scott-type spray chamber, an off-axis Omega lens ion focusing, an octopole reaction system with a quadrupole mass spectrometer analyzer operated at 3MHz.

3.6.20 Upconversion Photoluminescence Spectroscopy

The upconversion visible emission spectra of the oleate-$LiYF_4$:Tm^{3+}/Yb^{3+}, AZO-lipid-UCNPs, SLB-UCNPs and AZO-SLB-UCNPs were obtained upon 980 nm excitation, using a Coherent 6-pin fiber-coupled F6 series 980 nm laser diode (power of 450 mW), coupled to a 100 µm (core) fiber. For the upconversion studies, the samples (concentrations between 1- 0.24 mg/mL in HEPES buffer and a mixture of propylene glycol and ethanol 1:1) were placed in 1 cm path-length quartz cuvettes (Hellma® Analytics, QS). The upconverted UV and blue emissions were collected at right angle with respect to the incident beam and subsequently dispersed by a Spex Minimate 1⁄4 m monochromator and detected with an Oriel 70680 photomultiplier tube. A

preamplifier, model SR440 Stanford Research Systems, processed the photomultiplier signals and a gated photon counter model SR400 Stanford Research Systems data acquisition system was used as an interface between the computer and the spectroscopic hardware. The signal was recorded under computer control using the Stanford Research Systems SR465 software data acquisition/analyzer system.

3.6.21 Photoluminescence Decays

Photoluminescence decays of oleate-$LiYF_4$:Tm^{3+}/Yb^{3+} and AZO-lipid-UCNPs (in a 1:1 mixture of propylene glycol and ethanol) and SLB-UCNPs and AZO-SLB-UCNPs (in 5 mM HEPES, pH 7.4) were measured using a 365 ± 13 nm bandpass filter (Semrock) on a time-resolved fluorescence plate reader from Edinburgh Instruments equipped with a 2 W 980 nm laser from Changchun New Industries and a PM-1 laser modulator box from Edinburgh Instruments for controlled pulsed excitation (100 Hz). For all samples, volumes were 150 μL and concentrations were 100 μg/mL. FAST software (Edinburgh Instruments) was used for multi-exponential decay (and rise) time fitting.

3.6.22 Fluorescence Spectroscopy

Fluorescence spectra of Nile red in methanol and SLB-UCNPs and AZO-SLB-UCNPs with embedded Nile red in 5mM HEPES buffer were placed in 1 cm path-length, 100 μL quartz cuvette (Hellma® Analytics, QS). The fluorescence intensity was recorded using a Cary Eclipse Fluorescence Spectrophotometer using 553 nm excitation. For the measurements as function of irradiation time with 980 nm excitation, a portable 980 nm laser (0.8 W) from Sky-laser was used. The laser was chopped at 4 kHz using a 30 slot optical chopper blade controlled by a SR540 chopper controller from Stanford Research Systems Inc. The samples were placed in the spectrophotometer only after excitation with the 980 nm laser.

3.7 Author's notes and significance of this paper

This publication explored the development of a dynamic, multifunctional supported lipid bilayer at the surface of $LiYF_4:Tm^{3+}/Yb^{3+}$ upconverting nanoparticles that has been proposed as a nanoparticle-based drug delivery system. The supported lipid bilayer provides space for the encapsulation of small hydrophobic/lipophilic drugs and the physicochemical properties of the bilayer are photo-controlled *via* energy transfer from the nanoparticle through a photoswitchable azobenzene-derivative lipid. The energy transfer process mechanism between the nanoparticle and the azobenzene moiety was found to be mostly radiative *via* reabsorption of light with a minor component of FRET. Those findings are of great importance in the field because it is usually reported that the energy transfer process between donors and acceptors using Ln-UCNPs is *via* FRET without providing the lifetime measurements. The results in this publication showed that the FRET contribution is low, however the energy transfer from the nanoparticle to the acceptor in this case, the azobenzene moiety, was still possible *via* reabsorption of light. These results provide the fundamental understanding on how this NIR controlled nanoparticle-based drug delivery system works.

Inspired in the development of this dynamic multifunctional supported lipid bilayer we also proposed the development of a NIR photo-responsive hydrogel using azobenzene molecules and $LiYF_4:Tm^{3+}/Yb^{3+}$ upconverting nanoparticles. Hydrogels are a class of macroscopic materials that have gained attention in biomedical applications as matrices for bone and tissue regeneration that can be injectable or implantable to treat different diseases.[261] Supramolecular hydrogels (a class of hydrogels) have stimuli-responsive properties in which, through non-covalent interactions, the material can undergo a reversible gel-sol transition.[262] In collaboration with my lab colleague Gabrielle Mandl, we developed a novel NIR photo-responsive hydrogel by a guest-host interaction between azobenzene and β-cyclodextrin. The complexation between β-cyclodextrin and the *trans*-azobenzene is strong due to hydrophobic interactions with the internal cavity of β-cyclodextrin, however the *cis*-azobenzene does not associate with β-cyclodextrin due

to the higher polarity of this isomer.[263] The results of this project are published in RSC ChemCom journal as "*A NIR-responsive Azobenzene-based Supramolecular Hydrogel Using Upconverting Nanoparticles"* and are of great interest in the development of photo-responsive hydrogels for biological applications in which the use of UV light is undesirable.[264] We invite the reader to look into the publication for more details.

Both systems developed work though the photoswitching of the azobenzene moeties *via* energy transfer with of $LiYF_4:Tm^{3+}/Yb^{3+}$ upconverting nanoparticles. We proposed in Chapter 3 that the energy transfer mechanism was mostly through reabsorption of light with a minor contribution of FRET. We explaind trhough the chapter that the low FRET component could be due to the distance-dependence between the Tm^{3+} ions (core ions *vs*. surface ions) and the azobenzene moiety and possibly due to low quantum yields of the UV and blue emissions of $LiYF_4:Tm^{3+}/Yb^{3+}$. Driven by the curiosity to determine the quantum yield values of $LiYF_4:Tm^{3+}/Yb^{3+}$, the subsequent chapter presents the first multicenter study on the absolute upconversion quantum yields, and provides the first quantum yield values for $LiYF_4:Tm^{3+}/Yb^{3+}$ upconverting nanoparticles.

Chapter 4

Absolute Upconversion Quantum Yields of Blue-emitting $LiYF_4:Yb^{3+},Tm^{3+}$ Upconverting Nanoparticles

Publish as:

Michael S. Meijer,[1] Paola A. Rojas-Gutierrez,[2] Dmitry Busko,[3] Ian A. Howard,[3,4] Florian Frenzel,[5] Christian Würth,[5] Ute Resch-Genger,[5] Bryce S. Richards,[3,4] Andrey Turshatov,[3] John A. Capobianco,[2]* Sylvestre Bonnet[1]*

RSC Physical Chemistry Chemical Physics. **2018**, *35* (20), 22556–22562.

[1]Leiden Institute of Chemistry, Leiden University, Gorlaeus Laboratories, P.O. Box 9502, 2300 RA Leiden, The Netherlands; [2]Department of Chemistry and Biochemistry, and Centre for NanoScience Research, Concordia University, Montreal, Quebec, H4B 1R6, Canada; [3]Institute of Microstructure Technology, Karlsruhe Institute of Technology, Hermann-von-Helmholtz-Platz 1, 76344 Eggenstein-Leopoldshafen, Germany; [4]Light Technology Institute, Karlsruhe Institute of Technology, Engesserstrasse 13, 76131 Karlsruhe, Germany; [5]Federal Institute for Materials Research and Testing (BAM), Division Biophotonics, Richard-Willstätter-Straße 11, 12489 Berlin, Germany.

4.1 Abstract

The upconversion quantum yield (Φ_{UC}) is an essential parameter for the characterization of the optical performance of lanthanoid-doped upconverting nanoparticles (UCNPs). Despite its nonlinear dependence on excitation power density (P_{exc}), it is typically reported only as a single number. Here, we present the first measurement of absolute upconversion quantum yields of the individual emission bands of blue light-emitting $LiYF_4:Yb^{3+},Tm^{3+}$ UCNPs in toluene. Reporting the quantum yields for the individual emission bands is required for assessing the usability of UCNPs in various applications that require upconverted light of different wavelengths, such as bioimaging, photocatalysis and phototherapy. Here, the reliability of the Φ_{UC} measurements is demonstrated by studying the same batch of UCNPs in three different research groups. The results show that whereas the total upconversion quantum yield of these UCNPs is quite high — typically 0.02 at a power density of 5 $W \cdot cm^{-2}$ — most of the upconverted photon flux is emitted in the 794 nm upconversion band, while the blue emission band at 480 nm is very weak, with a much lower quantum yield of $\sim 6 \times 10^{-5}$ at 5 $W \cdot cm^{-2}$. Overall, although the total upconversion quantum yields of $LiYF_4:Yb^{3+},Tm^{3+}$ UCNPs seems satisfying, notably for NIR bioimaging, blue-light demanding phototherapy applications will require better-performing UCNPs with higher blue light upconversion quantum yields.

4.2 Introduction

Lanthanoid-doped upconverting nanoparticles (UCNPs) have attracted much attention over the last two decades as a result of their wide range of potential applications in bio-imaging and biosensing,[248,265–267] drug delivery,[268] phototherapy,[269–272] optical thermometry,[273–275] photocatalysis,[276–278] photovoltaics,[279] or security.[280] These nanomaterials show multiple sharp emission bands in the visible region of the spectrum upon sequential absorption of two or more near-infrared (NIR) photons, a non-linear process known as photon upconversion (UC). Typically, UCNPs have a crystalline fluoride host lattice, such as $NaYF_4$, doped with one or more lanthanoid ions. Most commonly, Yb^{3+} ions, capable of absorbing NIR light around 980 nm, are used as sensitizers, while secondary dopants, *e.g.* Er^{3+}, Tm^{3+}, or Ho^{3+} ions, are introduced in the crystal lattice as emitting activators, depending on the desired emission wavelength(s).[281–283] Compared to other upconverting systems, such as triplet-triplet annihilation upconversion (TTA-UC), UCNPs show long (ms) luminescence lifetimes, high photostability, insensitivity towards molecular oxygen, and no photoblinking.[284,285] In bio-imaging and phototherapy the use of NIR excitation is highly beneficial as it eliminates background fluorescence and reduces scattering, with the advantage of increased penetration depth of the excitation light.[72]

Initially, the main drawbacks of UCNPs were their low absorption cross-section and low internal upconversion photoluminescence quantum yields (Φ_{UC}); high excitation power densities (P_{exc} > 20 W·cm^{-2}) were often required to effectively trigger photochemical reactions using UCNPs.[286] In response to this shortcoming, a multitude of innovative strategies have been developed to increase the brightness of UCNPs, such as the application of core-shell structures or decoration of the surface with dyes to increase light absorption.[241,287–289] As a result of these efforts, 10- to 500-fold enhancement of the luminescence intensity has been reported, which appears to bring UCNPs to the efficiency level of other UC systems, such as those based on triplet-triplet annihilation upconversion (TTA-UC) that typically require P_{exc} on the level of mW·cm^{-2}.[290–292] Yet still, the daily practice requires several W·cm^{-2} of NIR light to obtain significant effects in phototherapy using UCNPs, in particular when large amounts of blue or UV

light are required. The aim of this collaborative paper was to investigate where this apparent discrepancy comes from; for example, why do systems containing UCNPs that show ~ 2% overall Φ_{UC} still require long irradiation times (> 2 h) and high P_{exc} to trigger blue-light sensitive photoreactions?

For a long time, most studies have focused on reporting upconversion intensities relative to other batches of UCNPs prepared in the same research laboratory. The broad range (from the UV to the NIR) and anti-Stokes nature of UCNP emission render the determination of quantum yields relative to a reference, such as an organic dye, very difficult,[293] thereby eliminating the method commonly used for the determination of the quantum yields of molecular dye solutions or dispersions of semiconductor quantum dots.[294] Furthermore, the lack of upconverting reference materials makes it *a priori* difficult to compare upconverting quantum yield values reported by different laboratories. Recently, the number of studies involving absolute measurements of Φ_{UC} has increased, in particular for Er- or Ho-doped UCNPs. This provided not only a few benchmark values, but also shone light upon the effect of excitation power density, particle size, and shell coating on the upconversion quantum yield.[295–304] To the best of our knowledge, the highest upconversion quantum yields for UCNPs were reported for 40-nm $LiLuF_4:Yb^{3+},Er^{3+}$ UCNPs (Φ_{UC} = 0.050) and $LiLuF_4:Yb^{3+},Tm^{3+}$ UCNPs (Φ_{UC} = 0.072).[305] However, even when absolutely measured Φ_{UC} values are provided, the methodologies for determining them are not always identical, and Φ_{UC} values are not seldom given as a single number without specific mention of the power density used for the measurement – probably for the sake of simplicity.

Whilst some studies reported on the relative intensities of thulium(III) emission lines,[273,306,307] these studies did not provide absolute Φ_{UC} values. Furthermore, as the NIR emissions in Tm-doped materials are known to be multiple orders of magnitude more intense than the blue emissions,[283,308,309] the efficiency of the blue emission bands cannot be deduced from their overall Φ_{UC},[310] and thus remains essentially unknown. This situation, coupled to the lively discussions within the European COST Action 1403 on upconverting materials, encouraged us to assess the Φ_{UC} of the individual upconversion bands of $LiYF_4:Yb^{3+},Tm^{3+}$

UCNPs. $LiYF_4$ was selected as it has been proposed as a very efficient host lattice for Tm-based UC nanomaterials, but its efficiency had not yet been studied with absolute methods.[67] In order to also assess the challenges and factors governing the reliability of such measurements, we independently determined the Φ_{UC} of the UCNPs in three European research groups (in Leiden, Karlsruhe, and Berlin) using absolute integrating sphere setups of different complexity. We discuss herein the setups, methodologies, and data from the three groups, to identify which parameters must be controlled for providing accurate and reliable Φ_{UC} values. The effects of power density, temperature, and excitation wavelength on the Φ_{UC} values are also discussed.

4.3 Results and Discussion

The tetragonal $LiYF_4$:Yb^{3+},Tm^{3+} (25% Yb^{3+}, 0.5% Tm^{3+}) UCNPs were synthesized as reported following a two-step thermal decomposition procedure.[67,236] Using transmission electron microscopy (TEM) it was shown that these oleate-capped UCNPs have a diamond-like morphology with an average size of 87 ± 9 nm along the long diagonal and 50 ± 4 nm along the short diagonal. A second batch of $LiYF_4$ nanoparticles was synthesized without the lanthanoid dopants. These undoped nanoparticles showed a morphology and size (87 ± 6 nm by 48 ± 3.5 nm) similar to the doped UCNPs, and served as a blank sample for some of the Φ_{UC} determinations (*vide infra*). Powder X-ray diffraction (XRD) spectra, TEM images and size distributions are shown in the Supporting Information (SI; Figure 4S.1–4S.3). Under NIR light excitation the UC emission spectrum of the Tm-doped UCNPs is clearly dominated by an emission band around 794 nm (**Figure 4.1**). This emission stems mainly from the thulium $^3H_4 \rightarrow {}^3H_6$ transition, with a small contribution from the $^1G_4 \rightarrow {}^3H_5$ transition. In addition, several blue and red Tm-based emission features are present, most notably around 451 nm ($^1D_2 \rightarrow {}^3F_4$), 480 nm ($^1G_4 \rightarrow {}^3H_6$), and 649 nm ($^1G_4 \rightarrow {}^3F_4$). These emissions bands are caused by three- and four-photon upconversion processes, and are multiple orders of magnitude less intense than the 794 nm emission band, resulting predominantly from a two-photon process.

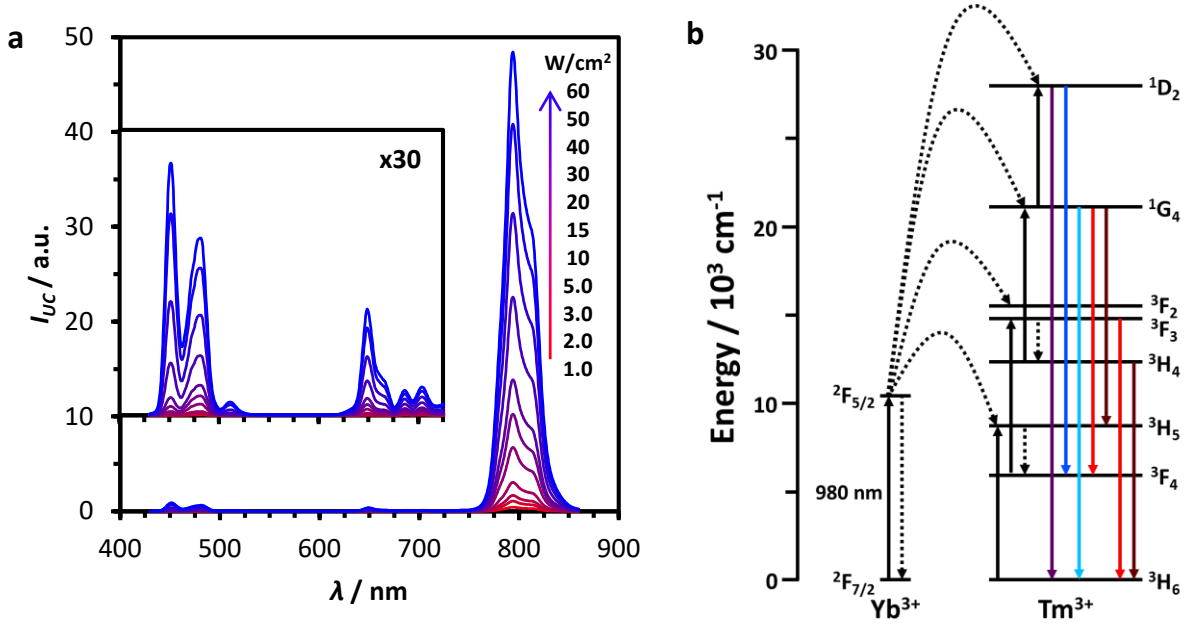

Figure 4. 1 (a) Emission intensity (I_{UC}) of $LiYF_4:Yb^{3+},Tm^{3+}$ (25%, 0.5%) UCNPs in toluene (10 mg·mL^{-1}) recorded in Leiden at various P_{exc} (1.0–60 W·cm^{-2}, λ_{exc} = 969 nm, T = 293 K). Comparable results were obtained in Karlsruhe and Berlin (Figure 4S.6). (b) Simplified energy level diagram depicting the energy transfer upconversion mechanism in Yb,Tm-based UCNPs, and the observed 4f–4f transitions.

The efficiency of the upconversion process in $LiYF_4:Yb^{3+},Tm^{3+}$ UCNPs in toluene dispersion was assessed by measuring Φ_{UC} absolutely, as defined by Equation 5.1.

$$\Phi_{UC} = \frac{number\ of\ photons\ emitted}{number\ of\ photons\ absorbed} = \frac{q_{p\text{-}em}}{q_{p\text{-}abs}}$$

In this equation, $q_{p\text{-}em}$ is the upconverted emission photon flux (in photons·s^{-1}) and $q_{p\text{-}abs}$ is the photon flux absorbed by the sensitizer species (in photons·s^{-1}). The assessment of Φ_{UC} was performed independently by the Leiden, Karlsruhe and Berlin research groups, using their respective standard methods and instrumentation. All three groups employed measurement

setups comprising of integrating spheres and fiber-coupled CCD spectrometers. Continuous wave (CW) laser diodes were used as the excitation source in all setups, although varying slightly in excitation wavelength. In Leiden, a 969 nm laser diode was employed, whereas excitation in Karlsruhe and Berlin was performed at 980 and 976 nm, respectively.

Measurements in Leiden were performed using the method described by Boyer and Van Veggel.[295] An sample of $LiYF_4$ UCNPs of similar size and morphology but without dopant was utilized as blank to ensure correction for the scattering properties of the UCNPs. In Karlsruhe, the three-measurement (3M) method previously described by De Mello *et al.* was used.[311,312] Rather than measuring a blank sample, in this method correction for scattering and the absorption of scattered photons is achieved by performing a series of three measurements, namely (a) irradiation of the empty sphere, (b) irradiation of the sample inside the sphere, but not directly in the path of the excitation beam (indirect excitation), and (c) irradiation of the sample inside the sphere and directly in the beam path (direct excitation). The measurement method utilized in Berlin is similar to the method employed in Leiden, and has been described previously.[297] In all systems, absorption and emission measurements were conducted separately in order to cope with the significant difference in intensity between the excitation light and the UC emission. Φ_{UC} values were measured at a high UCNP concentration (up to 40 mg·mL^{-1}) to ensure sufficient absorption (3–6%) of the excitation light. A full description of all three measurement setups is given in the SI (Sections 5.5.3–5.5.7), and the resulting Φ_{UC} values are reported in **Table 4.1** and 4S.1.

Table 4. 1 Upconversion photoluminescence quantum yields (Φ_{UC}) for $LiYF_4:Yb^{3+},Tm^{3+}$ UCNPs. Leiden data points for P_{exc} = 0.07, 1.0 and 50 W·cm^{-2} were measured relative to the absolute value at 5.0 W·cm^{-2}; T = 293 K. The full data sets are shown in Table 4S.1.

	P_{exc} [W.cm^{-2}]	$\Phi_{UC,451}$	$\Phi_{UC,480}$	$\Phi_{UC,649}$	$\Phi_{UC,794}$	$\Phi_{UC,total}$
Leiden [a]	0.07	n.d.	n.d.	n.d.	0.009(3)	0.009(3)
	1.0	6(2) × 10^{-7}	2.1(7) × 10^{-5}	1.1(4) × 10^{-5}	0.019(6)	0.019(6)
	5.0	7(2) × 10^{-6}	7(2) × 10^{-5}	3.3(10) × 10^{-5}	0.026(8)	0.026(8)
	50	2.3(7) × 10^{-4}	2.8(9) × 10^{-4}	1.4(5) × 10^{-4}	0.035(11)	0.035(11)
Karlsruhe [b]	0.20	n.d.	n.d.	n.d.	0.009(1)	0.009(1)
	0.95	n.d.	n.d.	n.d.	0.017(2)	0.017(2)
	5.0	1.6(10) × 10^{-5}	6.3(18) × 10^{-5}	n.d.	0.025(3)	0.025(3)
	13.5	4.5(14) × 10^{-5}	1.2(2) × 10^{-4}	6.7(19) × 10^{-5}	0.029(3)	0.029(3)
Berlin [c]	5.5	3.0 × 10^{-6}	4.48(2) × 10^{-5}	2.54(3) × 10^{-5}	0.0188	0.0189(5)
	48	9.08(5) × 10^{-5}	1.65(1) × 10^{-4}	8.48(5) × 10^{-5}	0.0255	0.0260(6)
	212	7.1 × 10^{-4}	5.15(3) × 10^{-4}	2.63 × 10^{-4}	0.0310	0.034(2)
	395	1.37 × 10^{-3}	8.78(2) × 10^{-4}	4.24(1) × 10^{-4}	0.0325	0.0371(7)

[a]λ_{exc} = 969 nm; [b]λ_{exc} = 980 nm; [c]λ_{exc} = 976 nm; n.d.: not determined. Uncertainties on the final digit are presented in parentheses.

The total internal upconversion photoluminescence quantum yield ($\Phi_{UC,total}$), determined by the integration of the UC spectra from 430 to 860 nm, at an excitation power density of 5.0 W·cm^{-2} was determined to be 0.026 ± 0.008 in Leiden, which is in good agreement with the value found in Karlsruhe (0.025 ± 0.003), and slightly above the value found in Berlin (0.0189 ± 0.0005, P_{exc} = 5.5 W·cm^{-2}). As explained above, it would be tempting to use $\Phi_{UC,total}$ as the sole way to quantify the efficiency of the UCNPs. However, in most applications only a fraction of the emission spectrum can be used. For example, if a dye or light-activated compound only absorbs blue light, then the 794 nm emission is not useful. Therefore, it can be much more relevant to report the Φ_{UC} values for the individual emission bands, as shown in Table 4.1 and 4S.1. For

example, at a P_{exc} of 5 W·cm^{-2}, the blue emission bands around 451 and 480 nm account only for 0.02–0.06% and 0.2–0.3% of the total UC emission, respectively, while 99.4% of the UC emission stems from the 2-photon NIR emission band around 794 nm. As a NIR-to-blue upconverting system at this P_{exc}, these UCNPs are thus best characterized by their blue emission quantum yield ($\Phi_{UC,blue}$) of 4.8−7.9 × 10^{-5}, rather than by their more encouraging total emission quantum yield ($\Phi_{UC,total}$) of 0.019–0.026.

Another difficulty in reporting and comparing upconversion quantum yields is that Φ_{UC} is highly dependent on the power density of the excitation beam, as upconversion is a non-linear multiphoton process. At low P_{exc}, the observed emission intensity, I_{UC}, is proportional to P^n, where P is the excitation power density, and n is the so-called slope factor, indicative of the number of photons involved in the process.[313,314] Hence, on a log-log plot, I_{UC} is proportional to n, where n is the slope of the linear least-squares curve through the data points (S.4 and 5S.7). As P_{exc} increases, saturation of the intermediate excited states occurs, and n slowly reduces to 1. As the upconversion quantum yield, Φ_{UC}, is proportional to $P^{(n-1)}$, it becomes constant at high P_{exc}; a regime often referred to as the saturation regime. Ideally, Φ_{UC} is measured in this saturated regime, where the value is maximal, and less dependent on P_{exc}. However, as Yb,Tm-doped UCNPs show multiple emission bands, each with their own power dependency, it is impossible to determine a single saturation point for the whole system. Furthermore, complete saturation of all these emission bands will not be observed unless extremely high P_{exc} are used (> 400 W·cm^{-2}). Such irradiation conditions are not available with all experimental setups, and generally speaking irrelevant for the intended applications of UCNPs, so that Φ_{UC} reported in many articles, including ours, is typically P_{exc}-dependent.

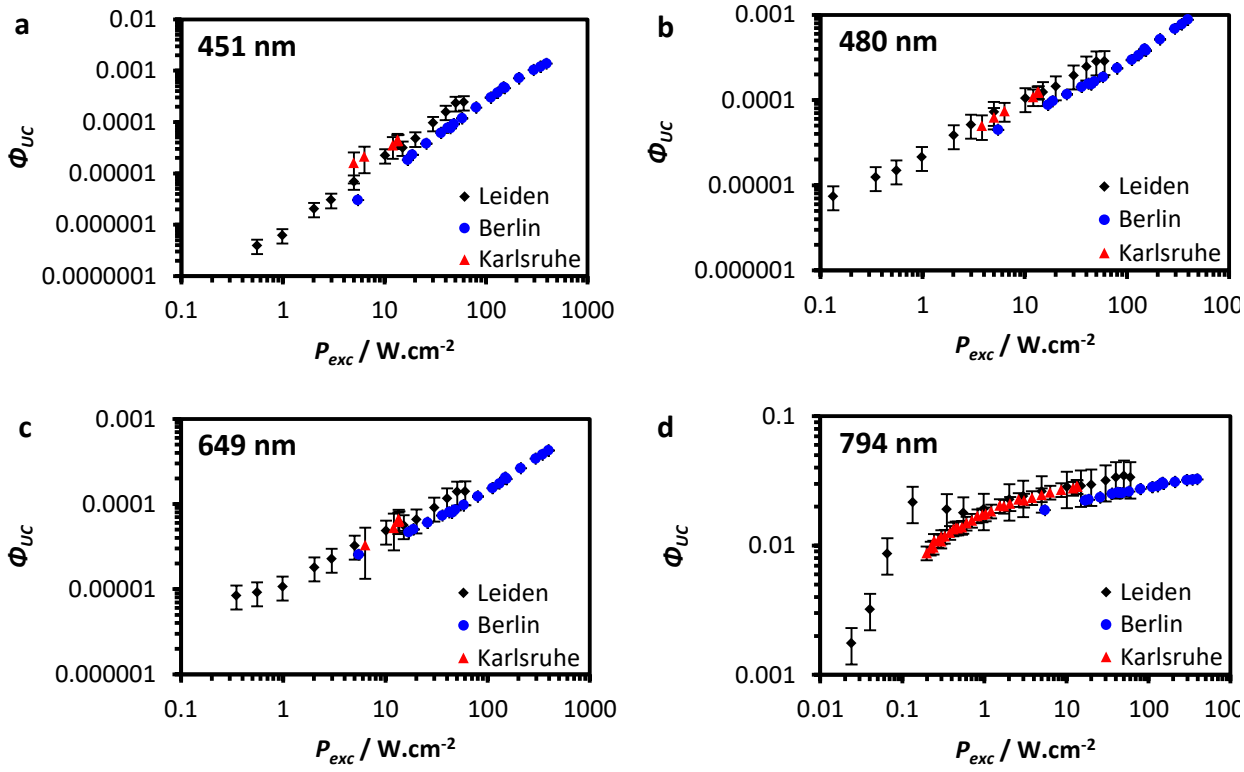

Figure 4. 2 P_{exc} dependence of Φ_{UC} of the thulium emission bands at (a) 451 nm, (b) 480 nm, (c) 649 nm, and (d) 794 nm in $LiYF_4:Yb^{3+},Tm^{3+}$ UCNPs in toluene, measured in Leiden (black diamonds), Berlin (blue circles), and Karlsruhe (red triangles).

The P_{exc} dependency of the upconverted emission of the $LiYF_4:Yb^{3+},Tm^{3+}$ UCNPs (**Figure 4.2** and Table 4.1) was examined for the four dominant emission bands. Using the three different spectroscopic setups, we were able to examine the P_{exc} dependence over three to four orders of magnitude, a larger range than typically possible for most setups. In Karlsruhe and Berlin, Φ_{UC} values were obtained absolutely, following the same protocol described above. In Leiden, limitations in the output power stability of the laser diode precluded direct Φ_{UC} measurements at high P_{exc}. Thus, the emission intensity was measured relative to the emission intensity at 5.0 W·cm^{-2}, and subsequently converted to a Φ_{UC} value using the absolute Φ_{UC}

values determined at 5.0 $W \cdot cm^{-2}$. Importantly, despite the differences in setup design and measurement protocols, the results from the different groups are in very good agreement.

In spite of this good overall agreement we did observe that the Φ_{UC} values obtained on the Berlin setup are typically somewhat lower than those obtained in Leiden and Karlsruhe (Figure 4.2). We believe that this may, in part, be attributed to the difference in beam profile used between the setups. Whereas the measurements in Berlin were performed using a top-hat beam profile that provides excellent homogeneity in space of the power density, the other setups employed more commonly used near-Gaussian beam profiles. As a result of the Gaussian beam profile, the P_{exc} is not homogeneous throughout the sample, and thus, at many points in the sample, it deviates from the reported average P_{exc}. Due to the multiphotonic nature of the upconversion process, these deviations lead to variations in upconversion efficiency throughout the sample that have been shown to potentially result in a higher apparent (i.e. spatially averaged) Φ_{UC}, especially in the unsaturated P_{exc}-regime.[297]

For the two-photon $^3H_4 \rightarrow {}^3H_6$ emission band at 794 nm, the onset of the saturation regime was observed around 0.1 $W \cdot cm^{-2}$, whereafter the slope factor n dropped from 2.5 to about 1.1 (Figure 4.2d, 4S.4 and 4S.7e). Contributions from the three-photon $^1G_4 \rightarrow {}^3H_5$ process to the 794-nm emission band may explain the fact that $n > 2.0$ for low P_{exc}, as well as the incomplete saturation ($n > 1.0$) at higher P_{exc}.[307] No saturation is found for the three major visible bands, and the slopes in Figure 2a-c are virtually constant. Close examination of the four-photon blue emission band at 451 nm ($^1D_2 \rightarrow {}^3F_4$) reveals that the slope is reduced from $n = 2.8$ to 2.0 as P_{exc} is increased to 395 $W \cdot cm^{-2}$ (Figure 4S.7e). This suggests that the first excited thulium state is saturated, but also indicates that the higher excited states in the thulium ions involved are far from saturation. Similarly, the three-photon emission features around 480 nm ($^1G_4 \rightarrow {}^3H_6$) and 649 nm ($^1G_4 \rightarrow {}^3F_4$), both show a slope factor of 1.6, that changes relatively little over the studied P_{exc} range. As P_{exc} in this study was limited to 395 $W \cdot cm^{-2}$, no saturation values for $\Phi_{UC,451}$, $\Phi_{UC,480}$, and $\Phi_{UC,649}$ can be given. Instead, in Table 4.1 and Figure 4.2, Φ_{UC} for these emission bands are given for various values of P_{exc}. Additionally, the lifetime of the downconverted Yb^{3+} emission at 998 nm ($^2F_{5/2} \rightarrow {}^2F_{7/2}$) was measured in Karlsruhe (Figure

4S.12), and, as expected, was found to decrease upon an increase of P_{exc}, from 0.69 ms (P_{exc} = 10 W·cm^{-2}) to 0.38 ms (P_{exc} = 220 W·cm^{-2}).

Although the relative contributions of the visible emission bands increase for higher P_{exc}, at 395 W·cm^{-2} the 794 nm emission still makes up 88% of the total emission, with the blue emission bands accounting for 2.4% (480 nm) and 3.7% (451 nm) of the total emission, respectively. The maximal Φ_{UC} measured for the total emission is 0.0371(7) (Berlin, P_{exc} = 394.9(6) W·cm^{-2}), while all the individual visible light emission showed quantum yields between 1×10^{-4} and 1.4×10^{-3} (Figure 4.2 and 4S.7, Table 4.1 and 4S.1). In comparison, Mousavi *et al.* recently reported a $\Phi_{UC,794}$ of 0.0039 at 14 W·cm^{-2} for $NaYF_4$:Yb^{3+},Tm^{3+} (25%, 0.3%) UCNPs, which makes it tempting to conclude that the $LiYF_4$ host lattice used in this work ($\Phi_{UC,794}$ = 0.022–0.029 at 15 ± 2 W·cm^{-2}) is more efficient, at least for NIR-to-NIR upconversion.[293] However, the use of a different solvent (cyclohexane *versus* toluene), different dopant concentrations, and the smaller size of the $NaYF_4$ particles (ø = 32 nm) preclude a direct comparison between the two values.

When high power densities are used for obtaining blue light, the temperature of the upconverting sample may rise. Thus, the effect of temperature on the relative UC efficiency was examined, performing emission spectroscopy in a temperature-controlled cuvette holder. Although an optimum of the $\Phi_{UC,total}$ was found around 18 °C ($\Phi_{UC,total}$ = 0.026), and upon heating the sample to 60 °C a 10% reduction in the overall emission was observed, no strong dependence of $\Phi_{UC,total}$ on the temperature was found (Figure 4S.11 and Table 4S.2). Thus, the temperature is of minor importance for upconversion quantum yields of $LiYF_4$:Yb^{3+},Tm^{3+} UCNPs, compared to the influence of other factors such as the surface coating or the nature of the solvent.[236,299]

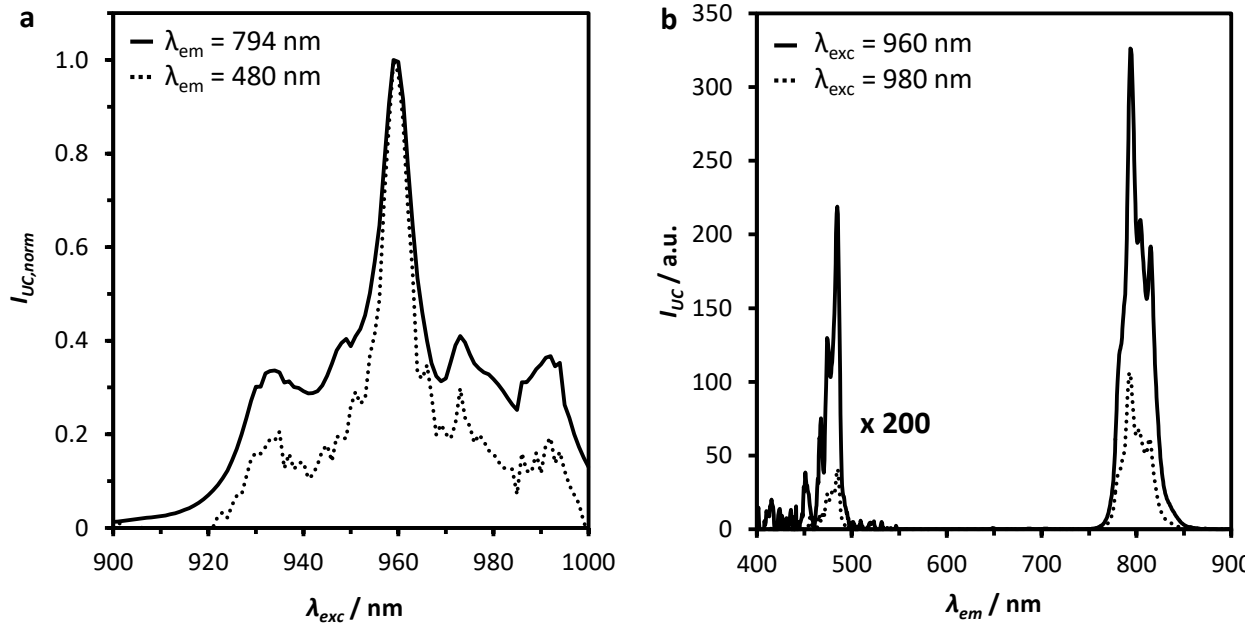

Figure 4. 3 (a) Normalized excitation spectrum recorded in Karlsruhe of $LiYF_4:Yb^{3+},Tm^{3+}$ UCNPs in toluene (10 mg·mL^{-1}) for 480 nm and 794 nm emission bands. Spectra were corrected for the small difference in P_{exc}, assuming n = 1.1 (794 nm) and 1.6 (480 nm). (b) Upconverted emission spectra recorded in Karlsruhe of $LiYF_4:Yb^{3+},Tm^{3+}$ UCNPs in toluene (10 mg·mL^{-1}) at various excitation wavelengths (P_{exc} = 4.11 W·cm^{-2} (960 nm), 4.15 W·cm^{-2} (980 nm)).

Finally, as the Φ_{UC} studies in Leiden and Karlsruhe were performed using different excitation wavelengths (969 and 980 nm, respectively (see Table 4.1)), also the influence of this parameter on the emission intensity and Φ_{UC} was assessed. **Figure 4.3a** depicts the integrated emission intensity of the NIR and blue emission bands as a function of excitation wavelength (excitation spectrum), which is in good agreement with the absorption spectrum of the $LiYF_4:Yb^{3+},Tm^{3+}$ UCNPs (Figure 4S.10). Only small differences in emission intensity can be observed between exciting at 969 and 980 nm. However, the sharp peak in the excitation spectrum in Figure 4.3a around 960 nm implies that the UC emission is far brighter at this excitation wavelength, compared to the conventional 980 nm excitation. An explanation of these

results can be found by looking at the fine structure of the $^2F_{7/2} \rightarrow {}^2F_{5/2}$ transition in Yb^{3+} ions. Under the influence of the crystal field, the Yb^{3+} energy levels split into a number of so-called Stark splitting levels (four and three levels for $^2F_{7/2}$ and $^2F_{5/2}$, respectively), resulting in several absorption bands corresponding to the $^2F_{7/2}(n=0) \rightarrow {}^2F_{5/2}(n=0',1',2')$ electronic transitions. The absorption between 970 nm and 990 nm is attributed to the $0 \rightarrow 0'$ transition, whereas the absorption bands near 960 nm and 930 nm correspond to the $0 \rightarrow 1'$ and $0 \rightarrow 2'$ transitions, respectively.[315] The relative intensity of these transitions is strongly influenced by the symmetry of the host lattice. Here, the tetragonal $LiYF_4$ host (scheelite structure) favors the $0 \rightarrow 1'$ transition, in contrast to the hexagonal $NaYF_4$ host, for which the $0 \rightarrow 0'$ transition is dominant. The preference towards the $0 \rightarrow 1'$ transition has been demonstrated before for $LiYF_4$ single crystals doped with Yb^{3+} ions.[315,316] Thus, in order to achieve maximal upconversion brightness, evaluation of the optimal excitation wavelength is crucial for every new host material. In the case of $LiYF_4$, the emission intensities of the NIR and blue UC bands increased considerably upon 960 nm excitation, by a factor of ~ 3 for the NIR emission and ~ 6 for the blue emission compared to 980 nm excitation at the used excitation power density (Figure 4.3b). Considering the good agreement between the excitation spectrum depicted in Figure 4.3a and the absorption spectrum in Figure 4S.10, we assume that the observed increase in UC emission intensity is caused by the increased absorption at 960 nm, rather than by a significant increase in Φ_{UC}.

4.4 Conclusions

In this work, we have presented the first multicenter absolute measurement of upconversion photoluminescence quantum yields (Φ_{UC}) of UCNPs, and provided the first Φ_{UC} values for $LiYF_4$:Yb^{3+},Tm^{3+} UCNPs. These measurements have been performed independently by three research groups, but using the same batch of nanomaterials. In spite of the quite different setups and methods used in the three labs, strikingly similar values were obtained, which underline that these measurements can give reproducible results not only when using state-of-the-art setups such as those available in Karlsruhe and Berlin, but also using relatively

inexpensive, modular spectroscopy setups such as the one in Leiden. Importantly, upconversion quantum yield values are given for the individual upconversion bands of $LiYF_4:Yb^{3+},Tm^{3+}$ UCNPs. By doing so we illustrate, as done recently for Yb,Er-doped UCNPs,[297,299,302] the strikingly large difference in intensity between the different emission bands of these UCNPs. Although Tm-doped UCNPs are usually described as blue-emitting UCNPs, Φ_{UC} of the blue emission bands are as low as 1×10^{-5} at 5 $W \cdot cm^{-2}$, while the NIR band at 794 nm has an excellent Φ_{UC} of ~ 0.02 at 5 $W \cdot cm^{-2}$. This discrepancy is especially important when selecting upconverting materials for different applications.[317] In security or bioimaging applications where the 794 nm emission is used, $\Phi_{UC,total}$ is a good measure for the efficiency of $LiYF_4:Yb^{3+},Tm^{3+}$ UCNPs, because the upconverted emission spectrum is strongly dominated by the 794 nm band. However, in phototherapeutic applications where only the blue thulium emission is used, for example in the activation of blue-light sensitive anticancer compounds,[235] the actual efficiency of these UCNPs is one to three orders of magnitude lower than $\Phi_{UC,total}$. Thus, reporting only the latter would give a misleading evaluation of the amount of excitation light needed to obtain a measurable photochemical effect via NIR-to-blue upconversion. The low efficiency of the blue upconverted emission in Tm-based UCNPs provides a good explanation why these systems are still difficult to apply in for example blue light-triggered phototherapy,[286] and justifies the need for further material research aimed at increasing the upconversion quantum yields of UCNPs in the blue region of the spectrum.

4.5 Supporting information

4.5.1 Nanoparticle synthesis (Experimental)

4.5.1.1 Materials and general methods

Thulium oxide (Tm_2O_3, 99.99+ %), ytterbium oxide (Yb_2O_3, 99.99%), yttrium oxide (Y_2O_3, 99.99+ %), trifluoroacetic acid (CF_3COOH, 99%), lithium trifluoroacetate (CF_3COOLi, 98%), oleic acid (technical grade, 90%), and 1-octadecene (technical grade, 90%) were all purchased from Sigma-Aldrich and were used without further purification. All other solvents were obtained from major chemical suppliers and used as received.

4.5.1.2 Synthesis of LiYF4:Yb^{3+},Tm^{3+} upconverting nanoparticles

$LiYF_4$:Tm^{3+},Yb^{3+} UCNPs were synthesized *via* thermal decomposition, which was comprised of a two-step process.[67,236] In the first step, a mixture of water/trifluoroacetic acid (10 mL, 1:1) was added to a 3-neck round-bottom flask containing Tm_2O_3 (0.0024 g, 6.25×10^{-6} mol, 0.5 mol% Tm^{3+}), Yb_2O_3 (0.1232 g, 3.13×10^{-4} mol, 25 mol% Yb^{3+}), and Y_2O_3 (0.2103 g, 9.31×10^{-4} mol). The cloudy solution was heated (80 °C) under reflux until it was clear. The resulting solution was then dried at 60 °C to form the trifluoroacetate lanthanide precursors. In the second step, CF_3COOLi (0.2999 g, 2.50×10^{-3} mol) was added to the dried precursor solids along with oleic acid (20 mL) and 1-octadecene (20 mL) and the mixture was degassed for 30 min at 120 °C. The temperature was increased at a rate of 10 °C·min^{-1} to 315 °C under an argon atmosphere. The reaction mixture was maintained at 315 °C under stirring for 60 min and under an argon atmosphere. After cooling to room temperature, absolute ethanol was added to the reaction mixture to precipitate the $LiYF_4$:Tm^{3+},Yb^{3+} UCNPs, which were subsequently isolated *via* centrifugation (3000 rpm, 15 min). The pellet was washed with a 1:3 hexane/ethanol mixture twice to remove any impurities. After purification, the sample was stored and shipped as a solid under a layer of ethanol.

4.5.1.3 Synthesis of $LiYF_4$ undoped nanoparticles

$LiYF_4$ undoped nanoparticles were synthesized by the same method as described for the doped nanoparticles in section 5.5.0, using only Y_2O_3 (0.2103 g, 9.31×10^{-4} mol) in the first step to form the yttrium trifluoroacetate precursor instead of a mixture with thulium and ytterbium oxides. The second step of the synthesis was followed as described in section 5.5.1.2.

4.5.2 Nanoparticle Characterization

4.5.2.1 X-ray Powder Diffraction (XRPD)

Figure 4.S1 shows the X-Ray powder diffraction (XRPD) of the oleate-capped $LiYF_4:Tm^{3+},Yb^{3+}$ UCNPs, undoped oleate-capped $LiYF_4$ UCNPs and the calculated standard of the JCPDS pattern. The peak positions correspond to the reported pattern of tetragonal $LiYF_4$ (JCPDS no. 81-2254). The patterns for both doped and undoped $LiYF_4$ nanoparticles were collected at room temperature using a Bruker D2 Phaser XRD System equipped with a LYNXEYE one-dimensional X-ray diffraction detector, based on Bruker AXS' compound silicon strip technology. Scan range was set from 15 – 90° 2θ with a step size of 0.5° and a count time of 1 s. A PMMA background insert disk was used as sample holder.

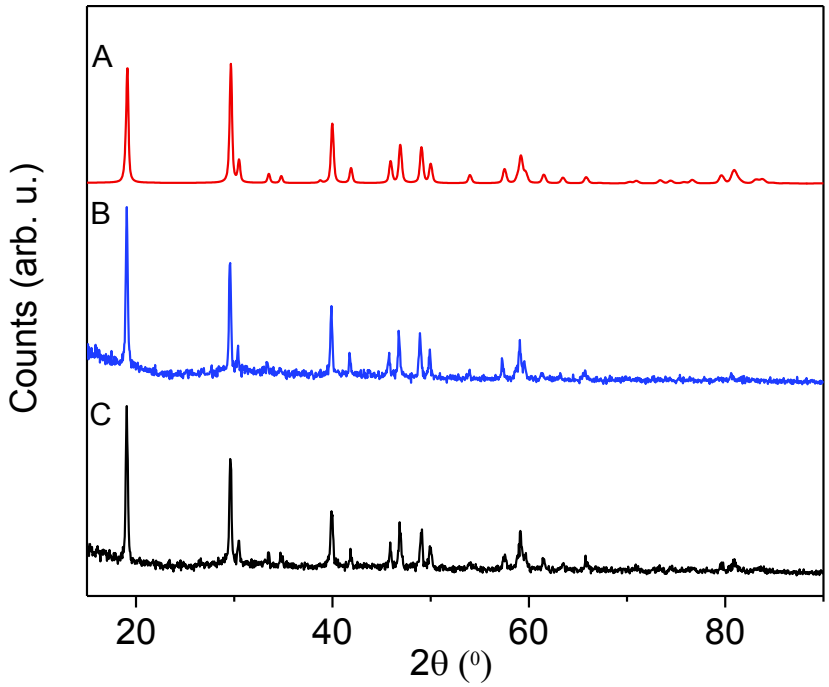

Figure 4S. 1 X-ray powder diffraction analysis of (A) calculated line pattern for tetragonal $LiYF_4$ shown for reference (JCPDS 81-2254), (B) undoped oleate capped $LiYF_4$ nanocrystals and (C) oleate-capped $LiYF_4$:Tm^{3+},Yb^{3+}nanocrystals.

4.5.2.2 Transmission electron microscopy (TEM) and size distribution

Transmission electron microscopy was used to evaluate the morphology and particle size distribution of the prepared nanoparticles. 300 particles of doped and undoped nanoparticles were evaluated to obtain the size distribution. The oleate-capped $LiYF_4$:Tm^{3+},Yb^{3+} UCNPs showed a diamond-like morphology with an average size of 87 nm (± 9 nm) long diagonal length and a small diagonal length of 50 nm (± 4 nm). The oleate-capped $LiYF_4$ NPs showed a diamond-like morphology with an average size of 87 nm (± 6 nm) long diagonal length and a small diagonal length of 48 nm (± 3.5 nm). The micrographs were collected using a Jeol JEM-2100F microscope operating at 120 kV capable of imaging resolution of 0.1 nm. Samples were prepared by dropping sample solutions (1 $mg.mL^{-1}$ in toluene) onto a 300-mesh Formvar/carbon coated copper grid (3 mm in diameter) followed by the evaporation of the solvent.

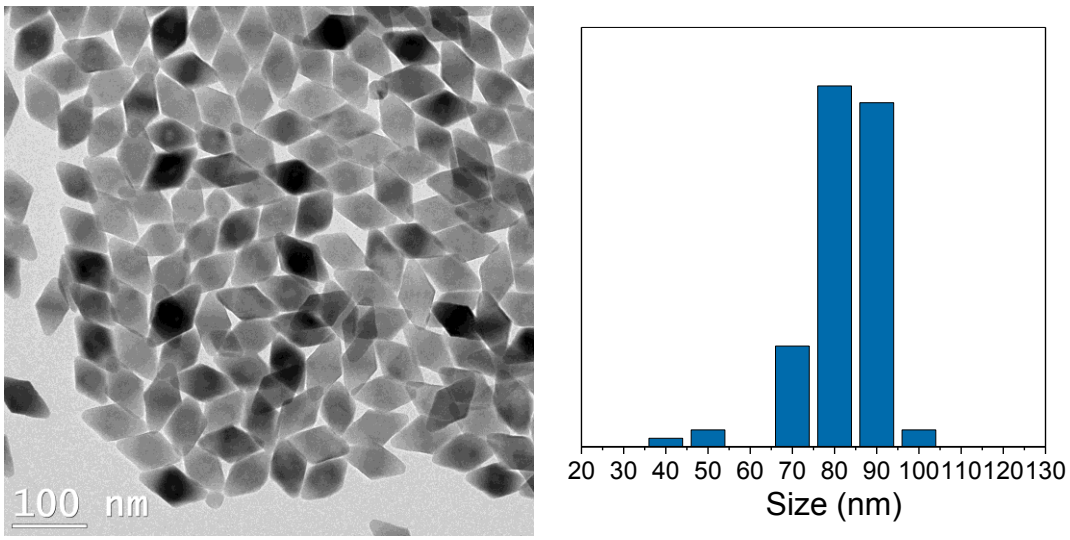

Figure 4S. 2 Transmission electron micrograph (left) of oleate-capped $LiYF_4:Tm^{3+},Yb^{3+}$ UCNPs (1 mg·ml^{-1} in toluene). Histogram (right) of the particle size distribution obtained with respect to the long diagonal 87 ± 9 nm from the TEM images (average of ~ 300 nanocrystals).

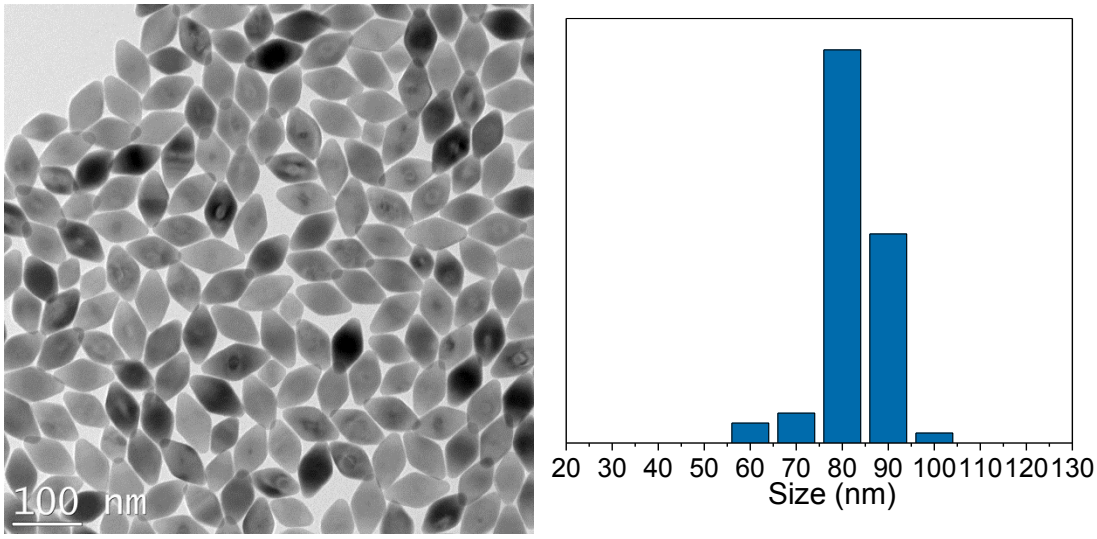

Figure 4S. 3 Transmission electron micrograph (left) of undoped oleate-capped $LiYF_4$ UCNPs (1 mg·ml^{-1} in toluene). Histogram (right) of the particle size distribution obtained with respect to the long diagonal 87 ± 6 nm from the TEM images (average of ~ 300 nanocrystals).

4.5.3 Absolute quantum yield determination using the Leiden setup

4.5.3.1 Experimental setup

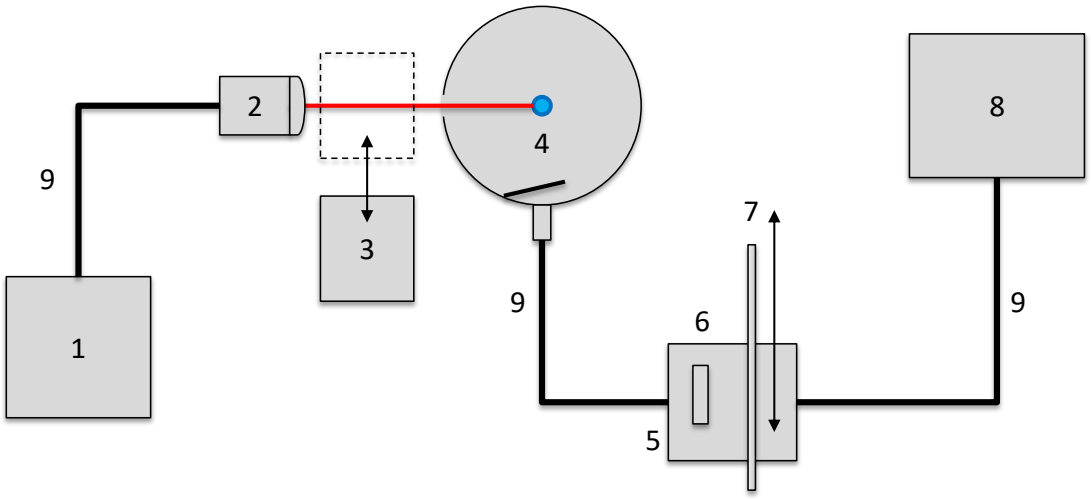

Scheme 4S. 1 Setup used for absolute quantum yield measurements. (1) laser source, (2) collimating lens, mechanical iris and focusing lenses, (3) power meter (adjustable in position), (4) integrating sphere with sample tube in the center, (5) filter holder, (6) 875-nm short pass filter that can be installed or removed, (7) variable neutral density filter that can be installed or removed, (8) CCD spectrometer, (9) optical fibers.

The integrating sphere setup used for determining the quantum yield of upconversion in Leiden in depicted in Scheme 4S.1 The excitation source was a fiber-coupled CW 969-nm diode laser (MDL-H-980-3W, CNI Laser, Changchun, China), coupled into a 200-µm multimode optical fiber, leading to a collimating lens (F220SMA-980, Thorlabs). After collimation, the light passed a mechanical iris, and two lenses (f = 10 and 5 cm) to produce a ca. 2 mm beam (*vide infra*) with 200 mW optical power (P_{exc} = 5.0 W·cm^{-2}). The excitation power was measured using a S310C thermal sensor connected to a PM100USB power meter (Thorlabs). A PTFE-coated AvaSphere-30-IRRAD integrating sphere (30 mm diameter, reflectance > 98%), fitted with three ports

(entry, exit and sample port), and an AvaSpec-ULS2048L StarLine CCD spectrometer were obtained from Avantes (Apeldoorn, The Netherlands). The integrating sphere and spectrometer were calibrated together using an Avalight-HAL-CAL-ISP30 NIST traceable calibration lamp from Avantes (9.5% relative uncertainty vs. NIST standard), so that the observed intensities are expressed as a photon flux (mol photons·s^{-1}·m^{-2}). The filter holder was fabricated by our own mechanical department, and held a NDL-25C-4 variable neutral density filter (Thorlabs) or an OD4 875 nm short pass filter (Edmund Optics, York, United Kingdom, part no. 86-106, $T_{430\text{-}860\ nm} \approx 97.3 \pm 1.3\%$). An Avalight-DHc (Avantes) deuterium-halogen lamp was used as a white light source for the determination of the transmission functions of the filters used. The spectra were recorded with Avasoft 8.5 software from Avantes, and further processed with Microsoft Office Excel 2010 and Origin Pro 9.1 software.

4.5.3.2 Quantum yield calculation method

The upconversion photoluminescence quantum yield (Φ_{UC}) is defined by (4S.1):

$$\Phi_{UC} = \frac{number\ of\ upconverted\ photons}{number\ of\ low\text{-}energy\ photons\ absorbed} = \frac{q_{p\text{-}em}}{q_{p\text{-}abs}} \qquad \textbf{(4S.1)}$$

Here, $q_{p\text{-}em}$ is the upconverted emission photon flux (in photons·s^{-1}) and $q_{p\text{-}abs}$ is the photon flux absorbed by the sensitizer species (in photons·s^{-1}).

Φ_{UC} can be calculated by (4S.2):

$$\Phi_{UC} = \frac{\int_{\lambda_1}^{\lambda_2} I_{UC}(\lambda) d\lambda}{q_{p\text{-}abs}} \qquad \textbf{(4S.2)}$$

Here, $I_{UC}(\lambda)$ is the spectral luminescence intensity (in photons·s^{-1}·nm^{-1}), and λ_1 and λ_2 are the low- and high-wavelength boundaries, respectively, of either the entire upconverted emission spectrum, or the 4f-4f transition of interest. $q_{p\text{-}abs}$ is determined by subtracting the spectral light

intensity of the excitation source that has passed through the sample ($I_{exc\text{-}sample}$, in photons·s^{-1}·nm^{-1}) from the spectral light intensity of the excitation source that has passed through a blank sample ($I_{exc\text{-}blank}$, in photons·s^{-1}·nm^{-1}), and by integrating over the excitation wavelength range λ_3 to λ_4, see (4S.3). The blank sample consisted of a dispersion of undoped $LiYF_4$ UCNPs of a similar size, dispersed in the same solvent at the same concentration as the sample. Due to the lack of photo-active dopants, it did not absorb at the excitation wavelength.

$$q_{p-abs} = \int_{\lambda_3}^{\lambda_4} (I_{exc\text{-}blank}(\lambda) - I_{exc\text{-}sample}(\lambda))d\lambda \qquad \textbf{(4S.3)}$$

(4S.2) can then be expressed as (4S.4):

$$\Phi_{UC} = \frac{\int_{\lambda_1}^{\lambda_2} I_{UC}(\lambda)d\lambda}{\int_{\lambda_3}^{\lambda_4} (I_{exc\text{-}blank}(\lambda) - I_{exc\text{-}sample}(\lambda))d\lambda} \qquad \textbf{(4S.4)}$$

The spectrometer and the integrating sphere were calibrated so that the observed intensities are directly proportional to the photon flux, i.e. $I(\lambda) \propto [\text{mol of photons} \cdot \text{s}^{-1} \cdot \text{nm}^{-1}]$. Therefore, integrating these values over the relevant wavelength regions directly provided the flux of photons that arrived at the spectrometer.

Because the intensity of the upconverted light is relatively low compared to that of the exciting laser source the absorption and emission of the sample cannot be measured at the same time. In other words, the laser light saturates the spectrometer, which prevents upconversion to be measured simultaneously. To circumvent this problem, the absorption was measured using a neutral density filter with known transmittance (typically $F_{attn} \approx 0.0015$, i.e., ~ 99.85% attenuation). This filter was placed between the integrating sphere and the spectrometer to measure the absorbed photon flux. For the measurement of the upconverted emission, this filter was replaced by an OD4 short pass filter (< 875 nm) to remove the excitation light. The attenuation factor F_{attn} was averaged over the wavelength range of the laser (950–990 nm).

Additionally, the intensity of the upconverted emission measured was corrected for the minimal absorbance of this light by the shortpass filter used. This was performed by dividing the upconversion luminescence intensity by the transmission curve *T(λ)* of the short pass filter in the wavelength range of the upconverted light. As the shortpass filter strongly absorbed light with a wavelength shorter than 430 nm, this prevented the measurement of any ultraviolet emission by this method. The accordingly corrected equation for Φ_{UC} is (4S.5):

$$\Phi_{UC} = \frac{\int_{\lambda_1}^{\lambda_2} \left(\frac{I_{UC}(\lambda)}{T(\lambda)}\right) d\lambda}{\int_{\lambda_3}^{\lambda_4} \frac{I_{exc\text{-}blank}(\lambda) - I_{exc\text{-}sample}\ (\lambda)}{F_{attn}} d\lambda} \equiv \frac{q_{p\text{-}em}}{q_{p\text{-}abs}} \qquad \textbf{(4S.5)}$$

4.5.3.3 Experimental procedure

For each measurement, two UCNP dispersions (4% w/v in toluene, ~ 500 µL) were prepared and dispersed thoroughly by sonication: one blank sample, containing undoped $LiYF_4$ nanoparticles, and the sample of interest, containing $LiYF_4$:Yb^{3+},Tm^{3+} nanoparticles. An aliquot (50 µL) of each sample was loaded into specially designed measurement tubes that were made of a quartz EPR-tube bottom (± 7 cm length) fused to a NS-14 glass connector (± 2 cm length), at the top of which a septum was adapted. The tube precisely fitted into a hole made in the integrating sphere, and was suspended in the center of the sphere, in the focal point of the excitation laser beam.

The laser diode was allowed to warm up for 10 minutes prior to the experiment to guarantee a stable output. The measurements were always performed in the same order, i.e. (1) absorption measurement of the blank, (2) absorption measurement of the sample, and (3) emission measurement of the sample. In this way, the neutral density filter is not moved between the measurement of the blank and sample, ensuring equal attenuation of the non-absorbed excitation light for both spectra. Equally, the sample is not moved between the measurement of its

absorption and emission. For the absorption measurements, the neutral density filter was placed in the filter, and replaced by the 875 nm shortpass filter for the emission measurement. All three spectra were recorded for a period of 10 minutes and subsequently averaged, in order to correct for minor instabilities (< 1.5%) in the intensity of the incident laser beam. These instabilities are a major contributing factor to the relative uncertainty in the reported quantum yield values. Integration of the emission bands was performed by fitting the emission bands with one or more Gaussian profiles, and integrating the area under these peaks. This treatment allowed deconvolution of the various emission bands, even though the emission data could only be recorded with a spectral resolution of 9 nm (slit size = 200 μm).

4.5.4 Relative excitation power dependence of the upconversion quantum yield (Leiden)

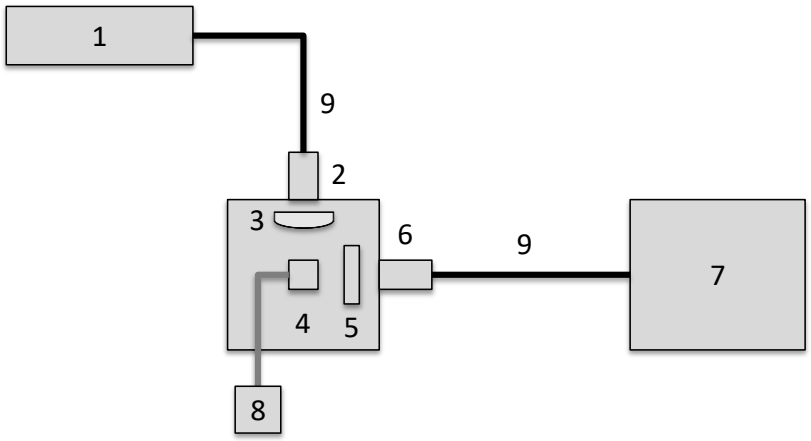

Scheme 4S. 2 Setup used for excitation power and temperature dependence measurements. (1) laser source, (2) collimating lens, (3) focusing lenses, (4) temperature-controlled cuvette holder, (5) 875-nm short pass filter, (6) double collimator, (7) CCD spectrometer, (8) thermocouple inserted into the sample, connected to a temperature logger (removed for power dependence measurements), (9) optical fibers.

Power dependence measurements were conducted with a custom-built setup shown in Scheme 4S.2. The excitation source was a fiber-coupled CW 969-nm diode laser (MDL-H-980-3W, CNI Laser, Changchun, China), coupled into a 200-μm multimode optical fiber, leading to a collimating lens (F220SMA-980, Thorlabs, Dachau, Germany). After collimation, the light passed a mechanical iris, and two lenses (f = 10 and 5 cm) to produce a ca. 2 mm beam (*vide infra*). The excitation power was measured using a S310C thermal sensor connected to a PM100USB power meter (Thorlabs). The focused beam passed through the center of a CUV-UV/VIS-TC temperature-controlled cuvette holder (Avantes, Apeldoorn, The Netherlands), typically set to 293.15 K. Temperature control was performed with the use of a TC-125 controller and T-app software from Quantum Northwest (Liberty Lake, WA, USA). The emission spectra were collected at a 90° angle with respect to the excitation beam. The emitted light passed through an OD4 875 nm short pass filter (Edmund Optics, York, United Kingdom, part no. 86-106) and a double collimator into an optical fiber, which led to an AvaSpec-ULS2048L StarLine CCD spectrometer obtained from Avantes. The spectrometer was calibrated using an Avalight-HAL-CAL-ISP30 NIST traceable calibration lamp from Avantes, so that the observed intensities are expressed as a photon flux (mol photons·s^{-1}).

Direct measurement of the quantum yield of the UCNPs at high excitation powers (> 10 W·cm^{-2}) was prohibited by the instability of the excitation laser, which was observed when the laser diode was used at such excitation powers for the prolonged amounts of time necessary for direct quantum measurements. Therefore, the power dependence of Φ_{UC} was estimated by measuring the upconverted emission in the temperature controlled cuvette holder setup (described above) at a range of power densities between 0.024 and 60 W·cm^{-2}, and scaling Φ_{UC} at 5.0 W·cm^{-2} with the ratio of the upconverted emission at P_{exc} = 5.0 W·cm^{-2} and the P_{exc} of interest by using Equation 4S.6:

$$\Phi_{UC}^{P} = \Phi_{UC}^{5.0\ W/cm2} * \frac{\int_{\lambda_1}^{\lambda_2} I_{UC}^{Pexc}(\lambda)d\lambda}{\int_{\lambda_1}^{\lambda_2} I_{UC}^{5.0\ W/cm2}(\lambda)d\lambda} \quad \textbf{(4S.6)}$$

The sample used for direct quantum yield measurements was diluted to a concentration of 10 mg·mL^{-1} in toluene. About 500 µL of this dispersion were placed in a 104F-QS semi-micro cuvette (Hellma Analytics, Müllheim, Germany). The cuvette was placed in the temperature-controlled cuvette holder and allowed to equilibrate for at least 2 minutes prior to starting the first measurement. Integration of the emission bands was performed by fitting the emission bands with one or more Gaussian profiles, and integrating the area under these peaks. This treatment allowed deconvolution of the various emission bands, even though the emission data could only be recorded with a spectral resolution of 9 nm (slit size = 200 µm).

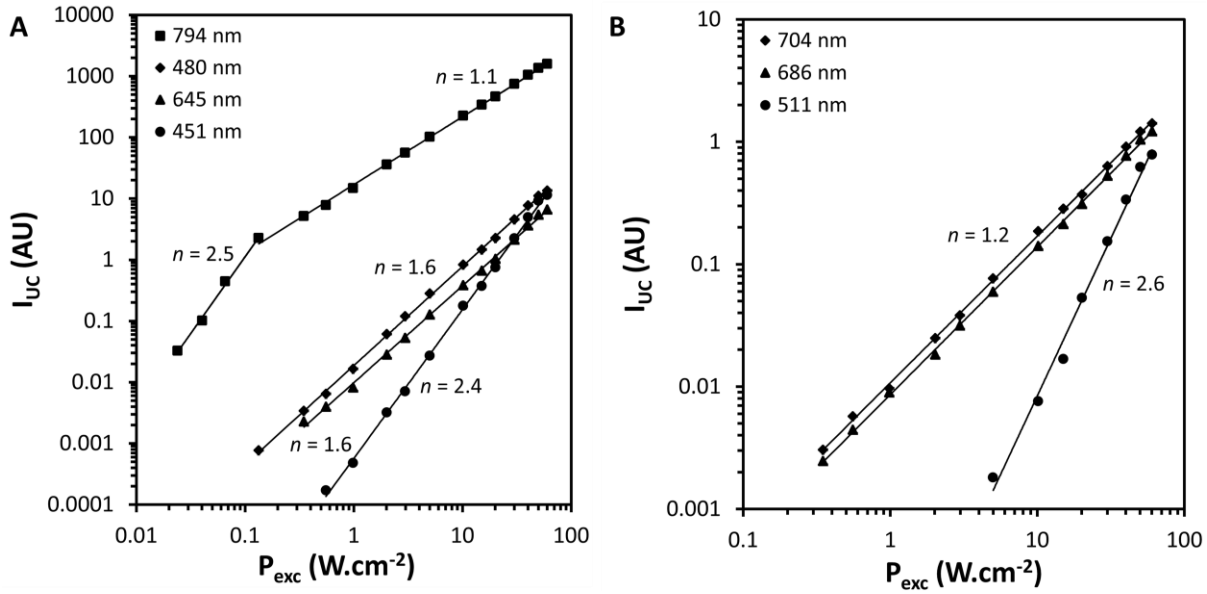

Figure 4S. 4 Excitation power dependence of the upconverted emission intensity I_{UC}, for the (a) major and (b) minor thulium emission bands in $LiYF_4:Tm^{3+},Yb^{3+}$ UCNPs in toluene as measured on the Leiden setup; λ_{exc} = 969 nm, T = 293 K, [UCNP] = 10 mg·mL^{-1}.

4.5.5 Leiden setup beam profiling

A beam profiler was used for measuring the beam diameters of the laser beams in the aforementioned setups and calculating the excitation power densities in $W.cm^{-2}$. The beam profiler consisted of a Trust Webcam Spotlight Pro, of which the front lens was pried off and replaced by NE510A (OD = 1) and NE520A (OD = 2) absorptive neutral density filters (Thorlabs). The focused laser beam, further attenuated using a variable neutral density filter (OD ≈ 2.8, NDL-25C-4, Thorlabs), was pointed directly on the photovoltaic chip of the webcam (4.80 mm wide and 3.60 mm high). Then, $1/e^2$ laser beam diameters in pixels were determined by Beams, an open source beam profiling software downloadable from http://ptomato.name/opensource/beams/beams.html. The beam diameter in millimeters was calculated by dividing the average beam diameter in pixels by the total number of horizontal pixels and multiplying this with the chip width (4.80 mm). Figure 4S.5 depicts an example output of the Beams software, in which the beam diameter of the laser beam was $\frac{277\text{ px}}{640\text{ px}} \times 4.80\text{ mm} = 2.08\text{ mm}$.

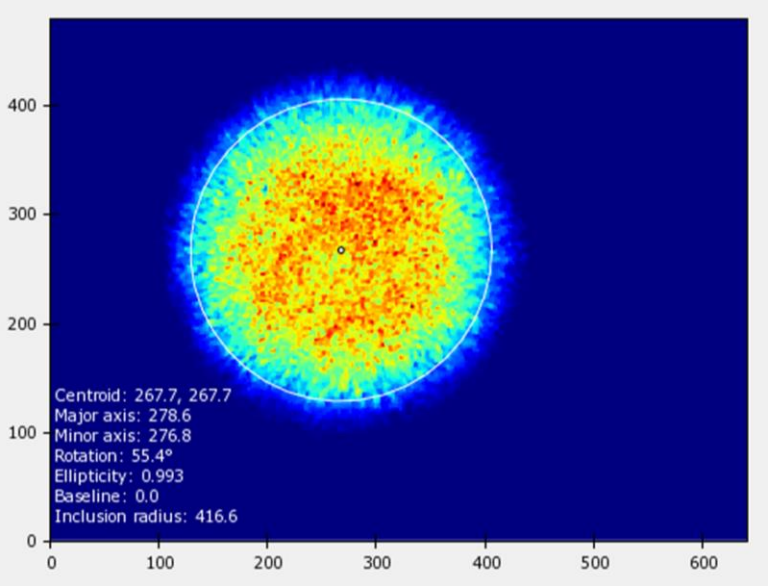

Figure 4S. 5 Leiden laser beam diameter (λ_{exc} = 969 nm) visualized by the beam profiling setup in combination with the Beams software package. Axes represent chip width and height in pixels. Colors represent light intensity in increasing order from blue to red.

4.5.6 Absolute upconversion quantum yield determination using the Karlsruhe setup

A CW 980 nm laser diode (L980P200, Thorlabs), mounted in a temperature stabilized mount (TCLDM9, Thorlabs) and driven by a laser diode controller (ITC4001, Thorlabs) was focused by a lens (focal length = 75 cm) and directed into an integrating sphere (Labsphere) with a diameter of 150 mm. The beam size on the sample, filled in a quartz cuvette with 5 mm optical path (Hellma Analytics), was measured with a scanning slit optical beam profiler (BP209, Thorlabs) to be equal to 0.9 × 1.3 mm (4σ). An optical fiber with a diameter of 1 mm (FP1000URT, Thorlabs) was used for the collection of the emission from the integrating sphere and to transfer this to the spectrometer (CCS200, Thorlabs). During the absorption measurement (measurement of the laser for direct and indirect excitation of the sample and empty sphere), short integration times, usually 20–50 times shorter than for UC detection, were used. All raw detected spectra were recalculated to give power spectra using an integration time value. The linearity of the signal versus the integration time of the CCD was controlled experimentally. The spectral response of the whole detection system was calibrated using a calibration lamp (HL-3plus-INT-CAL, Ocean Optics) and the correction was further applied to the power spectra. UCNP dispersions were prepared in a manner similar to described in the previous Section 4.3 by the Leiden group.

The quantum yield of upconversion (Φ_{UC}) was calculated according to the 3M procedure described in literature.[311,312] The formula for the calculation is given in Equation 4S.7:

$$\Phi_{UC} = \frac{PD - PI \cdot (1 - A)}{A \cdot ES} \qquad \textbf{(4S.7)}$$

where *PD* is the intensity of "photoluminescence direct" for the sample directly excited with the incident beam, *PI* is the intensity of "photoluminescence indirect", i.e. emission, caused by the diffusively reflected excitation radiation, first hitting the internal wall of the integrating sphere and then the sample, *ES* is the intensity measured for the "empty sphere" (without a sample). *A* is the absorption of the sample, which is calculated according to Equation 4S.8:

$$A = 1 - {}^{LD}/_{LI} \quad \textbf{(4S.8)}$$

Here, *LD* is the "laser direct" – intensity of the excitation source for direct excitation of the sample, and *LI* is the "laser indirect" – intensity of the excitation source for indirect excitation. The values are calculated from the measured spectral fluxes using Equation 4S.9 and 4S.10:

$$PD, PI = \int_{\lambda_1}^{\lambda_2} I_{PD,PI}(\lambda) d\lambda \quad \textbf{(4S.9)}$$

$$ES, LD, LI = \int_{\lambda_3}^{\lambda_4} I_{ES,LD,LI}(\lambda) d\lambda \quad \textbf{(4S.10)}$$

Here, λ_1 and λ_2 (and λ_3 and λ_4) are the low- and high-wavelength boundaries used for integration, respectively, of either the entire UC emission spectrum, or the excitation beam spectral profile. Because of the nonlinear intensity response of UC, the low absorption of the sample and a relatively low efficiency of UC, the PI is negligible for most of UC samples and is usually neglected for the subsequent calculations, simplifying the formula to:

$$\Phi_{UC} = \frac{PD}{A \cdot ES} \quad \textbf{(4S.11)}$$

4.5.7 Absolute upconversion quantum yield determination using the Berlin setup

The measurement procedure and the technical details of the homebuilt integrating sphere setup, which was used for the absolute quantum yield measurements done in Berlin have been previously described in M. Kaiser et al.[297] Briefly, P_{exc}-dependent Φ_{UC} values were obtained absolutely with an existing custom designed integrating sphere setup,[318] modified to meet the requirements of UC luminescence measurements. Its main parts are a highly stable 8 W 976 nm laser diode (wavelength stability < 0.3 nm, power stability < 0.1 %), collimating and focusing optics, and a laser clean filter, which is coupled via a 200 µm-sized optical fiber into a $BaSO_4$-

coated integrating sphere (diameter of 15 cm) equipped with a Si-CCD detection system. The intensity-weighted average emission wavelength of the laser diode was adjusted to match the Yb^{3+} absorption peak at 976.4 nm. To realize different beam profiles, lenses with focal lengths of 500 mm and 125 mm were integrated into the excitation light path, yielding a top-hat and a nearly Gaussian beam profile, respectively. For the measurements provided here, a top-hat beam profile was used. To enable precise tuning of the average P_{exc} for both beam shapes, two automated filter wheels equipped with reflective neutral density (ND) filters of known transmittance were placed between the laser diode and the integrating sphere.

Calibration of the integration sphere setup included calibration of the wavelength scale and range of linearity of the detection system following previously described procedures,[318–320] The wavelength-dependent spectral responsivity of the detection channel, including the integrating sphere, optical fiber, monochromator, and detector were characterized with a calibrated spectral radiance transfer standard (calibrated by the Physikalisch-Technische Bundesanstalt (PTB)) from 350–1050 nm using different bandpass filters. The spectral radiance transfer standard consists of a halogen lamp mounted inside an integrating sphere to guarantee a diffuse spectral radiance (Gigahertz-Optik GmbH). The reliability of the emission correction curve was controlled with the aid of the BAM spectral emission standards F003–F005.[321] The excitation beam profile reaching the sample and its power density were determined with a calibrated power meter (Gentec UP19K-1SS-H5-00).

Φ_{UC} was obtained from the directly measured number of emitted photons per number of absorbed photons at different P_{exc} considering solely emitted photons with $\lambda < 900$ nm (integration over all UC emission bands between 370 and 890 nm). For the detection of the scattered excitation light required for calculating the number of absorbed photons in Equation S1, the intense laser light was attenuated with an absorptive ND filter (attenuation factor of ca. 5600) to prevent detector saturation. With these filters, a P_{exc} range of 2 to 425 $W \cdot cm^{-2}$ can be covered for these UCNPs dispersed in toluene. For the determination of the incident photon flux mandatory for the calculation of the number of absorbed photons, the solvent employed for the

UCNP dispersion was used as a blank. The absorption of the UCNP samples in toluene was about 2% at the excitation wavelength of 980 nm. For the evaluation of the P_{exc}-dependent Φ_{UC}, the emission intensities I_{UC} (λ_{em}, P_{exc}) and the slope factors $n(P_{exc})$, we chose the following spectral regions: $^1D_2 \rightarrow {}^3F_4$: 433–462 nm, $^1G_4 \rightarrow {}^3H_6$: 462–500 nm, $^1I_6 \rightarrow {}^3F_3$: 505–516 nm, $^1G_4 \rightarrow {}^3F_4$: 610–675 nm, $^3F_2 \rightarrow {}^3H_6$: 675–720 nm, $^3F_3 \rightarrow {}^3H_6$: 675–720 nm and $^3H_4 \rightarrow {}^3H_6$: 720–890 nm. To obtain the number of emitted photons, the measured blank and spectrally corrected luminescence spectra/intensity values and spectral UC intensities were multiplied with λ/hc_0 to obtain spectral photon fluxes ($s^{-1} \cdot m^{-3}$) and luminescence quantum yields.

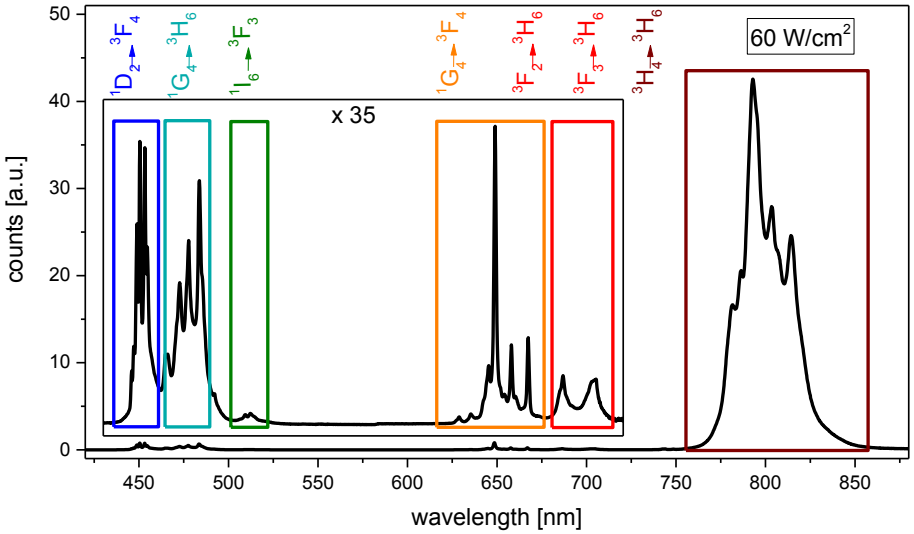

Figure 4S. 6 Upconversion emission spectra with color-encoded emission bands of the optical transitions $^1D_2 \rightarrow {}^3F_4$ (451 nm), $^1G_4 \rightarrow {}^3H_6$ (480 nm), $^1I_6 \rightarrow {}^3F_3$ (511 nm), $^1G_4 \rightarrow {}^3F_4$ (645 nm), $^3F_2 \rightarrow {}^3H_6$ (686 nm), $^3F_3 \rightarrow {}^3H_6$ (704 nm) and $^3H_4 \rightarrow {}^3H_6$ (794 nm), measured at P_{exc} = 60 W·cm^{-2}.

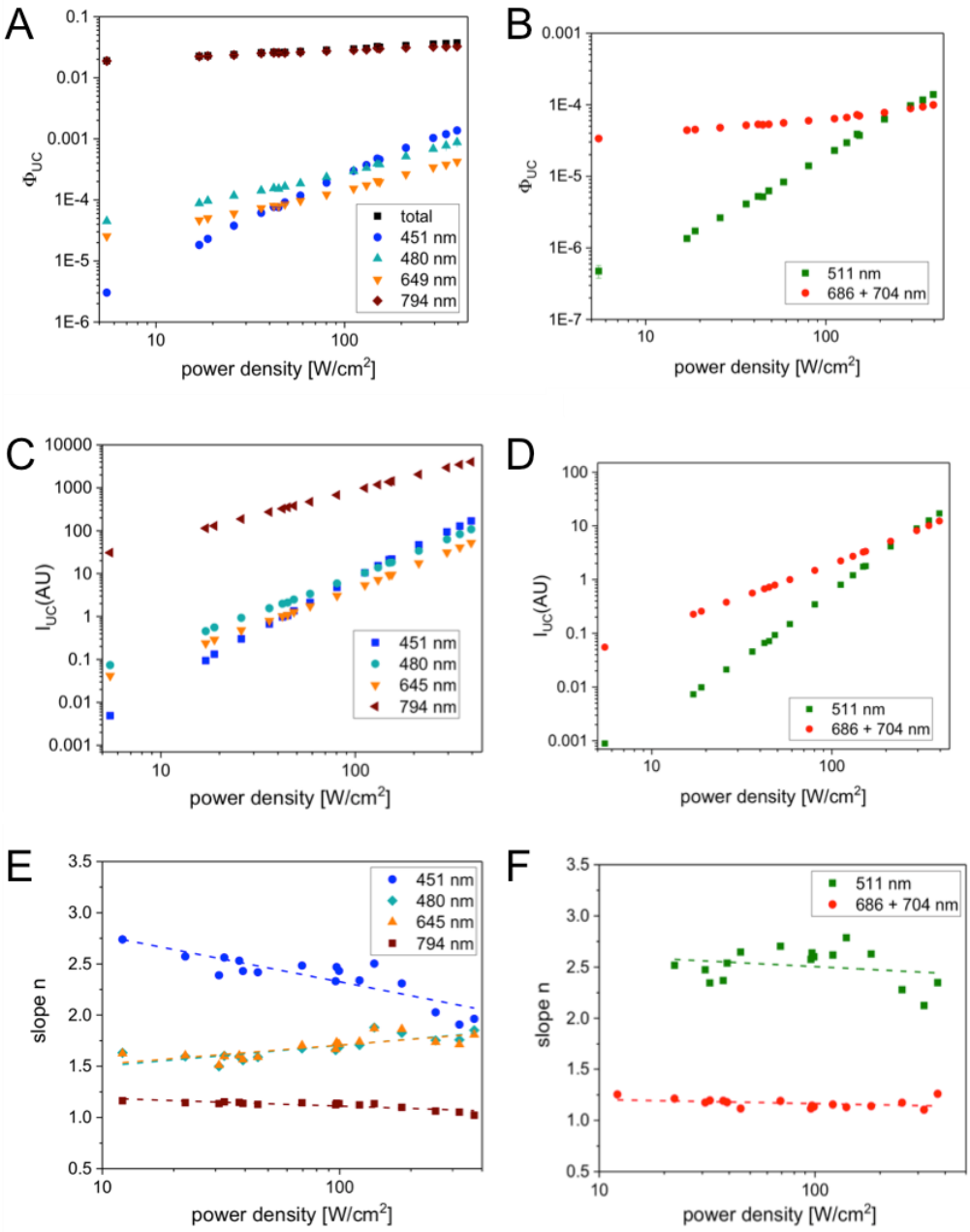

Figure 4S. 7 Panel A and B: Excitation power dependence of the absolute quantum yield Φ_{UC} of the major (A) and minor (B) emission bands. Panel C and D: power density dependent relative emitted intensities I_{UC} of the major (C) and minor (D) emission bands. Panel E and F: corresponding power density-dependent slope factors n.

4.5.8 Excitation power dependence of the upconversion quantum yield (comparison of data from all three groups)

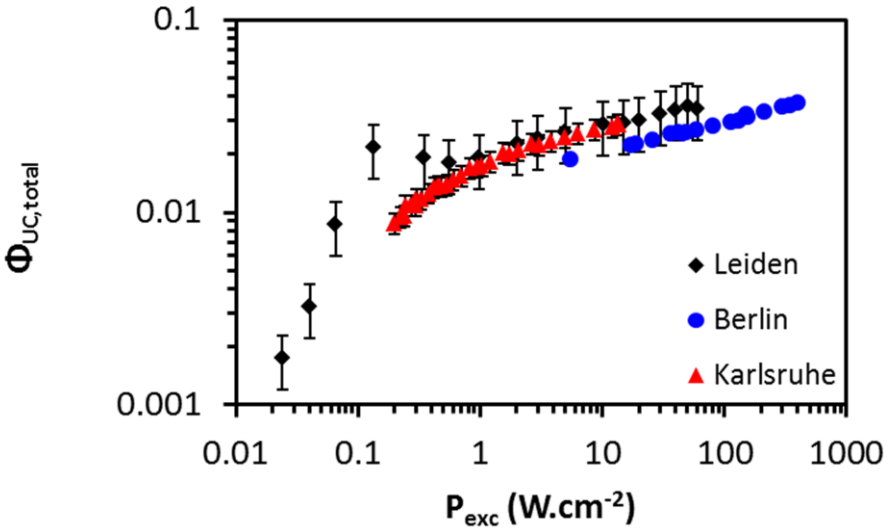

Figure 4S. 8 P_{exc} dependence of $\Phi_{UC,total}$ of $LiYF_4:Tm^{3+},Yb^{3+}$ UCNPs in toluene, measured in Leiden (black diamonds), Berlin (blue circles), and Karlsruhe (red triangles).

Table 4S. 1 Upconversion photoluminescence quantum yields ($\Phi_{UC,\lambda}$) for $LiYF_4:Tm^{3+},Yb^{3+}$ UCNPs in toluene. The data points from Leiden were measured relative to the value at 5.0 $W \cdot cm^{-2}$ at 293 K.

P_{exc} [$W.cm^{-2}$]		$\Phi_{UC,451}$	$\Phi_{UC,480}$	$\Phi_{UC,511}$	$\Phi_{UC,649}$	$\Phi_{UC,686+704}$	$\Phi_{UC,794}$	$\Phi_{UC,total}$
Leiden a)	0.024	n.d.	n.d.	n.d.	n.d.	n.d.	$1.8(5) \times 10^{-3}$	$1.8(5) \times 10^{-3}$
	0.04	n.d.	n.d.	n.d.	n.d.	n.d.	$3.2(10) \times 10^{-3}$	$3.2(10) \times 10^{-3}$
	0.07	n.d.	n.d.	n.d.	n.d.	n.d.	$9(3) \times 10^{-3}$	$9(3) \times 10^{-3}$
	0.13	n.d.	$7(2) \times 10^{-6}$	n.d.	n.d.	n.d.	0.021(7)	0.021(7)
	0.35	n.d.	$1.2(4) \times 10^{-5}$	n.d.	$8(3) \times 10^{-6}$	$2.0(6) \times 10^{-5}$	0.019(6)	0.019(6)
	0.56	$4(1) \times 10^{-7}$	$1.5(5) \times 10^{-5}$	n.d.	$9(3) \times 10^{-6}$	$2.4(7) \times 10^{-5}$	0.018(6)	0.018(6)
	0.98	$6(2) \times 10^{-7}$	$2.1(7) \times 10^{-5}$	n.d.	$1.1(3) \times 10^{-5}$	$2.4(8) \times 10^{-5}$	0.019(6)	0.019(6)
	2.0	$2.0(6) \times 10^{-6}$	$4(1) \times 10^{-5}$	n.d.	$1.8(6) \times 10^{-5}$	$2.7(9) \times 10^{-5}$	0.023(7)	0.023(7)
	3.0	$3(1) \times 10^{-6}$	$5(2) \times 10^{-5}$	n.d.	$2.3(7) \times 10^{-5}$	$3.0(9) \times 10^{-5}$	0.024(8)	0.024(8)
	5.0	$7(2) \times 10^{-6}$	$7(2) \times 10^{-5}$	$5(2) \times 10^{-7}$	$3.3(10) \times 10^{-5}$	$3.5(11) \times 10^{-5}$	0.026(8)	0.026(8)
	10	$2.2(7) \times 10^{-5}$	$1.0(3) \times 10^{-4}$	$1.0(3) \times 10^{-6}$	$5(2) \times 10^{-5}$	$4.1(13) \times 10^{-5}$	0.028(9)	0.029(9)
	15	$3.2(10) \times 10^{-5}$	$1.2(4) \times 10^{-4}$	$1.4(4) \times 10^{-6}$	$6(2) \times 10^{-5}$	$4.2(13) \times 10^{-5}$	0.029(9)	0.029(9)
	20	$5(2) \times 10^{-5}$	$1.4(5) \times 10^{-4}$	$3(1) \times 10^{-6}$	$7(2) \times 10^{-5}$	$4.3(14) \times 10^{-5}$	0.030(9)	0.030(9)
	30	$1.0(3) \times 10^{-4}$	$1.9(6) \times 10^{-4}$	$7(2) \times 10^{-6}$	$9(3) \times 10^{-5}$	$4.9(16) \times 10^{-5}$	0.032(10)	0.032(10)
	40	$1.6(5) \times 10^{-4}$	$2.5(8) \times 10^{-4}$	$1.1(3) \times 10^{-5}$	$1.2(4) \times 10^{-4}$	$5.4(17) \times 10^{-5}$	0.034(11)	0.034(11)
	50	$2.3(7) \times 10^{-4}$	$2.8(9) \times 10^{-4}$	$1.6(5) \times 10^{-5}$	$1.4(4) \times 10^{-4}$	$5.7(18) \times 10^{-5}$	0.035(11)	0.035(11)
	60	$2.4(8) \times 10^{-4}$	$2.9(9) \times 10^{-4}$	$1.7(5) \times 10^{-5}$	$1.4(4) \times 10^{-4}$	$5.6(18) \times 10^{-5}$	0.034(11)	0.034(11)
Karls-ruhe b)	0.20	n.d.	n.d.	n.d.	n.d.	n.d.	$9(1) \times 10^{-3}$	$9(1) \times 10^{-3}$
	0.27	n.d.	n.d.	n.d.	n.d.	n.d.	0.011(1)	0.011(1)
	0.33	n.d.	n.d.	n.d.	n.d.	n.d.	0.012(1)	0.012(1)
	0.38	n.d.	n.d.	n.d.	n.d.	n.d.	0.013(2)	0.013(2)
	0.48	n.d.	n.d.	n.d.	n.d.	n.d.	0.014(2)	0.014(2)
	0.54	n.d.	n.d.	n.d.	n.d.	n.d.	0.014(2)	0.014(2)
	0.61	n.d.	n.d.	n.d.	n.d.	n.d.	0.015(2)	0.015(2)
	0.70	n.d.	n.d.	n.d.	n.d.	n.d.	0.016(2)	0.016(2)
	0.95	n.d.	n.d.	n.d.	n.d.	n.d.	0.017(2)	0.017(2)
	1.04	n.d.	n.d.	n.d.	n.d.	n.d.	0.018(2)	0.018(2)
	1.21	n.d.	n.d.	n.d.	n.d.	n.d.	0.019(2)	0.019(2)
	1.54	n.d.	n.d.	n.d.	n.d.	n.d.	0.020(2)	0.020(2)
	2.1	n.d.	n.d.	n.d.	n.d.	n.d.	0.021(3)	0.021(3)
	2.6	n.d.	n.d.	n.d.	n.d.	n.d.	0.023(3)	0.023(3)
	3.1	n.d.	n.d.	n.d.	n.d.	n.d.	0.022(3)	0.022(3)
	3.8	n.d.	$5.0(16) \times 10^{-5}$	n.d.	n.d.	n.d.	0.023(3)	0.023(3)
	5.0	$1.6(10) \times 10^{-5}$	$6.3(18) \times 10^{-5}$	n.d.	n.d.	n.d.	0.025(3)	0.025(3)
	6.3	$2.1(11) \times 10^{-5}$	$7.4(18) \times 10^{-5}$	n.d.	$3.3(20) \times 10^{-5}$	n.d.	0.026(3)	0.026(3)
	8.7	n.d.	n.d.	n.d.	n.d.	n.d.	0.027(3)	0.027(3)
	12.1	$3.5(16) \times 10^{-5}$	$1.1(2) \times 10^{-4}$	n.d.	$5.3(24) \times 10^{-5}$	n.d.	0.028(3)	0.028(3)
	13.5	$4.5(14) \times 10^{-5}$	$1.2(2) \times 10^{-4}$	n.d.	$6.77(19) \times 10^{-5}$	n.d.	0.029(3)	0.029(3)

[a] λ_{exc} = 969 nm; [b] λ_{exc} = 980 nm; [c] λ_{exc} = 976 nm; n.d.: not determined.

Table 4S.1 (continue) Upconversion photoluminescence quantum yields ($\Phi_{UC,\lambda}$) for $LiYF_4:Yb^{3+},Tm^{3+}$ UCNPs in toluene. The data points from Leiden were measured relative to the value at 5.0 $W \cdot cm^{-2}$ at 293 K.

P_{exc} [$W.cm^{-2}$]		$\Phi_{UC,451}$	$\Phi_{UC,480}$	$\Phi_{UC,511}$	$\Phi_{UC,649}$	$\Phi_{UC,686+704}$	$\Phi_{UC,794}$	$\Phi_{UC,total}$
Berlin	5.5	3.02×10^{-6}	$4.48(2) \times 10^{-5}$	$4.7(9) \times 10^{-7}$	$2.54(3) \times 10^{-5}$	$3.356(9) \times 10^{-5}$	0.0188	0.0189(5)
c)	17	$1.83(1) \times 10^{-5}$	$8.80(3) \times 10^{-5}$	1.4×10^{-6}	$4.64(1) \times 10^{-5}$	$4.39(1) \times 10^{-5}$	0.0222	0.022(2)
	19	$2.30(1) \times 10^{-5}$	$9.68(1) \times 10^{-5}$	$1.7(1) \times 10^{-6}$	$5.03(1) \times 10^{-5}$	$4.48(1) \times 10^{-5}$	0.0226	0.023(1)
	26	$3.78(2) \times 10^{-5}$	$1.168(4) \times 10^{-4}$	2.6×10^{-6}	$6.01(1) \times 10^{-5}$	4.8×10^{-5}	0.0236	0.024(1)
	36	$6.12(1) \times 10^{-5}$	$1.42(1) \times 10^{-4}$	4.1×10^{-6}	$7.31(5) \times 10^{-5}$	$5.15(1) \times 10^{-5}$	0.0251	0.0256(8)
	42	$7.65(1) \times 10^{-5}$	$1.55(1) \times 10^{-4}$	5.2×10^{-6}	$7.99(7) \times 10^{-5}$	$5.29(1) \times 10^{-5}$	0.0256	0.0261(8)
	45	$7.59(6) \times 10^{-5}$	$1.52(2) \times 10^{-4}$	5.2×10^{-6}	$7.88(8) \times 10^{-5}$	$5.23(1) \times 10^{-5}$	0.0254	0.026(2)
	48	$9.08(5) \times 10^{-5}$	$1.65(1) \times 10^{-4}$	6.2×10^{-6}	$8.48(5) \times 10^{-5}$	5.3×10^{-5}	0.0255	0.0260(6)
	58	$1.177(1) \times 10^{-4}$	$1.86(1) \times 10^{-4}$	8.3×10^{-6}	$9.67(5) \times 10^{-5}$	5.5×10^{-5}	0.0261	0.027(1)
	80	$1.913(3) \times 10^{-4}$	$2.36(1) \times 10^{-4}$	$1.40(1) \times 10^{-5}$	$1.224(6) \times 10^{-4}$	$5.97(1) \times 10^{-5}$	0.0273	0.028(1)
	112	$2.987(3) \times 10^{-4}$	$2.96(2) \times 10^{-4}$	$2.29(1) \times 10^{-5}$	$1.53(1) \times 10^{-4}$	$6.37(3) \times 10^{-5}$	0.0283	0.029(1)
	131	$3.713(3) \times 10^{-4}$	$3.35(2) \times 10^{-4}$	2.9×10^{-5}	$1.73(1) \times 10^{-4}$	$6.63(3) \times 10^{-5}$	0.0288	0.030(1)
	149	$4.75(1) \times 10^{-4}$	$3.96(3) \times 10^{-4}$	$3.86(2) \times 10^{-5}$	$2.04(1) \times 10^{-4}$	$7.22(2) \times 10^{-5}$	0.0305	0.0323(2)
	154	$4.57(2) \times 10^{-4}$	$3.81(2) \times 10^{-4}$	$3.72(2) \times 10^{-5}$	$1.962(7) \times 10^{-4}$	$6.98(2) \times 10^{-5}$	0.0299	0.032(2)
	212	7.12×10^{-4}	$5.15(3) \times 10^{-4}$	6.3×10^{-5}	$2.631(8) \times 10^{-4}$	$7.8(1) \times 10^{-5}$	0.0310	0.034(2)
	295	1.03×10^{-3}	$6.84(3) \times 10^{-4}$	$9.74(2) \times 10^{-5}$	$3.406(9) \times 10^{-4}$	$8.89(2) \times 10^{-5}$	0.0321	0.036(2)
	345	1.19×10^{-3}	$7.729(7) \times 10^{-4}$	$1.166(9) \times 10^{-4}$	$3.790(9) \times 10^{-4}$	$9.37(2) \times 10^{-5}$	0.0322	0.0363(5)
	395	1.37×10^{-3}	$8.78(2) \times 10^{-4}$	$1.390(6) \times 10^{-4}$	$4.24(1) \times 10^{-4}$	$9.97(2) \times 10^{-5}$	0.0325	0.0371(7)

[a] λ_{exc} = 969 nm; [b] λ_{exc} = 980 nm; [c] λ_{exc} = 976 nm; n.d.: not determined.

4.5.9 Excitation wavelength dependence of the upconversion emission intensity (Karlsruhe)

The luminescence excitation spectra of the dispersed UCNPs were measured with a home-built setup. Continuous-wave (CW) tunable Ti-Sapphire laser (Solstis, M squared) was used as an excitation source. During a wavelength sweep the P_{exc} on the front surface of the sample was measured (PM100D with S121C head, Thorlabs Inc.) and used afterwards for the correction of the excitation spectrum. The luminescence was collected by an optical fiber and directed to a calibrated CCD spectrometer (AvaSpec-ULS2048, Avantes). A dichroic filter (FES0750, Thorlabs Inc.) was placed in front of the collecting edge of the optical fiber in order to block the scattered excitation radiation. For each excitation wavelength the emission was integrated from 440 to 500 nm for the blue emission and from 750 to 850 nm for the NIR emission, respectively. The spectra were normalized in such a way that similar P_{exc} (~5 $W \cdot cm^{-2}$) is used for each

excitation wavelength. For simplicity, we assume that at the given range of the excitation power density (1.0 – 10 W·cm^{-2}) the power coefficient n (in $I_{UC} \sim P_{exc}^{n}$) is constant with n = 1.1 for 794 nm emission and n = 1.6 for 480 nm emission in agreement with Figure 4S.4. Since the optical output power of our laser varies slightly (see Figure 4S.9) over this wavelength range, the raw data were corrected according to $I_{UC(corrected)} \sim I_{UC(measured)}/(P_{exc/5})^{n}$, followed by normalization of the spectra.

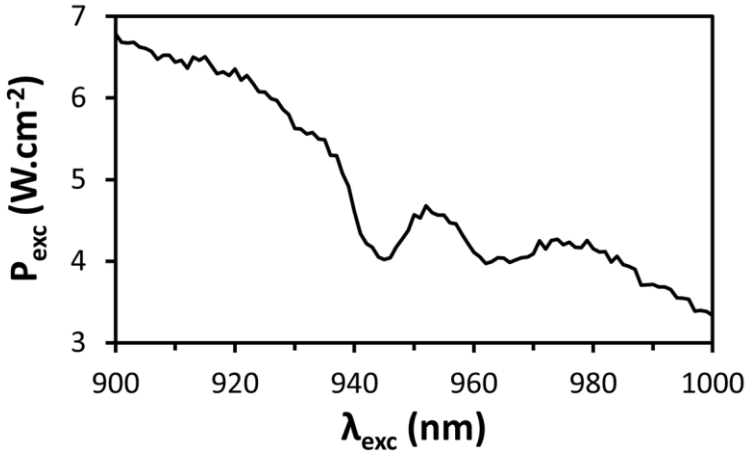

Figure 4S. 9 Optical output power density as a function of excitation wavelength for the laser system used for excitation wavelength dependence measurements in Karlsruhe**.**

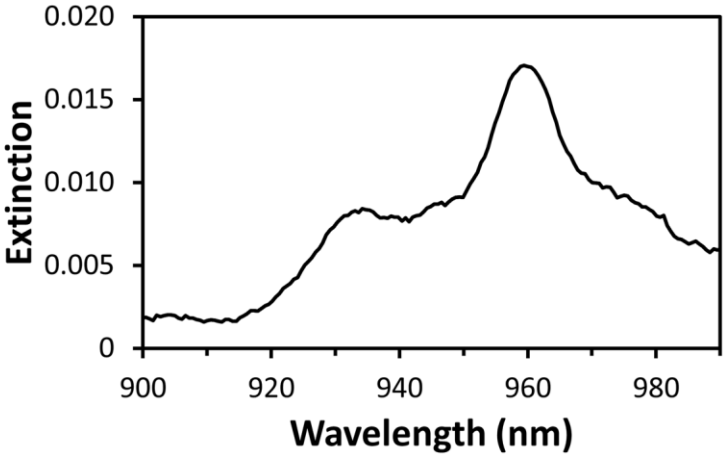

Figure 4S. 10 NIR absorption spectrum of $LiYF_4:Tm^{3+},Yb^{3+}$ UCNPs in toluene ([UCNP] = 10 mg·ml^{-1}) measured in Leiden.

4.5.10 Temperature dependence of the upconversion quantum yield (Leiden)

As integrating sphere setups do not feature temperature control, Φ_{UC} at other temperatures than 293 K was estimated from measuring the upconverted emission in the temperature-controlled cuvette holder setup (see Section 4.5.4) at a range of temperatures from 278 to 333 K and scaling Φ_{UC} at 293 K with the ratio of the upconversion emission at 293 K and the temperature of interest (T) by using Equation 4S.12:

$$\Phi_{UC}^{T} = \Phi_{UC}^{293\,K} * \frac{\int_{\lambda_1}^{\lambda_2} I_{UC}^{T}(\lambda)d\lambda}{\int_{\lambda_1}^{\lambda_2} I_{UC}^{293\,K}(\lambda)d\lambda} \quad \textbf{(4S.12)}$$

For these measurements, 1.8 mL of a 5 mg·mL^{-1} of $LiYF_4$:Tm^{3+},Yb^{3+} UCNPs dispersion in toluene were placed in a stirred 111-QS macro fluorescence cuvette (Hellma). The cuvette was placed in the temperature-controlled cuvette holder, and cooled to 278 K. After equilibrating for 10 minutes, the temperature was increased from 278 to 333 K with a rate of 1 K·min^{-1}, while recording the upconverted emission spectra. During the experiment, the temperature of the dispersion was monitored using a K-type probe submerged in the sample, and recorded on an Omega RDXL4SD thermometer. Integration of the emission bands was performed by fitting the emission bands with one or more Gaussian profiles, and integrating the area under these peaks. This treatment allowed deconvolution of the various emission bands, even though the emission data could only be recorded with a spectral resolution of 9 nm (slit size = 200 μm).

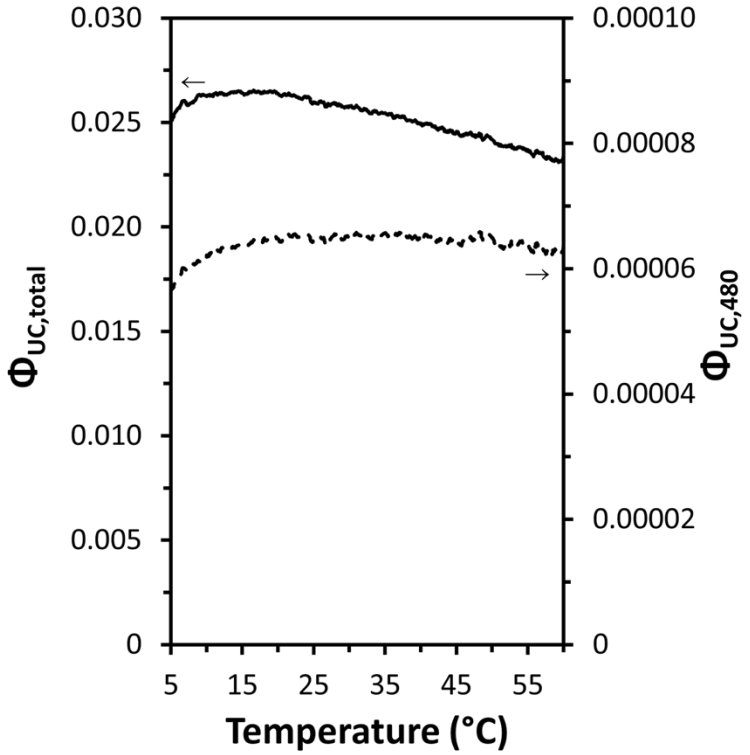

Figure 4S. 11 Temperature dependence of the total upconversion quantum yield $\Phi_{UC,total}$ (solid line, left axis) and of the upconversion quantum yield of the blue 480 nm band $\Phi_{UC,480}$ (dashed line, right axis) of $LiYF_4:Tm^{3+},Yb^{3+}$ UCNPs in toluene recorded in Leiden; λ_{exc} = 969 nm, P_{exc} = 5.0 $W \cdot cm^{-2}$, [UCNP] = 5 $mg \cdot mL^{-1}$.

Table 4S. 2 Temperature dependence of the upconversion quantum yield of $LiYF_4:Tm^{3+},Yb^{3+}$ UCNPs in toluene recorded in Leiden; λ_{exc} = 969 nm, [UCNP] = 5 $mg \cdot mL^{-1}$.

T [°C]	$\Phi_{UC,451}$	$\Phi_{UC,480}$	$\Phi_{UC,649}$	$\Phi_{UC,686}$	$\Phi_{UC,704}$	$\Phi_{UC,794}$	$\Phi_{UC,total}$
10	6.4×10^{-6}	6.2×10^{-5}	3.0×10^{-5}	1.5×10^{-5}	2.1×10^{-5}	0.026	0.026
20	6.4×10^{-6}	6.5×10^{-5}	3.1×10^{-5}	1.5×10^{-5}	2.1×10^{-5}	0.026	0.026
37	6.4×10^{-6}	6.6×10^{-5}	3.0×10^{-5}	1.6×10^{-5}	2.2×10^{-5}	0.025	0.025
50	6.2×10^{-6}	6.5×10^{-5}	3.0×10^{-5}	1.7×10^{-5}	2.3×10^{-5}	0.024	0.024

4.5.11 Luminescence lifetime measurements (Karlsruhe)

For the photoluminescence lifetime measurements, time-correlated single photon counting TCSPC and a multichannel scaling (MCS) card (Timeharp 260, PicoQuant) were used. The modulation of the diode laser was performed via a built-in function generator in the laser diode driver. In order to detect the rise and decay times of the emission, the TTL signal from the laser diode controller was delayed by the use of a delay generator (DG645, Stanford Research Systems). The spectral separation of the photoluminescence was achieved via a double monochromator (DTMS300, Bentham) and the emission at 998 nm was detected via a cooled InGaAs/InP avalanche photodiode ID220-FR (ID Quantique SA). The sample was excited with a 940 nm laser diode using 15 ms long pulses followed by a 20 ms dark time. These pulses are of sufficient length to drive the population processes into the steady state during the time in which the laser is on. After the laser is turned off we monitor how the downconverted luminescence of Yb^{3+} decays with time.

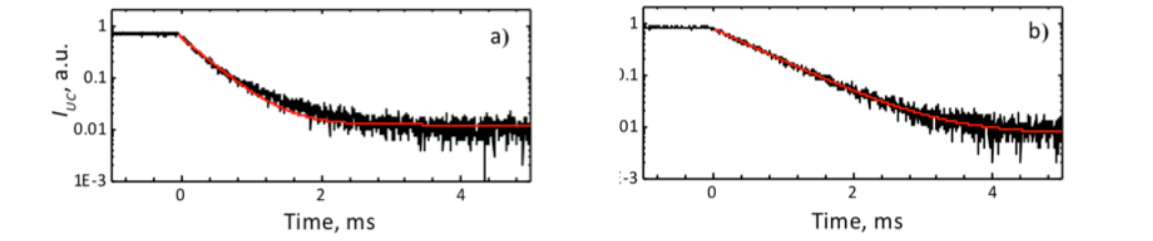

Figure 4S. 12 Luminescence decays of $LiYF_4:Tm^{3+},Yb^{3+}$ UCNPs excited at 940 nm for the Yb^{3+}: $^2F_{5/2} \rightarrow {}^2F_{7/2}$ emission, detected at 998 nm; P_{exc} = 220 W·cm^{-2} (a) and 10 W·cm^{-2} (b). Red lines are the single exponential fits. Data obtained in Karlsruhe.

4.6 Author's notes and significance of this paper

This publication is the first multicenter study on the absolute upconversion quantum yields, and provides the first quantum yield values for $LiYF_4:Tm^{3+}/Yb^{3+}$ upconverting nanoparticles. This study is of great contribution to the field as it shows that the measurements of quantum yields are reproducible between different laboratories with different spectroscopy setups. Also, it shows that the upconversion quantum yields of the individual emission bands are substantially different. These results are important for the understanding of the energy transfer process reported in Chapter 3 where it was proposed that the minor contribution of FRET on the energy transfer process between $LiYF_4:Tm^{3+}/Yb^{3+}$ and the azobenzene moiety was due to low quantum yields and the distance between the donor (Tm^{3+}) and the acceptor (azobenzene moiety). Even though the nanomaterial proposed in Chapter 3 produces the photoswitching of azobenzene mostly *via* reabsorption of light, there is a need to increase the upconversion quantum yield of the emissions in the visible and UV regions in Ln-UCNPs to produce more efficient energy transfer process *via* FRET.

In Chapter 2 and Chapter 3 it was presented the development of a nanoparticle-based drug delivery system using $LiYF_4:Tm^{3+}/Yb^{3+}$ upconverting nanoparticles with a supported lipid bilayer that includes a photo-responsive property when the azobenzene-derivative lipid is incorporated. The subsequent chapter discusses the cellular studies of this nanomaterial developed using human alveolar lung cancer A549 cells. This study contributes for the understanding of the nanoparticle-cell interactions, which is of great importance for the development of nanoparticle-based nanomedicines.

Chapter 5

Cellular Uptake, Cytotoxicity and Trafficking of Supported Lipid Bilayer Coated Lanthanide Upconverting Nanoparticles in Alveolar Lung Cancer Cells

Published as:

[1] Paola A. Rojas-Gutierrez, [2] Devesh Bekah, [2] Jan Seuntjens, [1] Christine DeWolf, and [1] John A. Capobianco*

ACS Applied Bio Materials, **2019** (doi.org/10.1021/acsabm.9b00649)

[1]Department of Chemistry and Biochemistry, and Centre for NanoScience Research, Concordia University, Montreal, Quebec, H4B 1R6, Canada; [2]Medical Physics Unit, Cedars Cancer Centre, McGill University Health Centre, 1001 Boulevard Décarie, Montréal, Canada

5.1 Abstract

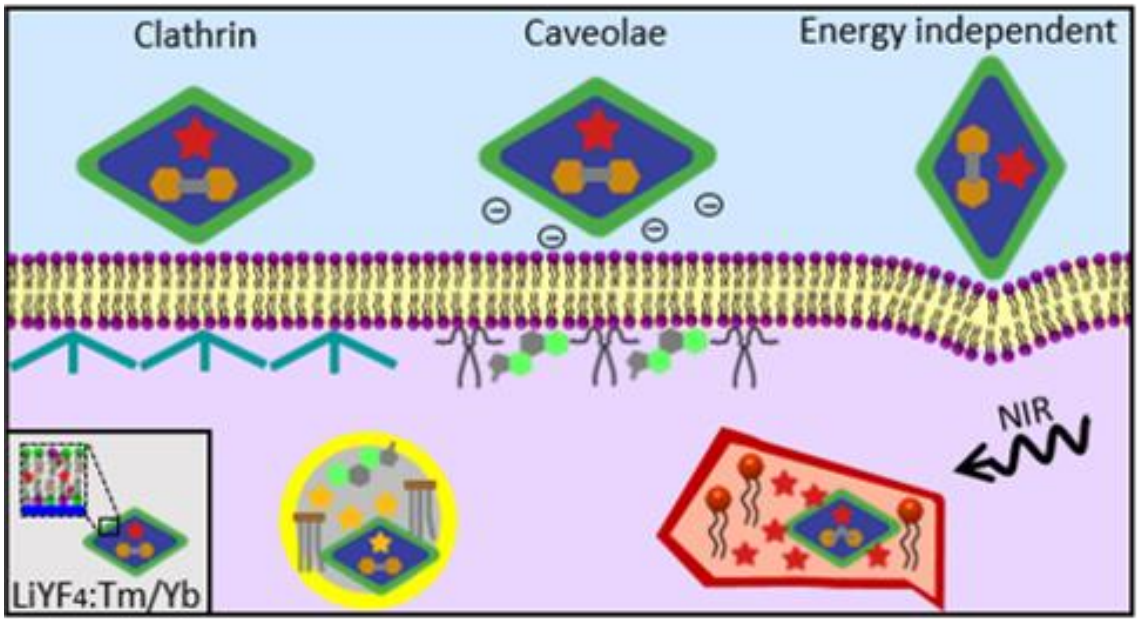

Scheme 5. 1 Graphical table of content of "Cellular Uptake, Cytotoxicity and Trafficking of Supported Lipid Bilayer Coated Lanthanide Upconverting Nanoparticles in Alveolar Lung Cancer Cells"

An understanding of the cellular uptake and trafficking of nanoparticles is important for the design of efficient nanoparticle-based nanomedicines. Herein we compare the uptake and cytotoxicity of diamond-shape, lanthanide upconverting nanoparticles ($LiYF_4:Tm^{3+}/Yb^{3+}$ UCNPs) with different surface properties. Coating the UCNP with a supported lipid bilayer yielded negligible cytotoxicity on A549 human lung cancer cells, albeit with a lower, but still significant, UCNP uptake compared to oleate-capped and oleate-free UCNPs. Using inhibition studies and cellular imaging we demonstrate that the UCNPs are internalized by endocytosis and energy independent pathways and trafficked to the endoplasmic reticulum, Golgi apparatus, lamellar and lipid bodies. Upon incorporation of a photo-stimulus within the bilayer coating, release of a Nile red as a hydrophobic drug model was demonstrated.

5.2 Introduction

There is considerable interest in developing nanomaterials to improve diagnosis and treatment of diseases. To achieve this goal, nanomedicine employs nanotechnology in order to enhance bioavailability and increase efficacy of drugs while reducing their side effects.[5] The cellular uptake of nanoparticles is essential for their action and has been shown to be influenced by their physical and chemical properties including size, shape, surface charge, hydrophobicity, chemical composition, and even the hardness of the nanomaterial.[136,322] These properties also govern the trafficking and fate of the nanoparticles after internalization.[135,137] Moreover, the mechanisms of internalization and trafficking are cell-specific. For example, different cell species present different uptake kinetics due differences in their plasma membrane composition and metabolic activities.[180] The understanding of these interactions will lead to more effective drug delivery strategies, especially in the case of active (triggered) delivery rather than passive. The use of remote triggers provides a mechanism to accelerate and control the drug release from the nanoparticles and potentially increase the drug efficacy.

Employing light-triggered photoresponsive molecules provides a route to controlled drug release. For biological applications, near-infrared (NIR) as the light source provides a number of advantages including higher tissue penetration, lack of cytotoxicity, and improved detection sensitivity due to the absence of autofluorescence.[72,244,323] Lanthanide upconverting nanoparticles (Ln-UCNPs) are interesting materials that absorb low NIR energy excitation and emit high energy light *via* a multiphoton process known as upconversion. Due to this property, Ln-UCNPs have been proposed for a number of bioapplications such as imaging probes,[73,324] light-activated delivery of therapeutics,[29] photodynamic therapy,[30,325] nanothermometry and thermal treatments,[75] and biosensors for disease detection.[326] The human lung adenocarcinoma cell line A549 used for this study are alveolar type I and II carcinoma epithelial cells of the distal lung [327]. The type I is responsible for the gas exchange in the alveoli and the type II controls the homeostasis of the lung surfactant by the biosynthesis, recycle and storage of lipids.[188] Type II contains secretory vesicles known as lamellar bodies, which store and release lipids to prevent the collapse of the lungs during the breathing cycle by regulating the surface tension.[188] Herein,

we report *in vitro* cellular studies using the cell line A549 to assess the cellular uptake, trafficking and cytotoxicity of the faceted, diamond morphology $LiYF_4:Tm^{3+}/Yb^{3+}$ UCNPs coated with a supported lipid bilayer (SLB-UCNPs). We demonstrate that the SLB-UCNPs are non-cytotoxic and can be used to deliver and release Nile red, representing a hydrophobic drug, upon NIR excitation.

5.3 Experimental

5.3.1 Synthesis of Nanoparticles

Oleate-capped $LiYF_4:Tm^{3+}/Yb^{3+}$ (0.2% Tm^{3+}, 25% Yb^{3+}) upconverting nanoparticles were synthesized *via* the thermal decomposition method.[67] The oleate-capped UCNPs were coated with a supported lipid bilayer composed of 1,2-di(9Z-octadecenoyl)-sn-glycero-3-phosphate (DOPA), 1,2-di(9Z-octadecenoyl)-sn-glycero-3-phosphocholine (DOPC), and cholesterol lipids (64:7:29 mole ratio) (termed SLB-UCNPs).[236] The oleate-free $LiYF_4:Tm^{3+}/Yb^{3+}$ (oleate-free UCNPs) were obtained after treating oleate-capped UCNPs with hydrochloride acid (pH 2) to protonate the oleate.[86] Details of synthetic procedures and physical characterization of all nanoparticles is provided in the Supporting Information section 5.6.1.

The dye, Nile red, was encapsulated into the SLB of the SLB-UCNPs as a representative of a hydrophobiuc drug (S1.4).[328] For phototriggered release of the dye, a nanocarrier containing azobenzene lipid analogue di(6-{[4-(4-butylphenyl)azo]-phenoxy}-hexyl)phosphate (AZO-lipid) incorporated in the SLB was employed (5.6.1.5-5.6.1.6).[328] The concentration of the nanoparticle dispersions was calculated using ICP-MS (Supporting Information Section 5.6.1.7).

5.3.2 Cellular Studies

Human alveolar carcinoma epithelial A549 cells were donated by Professor Norma Ybarra from the Medical Physics Unit at the Cancer Research Institute, McGill University. Cells were incubated at 37 °C with 5% CO_2 in cell culture media (Dulbecco's modified Eagle medium,

DMEM/F-12, Gibco®) supplemented with 10% fetal bovine serum (FBS) and 1% of antibiotic-antimycotic solution from Gibco®. Cells were passaged at 70-90% confluent using trypsin (0.25% trypsin-EDTA with phenol red, Gibco®).

5.3.3 Cellular Uptake, Uptake Mechanism and Trafficking of Nanoparticles

A dispersion of nanoparticles, 100 μg/mL, in cell culture media were prepared fresh from a dispersion of SLB-UCNPs (1 mg/mL in HEPES buffer), oleate-free UCNPs (1 mg/mL in HEPES buffer), oleate-capped UCNPs (10 mg/mL in DMSO), nanocarrier (1 mg/mL in HEPES buffer), or nanocarrier with AZO-lipid (1 mg/mL in HEPES buffer). To investigate the uptake, the endocytosis mechanism and the trafficking of the nanoparticles the following protocol was used: A549 lung cancer cells were seeded at 170000 cell density, after 24 hours of incubation they were co-cultured with the specified UCNPs at a concentration of 50 μg/mL (225 μM of Y) for the specified time. After the incubation of the cells with the nanoparticles, the cell culture media was removed and cells were washed twice with PBS to remove the excess of nanoparticles that were not taken up by the cells. 6-well plates or 35 mm glass bottom dishes (for imaging) were used to investigate the cellular uptake and trafficking of the nanoparticles. 24-well plates were used to investigate the endocytosis mechanism. Samples containing AZO-lipid were handled in minimal light conditions to prevent the photoisomerization and keep the AZO-lipid in the stable *trans*-isomer.

5.3.4 Endocytosis Mechanisms

For the study of the endocytosis mechanisms the previous protocol was followed, however after seeding the A549 lung cancer cells and incubating for 24 hours, the cells were washed twice with PBS and pre-incubated for half an hour with the inhibitors at 37 °C or at 4 °C. The cellular pathways inhibitors were prepared in cell culture media at the reported concentrations: sucrose 450 mM (Sigma-Aldrich),[329] amiloride hydrochloride 1 mM (Millipore Sigma),[165] ammonium chloride 18.7 mM (Sigma-Aldrich),[329] and methyl-beta-cyclodextrin 10 mM (Sigma-Aldrich).[165]

The nanoparticles were then added as described above and co-cultured with the A549 cells for 3 hours at 37 °C or 4 °C.

5.3.5 Cellular Uptake Quantification

For the quantification of the cellular uptake (in the absence and presence of endocytosis inhibitors) the described protocol above was followed. However, immediately after the wash with PBS of the excess of the nanoparticles that were not uptaken, in order to remove the cells from the plates, the cells were trypsinized (250 or 100 μL) and the reaction was stopped with (1 mL or 0.5 mL) of cell culture media depending if the cells were seeded in a 6- or 24-well plate respectively. Next, the cells were counted and the dispersions containing the cell with the internalized nanoparticles were collected and stored for ICP-MS analysis (Section 5.6.1.7).

5.3.6 Cellular Studies with Laser Scanning Confocal Microscope (LSCM)

The cellular uptake, trafficking and the controlled released from the nanocarriers in A549 lung cancer cells was studied using a Zeiss LSM780-NLO laser scanning confocal microscope. From the described protocol above, immediately after of the removal of the excess of the nanoparticles that were not internalized, cell culture media was added to keep the cells alive and they were imaged on the same day at 37 °C. The nanoparticles and the dye were observed under a 980 nm excitation source and an additional channel with an excitation source at 553 nm was used to directly excite only the dye. Images using the single scan mode of the LSCM were obtained using two different excitation sources (λ_{ex} 980 nm, λ_{em} 450 nm) and (λ_{ex} 553 nm, λ_{em} 620 nm). For the lambda mode the images were obtained using one excitation source (λ_{ex} 980 nm, λ_{em} 400-700 nm). For the controlled dye released Z-stacks images were acquired during 15 minutes with each laser. First the 980 nm laser was used and then the 553 nm laser, to image the nanoparticles and the dye, respectively.

5.3.7 Cellular Cytotoxicity

The cytotoxicity of the three surface-modified UCNPs nanoparticles on the A549 lung cancer cells was determined using the XTT viability assay. The A549 lung cancer cells were seeded at 50000 cell density and pre-incubated for 24 hours in 96-well plates. The nanoparticles (oleate-capped UCNPs, SLB-UCNPs and oleate-free UCNPs) were added at different concentrations (from 12.5 μg/mL up to 100 μg/mL) and co-cultured from 24 hours up to 120 hours. The cell media with the excess of nanoparticles was removed and the cells were washed with 250 μL of PBS before their evaluation with the XTT viability assay. Each well was treated with a mixture of 100 μL of cell culture media and 25 μL of activated XTT (2,3-Bis-(2-Methoxy-4-nitro-5-sulfophenyl)-2H-tetrazolium-5-carboxanilide, disodium salt) solution (Biotium, Hayward, CA). The activated XTT solution with PMS (phenazine methosulfate) was prepared following the Biotium protocol.[330] Afterwards the plates were incubated and the absorbance of the orange product was measured at 475 nm and corrected with the absorbance of the background at 660 nm using a microplate reader (TECAN infinite® 200 pro). Experiments under 120 hours of incubation time were also seeded at 10000 cell density. A control experiment with the carrying media (HEPES buffer) was performed to assess any cytotoxicity from it.

5.4 Results and Discussion

5.4.1 Cellular Uptake of the Nanoparticles

Figure 5.1 shows the uptake of the SLB-UCNPs by the A549 cells where Figure 5.1a is the confocal, bright field image and Figure 5.1b shows the blue upconversion emission produced by the SLB-UNCPs upon 980 nm excitation. Overlapping the bright field image and the image of the blue emission of the SLB-UNCPs clearly demonstrates that the SLB-UCNPs are in the cytoplasm rather than inside the nucleus (Figure 5.1c). Upon 980 nm excitation the Tm^{3+} ions emit at 450 nm ($^1D_2 \rightarrow {}^3F_4$), 480 nm ($^1G_4 \rightarrow {}^3H_6$), and 650 nm ($^1G_4 \rightarrow {}^3F_4$) (Figure 5.1d). It should be noted that at this excitation wavelength, autofluorescence from the cells is avoided.

The lambda scan (λ_{ex} 980 nm, λ_{em} 400-700 nm, Figure 5.1d, inset) confirms that the SLB-UCNPs are co-localized with the cells. The 3D image obtained from the Z-stacks scans of the 450 nm emission demonstrates that the nanoparticles are not only on the cell surface but are also distributed within the cell, indicating that they have crossed the cell membrane (Figure 5.1e).

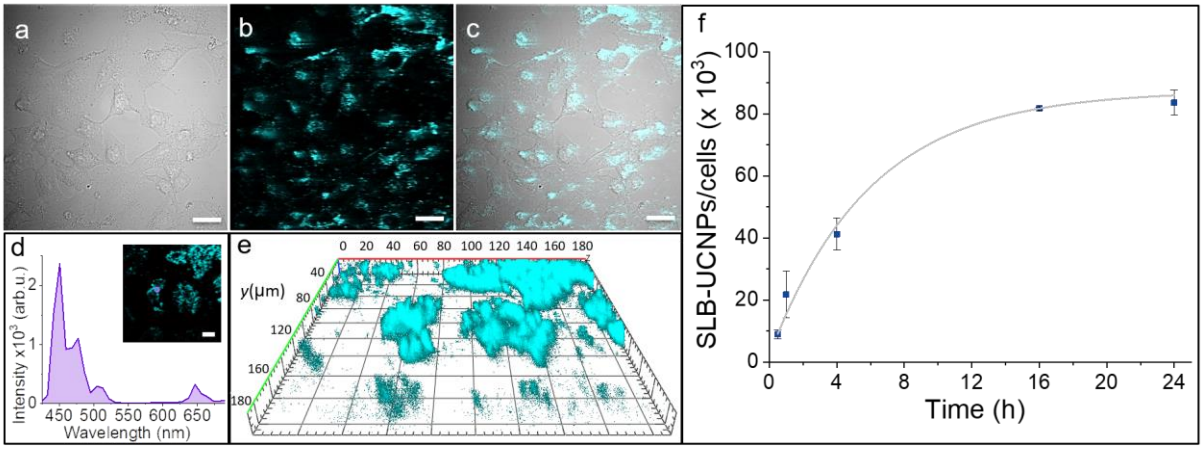

Figure 5. 1 Confocal images of fixed A549 alveolar lung cancer cells after 4 hours of incubation with SLB-UCNPs. a) A549 cells (bright field), b) SLB-UCNPs emission (λ_{ex} 980 nm, λ_{em} 450 nm), c) merge of channels a and b. d) Emission spectra obtained with the lambda scan (λ_{ex} 980 nm, λ_{em} 400-700 nm). e) Z-stacks of SLB-UCNP emission (λ_{ex} 980 nm, λ_{em} 450 nm). f) Number of SLB-UCNPs per cell as a function of the incubation time with A549 cells. Scale bar 20 µm.

The number of nanoparticles per cell and the total mass of nanoparticles per cell is important to understand the cell-nanoparticle interactions in order to more effectively develop nanoparticles for biological applications. The uptake can also be followed by confocal microscopy where the blue emission from the nanoparticles was detected within the first hour of incubation and increases with incubation time (Figure 5S.3). However, while laser scanning confocal microscopy provides a qualitative measure of the uptake of nanoparticles by cells, this can be determined quantitatively using ICP-MS and a cell counter whereby the concentration of lanthanide ions was determined and used to calculate the number of SLB-UCNPs inside the

cells. The impact of incubation time (from 0.5 up to 24 hours) on the uptake of the SLB-UCNPs by the A549 lung cancer cells is shown in Figure 5.1f. The uptake of the SLB-UCNPs follows an exponential relationship with time reaching approximately 84000 nanoparticles per cell (~12.7 pmol(Y)/cell, ~14.4 pg UCNPs/cell) after 24 hours of incubation. This corresponds to a 20% uptake of the total amount of nanoparticles incubated with the cells.

Jin *et al*.[331] studied the uptake of three polymer coated α-$NaYF_4$:Er^{3+}/Yb^{3+} UCNPs of 50 nm size in HeLa cells obtaining an uptake of 0.6 pmol/cell, under similar conditions, a 20-fold lower uptake than the SLB-UCNPs studies herein. The major difference between the two systems is the shape of the nanoparticles. $LiYF_4$ UCNPs has a faceted diamond-shape morphology that may facilitate the uptake. The energy required to envelop or wrap the nanoparticle by the cell membrane depends on the adhesion strength between the nanoparticle and the cell membrane, and the bending energy (rigidity) of the cell membrane.[162] The optimal size to minimize the wrapping energy was shown to be 50 nm,[162] which is corroborated by uptake studies employing different compositions of spherical nanoparticles (gold, silica, calcium oxalate).[164–167]. Additionally, with non-spherical particles, variables such the aspect ratio and angular edges on the nanoparticle, which lead to different apex angles, have been shown to influence the uptake. For example, silica nanorods showed a greater uptake with increasing aspect ratio, with an optimal aspect ratio range of 2.1 to 2.5.[171] Tree-Udom *et al*., observed a correlation between membrane association and cellular uptake as a function of UCNP shape. They found that the elongated spheres adsorb to membranes more favourably than spherical due to the differences in membrane curvature required for the particles to bind to and indent the membrane. In contrast, nanoparticles with morphologies containing angles of 90°, as is the case of hexagonal or cubic shape particles, the adsorption and uptake were reduced, attributed to the curvature that the membrane must undergo in order to wrap the nanoparticle.[332] The SLB-UCNPs used herein have a short axis of 53 nm, which lies close to the optimal size of 50 nm, and an aspect ratio of 1.74 both of which may contribute to facilitating the uptake, assuming the nanoparticle enters with its long axis perpendicular to the cell surface.

The physicochemical surface properties such as surface charge, hydrophobicity, chemical functionality, of nanoparticles has shown to have significant impact on the cellular uptake. Thus, to understand the role of the SLB on uptake, the oleic acid free $LiYF_4:Tm^{3+}/Yb^{3+}$ (oleate-free UCNPs) and oleate-capped UCNPs were also studied. The SLB-UCNPs present a negative surface charge with a ζ-potential of -50 ± 3.0 mV due to the negative charged lipid, DOPA, that is the main component of the SLB. The oleate-free UCNPs present a positive surface charge with ζ-potential of +12 ± 0.3 mV whereas the oleate-capped UCNPs present a ζ-potential of -24 ± 1.5 mV. Each of these nanoparticle types (oleate-capped UCNPs, SLB-UCNPs and oleate-free UCNPs) were incubated for 4 hours with A549 lung cancer cells to investigate the impact of the surface coatings on the cellular uptake of UCNPs. It was found that the oleate-free UCNPs have the largest uptake by the cells with 35% (~2.9 x 10^5 UCNPs/cell), followed by the oleate-capped UCNPs with 14% (~1.6 x 10^5 UCNPs/cell), and then the SLB-UCNPs with 5% (~4.1 x 10^4 UCNPs/cell), percentages given relative to the total amount of UCNPs added (**Figure 5.2**a).

This clear difference in the uptake of the UCNPs by A549 lung cancer cells may be due to their different surface charge properties. The increased uptake of positively charged nanoparticles compared to negatively charged nanoparticles has been reported for gold and silicon dioxide and attributed to the net negative charge of cell membranes.[183,184,333] Zhang et al. showed that this was independent of particle morphology.[334]

The A549 cell viability in the presence of the different UCNPs was evaluated using a XTT viability assay.[330] Figure 5.2b shows that after 24 hours, no statistically significant effect on the cell viability was observed for any of the UCNPs with respect to the control. However, there was a small but statistically significant reduced viability of the cells with the oleate-free UCNPs and oleate-capped UCNPs after 72 hours. On the other hand, the SLB-UCNPs did not show any change in cell viability. It is well known that the lanthanides themselves are non-toxic.[70] In such cases where the material is non-toxic, cytotoxicity may derive from the intrinsic physical properties shape and size or the surface coating.[322335] Herein, we show that the diamond-shaped UCNPs, all produce a low cytotoxicity effect on A549 lung cancer cells. The small differences in

the viability of the A549 cells over time could be due to the faster uptake of oleate-free UCNPs leading to a higher concentration inside the cell for the same incubation time.[336] Alternatively, it has also been reported that positive charged nanoparticles are more toxic than neutral and negative charged ones.[179]

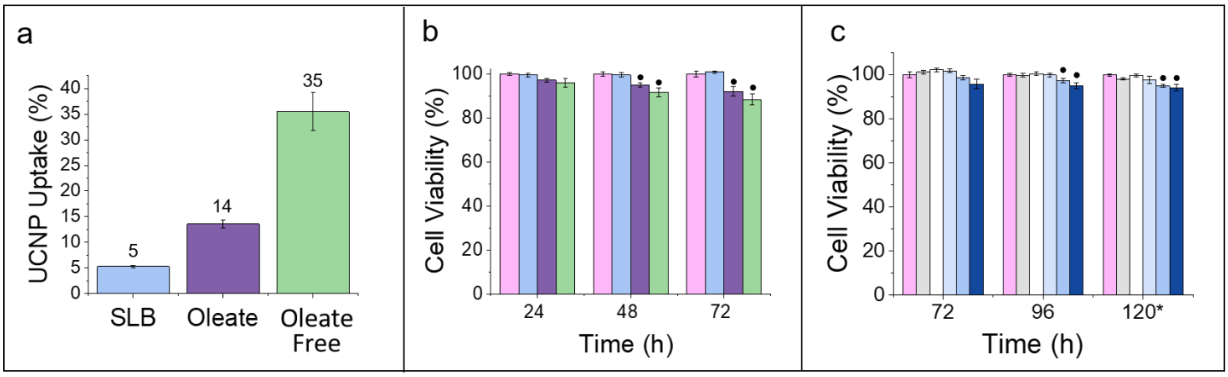

Figure 5. 2 a) Total cellular uptake of UCNPs (with respect to the amount of UCNP added) with different surface modifications after 4 hours of incubation at 37 °C with A549 cells. Values represent the mean standard deviation (n = 3); b) XTT assay for the cytotoxicity of UCNPs with different surface modifications after 24 hours of incubation at 37 °C with A549 cells, after which excess UCNPs were removed. Cells viability was followed after removal and times indicate total time from initial incubation. Pink shows the control cells (no UCNPs) and the other colours are as per 2a; c) XTT assay for the cytotoxicity of SLB-UCNPs nanoparticles as a function of concentration after 72, 96, and 120 hours of incubation at 37 °C with the A549 cells, (* denotes a different cell density). Cytotoxicity values were normalized with respect to the cells incubated without nanoparticles and represent the mean standard deviation (n = 5). Pink: control cells (without nanoparticles); grey: control with 100 µL HEPES buffer (without nanoparticles); white: 12.5 µg/mL SLB-UCNPs; light blue to dark blue 25, 50 and 100 µg/mL SLB-UCNPs, respectively. For all data (●) denotes a statistically significant difference ($P < 0.05$).

Having established the SLB-UCNPs showed negligible cytotoxicity at 50 μg/mL, incubation of the A549 cells with the SLB-UCNPs was evaluated over a larger concentration range (from 12.5 μg/mL up to 100 μg/mL) and longer timeframe (72, 96 and 120 hours of incubation). During the first 72 hours of incubation of the SLB-UCNPs with the A549 lung cancer cells did not produce a statistically significant cytotoxicity effect over the concentration range studied (Figure 5.2c). Only after 96 hours of incubation at concentrations of 50 μg/mL and 100 μg/mL was a statistically significant reduction in cell viability observed. Notably, even after 120 hours of incubation, the SLB-UCNPs exhibit a higher cell viability than either of the oleate-free UCNPs and oleate-capped UCNPs at shorter times.

There is conflicting evidence in the literature with respect to the toxicity of oleate-capped nanoparticles. Our previous work and herein, demonstrates a minimal toxicity for oleate-capped UCNPs.[337] However, in an earlier work by Das *et al*., it was proposed that the intercalation of PEG-oleate with the surface oleate generates a weakly bound outer layer that can dissociate from NPs, resulting in significant toxicity by exposing the hydrophobic oleate-capped NPs to the cell.[338] In the SLB-UCNPs, the bilayer is sufficiently stable due to the increased hydrophobic interactions that exist both within the plane of each bilayer leaflet as well as between the leaflets. Moreover, the bilayer presents a the greater coverage of the surface compared to the oleate-capped UCNPs, where the bilayer inner leaflet adheres to the UCNP surface via strong, electrostatic interactions.[236] The latter arises due to that all the eight crystal faces of $LiYF_4$ have the same energy favoring a homogeneous surface coverage.

In order to employ the SLB-UCNPs as a nanocarrier for hydrophobic or lipophilic drug delivery, their cellular uptake mechanism(s) and the fate of the nanoparticles inside the cell must first be understood. Inhibitory studies of the uptake of the SLB-UCNPs by A549 lung cancer cells was performed using different inhibitors of cellular uptake mechanisms. **Figure 5.3**, shows the uptake of SLB-UCNPs when A549 cells were pre-incubated with an inhibitor for 30 minutes prior to incubation with 50 μg/mL of SLB-UCNPs for 3 hours.

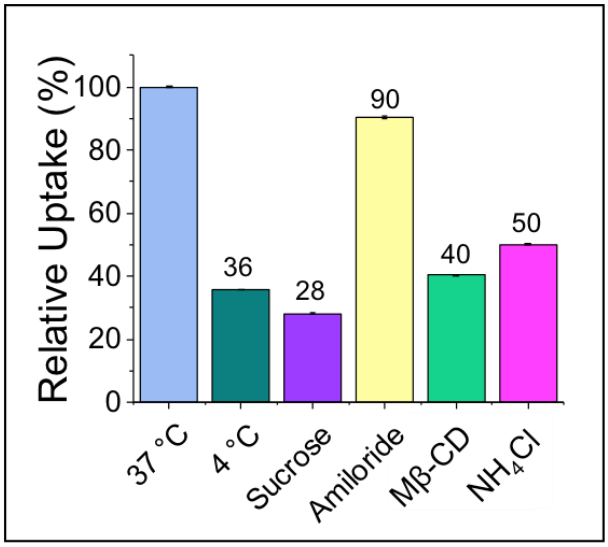

Figure 5. 3 Effect of different inhibitors on A549 cell internalization pathways of SLB-UCNPs after 3.5 hours of incubation at 37 °C. Values represent the mean standard deviation (n = 3).

Different inhibitors of the endocytosis pathways were employed, a hypertonic sucrose solution which inhibits the clathrin-mediated endocytosis pathway,[151] methyl-β-cyclodextrin (Mβ -CD) which inhibits the caveolae-dependent endocytosis pathway,[142,156,157] ammonium chloride which inhibits pathways that involves the formation of lysosomes,[339,340] and amiloride hydrochloride, which inhibits the macropinocytosis endocytosis.[160]

Clathrin-mediated pathways are known to occur for nanoparticles up to 200 nm in size, while caveolae-dependent mechanisms are viable for nanoparticles up to 120 nm.[137,167] Figure 5.3 clearly shows the relative importance of these two pathways for SLB-UCNPs uptake. Inhibiting either pathway reduces SLB-UCNP uptake, whereby inhibition of the clathrin-mediated endocytosis has a greater impact. This is not unexpected as clathrin-mediated endocytosis is known to be the major pathway to internalize cargoes inside the cells.[140] Moreover, this pathway has been reported for various nanoparticle types independent of their surface charge,[136] and it has been demonstrated that positively charged lipoplexes internalize only *via* the clathrin mediated endocytosis in A549 cells.[341] For the caveolae-dependent endocytosis, both cholesterol and negatively charged lipids such as DOPA, which are

components of the SLB, have been demonstrated to play a role in the assembly of the caveolin proteins required for the pathway.[142,342,343] There is evidence that negatively charged lipid-based nanoparticles are internalized *via* both the caveolae-dependent and clathrin-mediated mechanisms.[329]

Ammonium chloride, is a lysosomotropic agent known to destabilize the formation of lysosomes by increasing the intracellular pH.[339,340] Inhibition of this pathway did reduce the SLB-UCNP uptake by 50%, demonstrating the relevance of lysosome formation for the internalization of nanoparticles. Trafficking to the lysosomes is a chlathrin-mediated, and not a caveolae-dependent pathway.[137] On the other hand, inhibition of the macropinocytosis pathway using amiloride hydrochloride did not yield a large reduction in SLB-UCNP uptake, which is likely due to the small nanoparticle size.[167]

Additionally, low temperature (4 °C) experiments report on the energy dependence of the cellular uptake of nanoparticles. This temperature effectively eliminates the endocytosis pathway for uptake. Figure 5.3 clearly shows a significant reduction but not complete elimination of SLB-UCNP uptake (reduced to 36% compared to no inhibition). Thus, the SLB-UCNPs enter the A549 cells *via* energy-dependent pathways, which includes both the clathrin-mediated and the caveolae-dependent endocytosis mechanisms but also to some extent, by an energy-independent mechanism.[167] It was previously reported that A549 cells show a significant uptake of silica rods *via* an energy independent, non-specific membrane association mechanism.[167] This energy-independent mechanism is highly dependent on shape and orientation.[173] For nanoparticles with a similar aspect ratio to those used here (1.74), computational studies have shown that a perpendicular orientation (apex first) facilitates uptake, termed a “rocket” model.[169 175] The SLB-UCNPs studied present a unique diamond shape which appears to play an important role in the internalization by this mechanism.

5.4.2 Trafficking of the Nanoparticles and Delivery of Nile Red

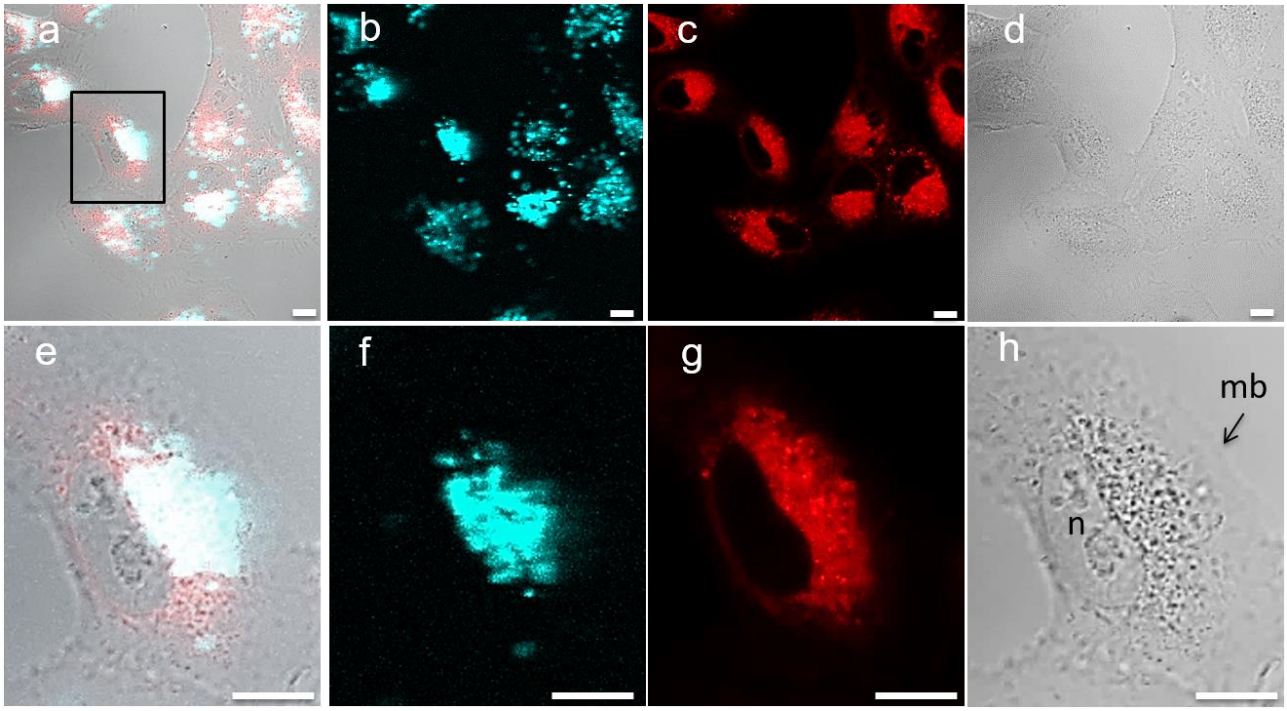

Figure 5. 4 Confocal images of live A549 lung cancer cells incubated with the nanocarrier (SLB-UCNPs loaded with Nile red). The cells were seeded at 85000 cell density with a nanocarrier concentration of 50 µg/mL in 35 mm plates. a,e) merged channels, b,f) SLB-UCNPs (λ_{ex} 980 nm, λ_{em} 450 nm), c,d) Nile red (λ_{ex} 553 nm, λ_{em} 620 nm), d,h) A549 cells (bright field). e-h) magnified view of the cell highlighted in a) for each channel. (n) nucleus, (mb) plasma membrane. Scale bar: 10 µm.

In order to probe the capacity of the SLB-UCNPs as potential drug delivery vehicles (nanocarrier), Nile red, used here as a hydrophobic drug model, was encapsulated into the SLB *via* hydrophobic interactions.[328] This nanocarrier, was co-cultured with A549 lung cancer cells for 4 hours. **Figures 5.4**a-d demonstrates that the nanocarrier is capable of transporting the dye inside the cell as the emissions of both the SLB-UCNP and the Nile red co-localize in the same regions. Figures 5.4e-h present a magnified view of the cell highlighted in Figure 5.4a. From the

magnified view, it is clear that the nanocarrier is in the perinuclear region rather than localized in the cytosol or the nucleus. The caveolae-dependent endocytosis traffics to the endoplasmic reticulum (ER) and Golgi apparatus through the formation of caveosomes avoiding the traffic into lysosomes.[143] This may explain the accumulation of the nanocarrier in the perinuclear region, where the ER and Golgi apparatus are found.[344] Additionally, cells commonly use the caveolae-dependent endocytosis for the regulation of lipids,[141] therefore the presence of the SLB at the surface of the UCNPs may influence the trafficking to this region of the cell.

The Stokes shift of the Nile red emission, which varies from blue (λ_{em} 484 nm, in n-hexane) to red (λ_{em} 638 nm, in pentafluorophenol) depending on the polarity of the environment,[109] can be used to localize the Nile red in different environments inside the cell. Nile red produces a yellow emission in low density lipoproteins and neutral lipids such as triacylglycerol and cholesterol, [114,345] while, in microsomal membranes (phospholipid-rich), high density lipoproteins and oleic acid, Nile red exhibits a red emission.[114,346] Nile red has been shown to have a yellow emission in lipid droplets,[117] and a red emission in lamellar bodies,[347,348] which are produced by the A549 cells. Both the SLB-UCNPs and Nile red can be excited using 980 nm excitation. The dye, Nile red is excited by a 2-photon absorption process *via* a virtual state and the SLB-UCNPs *via* upconversion. Incubation of the cells with Nile red (in the absence of the nanocarrier) served as a control (Figure 5S.5a). The resulting emission bands at 620 nm (red emission) and 584 nm (yellow emission) demonstrate two distinct environments with different polarities (Figure 5S.5b).

A representative confocal image taken using a lambda-scan configuration for the A549 lung cancer cells incubated with the nanocarrier (SLB-UCNPs loaded with Nile red) is shown in **Figure 5.5**. Different regions of the cells are highlighted (arrows in Figure 5.5a) and the corresponding spectra of each region show the characteristic emission of the Tm^{3+} ions and the Nile red (Figure 5.5b). The peak positions for the Nile red indicate different polarity environments, while the intensity of the upconverting emission peaks of Tm^{3+} ions reflects qualitatively different amounts of UCNPs in each region (grey > pink > yellow). The Nile red

quantum yield varies as a function of the polar environment thereby limiting any conclusion on the relative concentration of dye at the different regions.[111]

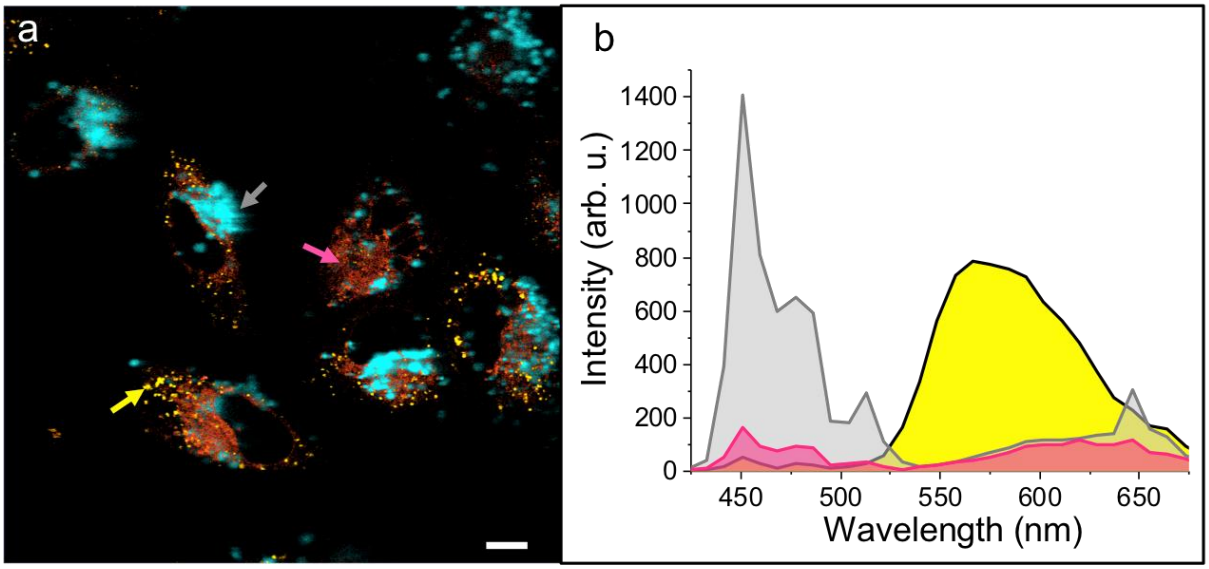

Figure 5. 5 a) Confocal image of live A549 lung cancer cells incubated with the SLB-UCNPs loaded with Nile red for 4 hours (λ_{ex} 980 nm, λ_{em} 400-700 nm). The cells were seeded at 85000 cell density with a nanocarrier concentration of 50 µg/mL in 35 mm plates. b) Emission spectra from the corresponding highlighted regions (arrows on the confocal image). Scale bar: 10 µm.

The spectra for the regions marked by the pink and grey arrows both exhibit a red emission from the Nile red indicating that the dye is in a polar phospholipid-rich environment.[114] As previously discussed, this reflects the accumulation of the SLB-UCNP in the ER and Golgi apparatus *via* the caveolae-dependent endocytosis. In addition, internalization by either the clathrin-mediated endocytosis or caveolae-dependent endocytosis mechanisms provide pathways for the SLB-UCNPs to be trafficked to different organelles including the lamellar bodies.[188 191] It may be that the nanocarriers escape the trafficking into the lysosomes through the surfactant-recycling pathway due to the presence of the SLB comprising negatively charged phospholipids and cholesterol. There are regions with high accumulation of SLB-UCNPs (grey arrow) and those

with lower accumulation of SLB-UCNPs (pink arrow). In each region, the spectra confirm that the dye is co-localized with the SLB-UCNPs, however, it cannot be unequivocally determined whether the dye remains associated with the SLB as the Golgi, ER and lamellar bodies also present a polar phospholipid environment.[176] This will be discussed further in the next section.

The spectrum taken from the region indicated by the yellow arrow, exhibits a blue shift in the Nile red emission indicating that the Nile red is now in a neutral lipid environment such as that found in the lipid bodies. The ER is known to be in contact with the lipid bodies, which would serve as a route for the SLB-UCNPs be trafficked to this organelle, whose role is to store lipids.[349] **Figure 5.6** summarizes the possible SLB-UCNPs internalization and trafficking pathways within the cell. Notably, although the Nile red clearly partitions from the SLB into the neutral lipid environment it is still co-localized with the SLB-UCNPs, albeit with low emission intensity from the Tm^{3+} of the SLB-UCNP, suggesting that only a small proportion of the nanocarriers are transported to these lipid bodies.

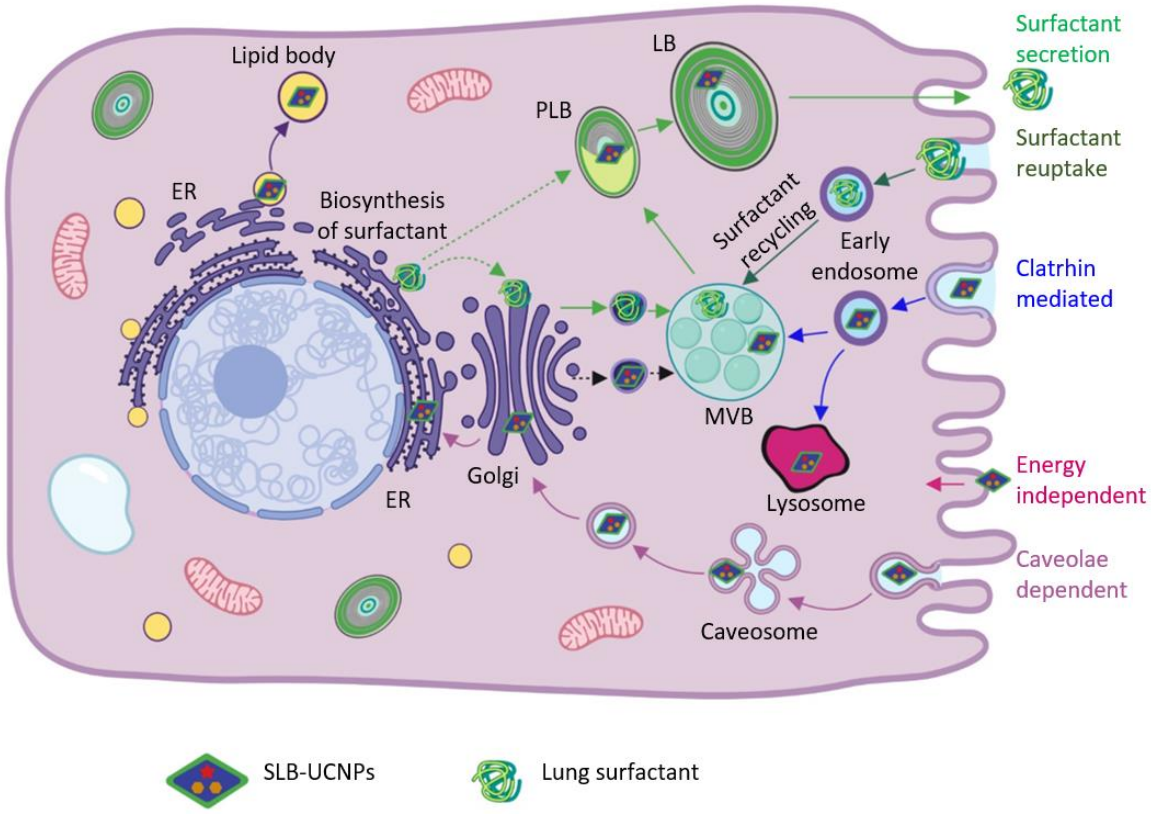

Figure 5. 6 Illustration of the internalization pathways and possible trafficking of the SLB-UCNPs in A549 lung cancer cells. The SLB-UCNPs may use clathrin-mediated and caveolae dependent endocytosis and an energy independent uptake mechanism. After clathrin-mediated endocytosis, the nanocarriers could be targeted to lysosomes for degradation or trafficked *via* the MVB/PLB network to LBs. From the caveolae-dependent endocytosis the nanocarrier could be trafficked to the Golgi apparatus and RE *via* caveosomes. Then, from the Golgi apparatus and ER some nanocarriers, after a post-Golgi sorting vesicle, could use the surfactant-biosynthesis pathway to be trafficked *via* the MVB/PLB network to LBs. At the same time, some of the SLB-UCNPs are trafficked from the ER to lipid bodies. Green: (light and dark) surfactant lifecycle in alveolar type II cells; blue: chlatrin-mediated endocytosis; red: energy independent uptake; purple: caveolae-dependent endocytosis. LB: lamellar body, PLB: prelamellar (composite) body, MVB: multivesicular body, ER: endoplasmic reticulum (figure generated using ©BioRender - biorender.com).

5.4.3 Near infrared controlled release Nile Red

An azobenzene lipid analogue di(6-{[4-(4-butylphenyl)azo]-phenoxy}-hexyl)phosphate (AZO-lipid) was incorporated inside the SLB for near infrared triggered release of the dye from the nanocarrier.[328] The radiative energy transfer from the Tm^{3+} of the SLB-UCNP to the AZO-lipid induces *trans* → *cis* photoswitching of the azobenzene, which disrupts the lipid bilayer and thus releasing the Nile red.

Dye release from the nanocarriers both with and without the AZO-lipid was evaluated *via* irradiation using 980 nm light. **Figure 5.7** shows confocal images of live cells incubated with the nanocarriers in the *x*,*y*-plane as well as the *z*-axis profile obtained from the Z-stacks mode. In the absence of AZO-lipid (Figure 5.7a-c) the blue emission of the SLB-UCNPs and the red emission of the Nile red are both distributed throughout the *z*-direction and are highly co-localized as indicated by the large proportion of white regions in the merged images. On the other hand, when the AZO-lipid is present (Figure 5.7d-f) after 15 minutes of irradiation at 980 nm, the blue emission of the nanoparticles and the red emission of the dye present different distribution profiles. Importantly, the low proportion of white regions in the merged image indicates the significantly reduced co-localization of the SLB-UCNPs and the Nile red, which appears to diffuse away from the nanoparticles. Enzymatic degradation of the lipid bilayer could potentially release the dye form the SLB-UCNP, however this process appears to be slow whereas a fast release is triggered using 980 nm excitation for 15 minutes and this process requires the presence of the photoswitchable molecule (AZO-lipid) embedded in the SLB.

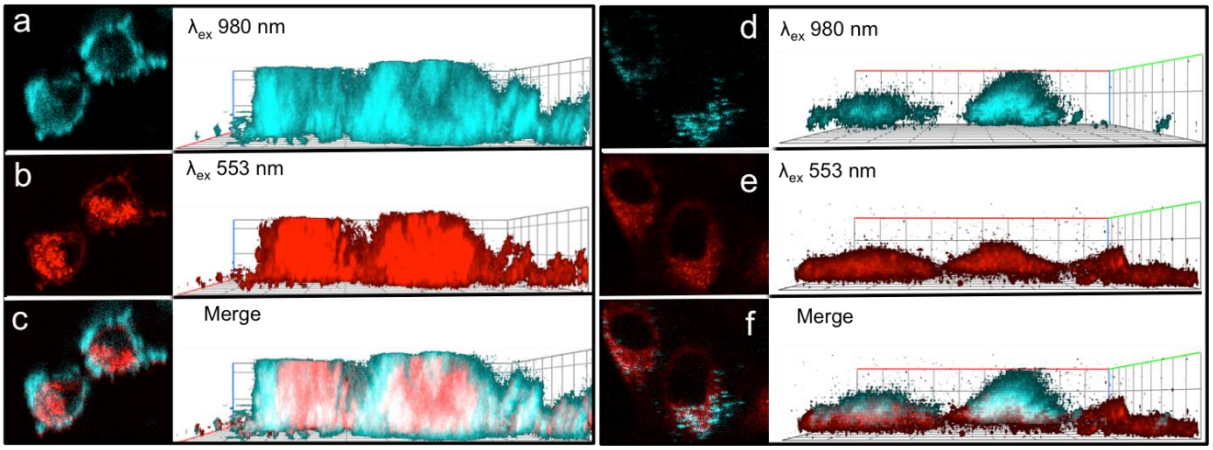

Figure 5. 7 Confocal images using the *z*-stacks mode on live A549 lung cancer cells incubated with the nanocarrier with and without the AZO-lipid after 4 hour of incubation. a-c) Nanocarrier without AZO-lipid in the SLB; d-f) Nanocarrier with AZO-lipid in the SLB. Black-background images are from the *x,y*-plane of the cells; white-background images are their corresponding images of the Z-stacks showing the *z*-axis profile. Blue represents the emission from the Tm^{3+} ions (λ_{ex} 980 nm, λ_{em} 450 nm), red represents the emission from the Nile red (λ_{ex} 553 nm, λ_{em} 620 nm) and white represents regions for which the Tm^{3+} ions and Nile red exhibit significant co-localization (merged images only).

5.5 Conclusions

Herein, we showed that UCNPs with a supported lipid bilayer coating are internalized to a lesser extent than the oleate-capped and oleate-free UCNPs. Consequently, they exhibit negligible cytotoxicity on A549 lung cancer cells while both oleate-free and oleate-capped UCNPs exhibit a small but statistically significant cytotoxicity after 72 hours. This lack of cytotoxicity may be a function of the lower uptake or the change in surface properties (charge and lipid composition) upon coating with the lipid bilayer. In particular the use of a lipid coating may play a role in the trafficking of the SLB-UCNP after internalization, while the size and shape appear to be important in the internalization process. It is proposed that the diamond-shape morphology facilitates uptake when the SLB-UCNP is oriented with the apex towards the cell i.e. with the

long axis perpendicular to the plane of the membrane. This orientation favours membrane association and subsequent wrapping of the SLB-UCNP for internalization *via* an energy independent uptake mechanism. The dominant uptake mechanisms for SLB-UCNPS into A549 cells were found to be the aforementioned energy independent pathway as well as clathrin-mediated and caveolae-dependent endocytosis.

To study the use of these SLB-UCNPs as potential photostimulated drug nanocarriers, we encapsulated the dye Nile red as a hydrophobic drug model in the SLB at the surface of the nanoparticles. Localization of the dye and the UCNP can be independently monitored using their respective emissions which showed that, after internalization, the nanoparticles traffic to the endoplasmic reticulum, Golgi apparatus, lysosomes, lipid and lamellar bodies. The Nile red was found to co-localize with the UCNPs, suggesting minimal release in the absence of an active release stimulus (i.e. with only through local biological triggers such as enzymatic degradation). Capitalizing on the optical properties of the UCNPs, we incorporated a photoswitchable molecule within the supported lipid bilayer to serve as a phototrigger upon NIR excitation of the UCNPs. In this case, a fast release of the Nile red was observed. Moreover, the Nile red appears to diffuse away from the UCNPs upon its photostimulated release. An understanding of the uptake and trafficking of lipid bilayer coated UCNPs and cancer cells may lead to more efficient nanoparticle-based nanomedicines specifically for pulmonary diseases on the distal lung. Drugs delivery that targets the ER, Golgi apparatus and lamellar bodies could be encapsulated in the SLB-UCNPs for chemotherapeutic treatment.

5.6 Supporting Information

5.6.1 Synthesis and characterization of the nanoparticles

5.6.1.1 Synthesis of oleate-$LiYF_4$:Tm^{3+}/Yb^{3+} upconverting nanoparticles (oleate-UCNPs)

Oleate-$LiYF_4$:Tm^{3+}, Yb^{3+} (0.2% Tm^{3+}, 25% Yb^{3+}) UCNPs were synthesized *via* one-pot thermal decomposition, as described in detail previously.[67,236] All reagents were purchased from Sigma-Aldrich and were used without further purification: thulium oxide (99.99+ %), ytterbium oxide (99.99%), yttrium oxide (99.99+ %), triflouroacetic acid (99%), lithium trifluoroacetate (98%), oleic acid (technical grade, 90%), and 1-octadecene (technical grade, 90%). By ICP-MS it was found that the dopant ion concentration of the nanoparticles was 0.2% Tm^{3+} and 29% Yb^{3+}.

The oleate-$LiYF_4$:Tm^{3+}/Yb^{3+} UCNPs have a faceted diamond-shape morphology with an average size of 92 nm (± 11 nm) with respect the long diagonal and 53 nm (± 4 nm) with respect the small diagonal and an aspect ratio of 1.74. The particle size distribution was obtained by measuring 300 nanoparticles using ImageJ. As previously shown,[236] the nanoparticles show a square base bipyramidal shape, for which we can calculate the surface area and volume of the average nanoparticle to be 7461 nm^2 and 43051 nm^3 respectively. From the reported density for $LiYF_4$ bulk material (3.995 g/cm^3) it was possible to calculate the mass of the nanoparticle to be 1.72 x 10^{-13} mg.[65] Additionally, the oleate UCNPs, have been shown to have a 40% of surface coverage with oleate.[236] The oleate at the surface renders the nanoparticle hydrophobic with a ζ-potential of -24 ± 1.5 mV.

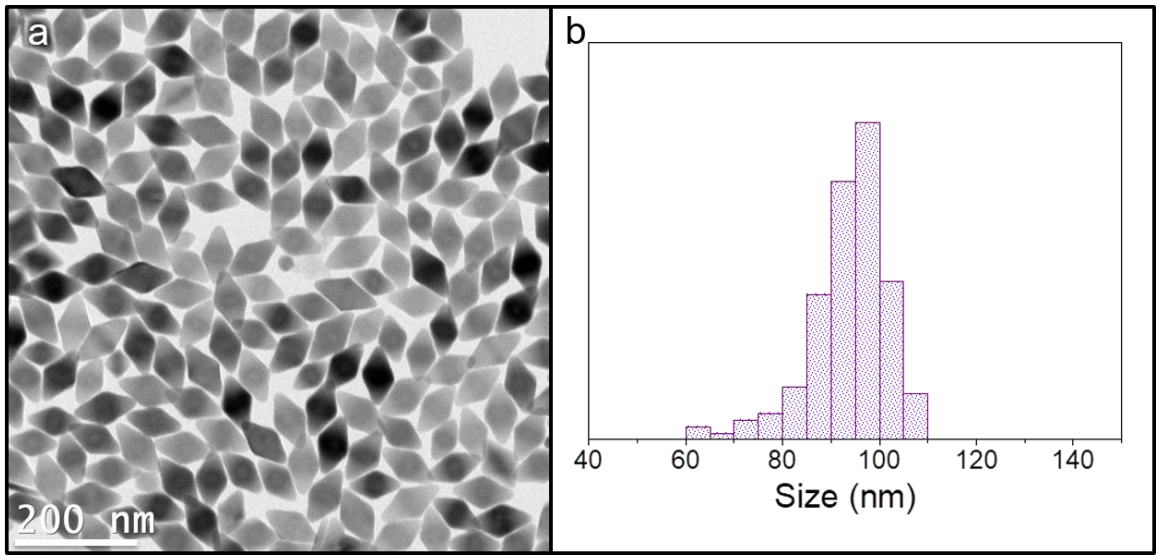

Figure 5S. 1 a) Transmission electron microscopy image of oleate-$LiYF_4$:Tm^{3+}/Yb^{3+} UCNPs (1 mg/mL in toluene). b) Particle size distribution of oleate-$LiYF_4$:Tm^{3+}/Yb^{3+} UCNPs with respect the long diagonal.

5.6.1.2 Supported lipid bilayer $LiYF_4$:Tm^{3+}/Yb^{3+} upconverting nanoparticles (SLB-UCNPs)

Oleate-$LiYF_4$:Tm^{3+}/Yb^{3+} with a supported lipid bilayer (SLB-UCNPs) were synthesized as described in detail previously.[236] 1,2-di-(9Z-octadecenoyl)-*sn*-glycero-3-phosphate (DOPA) and 1,2-di-(9Z-octadecenoyl)-*sn*-glycero-3-phosphocholine (DOPC) were purchased from Avanti Polar Lipids Inc., cholesterol (99+ %), and sodium acetate (99+%) was purchased from Sigma-Aldrich, chloroform (ACS grade) was purchased from Fisher Scientific, and HEPES (4-(2-hydroxyethyl)-1-piperazineethanesulfonic acid) was purchased from Bioshop®. All water used for the experiments was ultrapure (18.2 MΩ·cm) obtained from a Barnstead system.

These nanoparticles, referred to as SLB-UCNPs, present a soft matter shell that mimics the cell membrane with a thickness of 4.7 nm.[236] Negative stain TEM was used to characterized the SLB-UCNPs as shown previously (Figure 5.S2).[236] The SLB-UCNPs present a negative surface

charge with a ζ-potential of -50 ± 3.0 mV due to the negatively charged lipid, DOPA, that is the main component of the SLB.

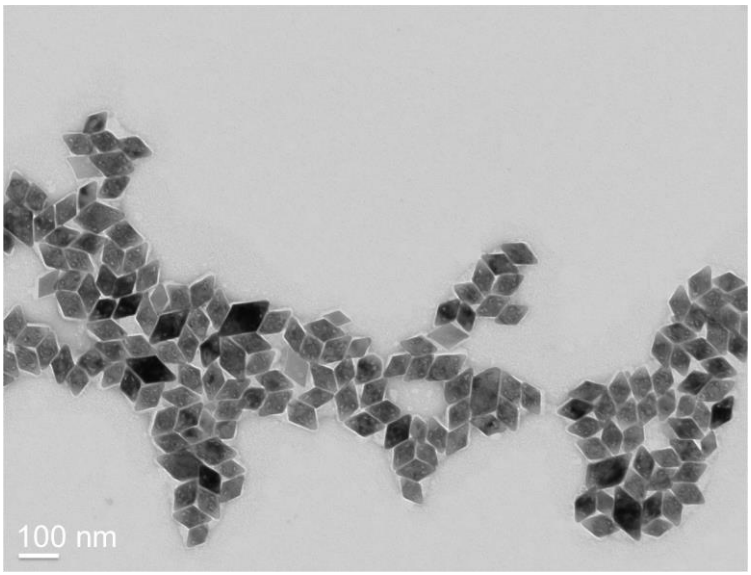

Figure 5S. 2 Negative stain-TEM image of the SLB-UCNPs (1 mg/mL) stain with 1.5% uranyl acetate. Withe layer around the nanoparticles represent the supported lipid bilayer.

5.6.1.3 Oleate-free $LiYF_4:Tm^{3+}/Yb^{3+}$ upconverting nanoparticles

The oleate at the surface of the nanoparticles was removed through an acid treatment.[86] Typically, 100 mg of nanoparticles were dispersed in 5 mL of hexanes and stirred with 5 mL of HCl at pH 2 solution. After 2 h of stirring, nanoparticles transfer from the organic layer to the aqueous layer removing the oleate at the surface of the nanoparticles. Oleic acid free nanoparticles were recovered from the aqueous layer through microcentrifugation. The oleate-free UCNPs present a positive surface charge with ζ-potential of (+12 ± 0.3 mV).

5.6.1.4 Nile red encapsulated in SLB-UCNPs (nanocarrier)

Nile red (9-Diethylamino-5Hbenzo[α]phenoxazin-5-one) was purchased from Sigma Aldrich (98%) and it was encapsulated via hydrophobic interaction with the lipids of the SLB as previously reported,[328] with one modification: hydrating the lipids cakes with the HEPES buffer for two days produced a higher yield of nanocarriers, as it facilitates the extrusion step and fewer nanoparticles are trapped in the filters. A total of 4 mole% of Nile red with respect to the total lipid in SLB was used.

5.6.1.5 Synthesis of AZO-lipid

Di(6-{[4-(4-butylphenyl)azo]-phenoxy}-hexyl)phosphate referred to as AZO-lipid was synthesized using the protocol we described previously following the synthetic route proposed by Kuiper.[246,328] All reagents were used without any further purification: butylaniline (97%), phenol (99.0+ %), carbon tetrachloride (99.9%), and pyridine (anhydrous, 99.8%) were purchased from Sigma-Aldrich; 6-bromohexanol (97%), trimethylamine (99%), and phosphorous trichloride (98%) were purchased from Alfa Aesar. The obtained yellow powder was characterized by ^{1}H NMR, ^{31}P NMR and mass spectrometry. ^{1}H NMR (500 MHz, $CDCl_3$, δ): 0.95 (t, J = 7.2 Hz, 6 H), 1.38 - 1.82 (m, 24 H), 2.68 (m, 4 H), 3.34 (s, 1 H), 4.01 - 4.07 (m, 8 H), 6.97 - 6.99 (m, 4 H), 7.27 - 7.30 (m, 4 H), 7.79 - 7.89 (m, 8 H). ^{31}P NMR (202 MHz, $CDCl_3$, δ): 1.46 (s). C) HRMS (ESI) m/z: $[M + H]^+$ calculated for $C_{44}H_{60}O_6N_4P$, 771.42475; found, 771.42450.

5.6.1.6 Nanocarrier with AZO-lipid in the SLB

Nanoparticles with a supported lipid bilayer containing AZO-lipid and Nile red were prepared by adding the AZO-lipid to the stock mixed lipid chloroform solution with the following mole ratio 50:14:7:29 (DOPA:AZO-lipid:DOPC:cholesterol) with or without Nile red (4 mole% of the total amount of lipids).[328] The samples were constantly covered with aluminum foil to prevent exposure to light and therefore keep the AZO-lipid in the stable *trans*-isomer.

5.6.1.7 Characterization of nanoparticle concentration using inductively coupled plasma mass spectrometry (ICP-MS)

ICP-MS measurements were performed to determine the nanoparticle concentration after surface modification (i.e. SLB, AZO-lipid in SLB**,** and nanocarriers with the Nile red encapsulated) and after the uptake of the nanoparticles by the A549 cells. The samples were analyzed using an Agilent 7500ce ICP-MS equipped quartz Scott-type spray chamber, an off-axis Omega lens ion focusing, an octopole reaction system with a quadrupole mass spectrometer analyzer operated at 3MHz.

Yttrium was evaluated in order to calculate the nanoparticles concentration. Multi-element solution 10 mg/L (Ce, Dy, Er, Eu, Gd, Ho, La, Lu, Nd, Sc, Sm, Tb, Th, Tm, Y, Yb) from Spex CertiPrep were used to prepare the calibration curve Y in 5% of HNO_3 solution (HNO_3, Trace metal grade from Fisher). The calibration curve was prepared in the concentration range between 0.01 ppm and 5 ppm.

To calculate the concentration of the nanoparticles or the nanocarrier 100 µL of each sample were first digested using 1000 µL of concentrated HCl (Trace metal grade from Fisher) with 100 µL of H_2O_2 (Ultratrex® Ultrapure reagent from Avantor Performance Materials, Inc.) and heated at 115 °C for 12 h under reflux. To determine the nanoparticle uptake by the A549 cells, 200 µL of each sample were first digested using 1000 µL of concentrated HCl (trace metal grade from Fisher) with 1000 µL of HNO_3 (trace metal grade from Fisher) and heated at 115 °C for 12 h under reflux.
The samples were then dried and re-dispersed in 2 mL of 5% HNO_3 prior to injection and analysis.

5.6.2 Cell Studies

5.6.2.1 Uptake of nanoparticles by A549 lung cancer cells

To investigate the uptake of SLB-UCNPs by A549 lung cancer cells using laser scanning confocal microscopy (LSMC) the nanoparticles were incubated as explained above. This time 35 mm glass bottom dishes were used and were incubated for specific times (from 0.5 h to 16 h). After the incubation time the excess of nanoparticles was washed twice with 1 mL of PBS buffer. Immediately afterwards the cells were fixed with 1 mL of 10% neutral buffered formalin (Sigma-Aldrich). After 15 min, the formalin was removed and the cells were washed three times with PBS. Finally, 1 mL of PBS was added to keep the cells hydrated. The fixed cells were imaged within a day.

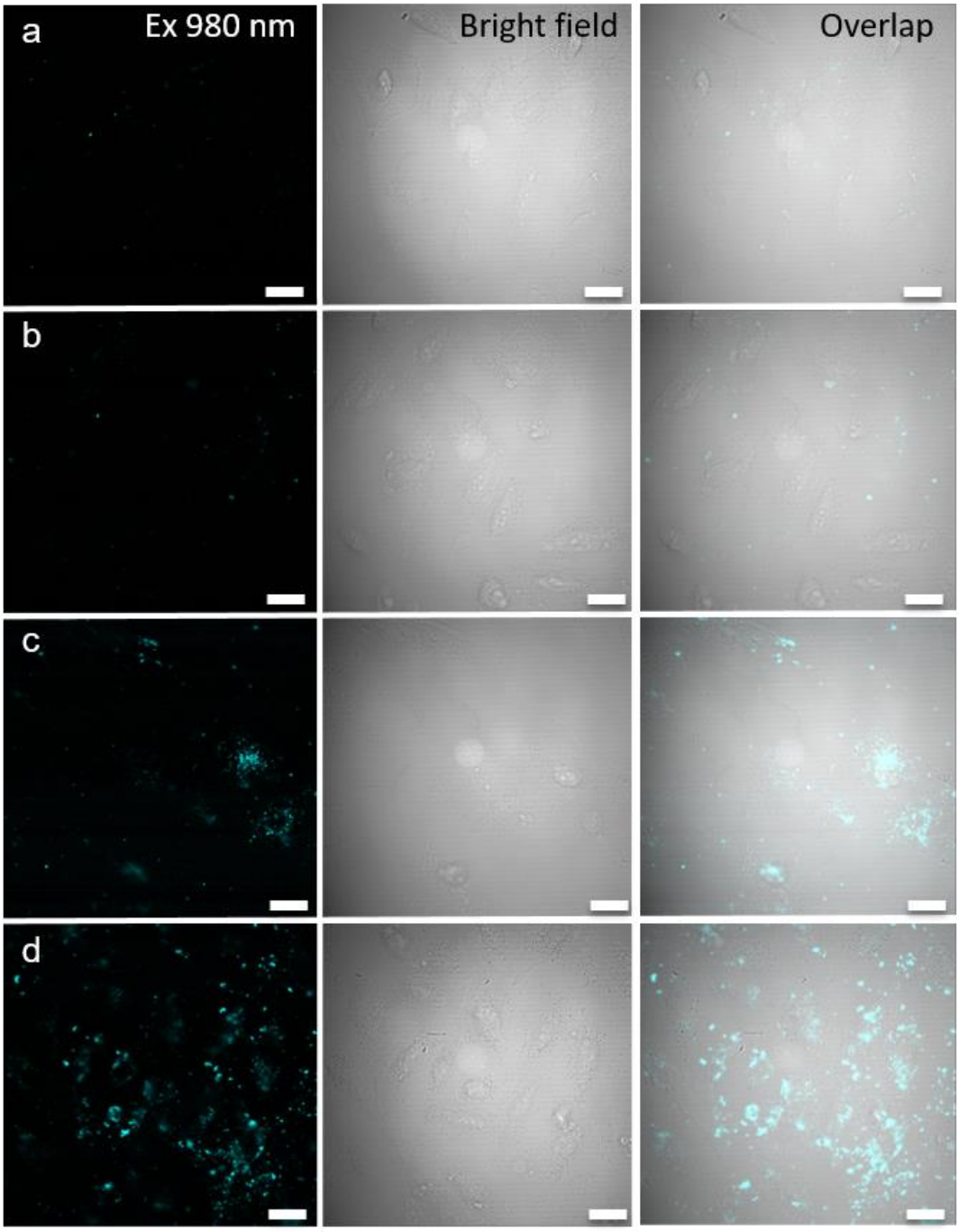

Figure 5S. 3 Confocal images of fixed A549 alveolar lung cancer cells incubated with SLB-UCNPs at different incubation times a) 0.5 h, b) 1.0 h, c) 4.0 h, and d) 16 h. (λ_{ex} 980 nm, λ_{em} 450 nm). Scale bar 20 μm

5.6.2.2 XTT Cell viability assay

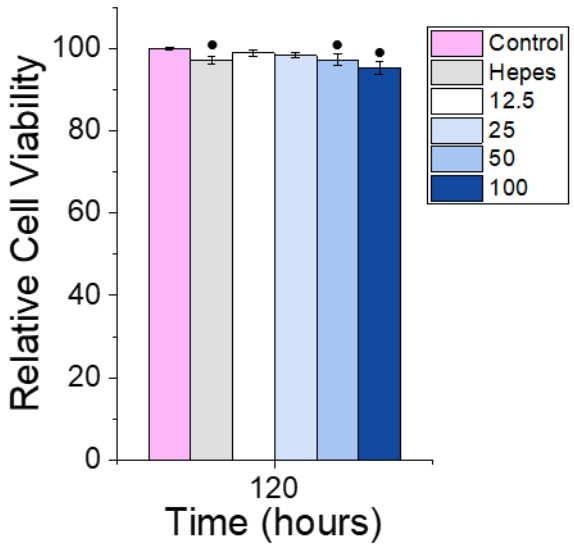

Figure 5S. 4 XTT assay for the cytotoxicity of SLB-UCNPs nanoparticles at different concentration after 120 hours of incubation at 37 °C with A549 cells. The cells were seed at 50000 cell density with the specific nanoparticle concentration in 96-well plates. Concentration is given in μg/mL. Cytotoxicity values were normalized against the cells incubated with no nanoparticles and represent the mean standard deviation (n = 5). (●) denotes statistically significant difference ($P < 0.05$).

5.6.2.3 Control experiment for the emission of Nile red

Nile red presents different emission according to the polarity of the environment. We evaluated the emission of the Nile red (in the absence of nanocarrier) inside the A549 lung cancer cells where emissions at 584 nm and at 620 nm were observed.

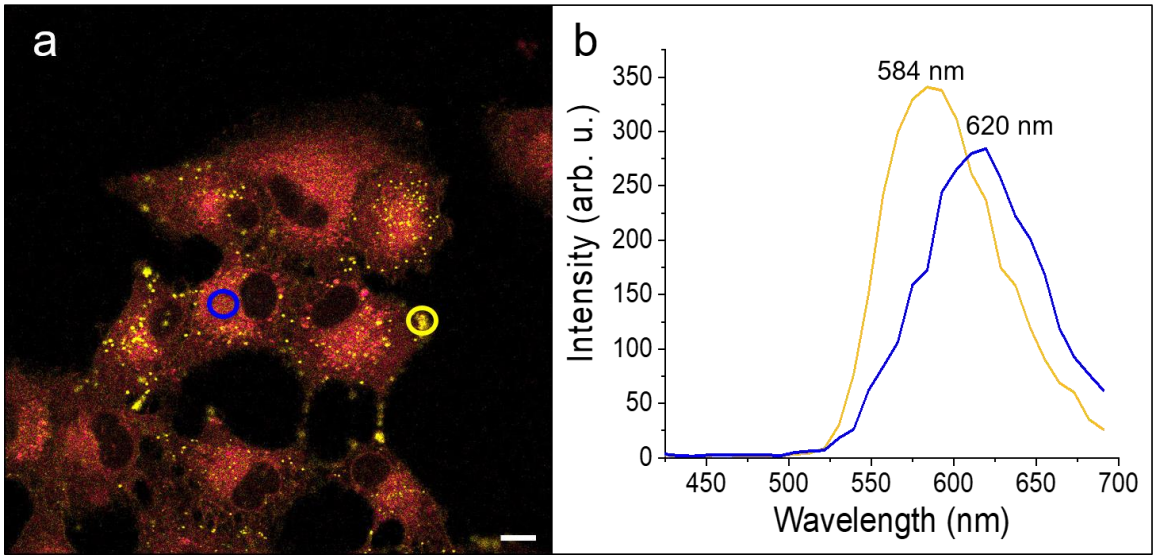

Figure 5S. 5 a) Confocal image of A549 lung cancer cells incubated with Nile red. b) Emission spectra produced form the areas enclosed within the correspondingly coloured circle in a). Scale bar 10 μm

5.6.3 Instrumentation

5.6.3.1 Laser Scanning Confocal microscope (LSCM)

A Zeiss LSM780-NLO laser scanning confocal with IR-OPO laser microscope was used for imaging the samples. The microscope is equipped with 32 GaASp detectors array between 400-700 nm. The infrared laser source is a CHAMELEON Ultra (II) with an OPO system that operates between 680-1300 nm. Additionally, the microscope is equipped with lasers at 405 nm,

458, 488 and 514 nm multiline, 553 nm and 633 nm. The microscope has a live cell chamber with CO_2 and temperature controller.

The microscope was operated using two different excitation sources (980 nm and 553 nm). The 980 nm excitation was obtained from the CHAMELEON Ultra (II) system that was operated with a 140 fs pulse (focusing mode-locked) and operated between 30-40% of the maximum power (~1W). The 553 nm laser was operated at 4% of the maximum power. A 760+ nm dichromic beam splitter was used together with filters between 410-695 nm for the 32 detectors. With this set-up, the microscope can take images at particular wavelength (single scan) or through a range of different wavelengths (lambda scan) while using a specific excitation source. It is also possible to scan at different focal planes across the *z*-axis (Z-stacks scan) using the single-scan mode. Zen 2.3 lite software was used to process the images.

5.6.3.2 Transmission electron microscopy (TEM)

The micrographs of $LiYF_4$: Tm^{3+}/Yb^{3+} were took using a Jeol JEM-2100F microscope operating at 200 kV. Samples were prepared by dropping 5 μL of sample with a concentration of 1 mg/mL in toluene onto a 300-mesh Formvar/carbon coated copper grid (3 mm in diameter) followed by the evaporation of the solvent.

5.6.3.3 Negative Stain TEM

Negative stain images were obtained using a Tecnai 12 Biotwin TEM microscope (FEI Electron Optics) equipped with a Tungsten filament at 120 kV and AMT XR80C CCD Camera System. Samples were prepared by dropping 5 μL of the sample (1 mg/mL in toluene) onto a 200-mesh carbon coated SPI grid. The drop was left on top of the grid for 1 minute before drying it softly with a filter paper. Immediately afterwards, it was stained with 5 μL of 2% uranyl acetate in 5 M NaOH solution, after 1 minute the excess solution was removed using a filter paper.

5.6.3.4 Cell counter

An Invitrogen Countess™ automated cell counter was used with trypan blue stain (0.4%) (Thermo fisher scientific). Typically, 12.5 µL of sample was mixed with 12.5 µL of trypan blue stain and added to the invitrogen countess cell counting chamber slides. Samples were measured in duplicate.

5.6.3.5 Inductively Coupled Plasma Mass Spectrometry (ICP-MS)

ICP-MS was use to determine the nanoparticles concentration after the surface modification and after the cellular uptake. The samples were analyzed using an Agilent 7500ce ICP-MS equipped quartz Scott-type spray chamber, an off-axis Omega lens ion focusing, an octopole reaction system with a quadrupole mass spectrometer analyzer operated at 3MHz.

5.6.3.6 ζ-Potential

The surface charge of the nanoparticles after surface modifications was measured using a Zetasizer Nano-S (Malvern Instruments Ltd, Worcestershire,UK). All experiments were performed using a disposable folded capillary cells (Malvern). Each sample was measured in triplicates. Each measurement comprised 10 measurements that each consist of 20 runs. Typically 100 µl of a sample with a concentration of 1 mg/mL is dissolved in 0.7 mL of ultrapure water. The concentration of the samples was ~0.15 mg/mL.

5.6.3.7 Multimode Microplate Reader

The absorbance of the XTT (cell viability assay) was measured using a Tecan infinite® 200 Pro multimode plate reader. The 96-well plates were shaken for 30 seconds before analysis using an amplitude of 1 mm. The absorption was measured at 475 nm and corrected for the background absorption at 660 nm from the cell culture media.

5.7 Author's notes and significance of this paper

This publication provides the first cellular studies with the crystal host $LiYF_4$ in upconverting nanoparticles. The results herein are of main importance for the understanding of the interactions of this nanomaterial for biological applications. This investigation studied and discussed the physicochemical properties of the nanoparticle (size, shape, and surface charged) in order to understand the nanoparticle-cell interactions. Cytotoxicity studies showed that the nanoparticles with the supported lipid bilayer do not produce cytotoxicity for up to 72 hours in lung cancer A549 cells. Studies on the cellular uptake, endocytosis mechanisms and trafficking of the nanomaterial showed that the nanoparticles internalize through different endocytosis mechanisms (clathrin-mediated, caveolae-dependent and energy independent) into the cell and transit to different cell organelles. Additionally, studies on the photo-controlled release of Nile red, as a hydrophobic model drug, encapsulated in the photoswitchable supported lipid bilayer shows that the release can be mediated *via* energy transfer from the nanoparticles using NIR light within in the cellular environment. These results show promising outcomes of this nanomaterial as a nanoparticle-based drug delivery system for hydrophobic drugs.

Additionally, knowing that this nanomaterial is not cytotoxic and can internalize into cells we foresee an additional application of this nanomaterial in fluorescence imaging to study intracellular thermal properties. Chapter 6 explores the application of the nanomaterial developed as a luminescent nanothermometer probe. Taking advantage of the design of the nanoparticles with the supported lipid bilayer and the optical properties of lanthanide-doped upconverting nanoparticles. In this case, $LiYF_4:Er^{3+}/Yb^{3+}$ UCNPs were synthesized with a supported lipid bilayer. In this chapter the thermal properties of the supported lipid bilayer were characterized. In addition, the possibility to use this nanomaterial for thermal sensing were studied by developing a model to measure the directional heat transfer between the nanoparticle, the lipid bilayer, and the surrounding environment. The use of this nanomaterial in fluorescence imaging will enable the characterization of thermal properties of biological membranes and also the heat transfer

between nanoparticles and its cellular or tissue environment. To our knowledge, this is the first nanomaterial capable of measuring directly the thermal properties of biological membranes. This application will be of main importance in cell biology and in the development of nanomaterials for biological applications. This project was developed in collaboration with Professor Luis Carlos at Aveiro University in Portugal.

Chapter 6

Thermal Properties of Lipid Bilayers Determined Using Upconversion Nanothermometry

Published as:

[1]Ana R. N. Bastos, [1] Carlos D. S. Brites, [2] Paola A. Rojas-Gutierrez, [2] Christine DeWolf, [1] Rute A. S. Ferreira, [2] John A. Capobianco,* [1] Luís D. Carlos*

Wiley-VCH Advance Functional Materials, **2019** (doi.org/10.1002/adfm.201905474)

[1] Department of Physics, CICECO - Aveiro Institute of Materials, University of Aveiro, 3810-193, Aveiro, Portugal; [2] Department of Chemistry and Biochemistry, and Centre for NanoScience Research, Concordia University, Montreal, Quebec, H4B 1R6, Canada.

6.1 Abstract

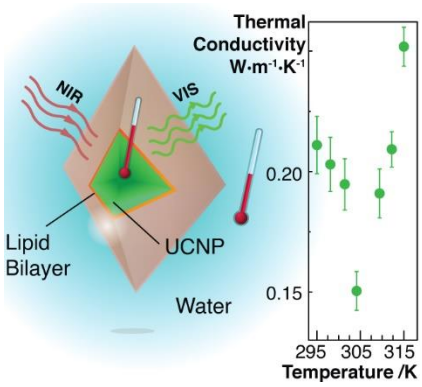

Scheme 6. 1 Graphical table of content of "Thermal properties of lipid bilayers determined using upconversion nanothermometry".

Luminescent nanomaterials have shown promise for thermal sensing in bio-applications, yet little is known of the role of organic coatings such as supported lipid bilayers on the thermal conductivity between the nanomaterial and its environment. Additionally, since the supported lipid bilayer mimics the cell membrane, its thermal properties are fundamentally important to understand the spatial variations of temperature and heat transfer across membranes. Herein we describe a new approach that enables direct measurement of these thermal properties using a $LiYF_4:Er^{3+}/Yb^{3+}$ upconverting nanoparticle encapsulated within a conformal supported lipid bilayer and dispersed in water as a temperature probe yielding the temperature gradient across the bilayer. The thermal conductivity of lipid bilayer was measured as function of the temperature, being 0.20±0.02 $W \cdot m^{-1} \cdot K^{-1}$ at 300 K. For the uncapped nanoparticles dispersed in water, the temperature dependence of the thermal conductivity was also measured in the 300–314 K range as [0.63–0.69]±0.11 $W \cdot m^{-1} \cdot K^{-1}$. Using a lumped elements model, we calculate the directional heat transfer at each of the system interfaces, namely nanoparticle-bilayer and bilayer-nanofluid, opening a new avenue to understand the membrane biophysical properties as well as the thermal properties of organic and polymer coatings.

6.2 Introduction

Temperature is a fundamental intrinsic property of all systems that governs the physical, chemical and biological properties and processes.[350–352] With respect to cellular and molecular biology, temperature can vary between cell types, environments and conditions, and as a result exerts control over cellular processes, biochemical reactions and organization/structure.[353–356]

Fluorescence imaging is a powerful method of intracellular thermometry owing to its high spatiotemporal resolution, and various types of luminescent nanothermometers have recently been developed for this purpose.[357–360] Examples include green fluorescence protein,[361] small organic molecules,[362] quantum dots,[363] polymers[364,365] and polymer dots[366] and lanthanide-doped nanoparticles.[367–369] Moreover, intracellular temperature mapping has revealed the existence of spatial variations in temperature within single cells.[361–365] However, extreme temperatures are well-known to have adverse impacts on biological systems at both extremes, *i.e.* both hypothermia and hyperthermia. These adverse impacts include cell death which has additionally generated interest in heating as a mode of selectively, eradicating unwanted cell types, for example cancer cells.[370,371] In addition, several examples of luminescent materials have been proposed for *in vivo* temperature sensing applications, including Ag_2S nanodots to monitor brain thermoregulation,[372] and lanthanide-doped nanoparticles for 2D subcutaneous dynamic thermal imaging.[373] The latter rely on the favorable optical properties of the lanthanide ions which includes the well-described process of upconversion. Upconversion is an anti-Stokes process by which near infrared (NIR) irradiation is converted into Ultraviolet-Visible and NIR emissions. The lanthanide-doped upconverting nanoparticles (UCNPs) present additional properties favorable to temperature sensing that include their resistance to photodegradation, ability to withstand high temperatures, insolubility in water generating stable colloidal solutions and chemical stability (*e.g.* lack of oxidation). In fact, UNCPs have emerged in the last decade as accurate luminescent thermometers for diverse applications,[42,287,374–376] such as understanding heat transfer in nanofluids (defined as the colloidal suspension of nanoparticles),[377] and monitoring the reverse quenching process in optoelectronic devices.[378]

Er^{3+} is commonly employed as the dopant for thermal sensing because of the thermally coupled $^2H_{11/2}$ and $^4S_{3/2}$ energy levels. The energy separation between the barycenter of these two states is $\Delta E \sim 700$ cm^{-1}, and, thus, their relative populations are temperature dependent following the Boltzmann distribution. The rate of equilibration of these two states is on the order of 10^{12} s^{-1}, which then dominates over the radiative, non-radiative and energy transfer rates.

While different nanomaterials have been proposed for *in vitro* and *in vivo* temperature sensing (as mentioned above), very little is known about the heat transfer properties between the nanoparticle and its cellular or tissue environment. An important question is whether the addition of an organic coating, to functionalize the nanoparticle for biocompatibility, water dispersibility and targeting, impacts its ability to accurately sense the local temperature, specifically if the transfer of heat from the external environment reaches the nanoparticle. If the coating comprises a lipid bilayer, then this also provides valuable information about the transfer of heat across cellular membranes. To date, the thermal conductivity across a lipid bilayer has only been estimated using computational methodologies,[379–381] as the conventional experimental electric methods (*e.g.* the 3ω-method) cannot easily access this property. For example, Youssefian *et al.* used computational methods to show that the thermal resistance was dependent on the temperature gradient across the bilayer, albeit using relatively high temperature gradients up to 68 K.[382]

Wang and Atia highlighted the lack of suitable tools for determining thermal properties at interfaces.[355,380] Thus, the need to understand heat transfer and accumulation in biological systems, arising from energy inputs to nanodevices, and the mechanisms of thermal management were cited as key questions to be addressed. Frequently the heat transfer is inferred from measurement of bilayer responses but, to our knowledge, were not directly measured or quantified.[381] Herein we describe a new experimental approach that enables direct measurement of the thermal properties of biological membranes using luminescence thermometry. The approach relies on an accurate determination of the thermal gradient across the bilayer which is only possible with the independent measurements of the core temperature inside the bilayer and the external medium temperature. The conformality of the bilayer is essential, as it has been

predicted using computational methods that the heat dissipation by structured water between a solid surface and a lipid bilayer increases with the thickness of the water layer.[380] Thus, we employ $LiYF_4:Er^{3+}/Yb^{3+}$ UCNPs encapsulated within a conformal supported lipid bilayer as luminescent thermal probes in order to calculate the temperature gradient between the particle and the surrounding medium. Moreover, we develop a steady-state temperature model based on the lumped resistance of the components that completely describes the directional heat transfer at each of the system interfaces, namely nanoparticle-bilayer and bilayer-aqueous medium, to determine experimentally the thermal conductivity of the supported lipid bilayer and its temperature dependence between 295 and 315 K. Additionally, the thermal conductivities of the $LiYF_4:Er^{3+}/Yb^{3+}$ core and of the nanofluid with $LiYF_4:Er^{3+}/Yb^{3+}$ UCNPs are calculated. Nanofluids are promising substitutes for conventional liquid coolants, due to a much higher temperature-dependent thermal conductivity (at very low particle concentrations).[383]

6.3 Results and Discussion

6.3.1 Upconverting nanoparticles and lipid bilayer capped upconverting nanoparticles

The oleate-capped $LiYF_4:Er^{3+}/Yb^{3+}$ UCNPs were synthesized using a thermal decomposition method (see Experimental for details) and show a diamond–like morphology with an average size of 86.4 ± 9.5 nm (long diagonal) by 52.2 ± 5.3 nm (short diagonal) with an aspect ratio of 1.7 (**Figure 6.1**a-c and Table 6S.1 in Supporting Information) obtained from transmission electron microscopy (TEM, Figures 6S.1 and 6S.2). From the high resolution TEM image, the distance between the lattice fringes was measured to be 4.6 Å, which corresponds to the d-spacing of the (101) planes in the tetragonal $LiYF_4$ structure. $LiYF_4:Er^{3+}/Yb^{3+}$ UCNPs coated with a supported lipid bilayer were prepared using a previously published procedure (see Experimental for details).[236]

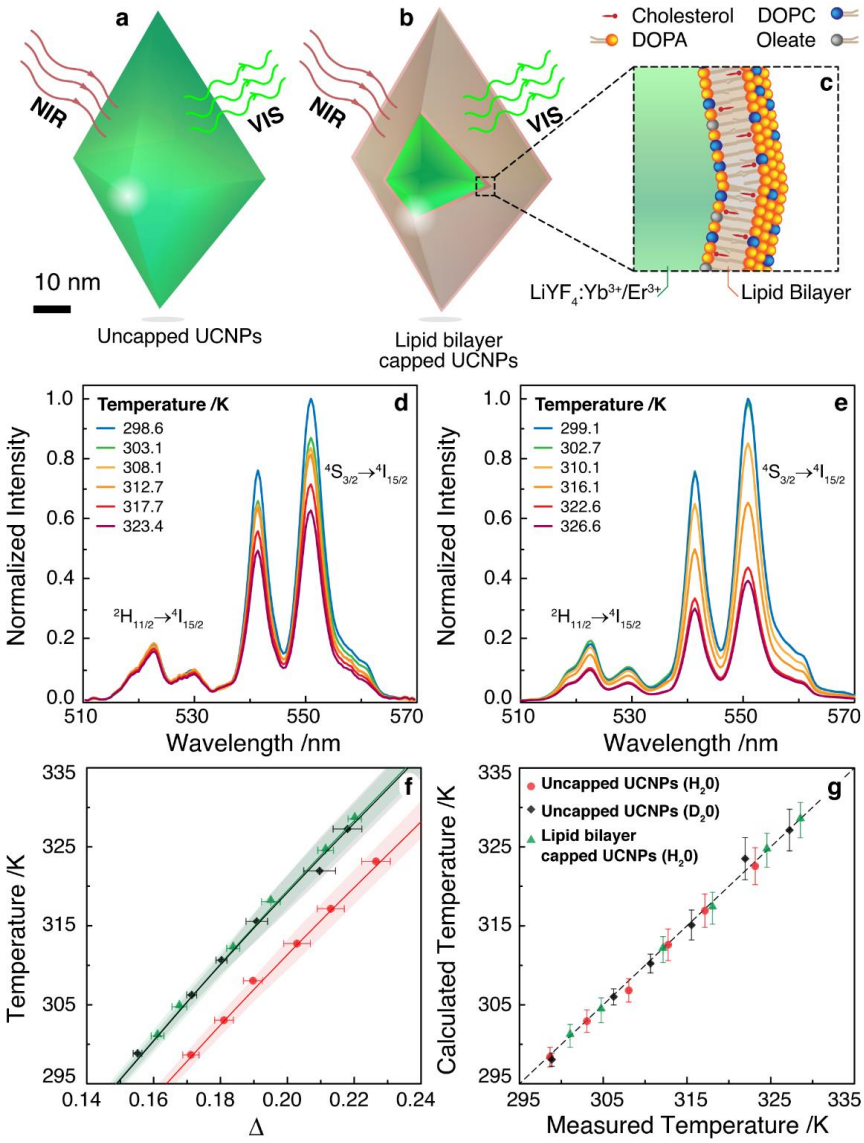

Figure 6. 1 Schematic representation of the **(a)** uncapped and **(b)** lipid bilayer capped $LiYF_4:Er^{3+}/Yb^{3+}$ UCNPs. The magnification **(c)** depicts a simplified one-dimensional model for the lipid bilayer coating. **(d)** and **(e)** Temperature dependent upconverting emission spectra of uncapped and lipid bilayer capped UCNPs dispersed in water, respectively. **(f)** Temperature calibration upon 980 nm irradiation of uncapped UCNPs dispersed in H_2O (red) and D_2O (black), and of lipid bilayer capped UCNPs dispersed in water (green). The solid lines correspond to the temperature calculated using Eq. 6S.5 and the shadowed areas are the corresponding uncertainties. **(g)** Comparison between the temperature determined using Eq.6S.2 (*y-axis*, calculated temperature) and that measured by an immersed thermocouple (*x-axis*, measured temperature) upon 980 nm irradiation. The line corresponds to $y=x$. In (d), (e), (f), and (g) the 980 nm laser power density is 67 $W \cdot cm^{-2}$.

The absorption spectra of uncapped UCNPs and lipid bilayer capped UCNPs in water suspension (1.0 $g \cdot L^{-1}$) were measured (Figure 6S.5) and the corresponding molar extinction coefficients at 980 nm are determined to be 1.5500 ± 0.0003 and 2.4500 ± 0.0001 $M^{-1} \cdot cm^{-1}$ for the uncapped UCNPs and the lipid bilayer capped UCNPs, respectively (Eq. 6S.1). The absorption cross section was also estimated, yielding values of $(1.1600 \pm 0.0002) \times 10^{-21}$ and $(1.1770 \pm 0.0008) \times 10^{-3}$ nm^2 for the uncapped UCNPs and the lipid bilayer capped UCNPs, respectively (Eq. 6S.2 and 6S.3).

The upconversion emission spectra were recorded in the 298–327 K range upon 980 nm laser excitation (Figure 6.1d,e). A significant variation in the thermometric parameter Δ, defined as the ratio between the intensity of the $^2H_{11/2} \rightarrow {}^4I_{15/2}$ and $^4S_{13/2} \rightarrow {}^4I_{15/2}$ transitions (Eq. 6.S4, Figure 6.1f), is observed for the uncapped and lipid bilayer capped UCNPs dispersed in H_2O and D_2O (Figures 6S.6 and 6S.11). Adopting a strategy reported by some of us previously,[384] the temperature of the suspensions was determined using Δ and Eq. 6S.5, knowing ΔE, the intensity ratio in the limit of low excitation power (Δ_0) and the corresponding temperature (T_0). An excellent agreement is observed between the temperature obtained from the immersed thermocouple and that calculated using Eq. 6S.5 (Figure 6.1g), demonstrating that UCNPs can operate as primary thermometers in all three nanofluids. The relative thermal sensitivity values at 300 K are 1.23, 1.26 and 1.27 $\%K^{-1}$ for the uncapped UCNPs dispersed in H_2O, the lipid bilayer capped UCNPs dispersed in H_2O, and the uncapped UCNPs dispersed in D_2O, respectively. The corresponding temperature uncertainties are 0.26, 0.20 and 0.11 K (Eqs. 6S.5, 6S.6 and details of in Section 6.6.4).

Irradiating the nanofluids with NIR radiation (980 nm) we observe a typical transient heating that is recorded by the immersed thermocouple as the temperature increase (ΔT) (**Figure 6.2**a,b). A dependence of ΔT on the laser power density (P_D), on the presence or absence of a conformal lipid bilayer and on the solvent used is observed. Note that, in this work, we will not discuss the transient regime and will focus on the temperature recorded in the stationary regime. Comparing the steady-state maximum temperature increase (ΔT_m) recorded for pure water with

that of the individual nanofluids it is possible to determine the thermal conductivities of the conformal lipid bilayer and nanofluid (and also their temperature dependences in the 291–315 K interval), and to model the heat transport for distinct heating conditions, as will be detailed below.

6.3.2 Determining the thermal conductivity of the nanofluids

For water, the experimental ΔT_m values were calculated using:[385]

$$\Delta T_m = \frac{\alpha L^2 A_b}{\kappa_w A_s} P_D \quad (6.1)$$

where α is the absorption coefficient at 980 nm, L is the laser pathlength, A_b is the laser beam spot area, κ_w is the thermal conductivity of water (the particle's surrounding medium), and A_s is the cross-sectional area of the heat flux (see Tables 6S.1 and 6S.2).[385] It should be noted that we are assuming that κ_w is constant over the range of the maximal temperature increase (ΔT_m), following the model describing the temperature increment of metallic particles under NIR irradiation.[365,386] Although there is a small temperature dependence of κ_w (in the temperature increment of Figure. 6S.15, 10 degrees, the variation in κ_w is ~2%, Figure 6S.3), the experimental results are in a good agreement with the ΔT_m values obtained from Eq. 6.1 (Figure 6S.15), indicating that we can rationalize the water heating process in the temperature range investigated using this model.

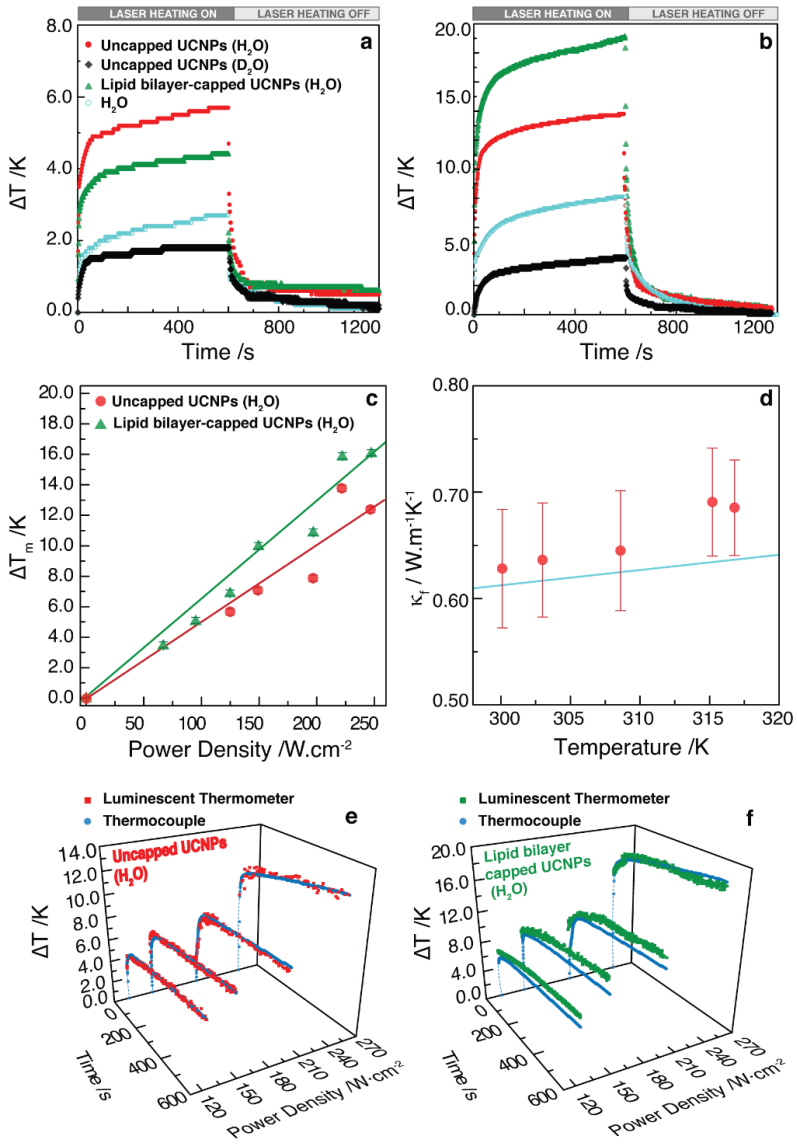

Figure 6. 2 Temperature increase profiles induced by 980 nm laser irradiation at laser power densities of **(a)** 125 and **(b)** 222 W·cm^{-2}, measured by an immersed thermocouple. In the cooling steady-state regime of the two water-based nanofluids the water's absorption of the irradiating laser pulses induces a ~0.5 degree temperature increment. **(c)** Temperature increase induced by laser excitation as function of the laser power density for uncapped UCNPs and lipid bilayer capped UCNPs dispersed in water, measured by the immersed thermocouple. The lines serve as a guide for the eyes only. **(d)** Thermal conductivity of the uncapped UCNPs dispersed in water as a function of temperature. The line corresponds to the standard reference data of the water thermal conductivity.[387] Temperature profiles of the **(e)** uncapped UCNPs and **(f)** lipid bilayer capped UCNPs dispersed in water, measured by the immersed thermocouple (circles) and luminescent thermometer (squares).

For the uncapped UCNPs dispersed in D_2O, the observed increase in temperature arises from the UCNPs radiation-to-heat conversion, as D_2O does not absorb significantly at 980 nm.[388] Following the uniform-temperature approximation (Section 6.6.5),[386] ΔT_m can be expressed as:

$$\Delta T_m = \frac{N\sigma_P}{4\pi\beta_P r_P \kappa_D} P_D \qquad (6.2)$$

where N is the number of UCNPs exposed to the laser radiation, σ_P is the nanoparticle absorption cross-section at 980 nm, β_P is the nanoparticle geometrical correction factor due to its faceted structure (Eq. 6S.16), r_P is the equivalent radius of a sphere with the same volume as the nanoparticle, and κ_D is the thermal conductivity of D_2O (particle's surrounding medium). We also assumed κ_D to be constant over the measured temperature range (in the temperature increment of Figure. 6S.15, 4 degrees, the variation in κ_D is ~1%, Figure 6S.4). Due to the instability of the UCNPs dispersed in D_2O under laser excitation, the measurements were only performed for two laser power densities. Employing the values in Table 6S.2, the resulting values predicted using Eq. 6.2 are in agreement with that obtained experimentally (Figure 6S.15), evidence that the UCNPs perform as radiation-to-heat converters.

As the water and the nanoparticles can both convert NIR radiation to heat and assuming that both contribute independently to the measured temperature increase, ΔT_m for the uncapped UCNPs dispersed in water is expressed by the linear combination of Eq. 6.1 and Eq. 6.2:

$$\Delta T_m = \frac{1}{\kappa_f}\left(\frac{\alpha L^2 A_b}{A_s} + \frac{N\sigma_P}{4\pi\beta_P r_P}\right) P_D \qquad (6.3)$$

where κ_f is the thermal conductivity of the nanofluid (uncapped UCNPs dispersed in water). Using the experimental data of ΔT_m *vs.* P_D (Figure 6.2c), κ_f was estimated for each P_D. A temperature dependence of κ_f was observed (Figure 6.2d), which is typical for aqueous nanofluids.[389] The addition of the uncapped UCNPs (volume fraction of 0.06%) yields approximately an 8% enhancement in the thermal conductivity with respect to water

([0.609–0.638] ± 0.004 $W \cdot m^{-1} \cdot K^{-1}$, in the temperature range 300–320 K, Figure 6.2d),[387] in line with those reported for nanofluids of metallic nanoparticles dispersed in water.[389] The established experimental techniques for determining the thermal conductivity at room temperature and its temperature dependence are contact electrical methods (*e.g.*, transient hot wire and 3-ω methods, respectively),[387,389,390] that use complicated experimental setups and data treatment, and are limited to non-conductive nanofluids. The optical method described here, in contrast, allows to easily measure the temperature dependence of the thermal conductivity of the nanofluid, with the advantage of being applicable to virtually any transparent fluid independently of its electrical conductivity.

6.3.3 Determining the thermal conductivity of the lipid bilayer

For the lipid bilayer capped UCNPs dispersed in water, the colloidal suspension temperature increases due to the radiation-to-heat conversion by both the water and the UCNPs (the lipid bilayer does not absorb 980 nm radiation) that are assumed to contribute independently to ΔT_m as described above (Figure 6.2c). The heat generated by the UCNPs is dissipated to its immediate surrounding medium, which in this case is the lipid bilayer. Thus the thermal conductivity of the lipid bilayer (κ_L) must be taken into account and can be estimated using Eq. 6.4:

$$\Delta T_m = \left[\frac{1}{\kappa_f}\left(\frac{\alpha L^2 A_b}{A_s} + \frac{N\sigma_L}{4\pi\beta_L r_L}\right) + \frac{N\sigma_P}{4\pi\beta_P r_P \kappa_L}\right] P_D \qquad (6.4)$$

where σ_L and β_L are the lipid bilayer absorption cross-section and geometrical correction factor (Eq. 6S.17), respectively, and r_L is the radius of a sphere with the same volume as the lipid bilayer. These parameters are given in Tables 6S.1 and 6S.2.

In this model, we are assuming that if any heat was to be generated by the lipid bilayer, it would be primarily dissipated through the water, due to the higher lipid bilayer contact surface area with the water in comparison with that of the UCNP. Therefore, the lipid bilayer

contribution in Eq. 6.4 is divided by the thermal conductivity of the nanofluid (κ_f). In this case, we assume κ_f to be the same as that calculated for the uncapped UCNPs dispersed in water, due to the low contribution of the lipid bilayer in the κ_f value. The heat generated by the UCNPs must be dissipated through the lipid bilayer and, consequently, the UCNP contribution term in Eq. 6.4 uses the lipid bilayer thermal conductivity. The σ_L value was calculated by subtracting the absorbance values at 980 nm of the two samples (Figure 6S.5), which is equivalent to considering that the absorption difference between the lipid bilayer capped UCNPs and the uncapped UCNP is only due to the conformal lipid bilayer around the nanoparticle. From the experimental data of ΔT_m *vs.* P_D (Figure 6.2c), and taking into account the temperature dependence of κ_f (Figure 6.2d), κ_L was estimated for each P_D using Eq. 6.4. Figure 6.3a shows the thermal conductivity of the lipid bilayer as a function of laser power density used in this study. To the best of our knowledge, this is the first time that the *in-situ* thermal conductivity of a lipid bilayer has been determined experimentally as function of temperature, for which there is an excellent agreement between the experimentally determined value for κ_L and the predicted ones for lipid bilayers.[35,45]

As observed in **Figure 6.3**a**,** κ_L does not follow a linear relationship with the laser power density, clearly presenting two regimes: (i) for laser power densities lower than 150 $W \cdot cm^{-2}$, the lipid bilayer thermal conductivity decreases, whereas (ii) for laser power densities above 150 $W \cdot cm^{-2}$, it increases. This is due to the marked dependence of κ_L on the temperature gradient across the bilayer that was proposed by Nakano *et al.*[391] based on simulations and determined experimentally (for the first time) in the current work. To understand these results, it is essential to recognize the role of the temperature gradient to which the lipid bilayer is subjected, that can only be accessed by measuring the temperature using both the thermocouple and luminescent thermometer.

6.3.4 Understanding the role of the lipid bilayer coating on heat transfer

Figure 6.2e,f compare the temperature profiles recorded with the immersed thermocouple and that calculated using the emission spectra and Eq. 6S.5. Within the experimental uncertainty of both measurements, the values are similar for the uncapped UCNPs dispersed in H_2O (Figure 6.2e) and D_2O (Figure 6S.16). For the lipid bilayer capped UCNPs the values measured by the luminescent thermometer are higher than those of the thermocouple (Figure 6.2f), showing that the lipid bilayer behaves as a thermal barrier between the UCNP and the water. The temperature difference between the two thermometers depends on the laser power density used: for 150 $W \cdot cm^{-2}$ the temperature difference between the two thermometers is maximized (~1.9 K), and for values higher than 222 $W \cdot cm^{-2}$ it is null within the experimental uncertainty. The temperature gradient across the lipid bilayer $T_P - T_f$, where T_P and T_f are the temperatures of the UCNP's core (measured by the luminescent thermometer) and the nanofluid (measured by the immersed thermocouple), is shown in Figure 6.3c for laser power densities up to 250 $W \cdot cm^{-2}$.

The two regimes for the κ_L dependence on the laser power density are also discerned in $T_P - T_f$. In regime (i) the lipid bilayer behaves as a thermal barrier, presenting a thermal resistance between the nanoparticle and the water, which leads to increasing temperature gradients (between the two thermometers) with increasing power density. A contributing factor to the ability of the lipid bilayer to serve as a thermal barrier was provided in the computational studies by Nakano,[391] Youssefian,[379] and Potdar,[381] which predicted a discontinuity in heat transfer at the interface between the two bilayer leaflets. In contrast, in regime (ii) the lipid bilayer thermal conductivity increases since it is saturated in the amount of thermal energy it can accept/store and therefore mitigates its ability to serve as a thermal barrier. In the saturation regime, the lipid bilayer allows the heat exchange between the UCNP and the water, eventually leading to no UCNP-water temperature gradient at a power density of 247 $W \cdot cm^{-2}$.

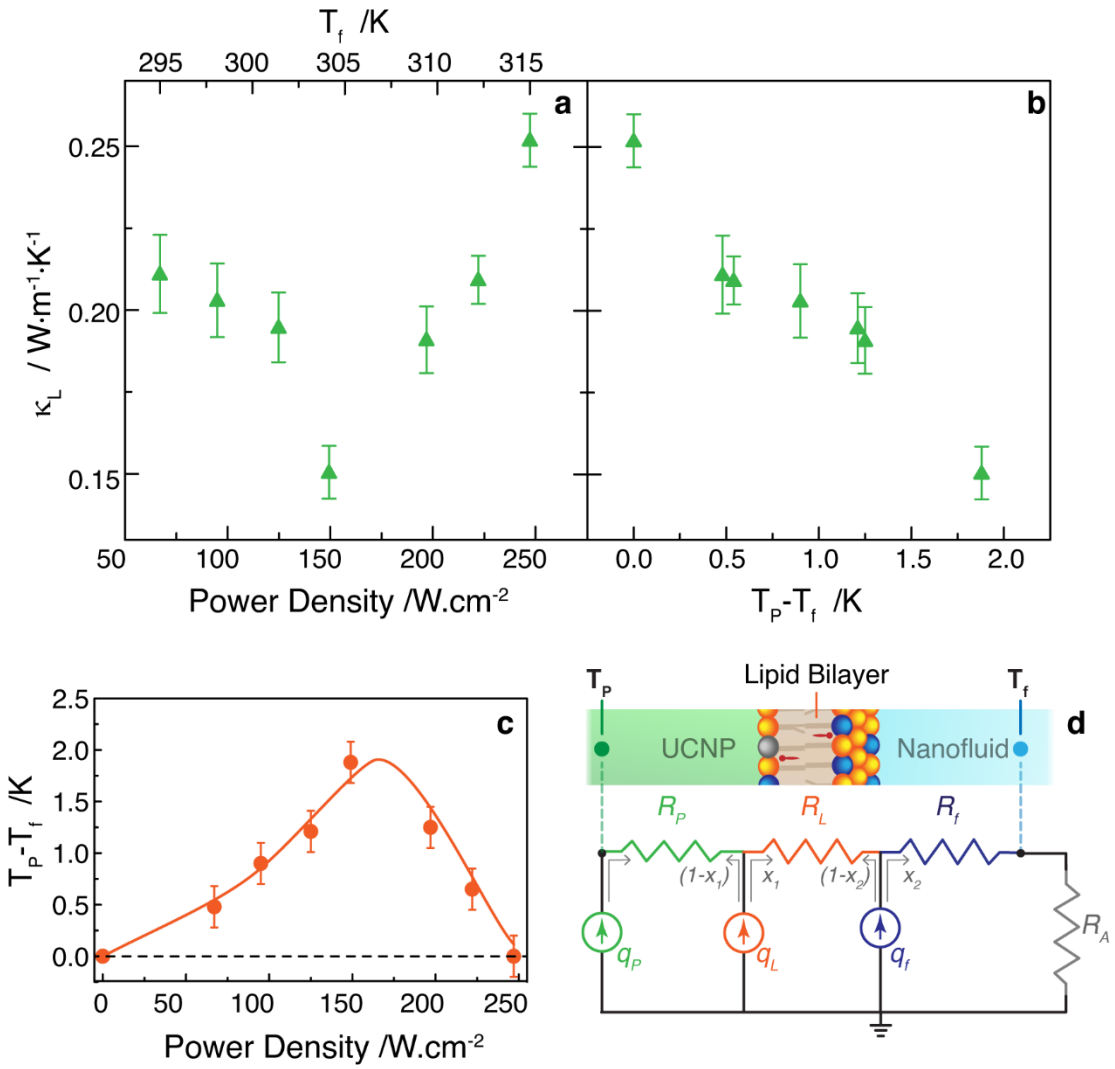

Figure 6. 3 Thermal conductivity of the lipid bilayer as a function of **(a)** laser power density or **(b)** temperature gradient between the upconversion thermometer and the immersed thermocouple at the stationary regime. **(c)** Temperature difference in the stationary regime ($T_P - T_f$) for lipid bilayer capped UCNPs dispersed in water, obtained experimentally (symbols) and calculated using Eq. 6.8 (line). **(d)** One-dimensional lumped elements of the thermal circuit model for the lipid bilayer capped UCNPs. The ground symbol denotes the reference temperature, and the arrows represent the heat flows. R_A is thermal resistance describing the convective heat transfer from the nanofluid container to the surrounding quiescent air.

Youssefian *et al.* used computational methods to predict that the thermal conductivity would increase at higher temperature gradients due to the increased thermal resistance at the interface of the two bilayer leaflets.[382] At first glance this appear to contrast our results. However, as in their work the temperature gradient was calculated considering the heat flow in the opposite direction of that imposed in the model discussed here the two trends for the temperature dependence of the thermal conductivity are, in fact, consistent.

Additionally, the thermal conductivity of the uncapped UCNPs (κ_P) can also be determined by rationalizing the heat transfer process based on the one-dimensional lumped elements model (Figure 6.3d).[392,393] In this model, the UCNPs, lipid bilayer and water are considered as independent heat sources denoted by q_P, q_L and q_f, respectively. The thermal contact resistances are taken as negligible in comparison with the conductive thermal resistances, denoted by R_P, R_L and R_f, for the UCNPs, lipid bilayer and water, respectively, which are given by:

$$R_P = \frac{1}{4\pi\beta_P r_P \kappa_P};\ R_L = \frac{1}{4\pi\beta_L r_L \kappa_L};\ R_f = \frac{L}{A_s \kappa_f}. \qquad (6.5)$$

The heat flow for UCNPs, lipid bilayer and water are given by:

$$q_P = N\sigma_P P_D;\ q_L = N\sigma_L P_D;\ q_f = \alpha L A_b P_D. \qquad (6.6)$$

The heat generated within the UNCPs flows outward, crossing the lipid bilayer to the surrounding medium, water (positive direction). Any heat originating in the lipid bilayer would be divided into a fraction x_1 moving towards the water and the remaining $(1-x_1)$ moving towards the particle's core. Finally, heat released by the water is distributed amongst the bulk water (fraction x_2) and inwards to the lipid bilayer $(1-x_2)$. The values of x_1 and x_2 were calculated using the thermal resistances:

$$x_1 = \frac{R_L + R_f}{R_P + R_L + R_f};\ x_2 = \frac{R_f}{R_P + R_L + R_f}\ . \tag{6.7}$$

Using the lumped elements model, the steady-state temperature gradient across the lipid bilayer $T_P - T_f$ can now be expressed as:

$$\begin{aligned} T_P - T_f = {} & q_P(R_P + R_L + R_f) + q_L x_1(R_L + R_f) - q_L(1 - x_1)R_P \\ & + q_f x_2 R_f - q_f(1 - x_2)(R_P + R_L) \end{aligned} \tag{6.8}$$

Accordingly to this model and to the κ_f and κ_L values estimated before, the UCNP core thermal conductivity (κ_P) was calculated by fitting Eq. 6.8 with the experimental $T_P - T_f$ values (Figure 6.3c), yielding to a value of 7.23±0.40 $W \cdot m^{-1} \cdot K^{-1}$ which is in agreement with values known for $LiYF_4$ crystals at room temperature.[394,395]

6.4 Conclusions

Herein we investigated the impact of an organic coating, specifically a supported lipid bilayer, on the ability of the UCNPs to measure temperature. We developed a model to ascertain whether the temperature measured by the nanoparticle using luminescence and that of the surrounding medium using a thermocouple are the same, and to determine the temperature dependence of the thermal conductivity of the lipid bilayer. $LiYF_4:Er^{3+}/Yb^{3+}$ UCNPs encapsulated within a conformal supported lipid bilayer and dispersed in H_2O or D_2O work as primary thermometers with a maximum thermal sensitivity of 1.27 $\%K^{-1}$ and a minimum temperature uncertainty of 0.11 K. For the uncapped UCNPs dispersed in water, the temperature increment induced both by the water and the particles permitted to estimate the temperature dependence of the nanofluid thermal conductivity, that show a up to ~8% enhancement, relatively to the values of pure water. In the case of uncapped UCNPs, in either H_2O or D_2O, the good agreement between the

thermocouple and the luminescent thermometer indicates full thermal equilibrium. On the other hand, in the case of the lipid bilayer capped UCNP, a temperature gradient is observed and found to depend on laser power density. The gradient arises due to both the water and the UCNP acting as independent radiation-to-heat converters. We experimentally determined a lipid bilayer thermal conductivity ($0.20\pm0.02\ W\cdot m^{-1}\cdot K^{-1}$ at 300 K) that decreases as a function of the temperature gradient across the lipid bilayer, which until now has only been predicted using numerical simulations. Furthermore, using a one-dimensional lumped elements model we demonstrate that at low power densities the lipid bilayer can serve as a thermal barrier, limiting the heat transfer between the UCNP and water. However, once a threshold power density (about $150\ W\cdot cm^{-2}$) has been exceeded, the bilayer can no longer serve as a thermal barrier, and the temperature differential between the two thermometers decreases until thermal equilibrium is reached. This must be taken into consideration when using coated nanoparticles for luminescence nanothermometry, especially in biological applications in which the UCNPs are used to measure the intracellular temperature. In such cases, where a coated particle (or an uncapped particle that acquires a protein corona) are used, the luminescent thermometer may not accurately reflect the cell temperature. Moreover, as the supported lipid bilayer mimics the cell membrane, the proposed method to estimate its thermal conductivity and understand its role on heat transfer has significant implications due to the importance of understanding the spatial variations of temperature and heat transfer across membranes.

6.5 Experimental Section

6.5.1 Materials

Oleate-capped $LiYF_4$ nanoparticles doped with Er^{3+} (0.6%) and Yb^{3+} (29%) $LiYF_4:Er^{3+}/Yb^{3+}$ UCNPs, were synthesized as described previously.[67] The removal of the oleate was achieved via treatment with HCl as described by Bogdan *et. al*.[86] These uncapped UCNPs are dispersed in either ultrapure water (18.2 MΩ·cm obtained from a Barnstead system) or D_2O (99.9% obtained from Sigma-Aldrich). $LiYF_4:Er^{3+}/Yb^{3+}$ UCNPs coated with a supported lipid bilayer were prepared without removal of the oleate coating using a previously published procedure.[37] The

lipids 1,2-di-(9Z-octadecenoyl)-sn-glycero-3-phosphate (DOPA) and 1,2-di-(9Z-octadecenoyl)-sn-glycero-3-phosphocholine (DOPC) were purchased from Avanti Polar Lipids Inc. Cholesterol (99+ %) and all synthetic reagents were purchased from Sigma-Aldrich. The lipid bilayer was prepared in a 64:7:29 DOPA:DOPC:Cholesterol ratio in HEPES buffer. Assuming no loss of oleate, the final bilayer composition was estimated to be Oleate:DOPA:DOPC:Cholesterol (21:51:5:24).[236]

6.5.2 Upconverting nanoparticle structural and chemical characterization

The images of oleate-capped $LiYF_4:Yb^{3+}/Er^{3+}$ UCNPs were collected using a Jeol JEM-2100F microscope operating at 200 keV. The sample was prepared by dropping the nanoparticle dispersion (1.0 g L^{-1} in toluene) onto a 300-mesh Formvar/carbon coated copper grid (3 mm in diameter) followed by evaporation of the solvent. Negative stain images were obtained using a Tecnai 12 Biotwin TEM microscope (FEI Electron Optics) equipped with a Tungsten filament at 120 keV and AMT XR80C CCD Camera System. The sample was prepared by dropping 5 µL of sample solution (1.0 g L^{-1}) onto 200-mesh carbon coated SPI grid and leaving it to be adsorbed during 1 minute before drying it gently with a filter paper. Immediately afterwards, it was stained with 5 µL of 2% uranyl acetate solution and after 1 minute the excess of uranyl acetate solution was removed using a filter paper.

ICP-MS measurements were carried out to determine the nanoparticle concentration after coating the UCNPs with the supported lipid bilayer. The samples were analyzed using an Agilent 7500ce ICP-MS equipped quartz Scott-type spray chamber, an off-axis Omega lens ion focusing, and octopole reaction system with a quadrupole mass spectrometer analyzer operated at 3MHz. Details of the methods can be found in ref.[236] and summarized in the Supplementary Information.

6.5.3 Visible-NIR absorption spectroscopy

Visible and NIR absorption spectra were recorded at room temperature, using a dual-beam spectrometer Lambda 950 (Perkin-Elmer) with a 150 mm diameter Spectralon integrating sphere over the range 200-1200 nm with a resolution of 1.0 nm. The baseline was recorded with two

10 mm path-length quartz cuvettes (2 polished windows) containing the reference fluid, H_2O or D_2O. The molar extinction coefficient was estimated from the Lambert-Beer law.

6.5.4 Dynamic temperature measurements

The pure water and the nanofluids were irradiated by a pulsed laser (BrixX 980-1000 HD) at 980 nm with power densities ranging from *ca.* 65 to 250 $W \cdot cm^{-2}$. In the heating regime, the water and the nanofluids were irradiated during 600 s with a pulse frequency of 1.5 MHz, and the consequent temperature increase was measured over time, using an immersed thermocouple (K-type, 0.1 K accuracy) in the water and the nanofluids, and also by upconversion thermometry in the nanofluids. For water, the cooling regime is achieved turned off the pulsed laser and the consequent temperature decrease was measured with the above-mentioned thermocouple. For the nanofluids, however, because the laser is required for the excitation of the nanoparticles the cooling regime was achieved using a much lower pulsed frequency (0.25−0.50 Hz) and a linewidth between 0.100 and 0.250 s, in order to allow the temperature decrease and its measurement using upconversion thermometry and the thermocouple. In both regimes, the emission spectra of the nanofluids were recorded by a portable spectrometer (MAYA Pro 2000, Ocean Optics) with an integration time of 0.500 and 0.250 s, for the nanofluids with the uncapped and lipid bilayer capped UCNPs, respectively. The integration time was chosen in order to maximize the number of recorded spectra, and the spectrum signal-to-noise ratio.

6.5.5 Thermal conductivity

Using the steady-state maximum temperature increase recorded with an immersed thermocouple for each of the individual nanofluids at different laser power densities, the thermal conductivities of the nanofluid and the conformal lipid bilayer were estimated as function of temperature using Eq. 6.3 and Eq. 6.4, respectively. Comparing the temperature values measured by the thermocouple and by the luminescent thermometer in the capped UCNPs dispersed in water, and considering the lumped elements model (Eq. 6.8), the thermal conductivity of the UCNP was estimated.

6.6 Supporting Information

6.6.1 Determination of UCNP concentration and physical properties

Inductively Coupled Plasma Mass Spectrometry (ICP-MS) measurements were performed to determine the concentration of the lipid bilayer capped UCNPs as reported previously.[236,328] The concentration of yttrium was determined in order to calculate the UCNP concentration. A multi-element solution 0.010 $g \cdot L^{-1}$ (Ce, Dy, Er, Eu, Gd, Ho, La, Lu, Nd, Sc, Sm, Tb, Th, Tm, Y, Yb) from Spex CertiPrep was used to prepare the calibration curve of yttrium in 5% of HNO_3 solution (HNO_3, trace metal grade from Fisher). The calibration curve was prepared in the concentration range 0.01 ppm to 10 ppm. 100 μL of sample was digested using 1000 □L of concentrated HCl (Trace metal grade from Fisher) with 100 μL of H_2O_2 (Ultratrex® Ultrapure reagent from Avantor Performance Materials, Inc.) and heated at 115°C for 12 h under reflux. The samples were dried, re-dispersed in 2 mL of 5% HNO_3, diluted 20-fold and then injected and analyzed for yttrium concentration.

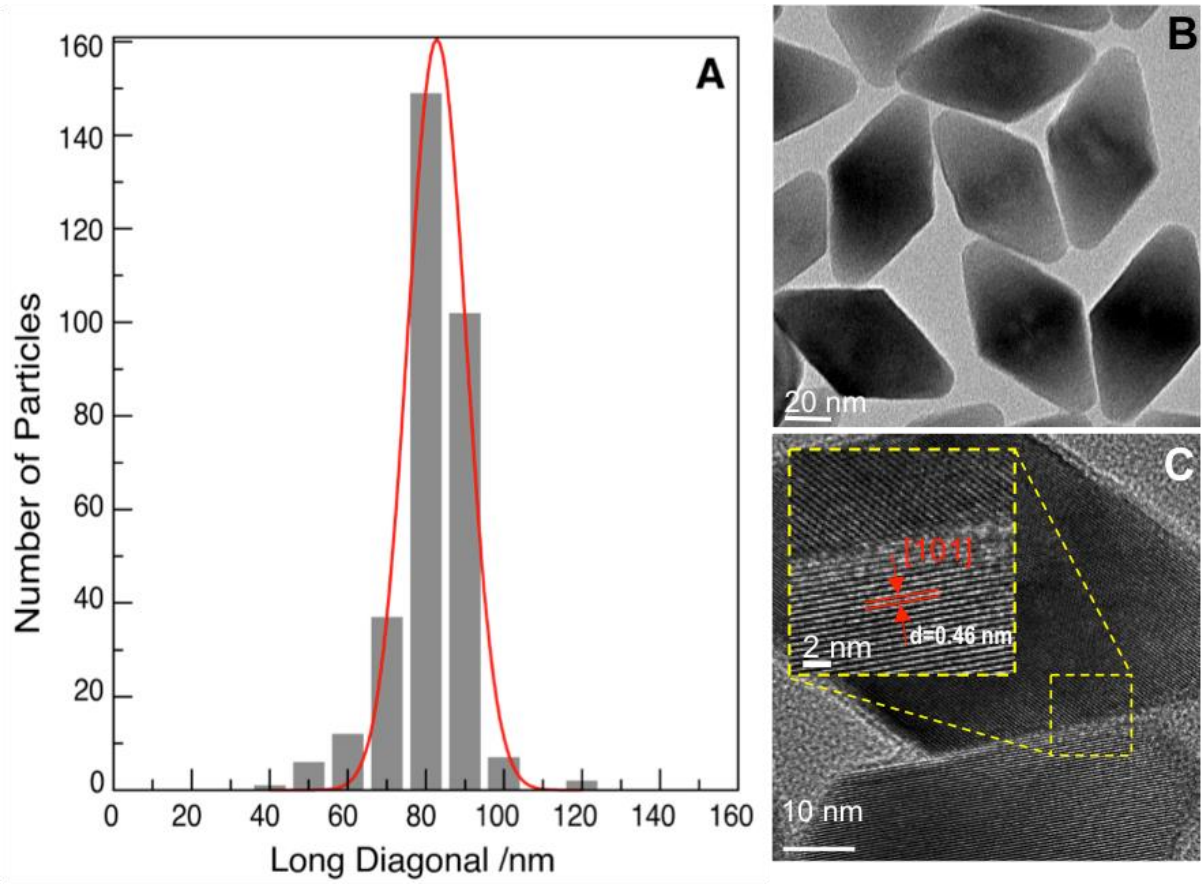

Figure 6S. 1 (a) Particle size distribution with respect the long diagonal. The particle aspect ratio is 1.65. The average particle size distribution is based on the analysis of 300 nanoparticles. (b) TEM image of oleate capped $LiYF_4:Er^{3+}/Yb^{3+}$ UCNPs. (c) HR-TEM of the oleate capped $LiYF_4:Er^{3+}/Yb^{3+}$ UCNPs showing the lattice fringes.

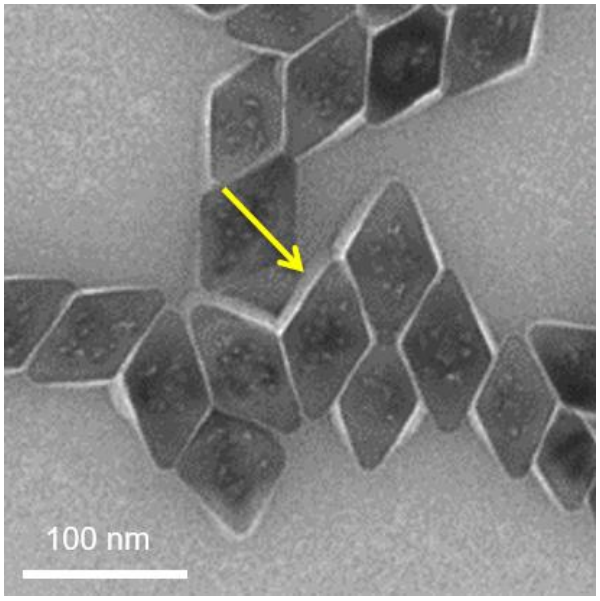

Figure 6S. 2 Negative stain TEM image of $LiYF_4:Er^{3+}/Yb^{3+}$ UCNPs coated with a supported lipid bilayer (highlighted by the yellow arrow). Stain: uranyl acetate at 2%.

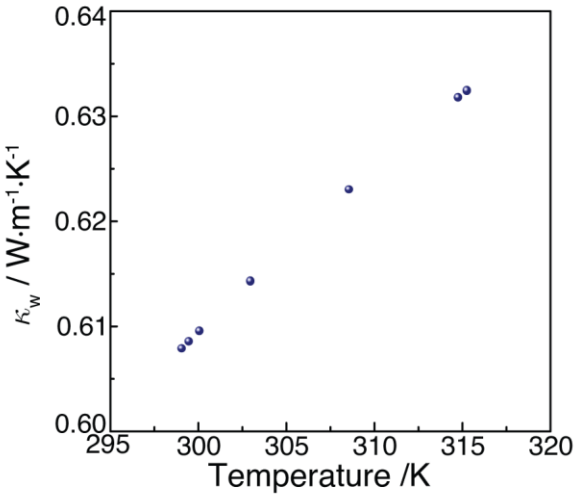

Figure 6S. 3 Standard reference data for the thermal conductivity of water as function of temperature.[387]

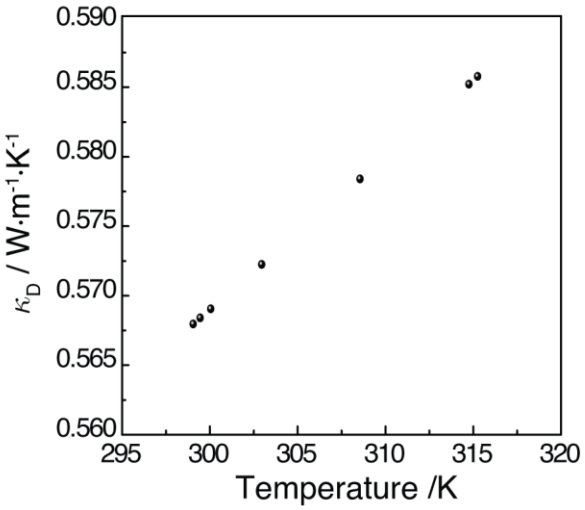

Figure 6S. 4 Standard reference data for the thermal conductivity of D_2O as function of temperature.[396]

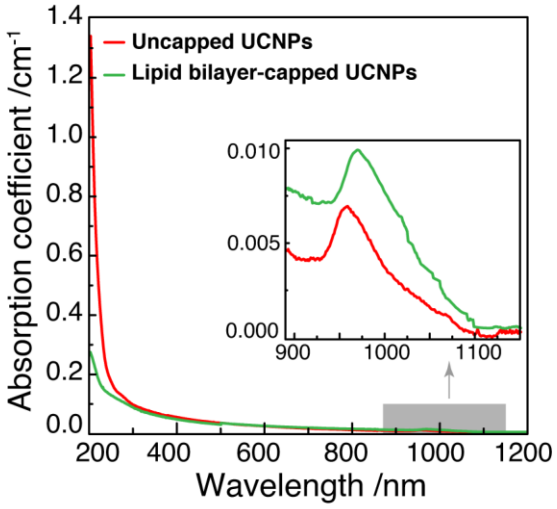

Figure 6S. 5 Visible NIR room temperature absorption spectra of uncapped UCNPs and lipid bilayer capped UCNPs dispersed in water. The inset presents a magnification of the spectral region, 875-1150 nm, showing the absorption band at 980 nm characteristic of the $^2F_{7/2} \rightarrow {}^2F_{5/2}$ absorption of Yb^{3+}.

Through the absorption spectra, the nanoparticles molar extinction coefficient at 980 nm (ε) was determined by the Beer-Lambert Law, Eq. (6(6S.1):

$$A = \varepsilon c L \tag{6S.1}$$

where A is the absorbance, c the concentration of nanoparticles in the nanofluid and L is the length of the light path (1 cm). The absorption cross section (σ) was also estimated using Eq. (6(6S.2):

$$\sigma = \frac{\alpha}{N}; \tag{6S.2}$$

where α is the absorption coefficient, N is the atomic number density given by

$$N = \frac{\rho N_A}{M} \tag{6S.3}$$

where ρ is nanoparticle density, N_A is the Avogadro number, and M is the molar mass.

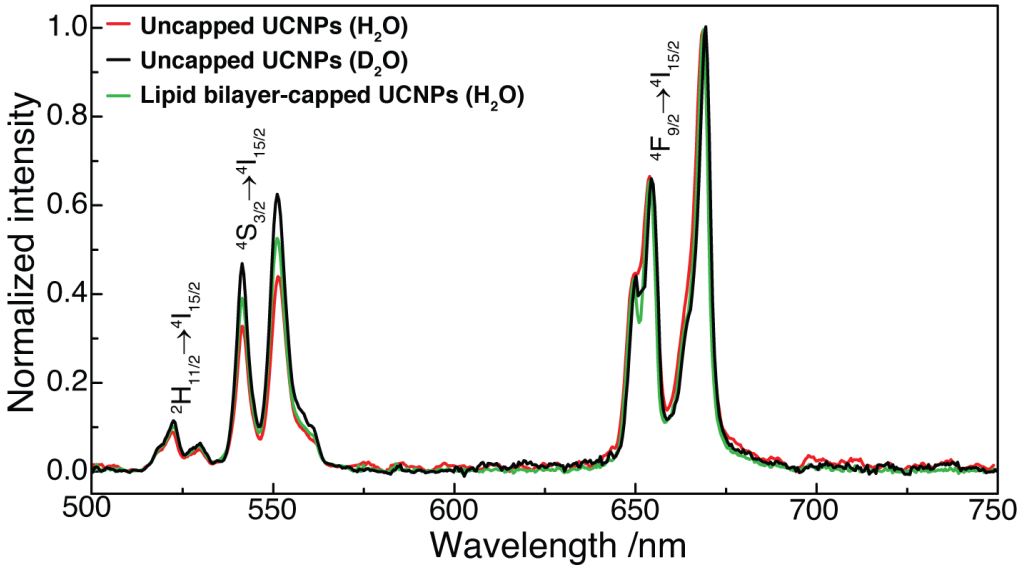

Figure 6S. 6 Normalized emission spectra acquired upon 980 nm excitation (149 $W \cdot cm^{-2}$) for each of the nanofluids. The Er^{3+} transitions are labeled. The ratios between the red and green emissions are, respectively 2.17 and 1.57 for uncapped UCNPs dispersed in water and D_2O, and 1.81 for the lipid bilayer capped UCNPs dispersed in water.

6.6.2 Photoluminescence setup

A Hellma Analytics quartz cuvette (104F-10-40) was filled with 0.80 mL of nanofluid (defined as the colloidal comprising the upconverting nanoparticles with or without the lipid bilayer and the corresponding solvent).

A pulsed laser (BrixX 980-1000 HD) operating at 980 nm was focused through an optical lens (7.5 cm focal distance) to irradiate the $LiYF_4:Yb^{3+}/Er^{3+}$ nanofluid placed in a quartz cuvette. To quantify the laser power density (P_D) delivered to the sample, the optical power and beam profile at the focal point were measured using a power meter (FieldMaxII-TOP OP-2 Vis,

Coherent), a CCD camera (BC106N-VIS/M, Thorlabs) and neutral density filters (NE10B-B, NE13B-B and NE20B-B, Thorlabs).

The detection system to collect the emission spectra uses an optical fiber (QP450-1-XSR, Ocean Optics) connected to a portable spectrometer (MAYA Pro 2000, Ocean Optics) which is controlled by a homemade MatLab® graphical user interface for real-time acquisition (integration time of 0.500 s).

The conversion from wavelength to energy units and the Jacobian transformation of the intensity values were performed as shown in Section 6S.3. The baselines of the emission spectra were corrected, and the integrated areas of the $^2H_{11/2} \rightarrow {}^4I_{15/2}$ (I_H, 510–535 nm) and $^4S_{3/2} \rightarrow {}^4I_{15/2}$ (I_S, 535–570 nm) transitions of the Er^{3+} ions were obtained. The thermometric parameter Δ was calculated for each recorded emission spectrum using:

$$\Delta \equiv \frac{I_H}{I_S} \qquad (6S.4)$$

6.6.2.1 Thermometer calibration

The intensity to temperature calibration of the nanofluids used the BrixX 980-1000 HD laser at frequency of 1.5 MHz in order to get approximately a continuous wave irradiation mode. The emission spectra (and subsequently the corresponding thermometric parameter Δ) were recorded in the temperature range 298–327 K and using an acquisition window of 50 s (100 readings). The temperature is increased at one side of the cuvette holding the nanofluid by thermal contact with a homemade Peltier system (0.1 K sensitivity) and recorded using an immersed thermocouple (0.1 K accuracy, K-type, VWR). To ensure that the nanofluids reached the steady-state temperature, a time interval of 900 s was allowed between consecutive temperature measurements. The temperature (T) was determined from the emission spectra by applying the following equation:[384]

$$\frac{1}{T} = \frac{1}{T_0} - \frac{k_B}{\Delta E} \ln\left(\frac{\Delta}{\Delta_0}\right) \quad (6S.5)$$

where T_0 corresponds to the temperature in the limit of null laser-induced heating, k_B is the Boltzmann constant, ΔE is the energy difference between the barycenter of the thermally coupled energetic levels, and Δ_0 the thermometric parameter at T_0. These parameters were calculated to validate the $LiYF_4:Yb^{3+}/Er^{3+}$ nanoparticles in the nanofluids as primary thermometers.

The energy difference ΔE between the barycenter of the $^2H_{11/2}$ and $^4S_{3/2}$ levels was estimated from the high spectral resolution emission spectra recorded using a Fluorolog$^{3®}$ Horiba Scientific (Model FL3-22) spectrofluorometer, with a TRIAX iHR320 single emission monochromator (fitted with a 1200 grooves/mm grating blazed at 500 nm, reciprocal linear density of 2.6 nm/mm), coupled to a FL1073 Horiba photomultiplier, using the lateral face acquisition mode. The excitation source was the BrixX 980-1000 HD laser at frequency of 1.5 MHz. The emission spectra were corrected considering the instrumental response of the spectrofluorometer. From the emission spectra, the ΔE was inferred by fitting the envelope of the $^2H_{11/2} \rightarrow {}^4I_{15/2}$ and $^4S_{13/2} \rightarrow {}^4I_{15/2}$ transitions using Gaussian functions. The barycenters of the $^2H_{11/2}$ and $^4S_{13/2}$ levels were calculated by a weighted arithmetic mean using the fitted area and peak energy of each Gaussian function. The energy gap ΔE was the difference between the barycenters of the transitions, yielding values of 775 ± 38 and 792 ± 42 cm^{-1} for the uncapped UCNPs in H_2O and D_2O, respectively, and 785 ± 36 cm^{-1} for the lipid bilayer capped UCNPs in D_2O (Figure 6S.7).

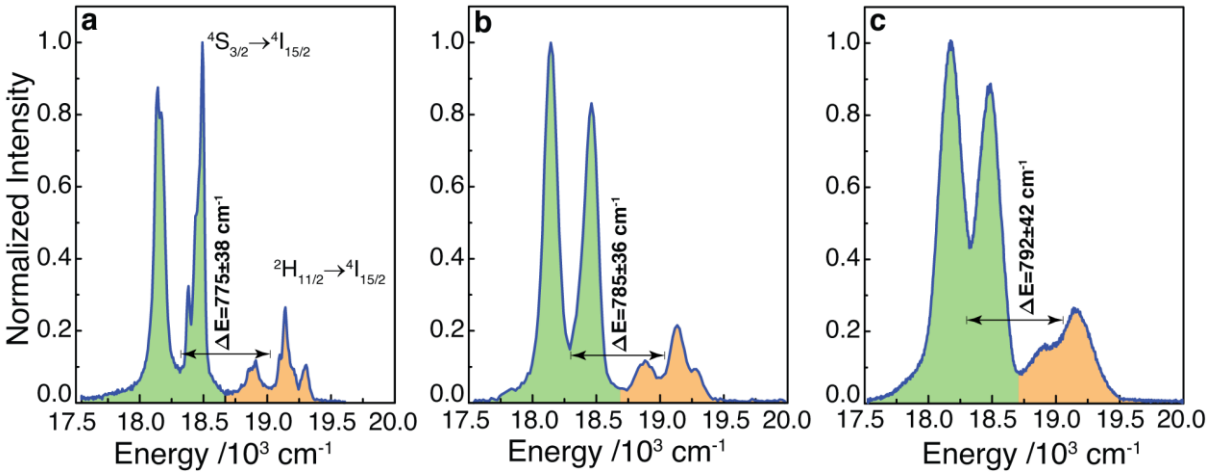

Figure 6S. 7 Normalized emission spectra acquired with 980 nm excitation (125 W·cm^{-2}) used to determine the energy gap, ΔE, of (a) uncapped UCNPs dispersed in water, (b) lipid bilayer capped UCNPs dispersed in water, (c) uncapped UCNPs dispersed in D_2O. The shadowed areas correspond to the energy ranges considered for each transition, and ΔE results from the difference between the barycenters of the transitions.

The Δ_0 values were obtained from the intercept of the linear regression of Δ as function of the laser power density (P_D), as shown in Figure 6S.8 and Figure 6S.9. The intercept corresponds to Δ_0 (Δ in the absence of laser excitation) when the sample temperature is 300 K (T_0, measured by the immersed thermocouple). The estimated Δ_0 values are given in Table 6S.3.

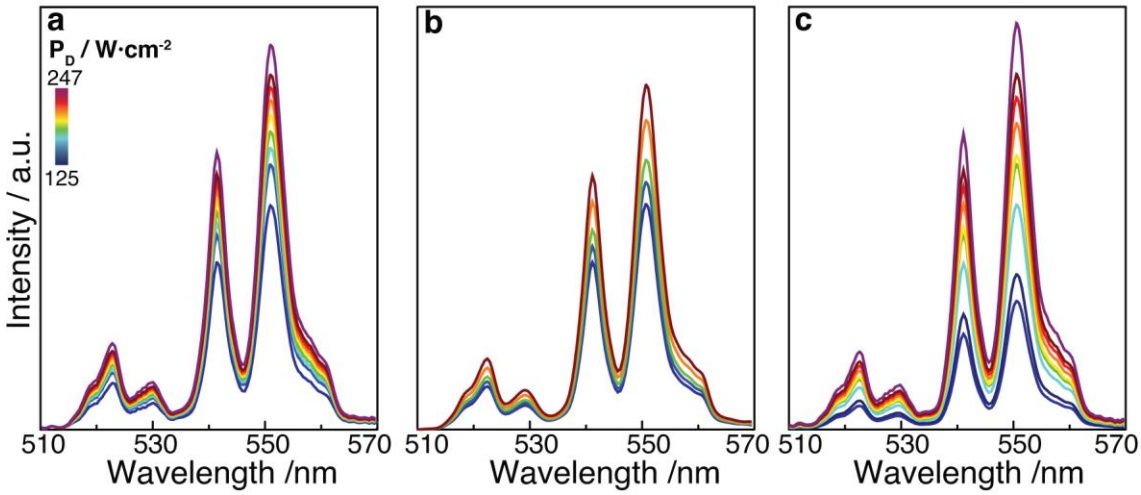

Figure 6S. 8 Upconversion emission spectra of (a) uncapped UCNPs dispersed in water, (b) lipid bilayer capped UCNPs dispersed in water, and (c) uncapped UCNPs dispersed in D_2O upon irradiation with 980 nm laser at different laser power densities.

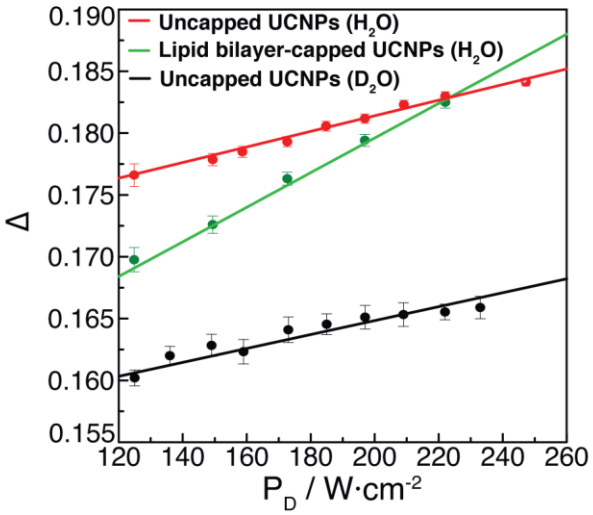

Figure 6S. 9 Dependence of the thermometric parameter Δ on the laser power density for all nanofluids. The solid lines represent the best linear fit to experimental data (r^2>0.99). The fitting parameters are given in Table 6S.3.

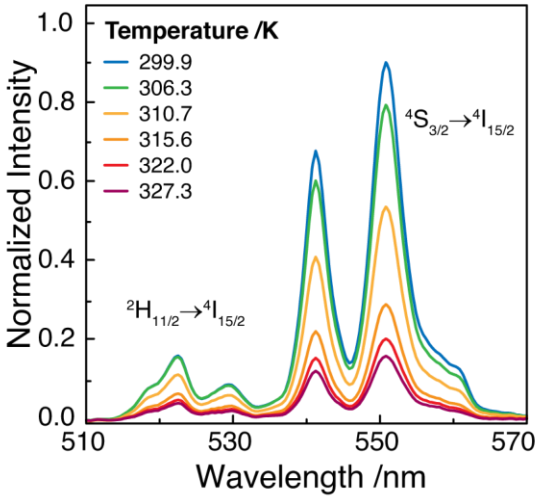

Figure 6S. 10 Temperature dependent upconverting emission spectra of uncapped UCNPs in D_2O upon 980nm excitation (67 $W \cdot cm^{-2}$).

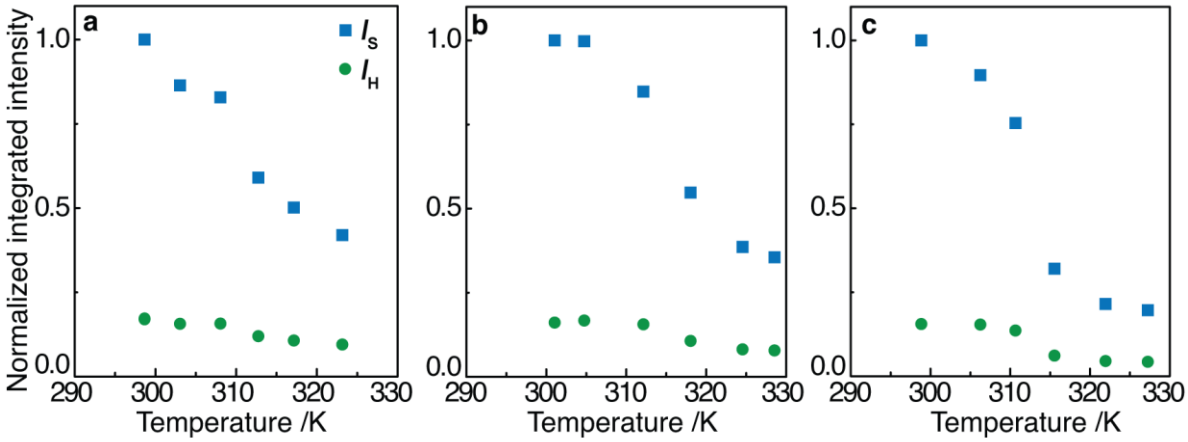

Figure 6S. 11 Integrated emission intensities of the spectral regions I_H ($^2H_{11/2}\rightarrow{}^4I_{15/2}$, 510–533 nm, green) and I_S ($^4S_{3/2}\rightarrow{}^4I_{15/2}$, 533–570 nm, blue) for (a) uncapped UCNPs dispersed in water, (b) lipid bilayer capped UCNPs dispersed in water, and (c) uncapped UCNPs dispersed in D_2O, upon 980 nm excitation (67 $W \cdot cm^{-2}$).

6.6.2.2 Laser power density calculations

To calculate the laser power density, the optical power (P_L) and the beam profile were measured by placing a power meter (FieldMaxII-TOP OP-2 Vis, Coherent) and a CCD camera (BC106N-VIS/M, Thorlabs), respectively, in the position where the sample will be positioned during all measurements. Through the 2D projection of the beam profile (inset of Figure 6S.12), the intensity in each pixel was correlated to the optical power measured and divided by the pixel area (6.45×6.45 μm^2). Then, an average laser power density was computed considering only the values higher than 36.8% (1/*e*, cut-off value for Gaussian beams), Figure 6S.12.

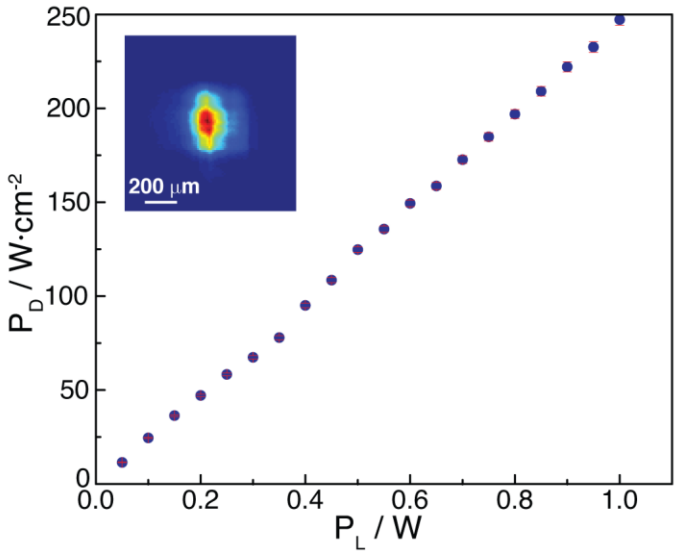

Figure 6S. 12 Laser power density as a function of the laser power as defined in the laser control software. The inset corresponds to the 2D projection of the beam profile for a laser power density of 125 $W \cdot cm^{-2}$.

6.6.2.3 Jacobian transformation

In order to properly treat the data for quantitative analysis, the signal data was converted from wavelength to energy units in all acquired spectra using Eq. (6S.6):

$$E = \frac{1}{\lambda \times 10^{-7}} \tag{6S.6}$$

where E is the energy in units of cm^{-1}, and λ is the wavelength in nm units. The Jacobian transformation given below was used to rescale the intensity values as a function of energy units:

$$I(\mathrm{E}) = I(\lambda)\frac{d\lambda}{dE} = \frac{I(\lambda)}{E^2 \times 10^{-7}} \tag{6S.7}$$

where $I(E)$ and $I(\lambda)$ are the intensity as function of energy and wavelength, respectively.

6.6.3 Thermometric characterization of the luminescent thermometers

To assess the thermometer performance, two figures of merit were calculated, the relative thermal sensitivity of the particles and the temperature uncertainty. The relative thermal sensitivity S_r indicates the relative change of Δ per degree of temperature change, and is defined by:

$$S_\mathrm{r} = \frac{1}{\Delta}\left|\frac{\partial \Delta}{\partial T}\right| = \frac{\Delta E}{k_\mathrm{B} T^2} \tag{6S.8}$$

where ΔE is the separation between the thermally coupled energy levels, k_B is the Boltzmann constant, T is the absolute temperature and Δ is the thermometric parameter. The error related to the sensitivity (δS_r) was derived from the errors of the parameters used in the calculation, as defined by:

$$\delta S_\mathrm{r} = \frac{\delta \Delta E}{k_\mathrm{B} T^2} \tag{6S.9}$$

where $\delta\Delta E$ is the ΔE error. The temperature uncertainty δT is the temperature resolution, *i.e.* the smallest temperature change that can be detected in a given measurement. The uncertainty of the thermometer temperature is given by:

$$\delta T = \frac{1}{S_{\mathrm{r}}}\frac{\delta\Delta}{\Delta} \tag{76S.10}$$

where $\delta\Delta/\Delta$ is the relative error in the thermometric parameter.

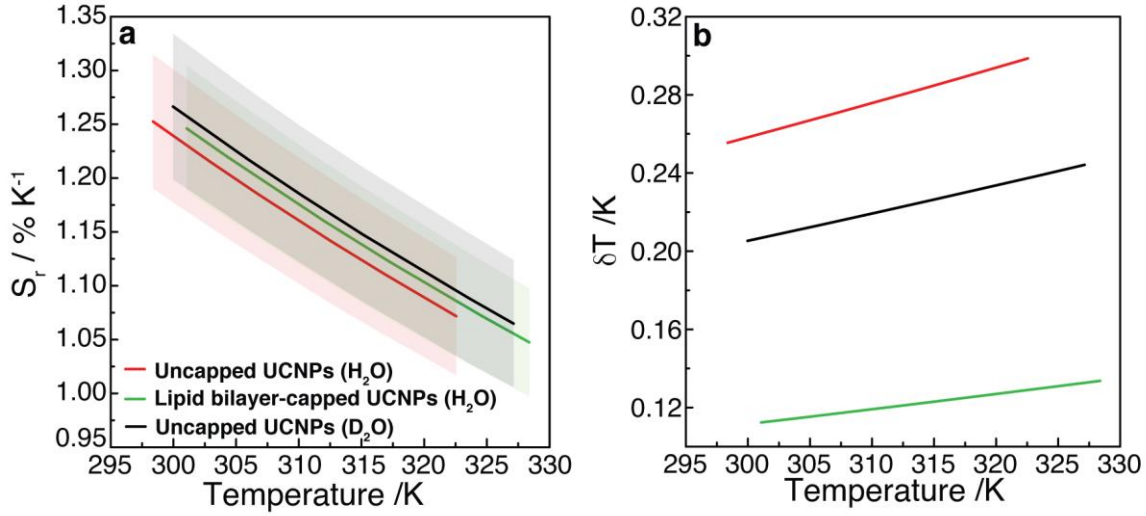

Figure 6S. 13 (a) Relative thermal sensitivity calculated using Eq. ((**6S.8**), the shadow area corresponds to the respective error calculated using Eq. (6S.9). (b) Temperature uncertainty calculated using Eq. (66S.10) for all nanofluids.

6.6.4 Model for the stationary regime

As the UCNPs are under external illumination, they will function as controlled sources of heat. To quantitatively analyze the increase of temperature in a single nanoparticle, the steady-state heat transport equation can be solved using the heat generated from the absorption of light. In the steady-state regime, the thermal diffusion equation is given by:

$$\nabla \cdot [\kappa(\mathbf{r})\nabla T(\mathbf{r})] = -p(\mathbf{r}) \tag{6S.11}$$

where $T(\mathbf{r})$ is the temperature distribution produced by an external heat source of power density $p(\mathbf{r})$ in an inhomogeneous medium characterized by a thermal conductivity which is position dependent $\kappa(\mathbf{r})$, and $\mathbf{r}$ represents the position vector. Considering, a spherical nanoparticle of radius R and the uniform-temperature approximation (*i.e.* in equilibrium, the temperature is uniform inside the nanoparticle), Eq. (6S.11) produces a temperature increase profile ΔT outside the particle given by a Coulomb potential:

$$\Delta T(\mathrm{r}) = \begin{cases} \Delta T_{\mathrm{NP}}, & r < R \\ \Delta T_{\mathrm{NP}} \dfrac{R}{r}, & r > R \end{cases} \tag{6S.12}$$

where r is the scalar distance to the nanoparticle center, ΔT_{NP} is the nanoparticle uniform temperature increase, generated by the total absorption power Q, as depicted in Eq. (6S.13).

$$Q = \int d\mathbf{r} p(\mathbf{r}) = \sigma P_{\mathrm{D}} \tag{6S.13}$$

where σ is the absorption cross section and P_{D} is the irradiance of the incoming radiation (power per unit of surface). Relating this with the Coulomb potential produced by a uniformly charged sphere in a homogeneous medium with an effective permittivity (κ plays the role of the local permittivity), ΔT_{NP} can be written as:

$$\Delta T_{\mathrm{NP}} = \frac{\sigma P_{\mathrm{D}}}{4\pi R\kappa} \qquad (6S.14)$$

For non-spherical UCNPs, Baffou *et al.*[386] proposed to use a dimensionless geometrical correction factor β such that the ΔT_{NP} is defined as:

$$\Delta T_{NP} = \frac{\sigma P_{\mathrm{D}}}{4\pi \beta_{\mathrm{P}} r_P \kappa} \qquad (6S.15)$$

where r_{P} is the radius of a sphere with the same volume as the particle. As the UCNPs have a faceted structure, the geometrical correction factor β_{P} was calculated assuming an ellipsoid morphology, Eq. (6S.16):

$$\beta_{\mathrm{P}} = \exp\left\{\sqrt{1 + 0.0416 \ln^2(D/1.85d)} + 0.092 \ln(D/1.85d) - 1\right\} \qquad (6S.16)$$

where D and d are the long and small diagonals of the nanoparticle, respectively.[386] For the lipid bilayer, the geometrical correction factor was estimated assuming a ring structure, Eq. (66S.17):

$$\beta_{\mathrm{L}} = 1.021 + 0.17442 \ln^2\left(\frac{D}{d} - 0.625\right) \qquad (6S.17)$$

6.6.5 Lumped elements thermal circuit

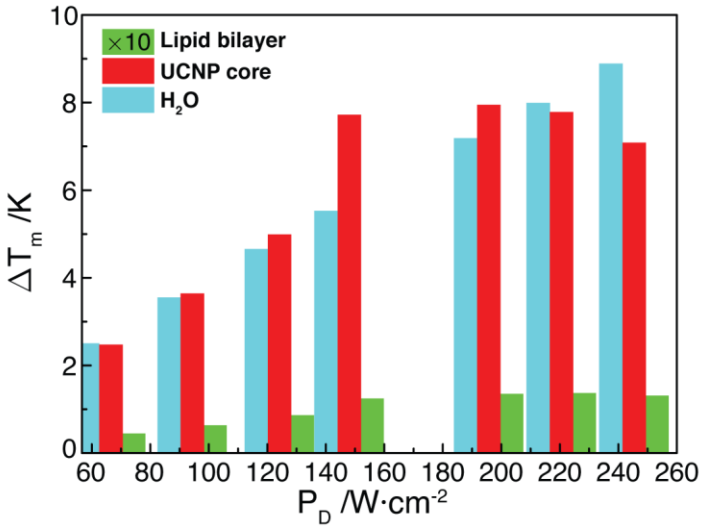

Figure 6S. 14 Contribution of each heat source (water, UCNP core and lipid bilayer) to the temperature increase induced by laser excitation as function of the laser power density for lipid bilayer capped UCNPs dispersed in water, measured by the immersed thermocouple. The lipid bilayer contribution has a magnification of ×10 for better visualization.

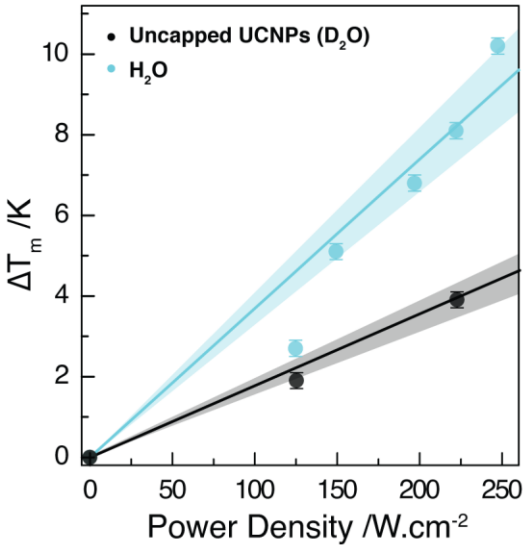

Figure 6S. 15 Maximum temperature increase induced by laser irradiation for water and uncapped UCNPs dispersed in D_2O, measured with a thermocouple. The line corresponds to the theoretical model described by Eq. (6.1) and (6.2) for water and uncapped UCNPs dispersed in D_2O, respectively. The shadowed areas correspond to the theoretical model error which is derived from the uncertainty of the parameters used to calculate it.

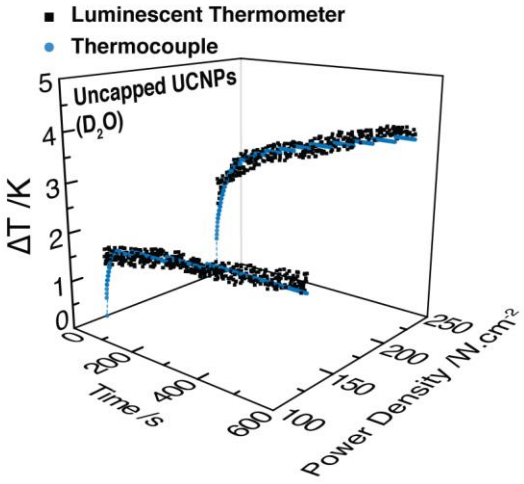

Figure 6S. 16 Temperature profiles of the uncapped UCNPs dispersed in D_2O.

6.6.6 Tables

Table 6S. 1 Physical properties of uncapped $LiYF_4:Er^{3+}/Yb^{3+}$ UCNPs and lipid bilayer (LB) capped $LiYF_4:Er^{3+}/Yb^{3+}$ UCNPs.

	Quantity	Value	Units	Ref
Uncapped UCNPs	Average molar mass ($LiYF_4$:Er 0.6%/Yb 29%)	172.14	$g \cdot mol^{-1}$	
	Size long diagonal	86.4±9.5	nm	
	Size small diagonal	52.2±5.3	nm	
	Volume one UCNP	4.01±1.2	10^{-17} cm^3	
	Density ($LiYF_4$)	3.995	$g \cdot cm^{-3}$	[65]
	Mass one UCNP	1.60±0.5	10^{-13} mg	
	Number of UCNPs exposed to the laser radiation	3.01±0.95	10^8	
	Absorption cross-section, σ_P	1.1600±0.0002	10^{-21} m^2	
	Geometrical correction factor, β_P	1.25±0.21		
	Equivalent radius, r_P	2.12±0.21	10^{-8} m	
Lipid bilayer capped UCNPs	Average molar mass LB (Oleate 20%: DOPA 51%: DOPC 5%: Chol 24%)	557.10	$g \cdot mol^{-1}$	
	Thickness LB	4.40±0.40	nm	[236]
	Mass one LB	0.53 ±0.08	10^{-13} mg	
	Mass one LB-UCNP	2.13 ±0.57	10^{-13} mg	
	Volume one LB-UCNP	4.99±1.43	10^{-17} cm^3	
	Number of LB-UCNPs exposed to the laser radiation	2.26±0.61	10^8	
	LB absorption cross-section, σ_L	1.7000±0.0008	10^{-23} m^2	
	LB geometrical correction factor, β_L	2.59±0.21		
	LB equivalent radius, r_L	1.33±0.10	10^{-8} m	

Table 6S. 2 Physical parameters of water, D_2O and experimental set-up.

Parameter	Value	Units	Ref.
Water absorption coefficient, α	50.2	m^{-1}	[397]
Cuvette pathlength, L	0.01	m	
Beam spot area, A_b	8.01±0.01	10^{-9} m^2	
Cross-sectional area, A_s	1.76±0.02	10^{-5} m^2	
Water thermal conductivity, κ_w	0.615±0.004	$W \cdot m^{-1} \cdot K^{-1}$	[387]
D_2O thermal conductivity	0.575±0.004		[398]

Table 6S. 3 Intercept (Δ_0) and slope ($\partial\Delta/\partial P_D$) resulting from the fit of straight lines to the experimental data presented in Figure 6S.9

Sample	Δ_0	$\partial\Delta/\partial P_D$ (10^{-5} $cm^2 \cdot W^{-1}$)
Uncapped UCNPs in H_2O	0.169±0.001	6.5±0.3
Lipid bilayer capped UCNPs in H_2O	0.152±0.002	13.2±0.4
Uncapped UCNPs in D_2O	0.153±0.001	5.0±0.4

Chapter 7

Conclusions

During the past two decades lanthanide upconverting nanoparticles have garnered significant attention due to their versatile optical properties. The results presented in this thesis have addressed solutions to the major challenges of Ln-UCNPs in order to bring this material into biological applications. In this thesis, the development, characterization and the potential biological applications of a nanomaterial using lanthanide upconverting nanoparticle ($LiYF_4$:Tm^{3+}/Yb^{3+}) with a supported lipid bilayer were investigated.

The surface modification on oleate-$LiYF_4$ upconverting nanoparticles using a type-add approach with a supported lipid bilayer was developed using a similar method to the hydration of the dry-lipid film method often used in liposome preparation. The supported lipid bilayer on the diamond-shape morphology of the nanoparticle was formed using liquid-phase lipids DOPA, DOPC and cholesterol (64:7:29 mole% respectively). Cholesterol was incorporated in the supported lipid bilayer to induce condensation of the acyl chains of the phospholipids and minimize the water permeability through the lipid bilayer. The surface modification of the nanoparticle with the lipid bilayer was formed *via* electrostatic interactions of the negatively charged phospholipids with the positively charged surface of the nanoparticle, and therefore is dependent on the negatively charged lipid composition. Additionally, $LiYF_4$ has a tetragonal crystal structure that yields eight identical {101} faces with equal surface energies and thus identical electrostatic interactions with the physisorbed lipids, enabling a homogeneous surface covering. The supported lipid bilayer was characterized through transmission electron microscopy where the thickness of the bilayer was measured to be 4.7 nm ± 1 nm using negative stain-TEM and 4.4 nm ± 0.4 nm using cryo-TEM and was found to be consistent with the thickness of a non-interdigitated lipid bilayer. This supported lipid bilayer yields biocompatible, water dispersible nanoparticles and acts as a soft-matter shell, protecting the emission of the

lanthanide upconverting nanoparticles from water-derived quenching phenomena. In addition, the supported lipid bilayer provides space for the encapsulation of small hydrophobic/lipophilic drugs, transforming this nanomaterial into a potential nanoparticle-based drug delivery system.

Incorporation of an azobenzene-derivative lipid (di(6-{[4-(4-butylphenyl)azo]-phenoxy}-hexyl)phosphate) in the supported lipid bilayer on $LiYF_4:Tm^{3+}/Yb^{3+}$ upconverting nanoparticles yields a dynamic multifunctional lipid bilayer. The physicochemical properties of the supported lipid bilayer can be photo-controlled *via* energy transfer from $LiYF_4:Tm^{3+}/Yb^{3+}$ upconverting nanoparticles to the azobenzene-derivative lipid molecule while still providing space for the encapsulation of small hydrophobic/lipophilic drugs. It was demonstrated that under NIR photo-irradiation stimulates $LiYF_4:Tm^{3+}/Yb^{3+}$ upconverting nanoparticles to photoswitch the azobenzene-derivative lipid from the *trans*- to the *cis*-isomer, which produces a change in the volume of the lipid bilayer. The change in volume of the azobenzene moiety disrupts the lipid bilayer and induces the release of the encapsulated model drug, Nile red. Upon 30 minutes of NIR irradiation 23% of energy was transfer from $LiYF_4:Tm^{3+}/Yb^{3+}$ to the azobenzene moiety producing the photoswitching and disrupting the supported lipid bilayer leading to 40% release of the model drug encapsulated. Longer period of irradiation led to a maximum release of 65% of the model drug encapsulated. Additionally, using time-resolved spectroscopy it was found that the energy transfer mechanism from $LiYF_4:Tm^{3+}/Yb^{3+}$ to the azobenzene-derivative lipid was predominantly radiative with a minor contribution of FRET. The latest was attributed to the low photoluminescence upconversion quantum yield on the UV ($^3P_0 \rightarrow {}^3H_6$, $^3P_0 \rightarrow {}^3F_4$, and $^1D_2 \rightarrow {}^3H_6$) and blue ($^1D_2 \rightarrow {}^3F_4$ and $^1G_4 \rightarrow {}^3H_6$) transitions and to the distance dependence between the Tm^{3+} ions and the azobenzene-derivative lipid with the possibility of FRET only with the Tm^{3+} ions close to the surface of the nanoparticle. Measurements on the absolute quantum yields of the individual upconversion bands of the $LiYF_4:Tm^{3+}/Yb^{3+}$ reveal a large difference between different transition bands. Even thought the NIR ($^3H_4 \rightarrow {}^3H_6$) band has an excellent quantum yield (~ 0.02 at 5 W cm^{-2}), the blue emission bands ($^1D_2 \rightarrow {}^3F_4$ and $^1G_4 \rightarrow {}^3H_6$) have a much lower quantum yield (~1×10^{-5} at 5 W cm^{-2}). Additionally, excitation spectrum of $LiYF_4:Tm^{3+}/Yb^{3+}$

revealed that the maximum absorption of Yb^{3+} in the $^2F_{7/2} \rightarrow {}^2F_{5/2}$ transition corresponds to the $0 \rightarrow 1'$ transition at 960 nm due to the symmetry of the tetragonal host lattice that favours the Stark splitting levels. In contrast, to the $0 \rightarrow 0'$ transition at 980 nm that is maximum in the hexagonal $NaYF_4$ host.

Cellular studies of the developed nanomaterial were performed using human alveolar lung cancer A549 cells to understand the nanoparticle-cell interactions. The results herein are the first cellular studies with the crystal host $LiYF_4$ in upconverting nanoparticles. The cellular uptake of the nanoparticles was characterized as function of surface properties and incubation time using ICP-MS to quantify the concentration of nanoparticles that have entered the cell. The results showed that positively charged nanoparticles (oleate free-$LiYF_4$:Tm^{3+}/Yb^{3+}) were uptaken 7-fold faster than negatively charged nanoparticles (SLB-$LiYF_4$:Tm^{3+}/Yb^{3+}), this behaviour has been observed in other kind of nanoparticles and it has been attributed mainly to a greater attraction due to an overall negative potential in cells. The nanoparticles surface coated with the supported lipid bilayer exhibited a decreased cellular uptake as it was mentioned above, however, the uptake was still 20-fold greater when compared to other studies on UCNPs (polymer-$NaYF_4$, 50 nm). The greater cellular uptake was attributed to the morphology of the nanoparticles (diamond-shape and size 92 × 53 nm) that may facilitate the association and wrapping with the cell membrane in order to be internalized. Also, it was proposed that the nanoparticles when oriented perpendicular with the apex towards the cell membrane required less energy and could internalize *via* an energy-independent pathway. The main internalization mechanisms for SLB-$LiYF_4$:Tm^{3+}/Yb^{3+} into A549 cells were found to be the clathrin-mediated, caveolae-dependent endocytosis and an energy-independent pathway. Cytotoxicity studies using the XTT assay showed that the nanoparticles with the supported lipid bilayer coating yield negligible apparent toxicity in A549 cells; this was attributed to the surface properties –lipid composition and negatively charged surface. Thus demonstrating the biocompatibility of the surface coating with the engineered supported lipid bilayer (DOPA, DOPC, and cholesterol).

The cellular internalization, trafficking and NIR triggered delivery of the developed nanomaterial were investigated using laser scanning confocal microscopy. Taking advantage of the optical upconversion properties of $LiYF_4:Tm^{3+}/Yb^3$ nanoparticles and the sensitivity of the emission of Nile red to the polar microenvironment, the delivery and trafficking were elucidated by co-localization of the emissions with the organelles in the cell. It was observed that the developed nanoparticle-based delivery system (SLB-$LiYF_4:Tm^{3+}/Yb^{3+}$) with Nile red (hydrophobic model drug) encapsulated, was able to carry the dye inside the A549 cells and traffic to different organelles including the endoplasmic reticulum, Golgi apparatus, lysosomes, lamellar and lipid bodies. The trafficking to different organelles inside the cell was attributed mainly to the surface properties (lipid coating and charge) of the nanomaterial. Moreover, it was demonstrated that under NIR photo-irradiation the developed nanoparticle-based delivery system with the dynamic supported lipid bilayer (containing the azobenzene-derivative lipid, AZO-SLB-$LiYF_4:Tm^{3+}/Yb^{3+}$) inside A549 lung cancer cells produced a fast release of the model drug (Nile red) in comparison to biological local triggers such as enzyme degradation.

The results presented in this thesis enrich the understanding of photo-stimulated nanomaterials, using Ln-UCNPs and demonstrate the development of a novel biocompatible, colloidally stable, nanoparticle-based drug delivery system for hydrophobic and/or lipophilic drugs using a photoswitchable supported lipid bilayer with NIR photo stimulation. The nanomaterial developed provides a solution to the delivery of hydrophobic drugs, which is one of the major challenges in the pharmaceutical industry. Additionally photo-activation using NIR light is of great importance for low toxicity and higher tissue penetration offering at the same time control both spatially and temporally for drug release. This kind of photo-controlled therapy may help to decrease the systemic toxicity of conventional medicines. The cellular studies herein contribute on the understanding of the nanoparticle-cell interactions, which are of great importance for the design and development of nanomedicines.

Chapter 8

Future Work

The studies presented herein are the fundamental studies for the development of a photo-mediated nanoparticle-based drug delivery system. However, there is still a long path to be able to achieve applications of these systems in a clinical setting. The nanoparticle-based delivery system proposed in this thesis was developed using the dye Nile red as a hydrophobic/lipophilic model drug. Further investigation on the encapsulation, photo-release and cellular studies using a drug are required to test the efficacy of this nanomaterial before moving into animal studies.

The versatility of the nanomaterial developed herein allows the encapsulation of different small hydrophobic drugs into the lipid bilayer. Two different kind of drugs will be proposed to test the efficacy of the nanoparticle-based delivery system one for chemotherapy with NIR-control release and another one for NIR-activation photodynamic therapy (PDT).

8.1 Chemotherapy application

An excellent candidate molecule to study the chemotherapeutic effect is the drug β-Lapachone, 3,4-dihydro-2,2-dimethyl-2H-naphtho[1,2-b]pyran-5,6-dione (**Figure 8.1**), which is an orthoquinone originally extracted from the Red Lapacho tree from the Amazon rain forest. β-Lapachone has shown to have chemotherapeutic effects in different cancer types including lung cancer.[399–403] However, its medical applications have been limited due to its hydrophobicity that causes low bioavailability (water solubility of 0.038 mg/mL).[404,405] Encapsulation of β-Lapachone in the lipid bilayer of the nanocarrier developed in this thesis could be an alternative to achieve the delivery of this drug.

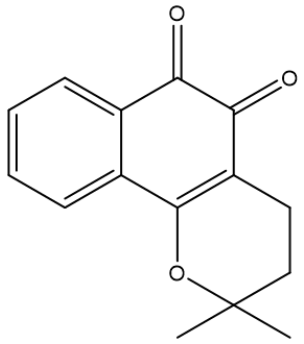

Figure 8. 1 Chemical structure of β-Lapachone

Additionally, the absorbance of β-Lapachone has a lower absorption coefficient than the azobenzene-derivative lipid in the region of 300-400 nm. Within this region the π-π* absorbance band of azobenzene-derivative lipid overlaps with the upconverted UV emission bands from the nanoparticle at 353 and 368 nm ($^3P_0 \rightarrow {}^3F_4$ and $^1D_2 \rightarrow {}^3H_6$ transitions respectively), which are important for the photoswitching of the *trans*-AZO-lipid to *cis*-AZO-lipid inside the supported lipid bilayer for the NIR-triggered release of the drug (**Figure 8.2**). Therefore, the drug β-Lapachone should not affect the photoswitching property of the nanocarrier. Additionally, it has been reported that β-lapachone exposure to A549 cells have inhibited the growth and caused apoptosis in a dose-time dependent fashion.[400] Cytotoxicity studies using the same cell line (A549) used in the studies presented herein could be expanded to include different cancer cell line since the nanocarrier-cell interaction may be different.

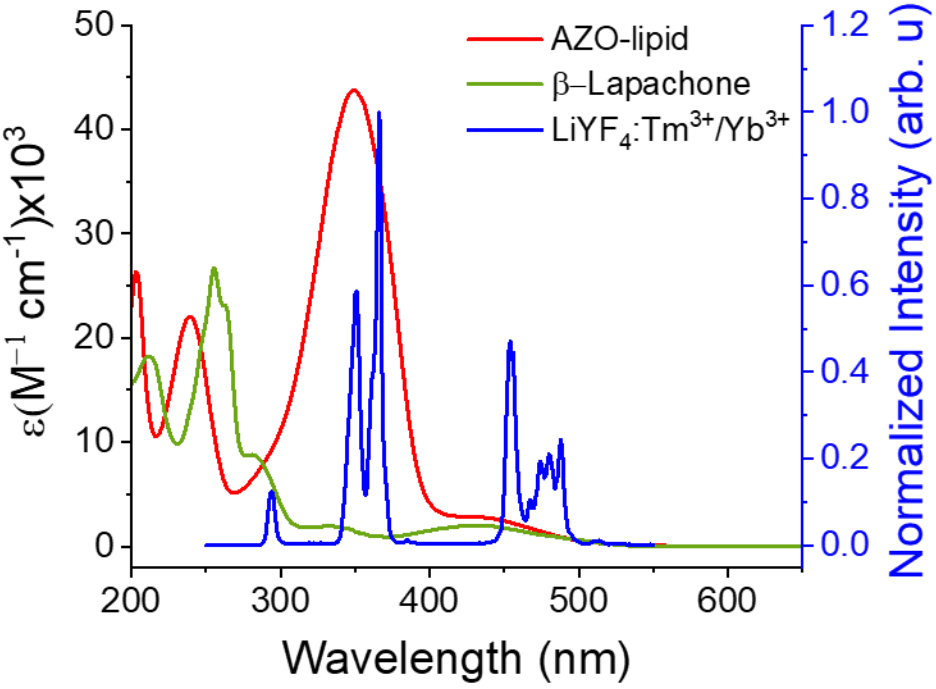

Figure 8. 2 Spectral overlap between the absorption spectra of Azobenzene-derivative lipid (AZO-lipid), β-Lapachone and the emission spectrum of $LiYF_4:Tm^{3+}/Yb^{3+}$ UCNPs excited at 980 nm.

8.2 Photodynamic therapy application

Photodynamic therapy is a treatment that uses a photosensitizer, which is activated by light, and in the presence of oxygen produce the therapeutic effect. When the photosensitizer is excited at a particular wavelength it can transfer the energy of its excited triplet state to the surrounding molecular oxygen producing singlet oxygen which is cytotoxic to cells.[406] Conventional photodynamic therapies use UV/visible light, which allows the treating of superficial tumours only.[407] Lanthanide upconverting nanoparticles have been proposed to activate photosensitizer *via* energy transfer using NIR excitation.[270,325] Activation of the photosensitizer using NIR light could provide a higher tissue penetration and reduce the cytotoxicity effects of UV light.

A good alternative of a photosensitizer drug that could be encapsulated inside the supported lipid bilayer of the nanoparticle-based delivery system developed is the benzo[α]phenoxazine analogue molecule showed in **Figure 8.3**. This molecule has a similar molecular structure to the lipophilic dye Nile blue. In addition, it has an absorption band maximum at 661 nm and a reported absolute quantum yield for singlet oxygen of 0.78,[110] similar to the one reported for the well-known photosensitizer Rose Bengal (0.76).[408]

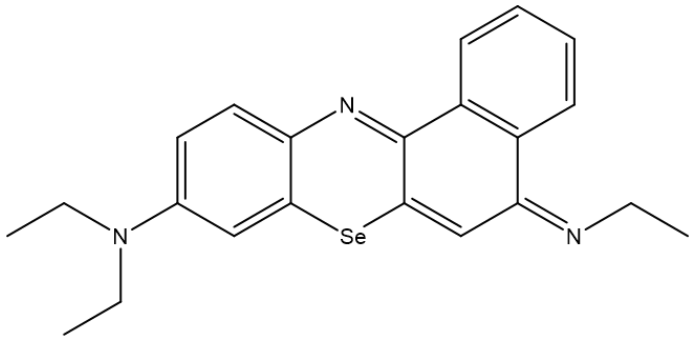

Figure 8. 3 molecular structure of benzo[α]phenoxazine analogue with selenium substituted at the 7-position.[110]

Therefore this molecule encapsulated in the nanoparticle-based delivery system could be a good candidate for NIR photodynamic therapy *via* energy transfer with the upconverting nanoparticles. However, $LiYF_4:Tm^{3+}/Yb^{3+}$ UCNPs is not the best candidate to activate this photosensitizer *via* energy transfer because the absorption band of the photosensitizer at 661 nm and the emissions bands of the Tm^{3+} ions do not overlap sufficiently. An excellent alternative to overcome this issue is using the co-dopant ion combination Er^{3+}/Yb^{3+}, which have shown to produce a strong upconversion emission of the Er^{3+} ion at 655 nm ($^4F_{9/2}\rightarrow{}^4I_{15/2}$).[200] Thus, the synthesis of $LiYF_4:Er^{3+}/Yb^{3+}$ upconverting nanoparticle will be suitable for the NIR-activation *via* energy transfer of this photosensitizer. Figure 8.4. shows the emission of the synthesized $LiYF_4:Er^{3+}/Yb^{3+}$ UCNPs with a emission at 655 nm ($^4F_{9/2}\rightarrow{}^4I_{15/2}$) ideal for the activation of the photosensitizer with absorption band at 661 nm.

Further surface modification with the supported lipid bilayer and encapsulation of the photosensitizer will produce a novel nanoparticle-based delivery system with NIR-activation photodynamic therapy. Also, characterization of the energy transfer between the nanoparticle and the photosensitizer, as well as the singlet oxygen production, and evaluation of the cytotoxicity will be require it to ascertain the efficacy.

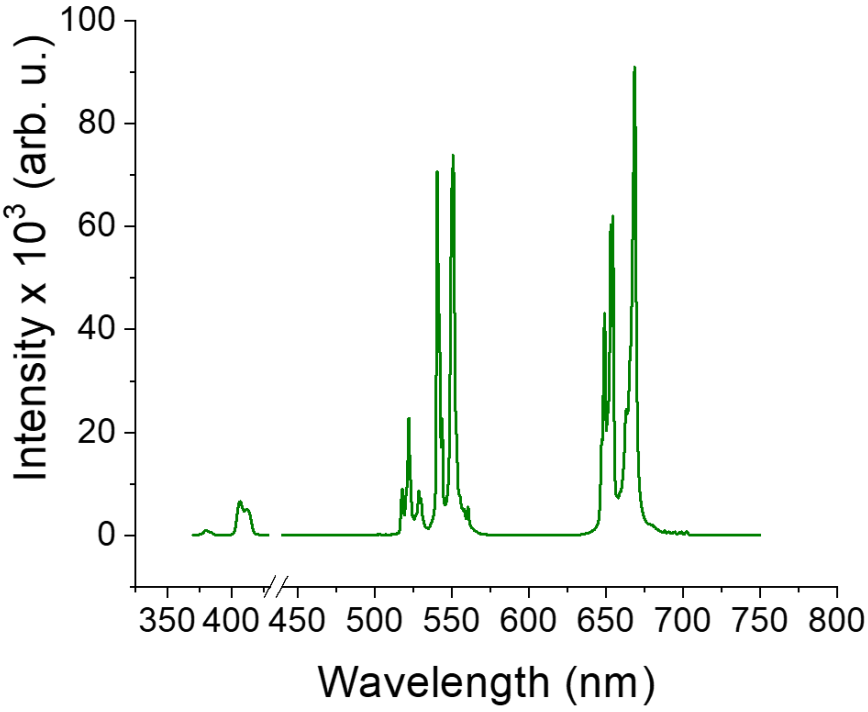

Figure 8. 4 Emission spectrum of $LiYF_4:Er^{3+}/Yb^{3+}$ (0.5% Er^{3+} , 25% Yb^{3+}) UCNPs in toluene excited at 980 nm.

Additionally, studies in microfluidics on this nanomaterial with unique morphology could help in the understanding on how nanoparticles could flow in the blood vessels.[409] Also, studies with different cell lines will give a better understanding on the nanoparticle-cell interactions. These studies will contribute in the understanding and development of nanoparticle-based delivery systems and revolutionize nanomedicine.

Appendix A

Table A. 1 Name for some shorthand designation of chains and head groups of lipids with the corresponding acyl chain length and head group charge: negative (-), positive (+), zwitterionic (+/-)

Chain	**n- system**	**Common name (X name)**
DM	14:0	Dimyristoyl (ditetradecanoyl)
DP	16:0	Dipalmitoyl (dihexadecanoyl)
DS	18:0	Distearoyl (dioctadecanoyl)
DO	18:1(n-9)	Dioleoyl (di(*cis*-9-octadecenoyl))
Head group	**Charge**	
PC	+/-	Phosphocholine
PE	+/-	Phosphoethanolamine
PS	-	Phosphoserine
PI	-	Phosphatidylinositol
PA	-	Phosphate
TAP	+	Trimethylammonium-propane

Table A. 2 Name for shorthand designation of common lipids

Abbreviation	**Common Name**
DMPC	1,2-dimyristoyl-sn-glycero-3-phosphocholine
DPPC	1,2-dipalmitoyl-sn-glycero-3-phosphocholine
DSPC	1,2-distearoyl-sn-glycero-3-phosphocholine
DSPE	1,2-distearoyl-sn-glycero-3-phosphoethanolamine
DOPC	1,2-dioleoyl-sn-glycero-3-phosphocholine
DOPS	1,2-dioleoyl-sn-glycero-3-phospho-L-serine
DOPA	1,2-dioleoyl-sn-glycero-3-phosphate
DOTAP	1,2-dioleoyl-3-trimethylammonium-propane

REFERENCES

(1) Feynman, R. P. There's Plenty of Room at the Bottom. *Engineering and Science* **1960**, *23*, 22–36.

(2) Taniguchi, N. On the Basic Concept of Nano-Technology. *Proc. Intl. Conf. Prod. London,* **1974**.

(3) Drexler, E. *Engines of Creation: The Coming Era of Nanotechnology*; Doubleday: New York, **1987**.

(4) Borm, P. J.; Robbins, D.; Haubold, S.; Kuhlbusch, T.; Fissan, H.; Donaldson, K.; Schins, R.; Stone, V.; Kreyling, W.; Lademann, J.; et al. The Potential Risks of Nanomaterials: A Review Carried out for ECETOC. *Part. Fibre Toxicol.* **2006**, *3* (1), 11.

(5) Freitas Jr, R. A. What Is Nanomedicine? *Nanomedicine: NBM* **2005**, *1* (1), 2–9.

(6) Kim, B. Y. S.; Rutka, J. T.; Chan, W. C. W. Nanomedicine. *New Eng. J. Med.* **2010**, *363* (25), 2434–2443.

(7) Chen, H.; Zhang, W.; Zhu, G.; Xie, J.; Chen, X. Rethinking Cancer Nanotheranostics. *Nat. Rev. Mater.* **2017**, *2* (7), 17024.

(8) Vizirianakis, I. S. Nanomedicine and Personalized Medicine toward the Application of Pharmacotyping in Clinical Practice to Improve Drug-Delivery Outcomes. *Nanomedicine: NBM* **2011**, *7* (1), 11–17.

(9) Bangham, A. D.; Standish, M. M.; Watkins, J. C. Diffusion of Univalent Ions across the Lamellae of Swollen Phospholipids. *J. Mol. Biol.* **1965**, *13* (1), 238–252.

(10) Gregoriadis, G.; Ryman, B. E. Liposomes as Carriers of Enzymes or Drugs: A New Approach to the Treatment of Storage Diseases. *Biochem. J.* **1971**, *124* (5), 58P.

(11) Gregoriadis, G.; Leathwood, P. D.; Ryman, B. E. Enzyme Entrapment in Liposomes. *FEBS Lett.* **1971**, *14* (2), 95–99.

(12) Barenholz, Y. (Chezy). Doxil® — The First FDA-Approved Nano-Drug: Lessons Learned. *J. Control. Release* **2012**, *160* (2), 117–134.

(13) Chan, W. C. W. Nanomedicine 2.0. *Acc. Chem. Res.* **2017**, *50* (3), 627–632.

(14) Nam, J.; Son, S.; Park, K. S.; Zou, W.; Shea, L. D.; Moon, J. J. Cancer Nanomedicine for Combination Cancer Immunotherapy. *Nat. Rev. Mater.* **2019**, *4* (6), 398.

(15) Shi, J.; Kantoff, P. W.; Wooster, R.; Farokhzad, O. C. Cancer Nanomedicine: Progress, Challenges and Opportunities. *Nat. Rev. Cancer* **2017**, *17* (1), 20–37.

(16) Rubinstein, I.; Weinberg, G. L. Nanomedicines for Chronic Non-Infectious Arthritis: The Clinician's Perspective. *Maturitas* **2012**, *73* (1), 68–73.

(17) Lobatto, M. E.; Fuster, V.; Fayad, Z. A.; Mulder, W. J. M. Perspectives and Opportunities for Nanomedicine in the Management of Atherosclerosis. *Nat. Rev. Drug Discov.* **2011**, *10* (11), 835–852.

(18) Veiseh, O.; Tang, B. C.; Whitehead, K. A.; Anderson, D. G.; Langer, R. Managing Diabetes with Nanomedicine: Challenges and Opportunities. *Nat. Rev. Drug Discov.* **2015**, *14* (1), 45–57.

(19) Mahmoudi, M.; Yu, M.; Serpooshan, V.; Wu, J. C.; Langer, R.; Lee, R. T.; Karp, J. M.; Farokhzad, O. C. Multiscale Technologies for Treatment of Ischemic Cardiomyopathy. *Nat. Nanotechnol.* **2017**, *12* (9), 845–855.
(20) Said, S. S.; Campbell, S.; Hoare, T. Externally Addressable Smart Drug Delivery Vehicles: Current Technologies and Future Directions. *Chem. Mater.* **2019**, *31* (14), 4971–4989.
(21) Liu, Q.; Zhan, C.; Kohane, D. S. Phototriggered Drug Delivery Using Inorganic Nanomaterials. *Bioconjugate Chem.* **2017**, *28* (1), 98–104.
(22) Nam, J.; Won, N.; Bang, J.; Jin, H.; Park, J.; Jung, S.; Jung, S.; Park, Y.; Kim, S. Surface Engineering of Inorganic Nanoparticles for Imaging and Therapy. *Adv. Drug Deliv. Rev.* **2013**, *65* (5), 622–648.
(23) Chen, G.; Qiu, H.; Prasad, P. N.; Chen, X. Upconversion Nanoparticles: Design, Nanochemistry, and Applications in Theranostics. *Chem. Rev.* **2014**, *114* (10), 5161–5214.
(24) Fan, W.; Bu, W.; Shi, J. On The Latest Three-Stage Development of Nanomedicines Based on Upconversion Nanoparticles. *Adv. Mater.* **2016**, *28* (21), 3987–4011.
(25) Naccache, R.; Yu, Q.; Capobianco, J. A. The Fluoride Host: Nucleation, Growth, and Upconversion of Lanthanide-Doped Nanoparticles. *Adv. Opt. Mater.* **2015**, *3* (4), 482–509.
(26) Naccache, R.; Chevallier, P.; Lagueux, J.; Gossuin, Y.; Laurent, S.; Vander Elst, L.; Chilian, C.; Capobianco, J. A.; Fortin, M.-A. High Relaxivities and Strong Vascular Signal Enhancement for $NaGdF_4$ Nanoparticles Designed for Dual MR/Optical Imaging. *Adv. Healthc. Mater.* **2013**, *2* (11), 1478–1488.
(27) Cooper, D. R.; Capobianco, J. A.; Seuntjens, J. Radioluminescence Studies of Colloidal Oleate-Capped β-$Na(Gd,Lu)F_4$:Ln^{3+} Nanoparticles (Ln = Ce, Eu, Tb). *Nanoscale* **2018**, *10* (16), 7821–7832.
(28) Kamkaew, A.; Chen, F.; Zhan, Y.; Majewski, R. L.; Cai, W. Scintillating Nanoparticles as Energy Mediators for Enhanced Photodynamic Therapy. *ACS Nano* **2016**, *10* (4), 3918–3935.
(29) Lee, G.; Park, Y. I. Lanthanide-Doped Upconversion Nanocarriers for Drug and Gene Delivery. *Nanomaterials (Basel)* **2018**, *8* (7).
(30) Qiu, H.; Tan, M.; Ohulchanskyy, T. Y.; Lovell, J. F.; Chen, G. Recent Progress in Upconversion Photodynamic Therapy. *Nanomaterials (Basel)* **2018**, *8* (5).
(31) Whynne-Hammond, C. *Elements of Human Geography*, 2nd Ed.; Unwin Hyman: London, **1985**.
(32) Hüfner, S. *Optical Spectra of Transparent Rare Earth Compounds*; Academic Press: New York, **1978**.
(33) Vleck, J. H. Van. The Puzzle of Rare-Earth Spectra in Solids. *J. Phys. Chem.* **1937**, *41* (1), 67–80.
(34) Russell, H. N.; Saunders, F. A. New Regularities in the Spectra of the Alkaline Earths. *The Astrophysical J.* **1925**, *61*, 38.

(35) Geusic, J. E.; Marcos, H. M.; Van Uitert, L. G. Laser Oscillations in Nd^{3+} Doped Yttrium Aluminum, Yttrium Gallium and Gadolinium Garnets. *Appl. Phys. Lett.* **1964**, *4* (10), 182–184.
(36) Bünzli, J.-C. G. Lanthanide Photonics: Shaping the Nanoworld. *Trends Chem.* **2019**, doi.org/10.1016/j.trechm.2019.05.012
(37) Qin, X.; Liu, X.; Huang, W.; Bettinelli, M.; Liu, X. Lanthanide-Activated Phosphors Based on 4f-5d Optical Transitions: Theoretical and Experimental Aspects. *Chem. Rev.* **2017**, *117* (5), 4488–4527.
(38) Bünzli, J.-C. G.; Chauvin, A.-S. Chapter 261 - Lanthanides in Solar Energy Conversion. In *Handbook on the Physics and Chemistry of Rare Earths*; Elsevier: Amsterdam, **2014**; Vol. 44, pp 169–281.
(39) Bünzli, J.-C. G. Lanthanide Luminescence for Biomedical Analyses and Imaging. *Chem. Rev.* **2010**, *110* (5), 2729–2755.
(40) Auzel, F. Upconversion and Anti-Stokes Processes with f and d Ions in Solids. *Chem. Rev.* **2004**, *104* (1), 139–174.
(41) Scheps, R. Upconversion Laser Processes. *Prog. Quant. Electron.* **1996**, *20* (4), 271–358.
(42) Nadort, A.; Zhao, J.; Goldys, E. M. Lanthanide Upconversion Luminescence at the Nanoscale: Fundamentals and Optical Properties. *Nanoscale* **2016**, *8* (27), 13099–13130.
(43) Auzel, F. Compteur Quantique Par Transfert d'energie Entre Deux Ions de Terres Rares Dans Un Tungstate Mixte et Dans Un Verre. *C. R. Acad. Sci. Paris* **1966**, *262*, 1016–1019.
(44) Auzel, M. F. Étude spectroscopique de l'ion Er^{3+} dans différents verres. *J. Phys. Colloques* **1966**, *27* (C2), C2-141-C2-141.
(45) Blasse, G.; Grabmaier, B. C. *Luminescent Materials*; Springer-Verlag: Berlin Heidelberg, **1994**.
(46) Dexter, D. L. A Theory of Sensitized Luminescence in Solids. *J. Chem. Phys.* **1953**, *21* (5), 836–850.
(47) Förster, Th. Zwischenmolekulare Energiewanderung Und Fluoreszenz. *Annalen der Physik* **1948**, *437* (1–2), 55–75.
(48) Bartolo, B. D.; Goldberg, V. *Radiationless Processes*; NATO Scientific Affairs Division; Springer: New York and London, **1980**.
(49) Selvin, P. R. Lanthanide-Based Resonance Energy Transfer. *IEEE J. Sel. Top. Quant.* **1996**, *2* (4), 1077–1087.
(50) Majoul, I.; Jia, Y.; Duden, R. Practical Fluorescence Resonance Energy Transfer or Molecular Nanobioscopy of Living Cells. In *Handbook Of Biological Confocal Microscopy*; Springer US: Boston, **2006**; pp 788–808.
(51) Andrews, D. L. A Unified Theory of Radiative and Radiationless Molecular Energy Transfer. *Chem. Phys.* **1989**, *135* (2), 195–201.
(52) Geißler, D.; Linden, S.; Liermann, K.; Wegner, K. D.; Charbonnière, L. J.; Hildebrandt, N. Lanthanides and Quantum Dots as Förster Resonance Energy Transfer Agents for Diagnostics and Cellular Imaging. *Inorg. Chem.* **2014**, *53* (4), 1824–1838.
(53) Selvin, P. R. The Renaissance of Fluorescence Resonance Energy Transfer. *Nat. Struct. Biol.* **2000**, *7* (9), 730.

(54) Heyduk, E.; Heyduk, T.; Claus, P.; Wiśniewski, J. R. Conformational Changes of DNA Induced by Binding ofChironomus High Mobility Group Protein 1a (CHMG1a). *J. Biol. Chem.* **1997**, *272* (32), 19763–19770.
(55) Israelachvili, J. N.; Mitchell, D. J.; Ninham, B. W. Theory of Self-Assembly of Lipid Bilayers and Vesicles. *BBA - Biomembranes* **1977**, *470* (2), 185–201.
(56) Cevc, G. *Phospholipids Handbook*; Marcel Dekker: New York, **1993**.
(57) Israelachvili, J. N. *Intermolecular and Surface Forces*; Academic Press; Elsevier: Amsterdam, **2011**.
(58) Frolov, V. A.; Shnyrova, A. V.; Zimmerberg, J. Lipid Polymorphisms and Membrane Shape. *Cold Spring Harb Perspect. Biol.* **2011**, *3* (11), a004747.
(59) Harayama, T.; Riezman, H. Understanding the Diversity of Membrane Lipid Composition. *Nat. Rev. Mol. Cell Bio.* **2018**, *19* (5), 281–296.
(60) Kranenburg, M.; Smit, B. Phase Behavior of Model Lipid Bilayers. *J. Phys. Chem. B* **2005**, *109* (14), 6553–6563.
(61) Bhattacharya, S.; Haldar, S. Interactions between Cholesterol and Lipids in Bilayer Membranes. Role of Lipid Headgroup and Hydrocarbon Chain–Backbone Linkage. *BBA - Biomembranes* **2000**, *1467* (1), 39–53.
(62) Semer, R.; Gelerinter, E. A Spin Label Study of the Effects of Sterols on Egg Lecithin Bilayers. *Chem. Phys. Lipids* **1979**, *23* (3), 201–211.
(63) Hung, W.-C.; Lee, M.-T.; Chen, F.-Y.; Huang, H. W. The Condensing Effect of Cholesterol in Lipid Bilayers. *Biophys. J.* **2007**, *92* (11), 3960–3967.
(64) Parker, A.; Miles, K.; Cheng, K. H.; Huang, J. Lateral Distribution of Cholesterol in Dioleoylphosphatidylcholine Lipid Bilayers: Cholesterol-Phospholipid Interactions at High Cholesterol Limit. *Biophys. J.* **2004**, *86* (3), 1532–1544.
(65) Shand, W. A. Single Crystal Growth and Some Properties of LiYF4. *J. Cryst. Growth* **1969**, *5* (2), 143–146.
(66) Jenssen, H. P.; Linz, A.; Leavitt, R. P.; Morrison, C. A.; Wortman, D. E. Analysis of the Optical Spectrum of Tm^{3+} in $LiYF_4$. *Phys. Rev. B* **1975**, *11* (1), 92–101.
(67) Mahalingam, V.; Vetrone, F.; Naccache, R.; Speghini, A.; Capobianco, J. A. Colloidal Tm^{3+}/Yb^{3+}-Doped $LiYF_4$ Nanocrystals: Multiple Luminescence Spanning the UV to NIR Regions via Low-Energy Excitation. *Adv. Mater.* **2009**, *21* (40), 4025–4028.
(68) Miller, S. A.; Rast, H. E.; Caspers, H. H. Lattice Vibrations of $LiYF_4$. *J. Chem. Phys.* **1970**, *52*, 4172–4175.
(69) Haase, M.; Schäfer, H. Upconverting Nanoparticles. *Angew. Chem. Int. Edit.* **2011**, *50* (26), 5808–5829.
(70) Gnach, A.; Lipinski, T.; Bednarkiewicz, A.; Rybka, J.; Capobianco, J. A. Upconverting Nanoparticles: Assessing the Toxicity. *Chem. Soc. Rev.* **2014**.
(71) Hirano, S.; Suzuki, K. T. Exposure, Metabolism, and Toxicity of Rare Earths and Related Compounds. *Environ. Health Perspect.* **1996**, *104* (Suppl 1), 85–95.
(72) Bashkatov, A. N.; Genina, E. A.; Kochubey, V. I.; Tuchin, V. V. Optical Properties of Human Skin, Subcutaneous and Mucous Tissues in the Wavelength Range from 400 to 2000 Nm. *J. Phys. D: Appl. Phys.* **2005**, *38* (15), 2543–2555.

(73) Prodi, L.; Rampazzo, E.; Rastrelli, F.; Speghini, A.; Zaccheroni, N. Imaging Agents Based on Lanthanide Doped Nanoparticles. *Chem. Soc. Rev.* **2015**, *44* (14), 4922–4952.
(74) Achatz, D. E.; Ali, R.; Wolfbeis, O. S. Luminescent Chemical Sensing, Biosensing, and Screening Using Upconverting Nanoparticles. In *Luminescence Applied in Sensor Science*; Springer: Berlin, Heidelberg, **2011**; pp 29–50.
(75) Zhou, H.; Sharma, M.; Berezin, O.; Zuckerman, D.; Berezin, M. Y. Nanothermometry: From Microscopy to Thermal Treatments. *ChemPhysChem* **2016**, *17* (1), 27–36.
(76) Zhang, B. F.; Frigoli, M.; Angiuli, F.; Vetrone, F.; Capobianco, J. A. Photoswitching of Bis-Spiropyran Using near-Infrared Excited Upconverting Nanoparticles. *Chem. Commun.* **2012**, *48* (58), 7244.
(77) Dcona, M. M.; Yu, Q.; Capobianco, J. A.; Hartman, M. C. T. Near Infrared Light Mediated Release of Doxorubicin Using Upconversion Nanoparticles. *Chem. Commun.* **2015**, *51* (40), 8477–8479.
(78) Zhu, M.-Q.; Zhang, G.-F.; Li, C.; Aldred, M. P.; Chang, E.; Drezek, R. A.; Li, A. D. Q. Reversible Two-Photon Photoswitching and Two-Photon Imaging of Immunofunctionalized Nanoparticles Targeted to Cancer Cells. *J. Am. Chem. Soc.* **2011**, *133* (2), 365–372.
(79) Bandara, H. M. D.; Burdette, S. C. Photoisomerization in Different Classes of Azobenzene. *Chemical Society Reviews* **2012**, *41* (5), 1809.
(80) Beharry, A. A.; Woolley, G. A. Azobenzene Photoswitches for Biomolecules. *Chem. Soc. Rev.* **2011**, *40* (8), 4422–4437.
(81) Kumar, G. S.; Neckers, D. C. Photochemistry of Azobenzene-Containing Polymers. *Chem. Rev.* **1989**, *89* (8), 1915–1925.
(82) Woolley, G. A. Photocontrolling Peptide Alpha Helices. *Acc. Chem. Res.* **2005**, *38* (6), 486–493.
(83) Morgan, C. G.; Bisby, R. H.; Johnson, S. A.; Mitchell, A. C. Fast Solute Release from Photosensitive Liposomes: An Alternative to 'Caged' Reagents for Use in Biological Systems. *FEBS Lett.* **1995**, *375* (1–2), 113–116.
(84) Arppe, R.; Hyppänen, I.; Perälä, N.; Peltomaa, R.; Kaiser, M.; Würth, C.; Christ, S.; Resch-Genger, U.; Schäferling, M.; Soukka, T. Quenching of the Upconversion Luminescence of $NaYF_4:Yb^{3+},Er^{3+}$ and $NaYF_4:Yb^{3+},Tm^{3+}$ Nanophosphors by Water: The Role of the Sensitizer Yb^{3+} in Non-Radiative Relaxation. *Nanoscale* **2015**, *7* (27), 11746–11757.
(85) Wilhelm, S.; Kaiser, M.; Würth, C.; Heiland, J.; Carrillo-Carrion, C.; Muhr, V.; Wolfbeis, O. S.; Parak, W. J.; Resch-Genger, U.; Hirsch, T. Water Dispersible Upconverting Nanoparticles: Effects of Surface Modification on Their Luminescence and Colloidal Stability. *Nanoscale* **2015**, *7* (4), 1403–1410.
(86) Bogdan, N.; Vetrone, F.; Ozin, G. A.; Capobianco, J. A. Synthesis of Ligand-Free Colloidally Stable Water Dispersible Brightly Luminescent Lanthanide-Doped Upconverting Nanoparticles. *Nano Lett.* **2011**, *11* (2), 835–840.

(87) Dong, A.; Ye, X.; Chen, J.; Kang, Y.; Gordon, T.; Kikkawa, J. M.; Murray, C. B. A Generalized Ligand-Exchange Strategy Enabling Sequential Surface Functionalization of Colloidal Nanocrystals. *J. Am. Chem. Soc.* **2011**, *133* (4), 998–1006.
(88) Guller, A. E.; Nadort, A.; Generalova, A. N.; Khaydukov, E. V.; Nechaev, A. V.; Kornienko, I. A.; Petersen, E. V.; Liang, L.; Shekhter, A. B.; Qian, Y.; et al. Rational Surface Design of Upconversion Nanoparticles with Polyethylenimine Coating for Biomedical Applications: Better Safe than Brighter? *ACS Biomater. Sci. Eng.* **2018**, *4* (9), 3143–3153.
(89) Michel, R.; Gradzielski, M. Experimental Aspects of Colloidal Interactions in Mixed Systems of Liposome and Inorganic Nanoparticle and Their Applications. *Int. J. Mol. Sci.* **2012**, *13* (9), 11610.
(90) Watts, T. H.; Brian, A. A.; Kappler, J. W.; Marrack, P.; McConnell, H. M. Antigen Presentation by Supported Planar Membranes Containing Affinity-Purified I-Ad. *Proc. Natl. Acad. Sci. USA* **1984**, *81* (23), 7564–7568.
(91) Reviakine, I.; Brisson, A. Formation of Supported Phospholipid Bilayers from Unilamellar Vesicles Investigated by Atomic Force Microscopy. *Langmuir* **2000**, *16* (4), 1806–1815.
(92) Anderson, T. H.; Min, Y.; Weirich, K. L.; Zeng, H.; Fygenson, D.; Israelachvili, J. N. Formation of Supported Bilayers on Silica Substrates. *Langmuir* **2009**, *25* (12), 6997–7005.
(93) Richter, R.; Mukhopadhyay, A.; Brisson, A. Pathways of Lipid Vesicle Deposition on Solid Surfaces: A Combined QCM-D and AFM Study. *Biophys. J.* **2003**, *85* (5), 3035–3047.
(94) Mornet, S.; Lambert, O.; Duguet, E.; Brisson, A. The Formation of Supported Lipid Bilayers on Silica Nanoparticles Revealed by Cryoelectron Microscopy. *Nano Lett.* **2005**, *5* (2), 281–285.
(95) Ahmed, S.; Wunder, S. L. Effect of High Surface Curvature on the Main Phase Transition of Supported Phospholipid Bilayers on SiO2 Nanoparticles. *Langmuir* **2009**, *25* (6), 3682–3691.
(96) Ahmed, S.; Nikolov, Z.; Wunder, S. L. Effect of Curvature on Nanoparticle Supported Lipid Bilayers Investigated by Raman Spectroscopy. *J. Phys. Chem. B* **2011**, *115* (45), 13181–13190.
(97) Savarala, S.; Monson, F.; Ilies, M. A.; Wunder, S. L. Supported Lipid Bilayer NanoSystems: Stabilization by Undulatory-Protrusion Forces and Destabilization by Lipid Bridging. *Langmuir* **2011**, *27* (10), 5850–5861.
(98) Tan, S.; Li, X.; Guo, Y.; Zhang, Z. Lipid-Enveloped Hybrid Nanoparticles for Drug Delivery. *Nanoscale* **2013**, *5* (3), 860–872.
(99) Bayerl, T. M.; Bloom, M. Physical Properties of Single Phospholipid Bilayers Adsorbed to Micro Glass Beads. A New Vesicular Model System Studied by 2H-Nuclear Magnetic Resonance. *Biophys. J.* **1990**, *58* (2), 357–362.
(100) Wang, H.; Zhao, P.; Su, W.; Wang, S.; Liao, Z.; Niu, R.; Chang, J. PLGA/Polymeric Liposome for Targeted Drug and Gene Co-Delivery. *Biomaterials* **2010**, *31* (33), 8741–8748.

(101) Li, J.; Yang, Y.; Huang, L. Calcium Phosphate Nanoparticles with an Asymmetric Lipid Bilayer Coating for SiRNA Delivery to the Tumor. *J. Control. Release* **2012**, *158* (1), 108–114.
(102) Morgan, C. G.; Thomas, E. W.; Yianni, Y. P.; Sandhu, S. S. Incorporation of a Novel Photochromic Phospholipid Molecule into Vesicles of Dipalmitoylphosphatidylcholine. *BBA - Biomembranes* **1985**, *820* (1), 107–114.
(103) Kuiper, J. M.; Engberts, J. B. F. N. H-Aggregation of Azobenzene-Substituted Amphiphiles in Vesicular Membranes. *Langmuir* **2004**, *20* (4), 1152–1160.
(104) Liu, Y.-C.; Le Ny, A.-L. M.; Schmidt, J.; Talmon, Y.; Chmelka, B. F.; Lee, C. T. Photo-Assisted Gene Delivery Using Light-Responsive Catanionic Vesicles. *Langmuir* **2009**, *25* (10), 5713–5724.
(105) Cui, Z.-K.; Phoeung, T.; Rousseau, P.-A.; Rydzek, G.; Zhang, Q.; Bazuin, C. G.; Lafleur, M. Nonphospholipid Fluid Liposomes with Switchable Photocontrolled Release. *Langmuir* **2014**, *30* (36), 10818–10825.
(106) Bisby, R. H.; Mead, C.; Morgan, C. G. Active Uptake of Drugs into Photosensitive Liposomes and Rapid Release on UV Photolysis. *Photochem. Photobiol.* **2000**, *72* (1), 57–61.
(107) Diguet, A.; Yanagisawa, M.; Liu, Y.-J.; Brun, E.; Abadie, S.; Rudiuk, S.; Baigl, D. UV-Induced Bursting of Cell-Sized Multicomponent Lipid Vesicles in a Photosensitive Surfactant Solution. *J. Am. Chem. Soc.* **2012**, *134* (10), 4898–4904.
(108) Bisby, R. H.; Mead, C.; Morgan, C. G. Photosensitive Liposomes as 'Cages' for Laser-Triggered Solute Delivery: The Effect of Bilayer Cholesterol on Kinetics of Solute Release. *FEBS Lett.* **1999**, *463* (1–2), 165–168.
(109) Deye, J. F.; Berger, T. A.; Anderson, A. G. Nile Red as a Solvatochromic Dye for Measuring Solvent Strength in Normal Liquids and Mixtures of Normal Liquids with Supercritical and near Critical Fluids. *Anal. Chem.* **1990**, *62* (6), 615–622.
(110) Martinez, V.; Henary, M. Nile Red and Nile Blue: Applications and Syntheses of Structural Analogues. *Chem. Eur. J.* **2016**, *22* (39), 13764–13782.
(111) Ghoneim, N. Photophysics of Nile Red in Solution: Steady State Spectroscopy. *Spectrochim. Acta A - Mol Biomol. Spect.* **2000**, *56* (5), 1003–1010.
(112) Dutta, A. K.; Kamada, K.; Ohta, K. Spectroscopic Studies of Nile Red in Organic Solvents and Polymers. *J. Photochem. Photobiol. A - Chem.* **1996**, *93* (1), 57–64.
(113) Jose, J.; Burgess, K. Benzophenoxazine-Based Fluorescent Dyes for Labeling Biomolecules. *Tetrahedron* **2006**, *62* (48), 11021–11037.
(114) Greenspan, P.; Fowler, S. D. Spectrofluorometric Studies of the Lipid Probe, Nile Red. *J. Lipid Res.* **1985**, *26* (7), 781–789.
(115) Halder, A.; Saha, B.; Maity, P.; Kumar, G. S.; Sinha, D. K.; Karmakar, S. Lipid Chain Saturation and the Cholesterol in the Phospholipid Membrane Affect the Spectroscopic Properties of Lipophilic Dye Nile Red. *Spectrochimi. Acta A - Mol. Biomol. Spect.* **2018**, *191*, 104–110.

(116) Mukherjee, S.; Raghuraman, H.; Chattopadhyay, A. Membrane Localization and Dynamics of Nile Red: Effect of Cholesterol. *BBA - Biomembranes* **2007**, *1768* (1), 59–66.
(117) Greenspan, P.; Mayer, E. P.; Fowler, S. D. Nile Red: A Selective Fluorescent Stain for Intracellular Lipid Droplets. *J. Cell Biol.* **1985**, *100* (3), 965–973.
(118) Bonilla, E.; Prelle, A. Application of Nile Blue and Nile Red, Two Fluorescent Probes, for Detection of Lipid Droplets in Human Skeletal Muscle. *J. Histochem. Cytochem.* **1987**, *35* (5), 619–621.
(119) Cole, T. A.; Fok, A. K.; Ueno, M. S.; Allen, R. D. Use of Nile Red as a Rapid Measure of Lipid Content in Ciliates. *Eur. J. Protistol.* **1990**, *25* (4), 361–368.
(120) Hjelle, J. T.; Golinska, B. T.; Waters, D. C.; Steidley, K. R.; McCarroll, D. R.; Pavlina, T.; Smith, S. L.; Lloyd, J. K.; Dobbie, J. W. In Vivo and in Vitro Characterization of Mesothelial Lipid Inclusions. *Perit. Dial. Int.* **1991**, *11* (3), 207–212.
(121) Alemán-Nava, G. S.; Cuellar-Bermudez, S. P.; Cuaresma, M.; Bosma, R.; Muylaert, K.; Ritmann, B. E.; Parra, R. How to Use Nile Red, a Selective Fluorescent Stain for Microalgal Neutral Lipids. *J. Microbiol. Meth.* **2016**, *128* (Supplement C), 74–79.
(122) Brown, W. J.; Sullivan, T. R.; Greenspan, P. Nile Red Staining of Lysosomal Phospholipid Inclusions. *Histochemistry* **1992**, *97* (4), 349–354.
(123) Oerlemans, C.; Deckers, R.; Storm, G.; Hennink, W. E.; Nijsen, J. F. W. Evidence for a New Mechanism behind HIFU-Triggered Release from Liposomes. *J. Control. Release* **2013**, *168* (3), 327–333.
(124) Qiao, Z.-Y.; Zhang, R.; Du, F.-S.; Liang, D.-H.; Li, Z.-C. Multi-Responsive Nanogels Containing Motifs of Ortho Ester, Oligo(Ethylene Glycol) and Disulfide Linkage as Carriers of Hydrophobic Anti-Cancer Drugs. *J Control. Release* **2011**, *152* (1), 57–66.
(125) Maggini, L.; Cabrera, I.; Ruiz-Carretero, A.; Prasetyanto, E. A.; Robinet, E.; Cola, L. D. Breakable Mesoporous Silica Nanoparticles for Targeted Drug Delivery. *Nanoscale* **2016**, *8* (13), 7240–7247.
(126) Mohammadifar, E.; Zabihi, F.; Tu, Z.; Hedtrich, S.; Kharat, A. N.; Adeli, M.; Haag, R. One-Pot and Gram-Scale Synthesis of Biodegradable Polyglycerols under Ambient Conditions: Nanocarriers for Intradermal Drug Delivery. *Polym. Chem.* **2017**, *8* (47), 7375–7383.
(127) Teeranachaideekul, V.; Boonme, P.; Souto, E. B.; Müller, R. H.; Junyaprasert, V. B. Influence of Oil Content on Physicochemical Properties and Skin Distribution of Nile Red-Loaded NLC. *J. Control. Release* **2008**, *128* (2), 134–141.
(128) Zhang, Z.; He, Z.; Liang, R.; Ma, Y.; Huang, W.; Jiang, R.; Shi, S.; Chen, H.; Li, X. Fabrication of a Micellar Supramolecular Hydrogel for Ocular Drug Delivery. *Biomacromolecules* **2016**, *17* (3), 798–807.
(129) Zabihi, F.; Koeppe, H.; Achazi, K.; Hedtrich, S.; Haag, R. One-Pot Synthesis of Poly(Glycerol-Co-Succinic Acid) Nanogels for Dermal Delivery. *Biomacromolecules* **2019**, *20* (5), 1867–1875.

(130) Yang, K.-J.; Son, J.; Jung, S. Y.; Yi, G.; Yoo, J.; Kim, D.-K.; Koo, H. Optimized Phospholipid-Based Nanoparticles for Inner Ear Drug Delivery and Therapy. *Biomaterials* **2018**, *171*, 133–143.
(131) Poelma, S. O.; Oh, S. S.; Helmy, S.; Knight, A. S.; Burnett, G. L.; Soh, H. T.; Hawker, C. J.; Alaniz, J. R. de. Controlled Drug Release to Cancer Cells from Modular One-Photon Visible Light-Responsive Micellar System. *Chem. Commun.* **2016**, *52* (69), 10525–10528.
(132) Jin, H.; Sun, M.; Shi, L.; Zhu, X.; Huang, W.; Yan, D. Reduction-Responsive Amphiphilic Polymeric Prodrugs of Camptothecin–Polyphosphoester for Cancer Chemotherapy. *Biomater. Sci.* **2018**, *6* (6), 1403–1413.
(133) Islam, M. S.; Reineke, J.; Kaushik, R.; Woyengo, T.; Baride, A.; Alqahtani, M. S.; Perumal, O. Bioadhesive Food Protein Nanoparticles as Pediatric Oral Drug Delivery System. *ACS Appl. Mater. Interfaces* **2019**, *11* (20), 18062–18073.
(134) Jäger, E.; Höcherl, A.; Janoušková, O.; Jäger, A.; Hrubý, M.; Konefał, R.; Netopilik, M.; Pánek, J.; Šlouf, M.; Ulbrich, K.; et al. Fluorescent Boronate-Based Polymer Nanoparticles with Reactive Oxygen Species (ROS)-Triggered Cargo Release for Drug-Delivery Applications. *Nanoscale* **2016**, *8* (13), 6958–6963.
(135) Ma, X.; Gong, N.; Zhong, L.; Sun, J.; Liang, X.-J. Future of Nanotherapeutics: Targeting the Cellular Sub-Organelles. *Biomaterials* **2016**, *97*, 10–21..
(136) Behzadi, S.; Serpooshan, V.; Tao, W.; A. Hamaly, M.; Y. Alkawareek, M.; C. Dreaden, E.; Brown, D.; M. Alkilany, A.; C. Farokhzad, O.; Mahmoudi, M. Cellular Uptake of Nanoparticles: Journey inside the Cell. *Chem. Soc. Rev.* **2017**, *46* (14), 4218–4244.
(137) Yameen, B.; Choi, W. I.; Vilos, C.; Swami, A.; Shi, J.; Farokhzad, O. C. Insight into Nanoparticle Cellular Uptake and Intracellular Targeting. *J. Control. Release* **2014**, *190*, 485–499.
(138) Hillaireau, H.; Couvreur, P. Nanocarriers' Entry into the Cell: Relevance to Drug Delivery. *Cell. Mol. Life Sci.* **2009**, *66* (17), 2873–2896.
(139) Conner, S. D.; Schmid, S. L. Regulated Portals of Entry into the Cell. *Nature* **2003**, *422* (6927), 37.
(140) Kaksonen, M.; Roux, A. Mechanisms of Clathrin-Mediated Endocytosis. *Nat. Rev. Mol. Cell Biol.* **2018**, *19* (5), 313–326.
(141) Cheng, J. P. X.; Nichols, B. J. Caveolae: One Function or Many? *Trends Cell Biol.* **2016**, *26* (3), 177–189.
(142) Lamaze, C.; Tardif, N.; Dewulf, M.; Vassilopoulos, S.; Blouin, C. M. The Caveolae Dress Code: Structure and Signaling. *Curr. Opin. Cell Biol.* **2017**, *47*, 117–125.
(143) Pfeffer, S. R. Caveolae on the Move. *Nat. Cell Biol.* **2001**, *3* (5), E108–E110.
(144) Damm, E.-M.; Pelkmans, L.; Kartenbeck, J.; Mezzacasa, A.; Kurzchalia, T.; Helenius, A. Clathrin- and Caveolin-1–Independent Endocytosis. *J. Cell Biol.* **2005**, *168* (3), 477–488.
(145) Mayor, S.; Parton, R. G.; Donaldson, J. G. Clathrin-Independent Pathways of Endocytosis. *CSH Perspect. Biol.* **2014**, *6* (6). a016758.
(146) Kirkham, M.; Parton, R. G. Clathrin-Independent Endocytosis: New Insights into Caveolae and Non-Caveolar Lipid Raft Carriers. *Biochim. Biophys. Acta* **2005**, *1745* (3), 273–286.

(147) Swanson, J. A. Shaping Cups into Phagosomes and Macropinosomes. *Nat. Rev. Mol. Cell Biol.* **2008**, *9* (8), 639–649.
(148) Aderem, A.; Underhill, D. M. Mechanisms of Phagocytosis in Macrophages. *Annu. Rev. Immunol.* **1999**, *17* (1), 593–623..
(149) Kleist, L. von; Haucke, V. At the Crossroads of Chemistry and Cell Biology: Inhibiting Membrane Traffic by Small Molecules. *Traffic* **2012**, *13* (4), 495–504.
(150) Dutta, D.; Donaldson, J. G. Search for Inhibitors of Endocytosis. *Cellular Logist.* **2012**, *2* (4), 203–208.
(151) Hansen, S. H.; Sandvig, K.; Deurs, B. van. Clathrin and HA2 Adaptors: Effects of Potassium Depletion, Hypertonic Medium, and Cytosol Acidification. *J. Cell Biol.* **1993**, *121* (1), 61–72.
(152) Wang, L. H.; Rothberg, K. G.; Anderson, R. G. Mis-Assembly of Clathrin Lattices on Endosomes Reveals a Regulatory Switch for Coated Pit Formation. *J. Cell Biol.* **1993**, *123* (5), 1107–1117.
(153) Yao, D.; Ehrlich, M.; Henis, Y. I.; Leof, E. B. Transforming Growth Factor-β Receptors Interact with AP2 by Direct Binding to B2 Subunit. *MBoC* **2002**, *13* (11), 4001–4012.
(154) Ros-Baró, A.; López-Iglesias, C.; Peiró, S.; Bellido, D.; Palacín, M.; Zorzano, A.; Camps, M. Lipid Rafts Are Required for GLUT4 Internalization in Adipose Cells. *PNAS* **2001**, *98* (21), 12050–12055.
(155) Schnitzer, J. E.; Oh, P.; Pinney, E.; Allard, J. Filipin-Sensitive Caveolae-Mediated Transport in Endothelium: Reduced Transcytosis, Scavenger Endocytosis, and Capillary Permeability of Select Macromolecules. *J. Cell Biol.* **1994**, *127* (5), 1217–1232.
(156) Kilsdonk, E. P. C.; Yancey, P. G.; Stoudt, G. W.; Bangerter, F. W.; Johnson, W. J.; Phillips, M. C.; Rothblat, G. H. Cellular Cholesterol Efflux Mediated by Cyclodextrins. *J. Biol. Chem.* **1995**, *270* (29), 17250–17256.
(157) Buschiazzo, J.; Bonini, I. C.; Alonso, T. S. Inhibition of Bufo Arenarum Oocyte Maturation Induced by Cholesterol Depletion by Methyl-β-Cyclodextrin. Role of Low-Density Caveolae-like Membranes. *BBA - Biomembranes* **2008**, *1778* (6), 1398–1406.
(158) Lin, H.-P.; Singla, B.; Ghoshal, P.; Faulkner, J. L.; Cherian-Shaw, M.; O'Connor, P. M.; She, J.-X.; Chantemele, E. J. B. de; Csányi, G. Identification of Novel Macropinocytosis Inhibitors Using a Rational Screen of Food and Drug Administration-Approved Drugs. *Br. J. Pharmacol.* **2018**, *175* (18), 3640–3655.
(159) Peterson, J. R.; Mitchison, T. J. Small Molecules, Big Impact: A History of Chemical Inhibitors and the Cytoskeleton. *Chem. Biol.* **2002**, *9* (12), 1275–1285.
(160) Koivusalo, M.; Welch, C.; Hayashi, H.; Scott, C. C.; Kim, M.; Alexander, T.; Touret, N.; Hahn, K. M.; Grinstein, S. Amiloride Inhibits Macropinocytosis by Lowering Submembranous PH and Preventing Rac1 and Cdc42 Signaling. *J. Cell Biol.* **2010**, *188* (4), 547–563.
(161) Araki, N.; Johnson, M. T.; Swanson, J. A. A Role for Phosphoinositide 3-Kinase in the Completion of Macropinocytosis and Phagocytosis by Macrophages. *J. Cell Biol.* **1996**, *135* (5), 1249–1260.

(162) Chaudhuri, A.; Battaglia, G.; Golestanian, R. The Effect of Interactions on the Cellular Uptake of Nanoparticles. *Phys. Biol.* **2011**, *8* (4), 046002.
(163) Smith, K. A.; Jasnow, D.; Balazs, A. C. Designing Synthetic Vesicles That Engulf Nanoscopic Particles. *J. Chem. Phys.* **2007**, *127* (8), 084703.
(164) Chithrani, B. D.; Ghazani, A. A.; Chan, W. C. W. Determining the Size and Shape Dependence of Gold Nanoparticle Uptake into Mammalian Cells. *Nano Lett.* **2006**, *6* (4), 662–668.
(165) Sun, X.-Y.; Gan, Q.-Z.; Ouyang, J.-M. Size-Dependent Cellular Uptake Mechanism and Cytotoxicity toward Calcium Oxalate on Vero Cells. *Sci. Rep.* **2017**, *7*, 41949.
(166) Jiang, W.; Kim, B. Y. S.; Rutka, J. T.; Chan, W. C. W. Nanoparticle-Mediated Cellular Response Is Size-Dependent. *Nat. Nanotechnol.* **2008**, *3* (3), 145–150.
(167) Zhu, J.; Liao, L.; Zhu, L.; Zhang, P.; Guo, K.; Kong, J.; Ji, C.; Liu, B. Size-Dependent Cellular Uptake Efficiency, Mechanism, and Cytotoxicity of Silica Nanoparticles toward HeLa Cells. *Talanta* **2013**, *107*, 408–415.
(168) Albanese, A.; Chan, W. C. W. Effect of Gold Nanoparticle Aggregation on Cell Uptake and Toxicity. *ACS Nano* **2011**, *5* (7), 5478–5489.
(169) Dasgupta, S.; Auth, T.; Gompper, G. Shape and Orientation Matter for the Cellular Uptake of Nonspherical Particles. *Nano Lett.* **2014**, *14* (2), 687–693.
(170) Qiu, Y.; Liu, Y.; Wang, L.; Xu, L.; Bai, R.; Ji, Y.; Wu, X.; Zhao, Y.; Li, Y.; Chen, C. Surface Chemistry and Aspect Ratio Mediated Cellular Uptake of Au Nanorods. *Biomaterials* **2010**, *31* (30), 7606–7619.
(171) Meng, H.; Yang, S.; Li, Z.; Xia, T.; Chen, J.; Ji, Z.; Zhang, H.; Wang, X.; Lin, S.; Huang, C.; et al. Aspect Ratio Determines the Quantity of Mesoporous Silica Nanoparticle Uptake by a Small GTPase-Dependent Macropinocytosis Mechanism. *ACS Nano* **2011**, *5* (6), 4434–4447.
(172) Shao, D.; Lu, M.; Zhao, Y.; Zhang, F.; Tan, Y.; Zheng, X.; Pan, Y.; Xiao, X.; Wang, Z.; Dong, W.; et al. The Shape Effect of Magnetic Mesoporous Silica Nanoparticles on Endocytosis, Biocompatibility and Biodistribution. *Acta Biomater.* **2017**, *49*, 531–540.
(173) Herd, H.; Daum, N.; Jones, A. T.; Huwer, H.; Ghandehari, H.; Lehr, C.-M. Nanoparticle Geometry and Surface Orientation Influence Mode of Cellular Uptake. *ACS Nano* **2013**, *7* (3), 1961–1973.
(174) Xie, X.; Liao, J.; Shao, X.; Li, Q.; Lin, Y. The Effect of Shape on Cellular Uptake of Gold Nanoparticles in the Forms of Stars, Rods, and Triangles. *Sci. Rep.* **2017**, *7* (1), 3827.
(175) Yang, K.; Ma, Y.-Q. Computer Simulation of the Translocation of Nanoparticles with Different Shapes across a Lipid Bilayer. *Nat. Nanotechnol.* **2010**, *5* (8), 579–583.
(176) van Meer, G.; Voelker, D. R.; Feigenson, G. W. Membrane Lipids: Where They Are and How They Behave. *Nat. Rev. Mol. Cell Biol.* **2008**, *9* (2), 112–124.
(177) Ma, Y.; Poole, K.; Goyette, J.; Gaus, K. Introducing Membrane Charge and Membrane Potential to T Cell Signaling. *Front Immunol.* **2017**, *8*. 1513.
(178) Goldenberg, N. M.; Steinberg, B. E. Surface Charge: A Key Determinant of Protein Localization and Function. *Cancer Res.* **2010**, *70* (4), 1277–1280.

(179) Fröhlich, E. The Role of Surface Charge in Cellular Uptake and Cytotoxicity of Medical Nanoparticles. *Int. J. Nanomed,* **2012**, *7*, 5577–5591.
(180) Kettler Katja; Veltman Karin; van de Meent Dik; van Wezel Annemarie; Hendriks A. Jan. Cellular Uptake of Nanoparticles as Determined by Particle Properties, Experimental Conditions, and Cell Type. *Environ. Toxicol. Chem.* **2014**, *33* (3), 481–492.
(181) Miller, C. R.; Bondurant, B.; McLean, S. D.; McGovern, K. A.; O'Brien, D. F. Liposome−Cell Interactions in Vitro: Effect of Liposome Surface Charge on the Binding and Endocytosis of Conventional and Sterically Stabilized Liposomes. *Biochemistry* **1998**, *37* (37), 12875–12883.
(182) Jeon, S.; Clavadetscher, J.; Lee, D.-K.; Chankeshwara, S. V.; Bradley, M.; Cho, W.-S. Surface Charge-Dependent Cellular Uptake of Polystyrene Nanoparticles. *Nanomaterials* **2018**, *8* (12), 1028.
(183) Hühn, D.; Kantner, K.; Geidel, C.; Brandholt, S.; De Cock, I.; Soenen, S. J. H.; Rivera_Gil, P.; Montenegro, J.-M.; Braeckmans, K.; Müllen, K.; et al. Polymer-Coated Nanoparticles Interacting with Proteins and Cells: Focusing on the Sign of the Net Charge. *ACS Nano* **2013**, *7* (4), 3253–3263.
(184) Sukhanova, A.; Bozrova, S.; Sokolov, P.; Berestovoy, M.; Karaulov, A.; Nabiev, I. Dependence of Nanoparticle Toxicity on Their Physical and Chemical Properties. *Nanoscale Res. Lett.* **2018**, *13* (1), 44.
(185) Asati, A.; Santra, S.; Kaittanis, C.; Perez, J. M. Surface-Charge-Dependent Cell Localization and Cytotoxicity of Cerium Oxide Nanoparticles. *ACS Nano* **2010**, *4* (9), 5321–5331.
(186) Lunnoo, T.; Assawakhajornsak, J.; Puangmali, T. In Silico Study of Gold Nanoparticle Uptake into a Mammalian Cell: Interplay of Size, Shape, Surface Charge, and Aggregation. *J. Phys. Chem. C* **2019**, *123* (6), 3801–3810.
(187) Li, X.; Tang, Y.; Xu, L.; Kong, X.; Zhang, L.; Chang, Y.; Zhao, H.; Zhang, H.; Liu, X. Dependence between Cytotoxicity and Dynamic Subcellular Localization of Up-Conversion Nanoparticles with Different Surface Charges. *RSC Adv.* **2017**, *7* (53), 33502–33509.
(188) Alcorn, J. L. Chapter 4 - Pulmonary Surfactant Trafficking and Homeostasis. In *Lung Epithelial Biology in the Pathogenesis of Pulmonary Disease*; Academic Press: Boston, **2017**; pp 59–75.
(189) Maina, J. N.; West, J. B. Thin and Strong! The Bioengineering Dilemma in the Structural and Functional Design of the Blood-Gas Barrier. *Physiol. Rev.* **2005**, *85* (3), 811–844.
(190) Schmitz, G.; Müller, G. Structure and Function of Lamellar Bodies, Lipid-Protein Complexes Involved in Storage and Secretion of Cellular Lipids. *J. Lipid Res.* **1991**, *32* (10), 1539–1570.
(191) Beers, M. F.; Nureki, S.-I.; Mulugeta, S. Chapter 8 - The Role of Epithelial Cell Quality Control in Health and Disease of the Distal Lung. In *Lung Epithelial Biology in the Pathogenesis of Pulmonary Disease*; Academic Press: Boston, **2017**; pp 133–163.
(192) Perez-Gil, J.; Weaver, T. E. Pulmonary Surfactant Pathophysiology: Current Models and Open Questions. *Physiology* **2010**, *25* (3), 132–141.

(193) Orgeig, S.; Daniels, C. B. The Roles of Cholesterol in Pulmonary Surfactant: Insights from Comparative and Evolutionary Studies. *Comp. Biochem. Physiol. A - Mol. Integrat. Physiol.* **2001**, *129* (1), 75–89.
(194) Wilhelm, S.; Tavares, A. J.; Chan, W. C. W. Reply to "Evaluation of Nanomedicines: Stick to the Basics." *Nat. Rev. Mater.* **2016**, *1* (10), 16074.
(195) Li, J.; Wang, X.; Zhang, T.; Wang, C.; Huang, Z.; Luo, X.; Deng, Y. A Review on Phospholipids and Their Main Applications in Drug Delivery Systems. *Asian J. Pharm. Sci.* **2015**, *10* (2), 81–98.
(196) Rojas-Gutierrez, P. A.; DeWolf, C.; Capobianco, J. A. Upconversion Nanoparticles: Formation of a Supported Lipid Bilayer on Faceted $LiYF_4$:Tm^{3+}/Yb^{3+} Upconversion Nanoparticles . *Part. Part. Syst. Charact.* **2016**, *33* (12), 859.
(197) Li, X.; Zhang, F.; Zhao, D. Lab on Upconversion Nanoparticles: Optical Properties and Applications Engineering via Designed Nanostructure. *Chem. Soc. Rev.* **2015**, *44* (6), 1346–1378.
(198) Naccache, R.; Rodríguez, E. M.; Bogdan, N.; Sanz-Rodríguez, F.; Cruz, M. del C. I. de la; Fuente, Á. J. de la; Vetrone, F.; Jaque, D.; Solé, J. G.; Capobianco, J. A. High Resolution Fluorescence Imaging of Cancers Using Lanthanide Ion-Doped Upconverting Nanocrystals. *Cancers* **2012**, *4* (4), 1067–1105.
(199) Bogdan, N.; Vetrone, F.; Roy, R.; Capobianco, J. A. Carbohydrate-Coated Lanthanide-Doped Upconverting Nanoparticles for Lectin Recognition. *J. Mater. Chem.* **2010**, *20* (35), 7543–7550.
(200) Boyer, J.-C.; Cuccia, L. A.; Capobianco, J. A. Synthesis of Colloidal Upconverting $NaYF_4$: Er^{3+}/Yb^{3+} and Tm^{3+}/Yb^{3+} Monodisperse Nanocrystals. *Nano Lett.* **2007**, *7* (3), 847–852.
(201) Li, L.-L.; Zhang, R.; Yin, L.; Zheng, K.; Qin, W.; Selvin, P. R.; Lu, Y. Biomimetic Surface Engineering of Lanthanide-Doped Upconversion Nanoparticles as Versatile Bioprobes. *Angew. Chem. Int. Ed.* **2012**, *51* (25), 6121–6125.
(202) Wang, H.; Dong, C.; Zhao, P.; Wang, S.; Liu, Z.; Chang, J. Lipid Coated Upconverting Nanoparticles as NIR Remote Controlled Transducer for Simultaneous Photodynamic Therapy and Cell Imaging. *Int. J. Pharm.* **2014**, *466* (1–2), 307–313.
(203) Yao, C.; Wang, P.; Zhou, L.; Wang, R.; Li, X.; Zhao, D.; Zhang, F. Highly Biocompatible Zwitterionic Phospholipids Coated Upconversion Nanoparticles for Efficient Bioimaging. *Anal. Chem.* **2014**, *86* (19), 9749–9757.
(204) Gopalakrishnan, G.; Rouiller, I.; Colman, D. R.; Lennox, R. B. Supported Bilayers Formed from Different Phospholipids on Spherical Silica Substrates. *Langmuir* **2009**, *25* (10), 5455–5458.
(205) Zhang, L.; Sun, X.; Song, Y.; Jiang, X.; Dong, S.; Wang, E. Didodecyldimethylammonium Bromide Lipid Bilayer-Protected Gold Nanoparticles: Synthesis, Characterization, and Self-Assembly. *Langmuir* **2006**, *22* (6), 2838–2843.
(206) Bhowmik, D.; Mote, K. R.; MacLaughlin, C. M.; Biswas, N.; Chandra, B.; Basu, J. K.; Walker, G. C.; Madhu, P. K.; Maiti, S. Cell-Membrane-Mimicking Lipid-Coated

Nanoparticles Confer Raman Enhancement to Membrane Proteins and Reveal Membrane-Attached Amyloid-β Conformation. *ACS Nano* **2015**, *9* (9), 9070–9077.
(207) Klapper, Y.; Maffre, P.; Shang, L.; Ekdahl, K. N.; Nilsson, B.; Hettler, S.; Dries, M.; Gerthsen, D.; Nienhaus, G. U. Low Affinity Binding of Plasma Proteins to Lipid-Coated Quantum Dots as Observed by in Situ Fluorescence Correlation Spectroscopy. *Nanoscale* **2015**, *7* (22), 9980–9984.
(208) Zhang, Y.; Zhao, Q.; Zhu, W.; Zhang, L.; Han, J.; Lin, Q.; Ai, F. Synthesis and Evaluation of Mesoporous Carbon/Lipid Bilayer Nanocomposites for Improved Oral Delivery of the Poorly Water-Soluble Drug, Nimodipine. *Pharm. Res.* **2015**, *32* (7), 2372–2383.
(209) Zhang, S.; Niu, H.; Zhang, Y.; Liu, J.; Shi, Y.; Zhang, X.; Cai, Y. Biocompatible Phosphatidylcholine Bilayer Coated on Magnetic Nanoparticles and Their Application in the Extraction of Several Polycyclic Aromatic Hydrocarbons from Environmental Water and Milk Samples. *J. Chromatogr. A* **2012**, *1238*, 38–45.
(210) Kolate, A.; Baradia, D.; Patil, S.; Vhora, I.; Kore, G.; Misra, A. PEG — A Versatile Conjugating Ligand for Drugs and Drug Delivery Systems. *J. Control. Release* **2014**, *192*, 67–81.
(211) Wang, F.; Liu, J. A Stable Lipid/TiO2 Interface with Headgroup-Inversed Phosphocholine and a Comparison with SiO2. *J. Am. Chem. Soc.* **2015**, *137* (36), 11736–11742.
(212) Alwarawrah, M.; Dai, J.; Huang, J. A Molecular View of the Cholesterol Condensing Effect in DOPC Lipid Bilayers. *J. Phys. Chem. B* **2010**, *114* (22), 7516–7523.
(213) Egerton, R. F.; Li, P.; Malac, M. Radiation Damage in the TEM and SEM. *Micron.* **2004**, *35* (6), 399–409.
(214) Hayat, M. A. Chapter 5: Negative Stain. In *Basic Techniques for Transmission Electron Microscopy*; Academic Press: San Diego, **1986**; pp 232–264.
(215) Kuntsche, J.; Horst, J. C.; Bunjes, H. Cryogenic Transmission Electron Microscopy (Cryo-TEM) for Studying the Morphology of Colloidal Drug Delivery Systems. *Int. J. Pharma.* **2011**, *417* (1–2), 120–137.
(216) Saito, H.; Shinoda, W. Cholesterol Effect on Water Permeability through DPPC and PSM Lipid Bilayers: A Molecular Dynamics Study. *J. Phys. Chem. B* **2011**, *115* (51), 15241–15250.
(217) Derjaguin, B.; Landau, L. Theory of the Stability of Strongly Sharged Lyophobic Sols and of the Adhesion of Strongly Charged Particles in Solutions of Electrolytes. *Acta Physicochim. URSS* **1941**, *14*, 633.
(218) Verwey, E. J. W.; Overbeek, J. T. G.; Nes, K. van. *Theory of the Stability of Lyophobic Colloids: The Interaction of Sol Particles Having an Electric Double Layer*; Elsevier: New York, **1948**.
(219) Chen, Z.; Chen, H.; Hu, H.; Yu, M.; Li, F.; Zhang, Q.; Zhou, Z.; Yi, T.; Huang, C. Versatile Synthesis Strategy for Carboxylic Acid−functionalized Upconverting Nanophosphors as Biological Labels. *J. Am. Chem. Soc.* **2008**, *130* (10), 3023–3029.
(220) Bergstrm, L.; Shinozaki, K.; Tomiyama, H.; Mizutani, N. Colloidal Processing of a Very Fine $BaTiO_3$ Powder—Effect of Particle Interactions on the Suspension Properties, Consolidation, and Sintering Behavior. *J. Am. Ceram. Soc.* **1997**, *80* (2), 291–300.

(221) Roiter, Y.; Ornatska, M.; Rammohan, A. R.; Balakrishnan, J.; Heine, D. R.; Minko, S. Interaction of Nanoparticles with Lipid Membrane. *Nano Lett.* **2008**, *8* (3), 941–944.
(222) Groves, J. T.; Dustin, M. L. Supported Planar Bilayers in Studies on Immune Cell Adhesion and Communication. *J. Immunol. Meth.* **2003**, *278* (1), 19–32.
(223) Sackmann, E. Supported Membranes: Scientific and Practical Applications. *Science* **1996**, *271* (5245), 43–48.
(224) Boxer, S. G. Molecular Transport and Organization in Supported Lipid Membranes. *Curr. Opin. Chem. Biol.* **2000**, *4* (6), 704–709.
(225) Tu, J.; Bussmann, J.; Du, G.; Gao, Y.; Bouwstra, J. A.; Kros, A. Lipid Bilayer-Coated Mesoporous Silica Nanoparticles Carrying Bovine Hemoglobin towards an Erythrocyte Mimic. *Int. J. Pharma.* **2018**, *543* (1), 169–178.
(226) Berti, D.; Caminati, G.; Baglioni, P. Functional Liposomes and Supported Lipid Bilayers: Towards the Complexity of Biological Archetypes. *Phys. Chem. Chem. Phys.* **2011**, *13* (19), 8769–8782.
(227) Roggers, R. A.; Lin, V. S.-Y.; Trewyn, B. G. Chemically Reducible Lipid Bilayer Coated Mesoporous Silica Nanoparticles Demonstrating Controlled Release and HeLa and Normal Mouse Liver Cell Biocompatibility and Cellular Internalization. *Mol. Pharma.* **2012**, *9* (9), 2770–2777.
(228) Wuttke, S.; Braig, S.; Preiß, T.; Zimpel, A.; Sicklinger, J.; Bellomo, C.; Rädler, J. O.; Vollmar, A. M.; Bein, T. MOF Nanoparticles Coated by Lipid Bilayers and Their Uptake by Cancer Cells. *Chem. Commun.* **2015**, *51* (87), 15752–15755.
(229) Ferris, D. P.; Zhao, Y.-L.; Khashab, N. M.; Khatib, H. A.; Stoddart, J. F.; Zink, J. I. Light-Operated Mechanized Nanoparticles. *J. Am. Chem. Soc.* **2009**, *131* (5), 1686–1688.
(230) Sadovski, O.; Beharry, A. A.; Zhang, F.; Woolley, G. A. Spectral Tuning of Azobenzene Photoswitches for Biological Applications. *Angew. Chem. Int. Ed.* **2009**, *48* (8), 1484–1486.
(231) Dong, M.; Babalhavaeji, A.; Collins, C. V.; Jarrah, K.; Sadovski, O.; Dai, Q.; Woolley, G. A. Near-Infrared Photoswitching of Azobenzenes under Physiological Conditions. *J. Am. Chem. Soc.* **2017**, *139* (38), 13483–13486.
(232) Liu, J.; Bu, W.; Pan, L.; Shi, J. NIR-Triggered Anticancer Drug Delivery by Upconverting Nanoparticles with Integrated Azobenzene-Modified Mesoporous Silica. *Angew. Chem. Int. Ed.* **2013**, *52* (16), 4375–4379.
(233) Yao, C.; Wang, P.; Li, X.; Hu, X.; Hou, J.; Wang, L.; Zhang, F. Near-Infrared-Triggered Azobenzene-Liposome/Upconversion Nanoparticle Hybrid Vesicles for Remotely Controlled Drug Delivery to Overcome Cancer Multidrug Resistance. *Adv. Mater.* **2016**, *28* (42), 9341–9348.
(234) Briuglia, M.-L.; Rotella, C.; McFarlane, A.; Lamprou, D. A. Influence of Cholesterol on Liposome Stability and on in Vitro Drug Release. *Drug Deliv. Transl. Res.* **2015**, *5* (3), 231–242.
(235) Yu, Q.; Rodriguez, E. M.; Naccache, R.; Forgione, P.; Lamoureux, G.; Sanz-Rodriguez, F.; Scheglmann, D.; Capobianco, J. A. Chemical Modification of Temoporfin – a Second

Generation Photosensitizer Activated Using Upconverting Nanoparticles for Singlet Oxygen Generation. *Chem. Commun.* **2014**, *50* (81), 12150–12153.
(236) Rojas-Gutierrez, P. A.; DeWolf, C.; Capobianco, J. A. Formation of a Supported Lipid Bilayer on Faceted $LiYF_4$:Tm^{3+}/Yb^{3+} Upconversion Nanoparticles. *Part. Part. Syst. Charact.* **2016**, *33* (12), 865–870.
(237) Dong, M.; Babalhavaeji, A.; Samanta, S.; Beharry, A. A.; Woolley, G. A. Red-Shifting Azobenzene Photoswitches for in Vivo Use. *Acc. Chem. Res.* **2015**, *48* (10), 2662–2670.
(238) Liu, D.; Xu, X.; Du, Y.; Qin, X.; Zhang, Y.; Ma, C.; Wen, S.; Ren, W.; Goldys, E. M.; Piper, J. A.; et al. Three-Dimensional Controlled Growth of Monodisperse Sub-50 Nm Heterogeneous Nanocrystals. *Nat. Commu.* **2016**, *7*, 10254.
(239) Na, H.; Jeong, J. S.; Chang, H. J.; Kim, H. Y.; Woo, K.; Lim, K.; Mkhoyan, K. A.; Jang, H. S. Facile Synthesis of Intense Green Light Emitting LiGdF4:Yb,Er-Based Upconversion Bipyramidal Nanocrystals and Their Polymer Composites. *Nanoscale* **2014**, *6* (13), 7461–7468.
(240) Wen, H.; Zhu, H.; Chen, X.; Hung, T. F.; Wang, B.; Zhu, G.; Yu, S. F.; Wang, F. Upconverting Near-Infrared Light through Energy Management in Core–Shell–Shell Nanoparticles. *Angew. Chem. Int. Ed.* **2013**, *52* (50), 13419–13423.
(241) Xie, X.; Gao, N.; Deng, R.; Sun, Q.; Xu, Q.-H.; Liu, X. Mechanistic Investigation of Photon Upconversion in Nd^{3+}-Sensitized Core–Shell Nanoparticles. *J. Am. Chem. Soc.* **2013**, *135* (34), 12608–12611.
(242) Beer, F.; Körpert, W.; Passow, H.; Steidler, A.; Meinl, A.; Buchmair, A. G.; Moritz, A. Reduction of Collateral Thermal Impact of Diode Laser Irradiation on Soft Tissue Due to Modified Application Parameters. *Lasers Med. Sci.* **2012**, *27* (5), 917–921.
(243) Kamalski, D. M. A.; de Boorder, T.; Bittermann, A. J. N.; Wegner, I.; Vincent, R.; Grolman, W. Capturing Thermal, Mechanical, and Acoustic Effects of the Diode (980 Nm) Laser in Stapedotomy. *Otol. Neurotol.* **2014**, *35* (6), 1070–1076.
(244) Wu, S.; Butt, H.-J. Near-Infrared-Sensitive Materials Based on Upconverting Nanoparticles. *Adv. Mater.* **2016**, *28* (6), 1208–1226.
(245) Morries, L. D.; Cassano, P.; Henderson, T. A. Treatments for Traumatic Brain Injury with Emphasis on Transcranial Near-Infrared Laser Phototherapy. *Neuropsychiatr. Dis. Treat.* **2015**, *11*, 2159–2175.
(246) Kuiper, J. M.; Hulst, R.; Engberts, J. B. A Selective and Mild Synthetic Route to Dialkyl Phosphates. *Synthesis* **2003**, *35* (5), 695–698.
(247) Bullock, D. J. W.; Cumper, C. W. N.; Vogel, A. I. 989. Physical Properties and Chemical Constitution. Part XLIII. The Electric Dipole Moments of Azobenzene, Azopyridines, and Azoquinolines. *J. Chem. Soc.* **1965**, *0* (0), 5316–5323.
(248) Mattsson, L.; Wegner, K. D.; Hildebrandt, N.; Soukka, T. Upconverting Nanoparticle to Quantum Dot FRET for Homogeneous Double-Nano Biosensors. *RSC Adv.* **2015**, *5* (18), 13270–13277.
(249) Serra, F.; Terentjev, E. M. Effects of Solvent Viscosity and Polarity on the Isomerization of Azobenzene. *Macromolecules* **2008**, *41* (3), 981–986.

(250) Han, M.; Ishikawa, D.; Honda, T.; Ito, E.; Hara, M. Light-Driven Molecular Switches in Azobenzene Self-Assembled Monolayers: Effect of Molecular Structure on Reversible Photoisomerization and Stable Cis State. *Chem. Commun.* **2010**, *46* (20), 3598–3600.
(251) Shimomura, M.; Ando, R.; Kunitake, T. Orientation and Spectral Characteristics of the Azobenzene Chromophore in the Ammonium Bilayer Assembly. *Berich. Bunsengesell. Physikal. Chem.* **1983**, *87* (12), 1134–1143.
(252) Yager, K. G.; Barrett, C. J. Novel Photo-Switching Using Azobenzene Functional Materials. *J. Photochem. Photobio. A: Chem.* **2006**, *182* (3), 250–261.
(253) Evans, S. D.; Johnson, S. R.; Ringsdorf, H.; Williams, L. M.; Wolf, H. Photoswitching of Azobenzene Derivatives Formed on Planar and Colloidal Gold Surfaces. *Langmuir* **1998**, *14* (22), 6436–6440.
(254) El Garah, M.; Palmino, F.; Cherioux, F. Reversible Photoswitching of Azobenzene-Based Monolayers Physisorbed on a Mica Surface. *Langmuir* **2010**, *26* (2), 943–949.
(255) Backus, E. H. G.; Kuiper, J. M.; Engberts, J. B. F. N.; Poolman, B.; Bonn, M. Reversible Optical Control of Monolayers on Water through Photoswitchable Lipids. *J. Phys. Chem. B* **2011**, *115* (10), 2294–2302.
(256) Song, X.; Perlstein, J.; Whitten, D. G. Supramolecular Aggregates of Azobenzene Phospholipids and Related Compounds in Bilayer Assemblies and Other Microheterogeneous Media: Structure, Properties, and Photoreactivity1. *J. Am. Chem. Soc.* **1997**, *119* (39), 9144–9159.
(257) Dickey, A.; Faller, R. Examining the Contributions of Lipid Shape and Headgroup Charge on Bilayer Behavior. *Biophys. J.* **2008**, *95* (6), 2636–2646.
(258) Langer, G.; Hochreiner, A.; Burgholzer, P.; Berer, T. A Webcam in Bayer-Mode as a Light Beam Profiler for the near Infra-Red. *Opt. Lasers Eng.* **2013**, *51* (5), 571–575.
(259) Askes, S. H. C.; Bahreman, A.; Bonnet, S. Activation of a Photodissociative Ruthenium Complex by Triplet–Triplet Annihilation Upconversion in Liposomes. *Angew. Chem. Int. Ed.* **2014**, *53* (4), 1029–1033.
(260) Schneider, C. A.; Rasband, W. S.; Eliceiri, K. W. NIH Image to ImageJ: 25 Years of Image Analysis. *Nat. Meth.* **2012**, *9* (7), 671–675.
(261) Ahmed, E. M. Hydrogel: Preparation, Characterization, and Applications: A Review. *J. Adv. Res.* **2015**, *6* (2), 105–121.
(262) Appel, E. A.; Barrio, J. del; Loh, X. J.; Scherman, O. A. Supramolecular Polymeric Hydrogels. *Chem. Soc. Rev.* **2012**, *41* (18), 6195–6214.
(263) Tamesue, S.; Takashima, Y.; Yamaguchi, H.; Shinkai, S.; Harada, A. Photoswitchable Supramolecular Hydrogels Formed by Cyclodextrins and Azobenzene Polymers. *Angew. Chem. Int. Ed.* **2010**, *49* (41), 7461–7464.
(264) Mandl, G. A.; Rojas-Gutierrez, P. A.; Capobianco, J. A. A NIR-Responsive Azobenzene-Based Supramolecular Hydrogel Using Upconverting Nanoparticles. *Chem. Commun.* **2018**, *54* (46), 5847–5850.
(265) Wang, R.; Zhang, F. Chapter 1: Lanthanide-Based Near Infrared Nanomaterials for Bioimaging. In *Near-infrared Nanomaterials: Preparation, Bioimaging and Therapy Applications*; The Royal Society of Chemistry: Cambridge, **2016**; pp 1–39.

(266) Näreoja, T.; Deguchi, T.; Christ, S.; Peltomaa, R.; Prabhakar, N.; Fazeli, E.; Perälä, N.; Rosenholm, J. M.; Arppe, R.; Soukka, T.; et al. Ratiometric Sensing and Imaging of Intracellular PH Using Polyethylenimine-Coated Photon Upconversion Nanoprobes. *Anal. Chem.* **2017**, *89* (3), 1501–1508.
(267) Drees, C.; Raj, A. N.; Kurre, R.; Busch, K. B.; Haase, M.; Piehler, J. Engineered Upconversion Nanoparticles for Resolving Protein Interactions inside Living Cells. *Angew. Chem. Int. Ed.* **2016**, *55* (38), 11668–11672.
(268) Bagheri, A.; Arandiyan, H.; Boyer, C.; Lim, M. Lanthanide-Doped Upconversion Nanoparticles: Emerging Intelligent Light-Activated Drug Delivery Systems. *Adv. Sci.* **2016**, *3* (7), 1500437.
(269) Ruggiero, E.; Castro, S. A.; Habtemariam, A.; Salassa, L. Upconverting Nanoparticles for the near Infrared Photoactivation of Transition Metal Complexes: New Opportunities and Challenges in Medicinal Inorganic Photochemistry. *Dalton Trans.* **2016**, *45* (33), 13012–13020.
(270) Deng, K.; Li, C.; Huang, S.; Xing, B.; Jin, D.; Zeng, Q.; Hou, Z.; Lin, J. Recent Progress in Near Infrared Light Triggered Photodynamic Therapy. *Small* **2017**, *13* (44).
(271) Wang, D.; Xue, B.; Kong, X.; Tu, L.; Liu, X.; Zhang, Y.; Chang, Y.; Luo, Y.; Zhao, H.; Zhang, H. 808 Nm Driven Nd^{3+}-Sensitized Upconversion Nanostructures for Photodynamic Therapy and Simultaneous Fluorescence Imaging. *Nanoscale* **2014**, *7* (1), 190–197.
(272) Chen, Z.; Thiramanas, R.; Schwendy, M.; Xie, C.; Parekh, S. H.; Mailänder, V.; Wu, S. Upconversion Nanocarriers Encapsulated with Photoactivatable Ru Complexes for Near-Infrared Light-Regulated Enzyme Activity. *Small* **2017**, *13* (46), 1700997.
(273) Chen, W.; Shi, C.; Tao, T.; Ji, M.; Zheng, S.; Sang, X.; Liu, X.; Qiu, J. Optical Temperature Sensing with Minimized Heating Effect Using Core–Shell Upconversion Nanoparticles. *RSC Adv.* **2016**, *6* (26), 21540–21545.
(274) Kilbane, J. D.; Chan, E. M.; Monachon, C.; Borys, N. J.; Levy, E. S.; Pickel, A. D.; Urban, J. J.; Schuck, P. J.; Dames, C. Far-Field Optical Nanothermometry Using Individual Sub-50 Nm Upconverting Nanoparticles. *Nanoscale* **2016**, *8* (22), 11611–11616.
(275) Sedlmeier, A.; Achatz, D. E.; Fischer, L. H.; Gorris, H. H.; Wolfbeis, O. S. Photon Upconverting Nanoparticles for Luminescent Sensing of Temperature. *Nanoscale* **2012**, *4* (22), 7090–7096.
(276) Liu, X.; Chen, H.-C.; Kong, X.; Zhang, Y.; Tu, L.; Chang, Y.; Wu, F.; Wang, T.; Reek, J. N. H.; Brouwer, A. M.; et al. Near Infrared Light-Driven Water Oxidation in a Molecule-Based Artificial Photosynthetic Device Using an Upconversion Nano-Photosensitizer. *Chem. Commun.* **2015**, *51* (65), 13008–13011.
(277) Tang, Y.; Di, W.; Zhai, X.; Yang, R.; Qin, W. NIR-Responsive Photocatalytic Activity and Mechanism of NaYF4:Yb,Tm@TiO2 Core–Shell Nanoparticles. *ACS Catal.* **2013**, *3* (3), 405–412.
(278) Xu, Z.; Quintanilla, M.; Vetrone, F.; Govorov, A. O.; Chaker, M.; Ma, D. Harvesting Lost Photons: Plasmon and Upconversion Enhanced Broadband Photocatalytic Activity in

Core@Shell Microspheres Based on Lanthanide-Doped $NaYF_4$, TiO_2, and Au. *Adv. Funct. Mater.* **2015**, *25* (20), 2950–2960.
(279) Hofmann, C. L. M.; Eriksen, E. H.; Fischer, S.; Richards, B. S.; Balling, P.; Goldschmidt, J. C. Enhanced Upconversion in One-Dimensional Photonic Crystals: A Simulation-Based Assessment within Realistic Material and Fabrication Constraints. *Opt. Express* **2018**, *26* (6), 7537–7554.
(280) Kim, W. J.; Nyk, M.; Prasad, P. N. Color-Coded Multilayer Photopatterned Microstructures Using Lanthanide (III) Ion Co-Doped NaYF4nanoparticles with Upconversion Luminescence for Possible Applications in Security. *Nanotechnology* **2009**, *20* (18), 185301.
(281) Gao, W.; Zheng, H.; Han, Q.; He, E.; Wang, R. Unusual Upconversion Emission from Single $NaYF_4$:Yb^{3+}/Ho^{3+} Microrods under NIR Excitation. *CrystEngComm.* **2014**, *16* (29), 6697–6706.
(282) Boyer, J.-C.; Vetrone, F.; Cuccia, L. A.; Capobianco, J. A. Synthesis of Colloidal Upconverting $NaYF_4$ Nanocrystals Doped with Er^{3+}, Yb^{3+} and Tm^{3+}, Yb^{3+} *via* Thermal Decomposition of Lanthanide Trifluoroacetate Precursors. *J. Am. Chem. Soc.* **2006**, *128* (23), 7444–7445.
(283) Wang, F.; Liu, X. Upconversion Multicolor Fine-Tuning: Visible to Near-Infrared Emission from Lanthanide-Doped $NaYF_4$ Nanoparticles. *J. Am. Chem. Soc.* **2008**, *130* (17), 5642–5643.
(284) Ostrowski, A. D.; Chan, E. M.; Gargas, D. J.; Katz, E. M.; Han, G.; Schuck, P. J.; Milliron, D. J.; Cohen, B. E. Controlled Synthesis and Single-Particle Imaging of Bright, Sub-10 Nm Lanthanide-Doped Upconverting Nanocrystals. *ACS Nano* **2012**, *6* (3), 2686–2692.
(285) Liu, G. Advances in the Theoretical Understanding of Photon Upconversion in Rare-Earth Activated Nanophosphors. *Chem. Soc. Rev.* **2015**, *44* (6), 1635–1652.
(286) Ruggiero, E.; Habtemariam, A.; Yate, L.; Mareque-Rivas, J. C.; Salassa, L. Near Infrared Photolysis of a Ru Polypyridyl Complex by Upconverting Nanoparticles. *Chem. Commun.* **2014**, *50* (14), 1715–1718.
(287) Chen, G.; Ågren, H.; Y. Ohulchanskyy, T.; N. Prasad, P. Light Upconverting Core–Shell Nanostructures: Nanophotonic Control for Emerging Applications. *Chem. Soc. Rev.* **2015**, *44* (6), 1680–1713.
(288) Zou, W.; Visser, C.; Maduro, J. A.; Pshenichnikov, M. S.; Hummelen, J. C. Broadband Dye-Sensitized Upconversion of near-Infrared Light. *Nat. Photonics* **2012**, *6* (8), 560–564.
(289) Garfield, D. J.; Borys, N. J.; Hamed, S. M.; Torquato, N. A.; Tajon, C. A.; Tian, B.; Shevitski, B.; Barnard, E. S.; Suh, Y. D.; Aloni, S.; et al. Enrichment of Molecular Antenna Triplets Amplifies Upconverting Nanoparticle Emission. *Nat. Photonics* **2018**, *12* (7), 402–407.
(290) Dou, Q.; Jiang, L.; Kai, D.; Owh, C.; Loh, X. J. Bioimaging and Biodetection Assisted with TTA-UC Materials. *Drug Discov. Today* **2017**, *22* (9), 1400–1411.

(291) Askes, S. H. C.; Brodie, P.; Bruylants, G.; Bonnet, S. Temperature Dependence of Triplet–Triplet Annihilation Upconversion in Phospholipid Membranes. *J. Phys. Chem. B* **2017**, *121* (4), 780–786.
(292) Gray, V.; Moth-Poulsen, K.; Albinsson, B.; Abrahamsson, M. Towards Efficient Solid-State Triplet–Triplet Annihilation Based Photon Upconversion: Supramolecular, Macromolecular and Self-Assembled Systems. *Coordina. Chem. Rev.* **2018**, *362*, 54–71.
(293) Mousavi, M.; Thomasson, B.; Li, M.; Kraft, M.; Würth, C.; Resch-Genger, U.; Andersson-Engels, S. Beam-Profile-Compensated Quantum Yield Measurements of Upconverting Nanoparticles. *Phys. Chem. Chem. Phys.* **2017**, *19* (33), 22016–22022.
(294) Würth, C.; Grabolle, M.; Pauli, J.; Spieles, M.; Resch-Genger, U. Relative and Absolute Determination of Fluorescence Quantum Yields of Transparent Samples. *Nat. Proto.* **2013**, *8* (8), 1535–1550.
(295) Boyer, J.-C.; Veggel, F. C. J. M. van. Absolute Quantum Yield Measurements of Colloidal $NaYF_4$: Er^{3+}, Yb^{3+} Upconverting Nanoparticles. *Nanoscale* **2010**, *2* (8), 1417–1419.
(296) Fischer, S.; Johnson, N. J. J.; Pichaandi, J.; Goldschmidt, J. C.; van Veggel, F. C. J. M. Upconverting Core-Shell Nanocrystals with High Quantum Yield under Low Irradiance: On the Role of Isotropic and Thick Shells. *J. Appl. Phys.* **2015**, *118* (19), 193105.
(297) Kaiser, M.; Würth, C.; Kraft, M.; Hyppänen, I.; Soukka, T.; Resch-Genger, U. Power-Dependent Upconversion Quantum Yield of $NaYF_4$:Yb^{3+},Er^{3+} Nano- and Micrometer-Sized Particles – Measurements and Simulations. *Nanoscale* **2017**, *9* (28), 10051–10058.
(298) Balabhadra, S.; Debasu, M. L.; Brites, C. D. S.; Ferreira, R. A. S.; Carlos, L. D. A Cost-Effective Quantum Yield Measurement Setup for Upconverting Nanoparticles. *J. Lumin.* **2017**, *189*, 64–70.
(299) Würth, C.; Kaiser, M.; Wilhelm, S.; Grauel, B.; Hirsch, T.; Resch-Genger, U. Excitation Power Dependent Population Pathways and Absolute Quantum Yields of Upconversion Nanoparticles in Different Solvents. *Nanoscale* **2017**, *9* (12), 4283–4294.
(300) Pilch, A.; Wawrzyńczyk, D.; Kurnatowska, M.; Czaban, B.; Samoć, M.; Strek, W.; Bednarkiewicz, A. The Concentration Dependent Up-Conversion Luminescence of Ho^{3+} and Yb^{3+} Co-Doped β-$NaYF_4$. *J. Lumin.* **2017**, *182*, 114–122.
(301) Pilch-Wrobel, A.; Czaban, B.; Wawrzyńczyk, D.; Bednarkiewicz, A. Quantum Yield Measurements of Yb,Ho Co-Doped Upconverting Nanomaterials: The Impact of Methods, Reference Materials and Concentration. *J. Lumin.* **2018**, *198*, 482–487.
(302) Würth, C.; Fischer, S.; Grauel, B.; Alivisatos, A. P.; Resch-Genger, U. Quantum Yields, Surface Quenching, and Passivation Efficiency for Ultrasmall Core/Shell Upconverting Nanoparticles. *J. Am. Chem. Soc.* **2018**, *140* (14), 4922–4928.
(303) Homann, C.; Krukewitt, L.; Frenzel, F.; Grauel, B.; Würth, C.; Resch-Genger, U.; Haase, M. $NaYF_4$:Yb,Er/$NaYF_4$ Core/Shell Nanocrystals with High Upconversion Luminescence Quantum Yield. *Angew. Chem. Int. Ed.* **2018**, *57* (28), 8765–8769.
(304) Hossan, M. Y.; Hor, A.; Luu, Q.; Smith, S. J.; May, P. S.; Berry, M. T. Explaining the Nanoscale Effect in the Upconversion Dynamics of β-$NaYF_4$:Yb^{3+}, Er^{3+} Core and Core–Shell Nanocrystals. *J. Phys. Chem. C* **2017**, *121* (30), 16592–16606.

(305) Huang, P.; Zheng, W.; Zhou, S.; Tu, D.; Chen, Z.; Zhu, H.; Li, R.; Ma, E.; Huang, M.; Chen, X. Lanthanide-Doped $LiLuF_4$ Upconversion Nanoprobes for the Detection of Disease Biomarkers. *Angew. Chem. Int. Ed.* **2014**, *53* (5), 1252–1257.
(306) Krämer, K. W.; Biner, D.; Frei, G.; Güdel, H. U.; Hehlen, M. P.; Lüthi, S. R. Hexagonal Sodium Yttrium Fluoride Based Green and Blue Emitting Upconversion Phosphors. *Chem. Mater.* **2004**, *16* (7), 1244–1251.
(307) Quintanilla, M.; Cantarelli, I. X.; Pedroni, M.; Speghini, A.; Vetrone, F. Intense Ultraviolet Upconversion in Water Dispersible SrF_2:Tm^{3+},Yb^{3+} Nanoparticles: The Effect of the Environment on Light Emissions. *J. Mater. Chem. C* **2015**, *3* (13), 3108–3113.
(308) Heer, S.; Lehmann, O.; Haase, M.; Güdel, H.-U. Blue, Green, and Red Upconversion Emission from Lanthanide-Doped $LuPO_4$ and $YbPO_4$ Nanocrystals in a Transparent Colloidal Solution. *Angew. Chem. Int. Ed.* **2003**, *42* (27), 3179–3182.
(309) Liu, X.; Zhao, J.; Sun, Y.; Song, K.; Yu, Y.; Du, C.; Kong, X.; Zhang, H. Ionothermal Synthesis of Hexagonal-Phase $NaYF_4$:Yb^{3+},Er^{3+}/Tm^{3+} Upconversion Nanophosphors. *Chem. Commun.* **2009**, No. 43, 6628–6630.
(310) Fischer, S.; Swabeck, J. K.; Alivisatos, A. P. Controlled Isotropic and Anisotropic Shell Growth in β-$NaLnF_4$ Nanocrystals Induced by Precursor Injection Rate. *J. Am. Chem. Soc.* **2017**, *139* (35), 12325–12332.
(311) Faulkner, D. O.; McDowell, J. J.; Price, A. J.; Perovic, D. D.; Kherani, N. P.; Ozin, G. A. Measurement of Absolute Photoluminescence Quantum Yields Using Integrating Spheres – Which Way to Go? *Laser Photonics Rev.* **2012**, *6* (6), 802–806.
(312) Mello, J. C. de; Wittmann, H. F.; Friend, R. H. An Improved Experimental Determination of External Photoluminescence Quantum Efficiency. *Adv. Mater.* **1997**, *9* (3), 230–232.
(313) Suyver, J. F.; Aebischer, A.; García-Revilla, S.; Gerner, P.; Güdel, H. U. Anomalous Power Dependence of Sensitized Upconversion Luminescence. *Phys. Rev. B* **2005**, *71* (12), 125123.
(314) Pollnau, M.; Gamelin, D. R.; Lüthi, S. R.; Güdel, H. U.; Hehlen, M. P. Power Dependence of Upconversion Luminescence in Lanthanide and Transition-Metal-Ion Systems. *Phys. Rev. B* **2000**, *61* (5), 3337–3346.
(315) Sugiyama, A.; Katsurayama, M.; Anzai, Y.; Tsuboi, T. Spectroscopic Properties of Yb Doped YLF Grown by a Vertical Bridgman Method. *J. Alloys Compd.* **2006**, *408–412*, 780–783.
(316) DeLoach, L. D.; Payne, S. A.; Chase, L. L.; Smith, L. K.; Kway, W. L.; Krupke, W. F. Evaluation of Absorption and Emission Properties of Yb^{3+} Doped Crystals for Laser Applications. *IEEE J. Quantum Elect.* **1993**, *29* (4), 1179–1191.
(317) Jalani, G.; Naccache, R.; H. Rosenzweig, D.; Lerouge, S.; Haglund, L.; Vetrone, F.; Cerruti, M. Real-Time, Non-Invasive Monitoring of Hydrogel Degradation Using $LiYF_4$:Yb^{3+}/Tm^{3+} NIR-to-NIR Upconverting Nanoparticles. *Nanoscale* **2015**, *7* (26), 11255–11262.
(318) Würth, C.; Pauli, J.; Lochmann, C.; Spieles, M.; Resch-Genger, U. Integrating Sphere Setup for the Traceable Measurement of Absolute Photoluminescence Quantum Yields in the Near Infrared. *Anal. Chem.* **2012**, *84* (3), 1345–1352.

(319) Würth, C.; Grabolle, M.; Pauli, J.; Spieles, M.; Resch-Genger, U. Comparison of Methods and Achievable Uncertainties for the Relative and Absolute Measurement of Photoluminescence Quantum Yields. *Anal. Chem.* **2011**, *83* (9), 3431–3439.
(320) Hatami, S.; Würth, C.; Kaiser, M.; Leubner, S.; Gabriel, S.; Bahrig, L.; Lesnyak, V.; Pauli, J.; Gaponik, N.; Eychmüller, A.; et al. Absolute Photoluminescence Quantum Yields of IR26 and IR-Emissive $Cd_{(1-x)}Hg_{(x)}Te$ and PbS Quantum Dots--Method- and Material-Inherent Challenges. *Nanoscale* **2015**, *7* (1), 133–143.
(321) Resch-Genger, U.; Bremser, W.; Pfeifer, D.; Spieles, M.; Hoffmann, A.; DeRose, P. C.; Zwinkels, J. C.; Gauthier, F.; Ebert, B.; Taubert, R. D.; et al. State-of-the Art Comparability of Corrected Emission Spectra.1. Spectral Correction with Physical Transfer Standards and Spectral Fluorescence Standards by Expert Laboratories. *Anal. Chem.* **2012**, *84* (9), 3889–3898.
(322) Sharifi, S.; Behzadi, S.; Laurent, S.; Forrest, M. L.; Stroeve, P.; Mahmoudi, M. Toxicity of Nanomaterials. *Chemical Society Reviews* **2012**, *41* (6), 2323–2343.
(323) Zhang, X.; Bloch, S.; Akers, W.; Achilefu, S. Near-Infrared Molecular Probes for *in vivo* Imaging. *Curr. Protoc. Cytom.* **2012**, *CHAPTER*, Unit12.27.
(324) Park, Y. I.; Lee, K. T.; Suh, Y. D.; Hyeon, T. Upconverting Nanoparticles: A Versatile Platform for Wide-Field Two-Photon Microscopy and Multi-Modal in Vivo Imaging. *Chem. Soc. Rev.* **2015**, *44* (6), 1302–1317.
(325) Sabri, T.; Pawelek, P. D.; Capobianco, J. A. Dual Activity of Rose Bengal Functionalized to Albumin-Coated Lanthanide-Doped Upconverting Nanoparticles: Targeting and Photodynamic Therapy. *ACS Appl. Mater. Interfaces* **2018**, *10* (32), 26947–26953.
(326) Martín Rodríguez, E.; Bogdan, N.; Capobianco, J. A.; Orlandi, S.; Cavazzini, M.; Scalera, C.; Quici, S. A Highly Sensitive Luminescent Lectin Sensor Based on an α-D-Mannose Substituted Tb^{3+} Antenna Complex. *Dalton Trans* **2013**, *42* (26), 9453–9461.
(327) Rock, J. R.; Hogan, B. L. M. Epithelial Progenitor Cells in Lung Development, Maintenance, Repair, and Disease. *Annu. Rev. Cell Dev. Biol.* **2011**, *27*, 493–512.
(328) Rojas-Gutierrez, P. A.; Bhuckory, S.; Mingoes, C.; Hildebrandt, N.; DeWolf, C.; Capobianco, J. A. A Route to Triggered Delivery *via* Photocontrol of Lipid Bilayer Properties Using Lanthanide Upconversion Nanoparticles. *ACS Appl. Nano Mater.* **2018**, *1* (9), 5345–5354.
(329) Neves, A. R.; Queiroz, J. F.; Costa Lima, S. A.; Figueiredo, F.; Fernandes, R.; Reis, S. Cellular Uptake and Transcytosis of Lipid-Based Nanoparticles across the Intestinal Barrier: Relevance for Oral Drug Delivery. *J. Colloid Interf. Sci.* **2016**, *463*, 258–265.
(330) Scudiero, D. A.; Shoemaker, R. H.; Paull, K. D.; Monks, A.; Tierney, S.; Nofziger, T. H.; Currens, M. J.; Seniff, D.; Boyd, M. R. Evaluation of a Soluble Tetrazolium/Formazan Assay for Cell Growth and Drug Sensitivity in Culture Using Human and Other Tumor Cell Lines. *Cancer Res.* **1988**, *48* (17), 4827–4833.
(331) Jin, J.; Gu, Y.-J.; Man, C. W.-Y.; Cheng, J.; Xu, Z.; Zhang, Y.; Wang, H.; Lee, V. H.-Y.; Cheng, S. H.; Wong, W.-T. Polymer-Coated $NaYF_4$:Yb^{3+},Er^{3+} Upconversion Nanoparticles for Charge-Dependent Cellular Imaging. *ACS Nano* **2011**, *5* (10), 7838–7847.

(332) Tree-Udom, T.; Seemork, J.; Shigyou, K.; Hamada, T.; Sangphech, N.; Palaga, T.; Insin, N.; Pan-In, P.; Wanichwecharungruang, S. Shape Effect on Particle-Lipid Bilayer Membrane Association, Cellular Uptake, and Cytotoxicity. *ACS Appl. Mater. Interfaces* **2015**, *7* (43), 23993–24000.
(333) Bhattacharjee, S.; de Haan, L. H. J.; Evers, N. M.; Jiang, X.; Marcelis, A. T. M.; Zuilhof, H.; Rietjens, I. M. C. M.; Alink, G. M. Role of Surface Charge and Oxidative Stress in Cytotoxicity of Organic Monolayer-Coated Silicon Nanoparticles towards Macrophage NR8383 Cells. *Part. Fibre Toxicol.* **2010**, *7*, 25.
(334) Zhang, D.; Wei, L.; Zhong, M.; Xiao, L.; Li, H.-W.; Wang, J. The Morphology and Surface Charge-Dependent Cellular Uptake Efficiency of Upconversion Nanostructures Revealed by Single-Particle Optical Microscopy. *Chem. Sci.* **2018**, *9* (23), 5260–5269.
(335) Guller, A. E.; Generalova, A. N.; Petersen, E. V.; Nechaev, A. V.; Trusova, I. A.; Landyshev, N. N.; Nadort, A.; Grebenik, E. A.; Deyev, S. M.; Shekhter, A. B.; et al. Cytotoxicity and Non-Specific Cellular Uptake of Bare and Surface-Modified Upconversion Nanoparticles in Human Skin Cells. *Nano Res.* **2015**, *8* (5), 1546–1562.
(336) Chen, S.; Zhang, C.; Jia, G.; Duan, J.; Wang, S.; Zhang, J. Size-Dependent Cytotoxicity of Europium Doped NaYF4 Nanoparticles in Endothelial Cells. *Mater. Sci. Eng. C* **2014**, *43*, 330–342.
(337) Stochaj, U.; Burbano, D. C. R.; Cooper, D. R.; Kodiha, M.; Capobianco, J. A. The Effects of Lanthanide-Doped Upconverting Nanoparticles on Cancer Cell Biomarkers. *Nanoscale* **2018**, *10* (30), 14464–14471.
(338) Das, G. K.; Stark, D. T.; Kennedy, I. M. Potential Toxicity of Up-Converting Nanoparticles Encapsulated with a Bilayer Formed by Ligand Attraction. *Langmuir* **2014**, *30* (27), 8167–8176.
(339) Ashfaq, U. A.; Javed, T.; Rehman, S.; Nawaz, Z.; Riazuddin, S. Lysosomotropic Agents as HCV Entry Inhibitors. *Virol. J.* **2011**, *8* (1), 163.
(340) De Duve, C.; De Barsy, T.; Poole, B.; Trouet, A.; Tulkens, P.; Van Hoof, F. Lysosomotropic Agents. *Biochem. Pharmacol.* **1974**, *23* (18), 2495–2531.
(341) Rejman, J.; Bragonzi, A.; Conese, M. Role of Clathrin- and Caveolae-Mediated Endocytosis in Gene Transfer Mediated by Lipo- and Polyplexes. *Mol. Therapy* **2005**, *12* (3), 468–474.
(342) Sharma, D. K.; Brown, J. C.; Choudhury, A.; Peterson, T. E.; Holicky, E.; Marks, D. L.; Simari, R.; Parton, R. G.; Pagano, R. E. Selective Stimulation of Caveolar Endocytosis by Glycosphingolipids and Cholesterol. *Mol. Biol. Cell* **2004**, *15* (7), 3114–3122.
(343) Stoeber, M.; Schellenberger, P.; Siebert, C. A.; Leyrat, C.; Helenius, A.; Grünewald, K. Model for the Architecture of Caveolae Based on a Flexible, Net-like Assembly of Cavin1 and Caveolin Discs. *PNAS* **2016**, *113* (50), E8069–E8078.
(344) Brandizzi, F.; Barlowe, C. Organization of the ER–Golgi Interface for Membrane Traffic Control. *Nat. Rev. Mol. Cell Biol.* **2013**, *14* (6), 382–392.
(345) Greenspan, P.; Lou, P. Spectrofluorometric Studies of Nile Red Treated Native and Oxidized Low Density Lipoprotein. *Int. J. Biochem.* **1993**, *25* (7), 987–991.

(346) Diaz, G.; Melis, M.; Batetta, B.; Angius, F.; Falchi, A. M. Hydrophobic Characterization of Intracellular Lipids in Situ by Nile Red Red/Yellow Emission Ratio. *Micron* **2008**, *39* (7), 819–824.
(347) Liu, L.; Wang, M.; Fisher, A. B.; Zimmerman, U. J. Involvement of Annexin II in Exocytosis of Lamellar Bodies from Alveolar Epithelial Type II Cells. *Am. J. Physiol-Lung C.* **1996**, *270* (4), L668-L676.
(348) Beers, M. F. Inhibition of Cellular Processing of Surfactant Protein C by Drugs Affecting Intracellular PH Gradients. *J. Biol. Chem.* **1996**, *271* (24), 14361–14370.
(349) Olzmann, J. A.; Carvalho, P. Dynamics and Functions of Lipid Droplets. *Nat. Rev. Mol. Cell Biol.* **2019**, *20* (3), 137-155.
(350) Brites, C. D. S.; Balabhadra, S.; Carlos, L. D. Lanthanide-Based Thermometers: At the Cutting-Edge of Luminescence Thermometry. *Adv. Opt. Mater.* **2019**, *7* (5), 1801239.
(351) Dramićanin, M. *Luminescence Thermometry: Methods, Materials, and Applications*; Woodhead Publishing: Cambridge, **2018**.
(352) Carlos, L. D.; Palacio, F. *Thermometry at the Nanoscale: Techniques and Selected Applications*, 1 edition.; Royal Society of Chemistry: Cambridge, **2015**.
(353) Lowell, B. B.; Spiegelman, B. M. Towards a Molecular Understanding of Adaptive Thermogenesis. *Nature* **2000**, *404* (6778), 652–660.
(354) Guo, M.; Xu, Y.; Gruebele, M. Temperature Dependence of Protein Folding Kinetics in Living Cells. *PNAS* **2012**, *109* (44), 17863–17867.
(355) Atia, L.; Givli, S. A Theoretical Study of Biological Membrane Response to Temperature Gradients at the Single-Cell Level. *J R Soc. Interface* **2014**, *11* (95), 20131207.
(356) Ibraimov, A. I. Cell Thermoregulation: Problems, Advances and Perspectives. *J. Mol. Biol. Res.* **2017**, *7* (1), 58-79.
(357) Jaque, D.; Rosal, B. del; Rodríguez, E. M.; Maestro, L. M.; Haro-González, P.; Solé, J. G. Fluorescent Nanothermometers for Intracellular Thermal Sensing. *Nanomed.* **2014**, *9* (7), 1047–1062.
(358) Bai, T.; Gu, N. Micro/Nanoscale Thermometry for Cellular Thermal Sensing. *Small* **2016**, *12* (34), 4590–4610.
(359) Uchiyama, S.; Gota, C.; Tsuji, T.; Inada, N. Intracellular Temperature Measurements with Fluorescent Polymeric Thermometers. *Chem. Commun.* **2017**, *53* (80), 10976–10992.
(360) Okabe, K.; Sakaguchi, R.; Shi, B.; Kiyonaka, S. Intracellular Thermometry with Fluorescent Sensors for Thermal Biology. *Pflugers Arch - Eur. J. Physiol.* **2018**, *470* (5), 717–731.
(361) Savchuk, O. A.; Silvestre, O. F.; Adão, R. M. R.; Nieder, J. B. GFP Fluorescence Peak Fraction Analysis Based Nanothermometer for the Assessment of Exothermal Mitochondria Activity in Live Cells. *Sci. Rep.* **2019**, *9* (1), 1–11.
(362) Chrétien, D.; Bénit, P.; Ha, H.-H.; Keipert, S.; El-Khoury, R.; Chang, Y.-T.; Jastroch, M.; Jacobs, H. T.; Rustin, P.; Rak, M. Mitochondria Are Physiologically Maintained at Close to 50 °C. *PLOS Biology* **2018**, *16* (1), e2003992.
(363) Tanimoto, R.; Hiraiwa, T.; Nakai, Y.; Shindo, Y.; Oka, K.; Hiroi, N.; Funahashi, A. Detection of Temperature Difference in Neuronal Cells. *Sci. Rep.* **2016**, *6*, 22071.

(364) Okabe, K.; Inada, N.; Gota, C.; Harada, Y.; Funatsu, T.; Uchiyama, S. Intracellular Temperature Mapping with a Fluorescent Polymeric Thermometer and Fluorescence Lifetime Imaging Microscopy. *Nat. Commun.* **2012**, *3*, 705.
(365) Chen, X.; Xia, Q.; Cao, Y.; Min, Q.; Zhang, J.; Chen, Z.; Chen, H.-Y.; Zhu, J.-J. Imaging the Transient Heat Generation of Individual Nanostructures with a Mechanoresponsive Polymer. *Nat. Commun.* **2017**, *8* (1), 1–10.
(366) Ye, F.; Wu, C.; Jin, Y.; Chan, Y.-H.; Zhang, X.; Chiu, D. T. Ratiometric Temperature Sensing with Semiconducting Polymer Dots. *J. Am. Chem. Soc.* **2011**, *133* (21), 8146–8149.
(367) Suzuki, M.; Tseeb, V.; Oyama, K.; Ishiwata, S. Microscopic Detection of Thermogenesis in a Single HeLa Cell. *Biophys. J.* **2007**, *92* (6), L46–L48.
(368) Vetrone, F.; Naccache, R.; Zamarrón, A.; Juarranz de la Fuente, A.; Sanz-Rodríguez, F.; Martinez Maestro, L.; Martín Rodriguez, E.; Jaque, D.; García Solé, J.; Capobianco, J. A. Temperature Sensing Using Fluorescent Nanothermometers. *ACS Nano* **2010**, *4* (6), 3254–3258.
(369) Piñol, R.; Brites, C. D. S.; Bustamante, R.; Martínez, A.; Silva, N. J. O.; Murillo, J. L.; Cases, R.; Carrey, J.; Estepa, C.; Sosa, C.; et al. Joining Time-Resolved Thermometry and Magnetic-Induced Heating in a Single Nanoparticle Unveils Intriguing Thermal Properties. *ACS Nano* **2015**, *9* (3), 3134–3142.
(370) Jain, S.; Hirst, D. G.; O'Sullivan, J. M. Gold Nanoparticles as Novel Agents for Cancer Therapy. *BJR* **2012**, *85* (1010), 101–113.
(371) Baffou, G.; Quidant, R. Thermo-Plasmonics: Using Metallic Nanostructures as Nano-Sources of Heat. *Laser Photonics Rev.* **2013**, *7* (2), 171–187.
(372) Rosal, B. del; Ruiz, D.; Chaves-Coira, I.; Juárez, B. H.; Monge, L.; Hong, G.; Fernández, N.; Jaque, D. In Vivo Contactless Brain Nanothermometry. *Adv. Funct. Mater.* **2018**, *28* (52), 1806088.
(373) Ximendes, E. C.; Rocha, U.; Sales, T. O.; Fernández, N.; Sanz-Rodríguez, F.; Martín, I. R.; Jacinto, C.; Jaque, D. In Vivo Subcutaneous Thermal Video Recording by Supersensitive Infrared Nanothermometers. *Adv. Funct. Mater.* **2017**, *27* (38), 1702249.
(374) Zhou, B.; Shi, B.; Jin, D.; Liu, X. Controlling Upconversion Nanocrystals for Emerging Applications. *Nat. Nanotechnol.* **2015**, *10* (11), 924–936.
(375) Bettinelli, M.; Carlos, L.; Liu, X. Lanthanide-Doped Upconversion Nanoparticles. *Phys. Today* **2015**, *68* (9), 38–44.
(376) Zhou, J.; Liu, Q.; Feng, W.; Sun, Y.; Li, F. Upconversion Luminescent Materials: Advances and Applications. *Chem. Rev.* **2015**, *115* (1), 395–465.
(377) Brites, C. D. S.; Xie, X.; Debasu, M. L.; Qin, X.; Chen, R.; Huang, W.; Rocha, J.; Liu, X.; Carlos, L. D. Instantaneous Ballistic Velocity of Suspended Brownian Nanocrystals Measured by Upconversion Nanothermometry. *Nat. Nanotechnol.* **2016**, *11* (10), 851–856.
(378) Martínez, E. D.; Brites, C. D. S.; Carlos, L. D.; García-Flores, A. F.; Urbano, R. R.; Rettori, C. Electrochromic Switch Devices Mixing Small- and Large-Sized Upconverting Nanocrystals. *Adv. Func. Mater.* **2019**, *29* (8), 1807758.

(379) Youssefian, S.; Rahbar, N.; Van Dessel, S. Thermal Conductivity and Rectification in Asymmetric Archaeal Lipid Membranes. *J. Chem. Phys.* **2018**, *148* (17), 174901.
(380) Wang, Y.; Qin, Z.; Buehler, M. J.; Xu, Z. Intercalated Water Layers Promote Thermal Dissipation at Bio–Nano Interfaces. *Nat. Commun.* **2016**, *7*, 12854.
(381) Potdar, D.; Sammalkorpi, M. Asymmetric Heat Transfer from Nanoparticles in Lipid Bilayers. *Chem. Phys.* **2015**, *463*, 22–29.
(382) Youssefian, S.; Rahbar, N.; Lambert, C. R.; Van Dessel, S. Variation of Thermal Conductivity of DPPC Lipid Bilayer Membranes around the Phase Transition Temperature. *J. R. Soc. Interface* **2017**, *14* (130), 20170127.
(383) Saidur, R.; Leong, K. Y.; Mohammad, H. A. A Review on Applications and Challenges of Nanofluids. *Renew. Sust. Energ. Rev.* **2011**, *15* (3), 1646–1668.
(384) Balabhadra, S.; Debasu, M. L.; Brites, C. D. S.; Ferreira, R. A. S.; Carlos, L. D. Upconverting Nanoparticles Working As Primary Thermometers In Different Media. *J. Phys. Chem. C* **2017**, *121* (25), 13962–13968.
(385) Brites, C. D. S.; Fuertes, M. C.; Angelomé, P. C.; Martínez, E. D.; Lima, P. P.; Soler-Illia, G. J. A. A.; Carlos, L. D. Tethering Luminescent Thermometry and Plasmonics: Light Manipulation to Assess Real-Time Thermal Flow in Nanoarchitectures. *Nano Lett.* **2017**, *17* (8), 4746–4752.
(386) Baffou, G.; Quidant, R.; García de Abajo, F. J. Nanoscale Control of Optical Heating in Complex Plasmonic Systems. *ACS Nano* **2010**, *4* (2), 709–716.
(387) Ramires, M. L. V.; Nieto de Castro, C. A.; Nagasaka, Y.; Nagashima, A.; Assael, M. J.; Wakeham, W. A. Standard Reference Data for the Thermal Conductivity of Water. *J. Phys. Chem. Ref. Data* **1995**, *24* (3), 1377–1381.
(388) Kedenburg, S.; Vieweg, M.; Gissibl, T.; Giessen, H. Linear Refractive Index and Absorption Measurements of Nonlinear Optical Liquids in the Visible and Near-Infrared Spectral Region. *Opt. Mater. Express* **2012**, *2* (11), 1588–1611.
(389) Angayarkanni, S. A.; Philip, J. Review on Thermal Properties of Nanofluids: Recent Developments. *Adv. Colloid Interface Sci.* **2015**, *225*, 146–176.
(390) Lee, S.; Choi, S. U.-S.; Li, S.; Eastman, J. A. Measuring Thermal Conductivity of Fluids Containing Oxide Nanoparticles. *J. Heat Transfer* **1999**, *121* (2), 280–289.
(391) Nakano, T.; Kikugawa, G.; Ohara, T. Molecular Heat Transfer in Lipid Bilayers With Symmetric and Asymmetric Tail Chains. *J. Heat Transfer* **2013**, *135* (6), 061301-061301–061308.
(392) Lienhard IV, J. H.; Lienhard V, J. H. *A Heat Transfer Textbook, Third Edition*, 3rd edition.; Phlogiston Press: Cambridge, **2003**.
(393) Schilling, A.; Zhang, X.; Bossen, O. Heat Flowing from Cold to Hot without External Intervention by Using a "Thermal Inductor." *Sci. Adv.* **2019**, *5* (4), eaat9953.
(394) Aggarwal, R. L.; Ripin, D. J.; Ochoa, J. R.; Fan, T. Y. Measurement of Thermo-Optic Properties of $Y_3Al_5O_{12}$, $Lu_3Al_5O_{12}$, $YAlO_3$, $LiYF_4$, $LiLuF_4$, BaY_2F_8, $KGd(WO_4)_2$, and $KY(WO_4)_2$ Laser Crystals in the 80–300K Temperature Range. *J. Appl. Phys.* **2005**, *98* (10), 103514.

(395) Semashko, V. V.; Korableva, S. L.; Nizamutdinov, A. S.; Kuznetsov, S. V.; Pynenkov, A. A.; Popov, P. A.; Baranchikov, A. E.; Nishchev, K. N.; Ivanov, V. K.; Fedorov, P. P. Phase Equilibria in $LiYF_4$–$LiLuF_4$ System and Heat Conductivity of $LiY_{1-X}Lu_xF_4$ Single Crystals. *Russ. J. Inorg. Chem.* **2018**, *63* (4), 433–438.
(396) Challoner A. R.; Powell R. W.; Griffiths Ezer. Thermal Conductivities of Liquids: New Determinations for Seven Liquids and Appraisal of Existing Values. *Proc. R. Soc. Lond. A. Mat. Phys. Sci.* **1956**, *238* (1212), 90–106.
(397) Palmer, K. F.; Williams, D. Optical Properties of Water in the near Infrared*. *J. Opt. Soc. Am., JOSA* **1974**, *64* (8), 1107–1110.
(398) Saxena, S. C.; Saxena, V. K. Thermal Conductivity Data for Hydrogen and Deuterium in the Range 100-1100 Degrees C. *J. Phys. A: Gen. Phys.* **1970**, *3* (3), 309–320.
(399) Bey, E. A.; Bentle, M. S.; Reinicke, K. E.; Dong, Y.; Yang, C.-R.; Girard, L.; Minna, J. D.; Bornmann, W. G.; Gao, J.; Boothman, D. A. An NQO1- and PARP-1-Mediated Cell Death Pathway Induced in Non-Small-Cell Lung Cancer Cells by β-Lapachone. *PNAS* **2007**, *104* (28), 11832–11837.
(400) Woo, H. J.; Choi, Y. H. Growth Inhibition of A549 Human Lung Carcinoma Cells by β-Lapachone through Induction of Apoptosis and Inhibition of Telomerase Activity. *Int. J. Oncol.* **2005**, *26* (4), 1017–1023.
(401) Planchon, S. M.; Pink, J. J.; Tagliarino, C.; Bornmann, W. G.; Varnes, M. E.; Boothman, D. A. Beta-Lapachone-Induced Apoptosis in Human Prostate Cancer Cells: Involvement of NQO1/Xip3. *Exp. Cell Res.* **2001**, *267* (1), 95–106.
(402) Lee, J. I.; Choi, D. Y.; Chung, H. S.; Seo, H. G.; Woo, H. J.; Choi, B. T.; Choi, Y. H. Beta-Lapachone Induces Growth Inhibition and Apoptosis in Bladder Cancer Cells by Modulation of Bcl-2 Family and Activation of Caspases. *Exp. Oncol.* **2006**, *28* (1), 30–35.
(403) Lai, C. C.; Liu, T. J.; Ho, L. K.; Don, M. J.; Chau, Y. P. Beta-Lapachone Induced Cell Death in Human Hepatoma (HepA2) Cells. *Histol. Histopathol.* **1998**, *13* (1), 89–97.
(404) Nasongkla, N.; Wiedmann, A. F.; Bruening, A.; Beman, M.; Ray, D.; Bornmann, W. G.; Boothman, D. A.; Gao, J. Enhancement of Solubility and Bioavailability of β-Lapachone Using Cyclodextrin Inclusion Complexes. *Pharm. Res.* **2003**, *20* (10), 1626–1633.
(405) Kim, I.; Kim, H.; Ro, J.; Jo, K.; Karki, S.; Khadka, P.; Yun, G.; Lee, J. Preclinical Pharmacokinetic Evaluation of β-Lapachone: Characteristics of Oral Bioavailability and First-Pass Metabolism in Rats. *Biomol. Ther. (Seoul)* **2015**, *23* (3), 296–300.
(406) DeRosa, M. C.; Crutchley, R. J. Photosensitized Singlet Oxygen and Its Applications. *Coord. Chem. Rev.* **2002**, *233–234*, 351–371.
(407) Hopper, C. Photodynamic Therapy: A Clinical Reality in the Treatment of Cancer. *Lancet Oncol.* **2000**, *1* (4), 212–219.
(408) Lamberts, J. J. M.; Schumacher, D. R.; Neckers, D. C. Novel Rose Bengal Derivatives: Synthesis and Quantum Yield Studies. *J. Am. Chem. Soc.* **1984**, *106* (20), 5879–5883.
(409) Toy, R.; Peiris, P. M.; Ghaghada, K. B.; Karathanasis, E. Shaping Cancer Nanomedicine: The Effect of Particle Shape on the *in vivo* Journey of Nanoparticles. *Nanomedicine (Lond)* **2014**, *9* (1), 121–134.